OPTICAL BEAM INDUCED PHENOMENA IN SEMICONDUCTORS

By

Paul D. Pester

Brasenose College

Trinity Term, 1988

A THESIS
SUBMITTED FOR THE DEGREE OF
DOCTOR OF PHILOSOPHY
AT THE UNIVERSITY OF OXFORD

The Department of Engineering Science
Parks Road
Oxford

ABSTRACT

Paul D. Pester
Brasenose College

Thesis submitted for the D. Phil. degree
Trinity Term 1988

OPTICAL BEAM INDUCED PHENOMENA IN SEMICONDUCTORS

This thesis is concerned with the interaction of a finely focussed light beam and a semiconductor. The object of the work is to develop a consistent theory which explains the formation of both the optical beam induced current and photoluminescence signals with a view to using these techniques to characterize semiconductor materials.

Here we extend previous theories by considering a light beam which is *focussed* through a lens of finite numerical aperture. Expressions are derived which give the distribution of excess minority carriers injected into a semi-infinite semiconductor by the focussed light beam. The injected minority carrier distribution is then used to predict the imaging properties of the optical beam induced current and photoluminescence techniques when used to image electrically active defects in semiconductors. High resolution scanning photoluminescence images of indium phosphide are presented showing a resolution which is in good agreement with theory.

The form of both the steady state and time dependent optical beam induced current in Schottky barrier diodes, planar junction diodes and devices where the p-n junction is perpendicular to the semiconductor surface is derived. Various methods are suggested for measuring the minority carrier diffusion length and lifetime. An extension to previous analyses is given by considering the effect of *scanning* the light beam, at some arbitrary velocity, on the form of the optical beam induced current collected by a p-n junction either parrallel or perpendicular to the semiconductor surface. It is also shown how the scan speed can effect the imaging of electrically active defects producing a contrast function which is asymmetric and reduced in magnitude.

An analysis of the photoluminescence signal generated from a semi-infinite semiconductor by a finely focussed light beam is given. Various methods based on the photoluminescence technique are suggested for measuring the minority carrier lifetime.

To my parents

for their endless support and encouragement

Acknowledgements

It is with the greatest pleasure that I thank my supervisor, Dr. Tony Wilson, with whom it has been a privilege to work so closely during my three years in Oxford, for his guidance, friendship and encouragement.

I am also indebted to many members of the physical electronics group, especially Dr. Hubert Mathews for his help with many of the early computer programs and Dr. Doug Hamilton whose help with the experimental work was much valued. I would also like to thank Dr. Colin Sheppard for many interesting conversations, including the ones concerned with the work in this thesis, and for often offering useful advice on the mathematics.

I would like to thank Texas Instruments Ltd. of Bedford who provided some of the funding for the work reported in this thesis, and especially my industrial supervisor Dr. Dave Cotton whose enthusiasm and interest were very appreciated.

And finally thanks are due to my fellow graduate students, most notably the *Benson Road inmates*; Brian *"helpful"* Holcroft, Adrian *"slappy"* Hughes and Tina *"I'll do the washing-up"* Blake without whom the last three years would not have been quite the same!

CONTENTS

CHAPTER 1: INTRODUCTION

Since the invention of the transistor by Bardeen and Brattain in 1948 [1,2,3] when interest in semiconductor physics increased dramatically various methods for have been proposed for the characterization of semiconductor materials. The vast majority of these methods are ones where current carriers are added at one location and the resulting added carrier concentration or flow density determined at another. Initially the excess carriers were injected by passing a small current through a metalic point probe which was in contact with the semiconductor surface [4,5], with another probe being used to measure the resulting induced minority carrier distribution [6] as a function of position.

In 1950 Goucher [7] showed that light could provide a convenient means of carrier injection since electron hole pairs are produced with a quantum efficiency close to unity over a large range of excitation wavelengths. Using light to excite excess carriers in samples, where there existed a large applied electric field and hence drift current, enabled the minority carrier diffusion length to be found by measurement of the change in the drift current due to the photo-injected carriers. This change in the drift current has been measured via the steady state photovoltage of a point contact [8] and the drift photocurrent through a p-n juction [9]. There are various attractions to using light instead of the point probe to inject the excess carriers, one of the main ones being that it is fairly easy to ensure the concentration of carriers injection is low compared to the background doping which in turn means that, when the drift current dominates over the diffusion current, simple proportionalities apply between the injected minority carrier distribution and the measured photovoltage or photocurrent [4,6]. It is also easy to vary the depth at which the majority of the excess carriers are generated by simply varing the wavelength of the light and so either bulk [10] or surface effects [9] may be investigated and, of course, all these methods benefit from the nondestructive nature of the light probe.

With the advent of the Scanning Electron Microscope (SEM) there was great interest in using the primary electron beam to excite excess current carriers in a semiconducting sample and hence measure material parameters [11,12] by a study of the *Electron*

Beam Induced Current (EBIC) signal. In this technique excess carriers are excited in the sample, usually when there is no applied electric field, and diffuse and recombine until they are separated by a rectifying contact to constitute a current. The great attraction of using the primary electron beam to inject carriers lies in the high spatial resolution that is obtainable since, at high beam energies, the position of the beam is very well defined which in turn means that the point of carrier injection is well known. This allows different imaging modes to be developed since, for instance, if the EBIC signal is measured and used to modulate the brightness of a monitor, which is scanning in synchronism with the electron beam, an image of the current induced as the beam scans over the surface of the device may be formed [11]. It is also possible to image electrically active defects near the surface of a sample since, in the region of the defect where the minority carrier recombination rate *increases*, the induced current *decreases* which leads to a fall in the EBIC signal which in turn is visualised as a dark region on the monitor. Another method by which it is possible to investigate electrically active defects is by observing the radiation emitted when a carrier, which has been excited by the primary electron beam, recombines via a radiative recombination. The emmited radiation is termed *cathodoluminescence* (CL) [13] and, just as in the EBIC case, it is possible to modulate the brightness of a monitor to form a cathodoluminescence image of the sample, this technique has the advantage that no contacts have to be made to the sample and so semiconductor wafers may be examined prior to processing.

However, there are severe drawbacks associated with these electron beam based methods. The main problem is two fold in nature; firstly, when the primary electron beam enters the semiconductor the primary electrons undergo high energy collisions with the constituent atoms and it has been shown, by both experiment [14,15] and Monte Carlo simulations [15,16], that, as a result, the probe tends to spread out under the surface into a rather pair shaped region which is difficult to represent analytically [17] and leads to a decrease in the maximum resolution obtainable in the beam induced carrier methods, since the position of the *subsurface* probe is not well known. Secondly problems arise from the charged nature of the probe since it is possible for primary electrons to become trapped in nonconducting surface layers causing the formation of surface states, which in turn modify the electrical properties of the device under test and can also cause distortion of the SEM image. Other problems associated with the electron beam method stem from the need for a vacuum system since, in the region of local heating were the beam impinges on the sample surface, it is possible for organic vapours which are always present in the vacuum systems to be absorbed by the semiconducting sample and again cause permanent damage. For these reasons the electron beam testing system, as applied to semiconductor examination, *cannot* be thought of as being truly nondestructive.

A solution to the problems caused by the electron beam in the EBIC and CL techniques is to replace the beam of electrons with its optical analogue, that is the photon beam of a laser, and use a Scanning Optical Microscope (SOM) [18] to return to the case where light is used to excite the excess carriers. It is then possible to obtain the optical equivalent of the EBIC and CL signals, that is, *Optical Beam Induced Current* (OBIC) [19] and *Photoluminescence* (PL) [20,21] images of semiconducting samples. The use of the SOM has the advantages of the SEM in that it is a high resolution system capable of injecting carriers at well defined positions and, as such, is able to image electrically active defects with both the OBIC and PL techniques, although it suffers from none of the disadvantages since the laser beam can be of low intensity and so nondestructive in nature [22].

Figure (1.1) shows a comparison of OBIC and EBIC images of defects in a silicon bipolar transitor [22]. It is clear from Figure (1.1) that the resolution and contrast obtained in the two techniques is similar although there are some extra horizontal lines present in the OBIC image. This is because the EBIC image was obained first and in the process the electron beam was scanned across the device in a line scan to take contrast measurements which lead to the electron beam damage as seen in the OBIC image.

Even though the EBIC and OBIC images are similar the physical mechanism by which each image is formed is very different. There are also fundamental differences in using the SOM to examine semiconductors in the OBIC and PL techniques and using light to excite carries as in the early experiments of the 1950's [7,8,9,10]. These differences arise since, in the SOM, a monochromatic light beam (usually from a laser) is focussed through a high numerical aperture lens onto the surface of the sample and, as such, the light distribution inside the semiconductor [23], which leads to the excess carrier distribution, is very different from that when there is no focussing present, as was the situation in the early experiments, or from the case when an electron beam provides the excitation. Also, in the experiments of the 1950's, rods or simple slabs of semiconducting material were used with a high applied electric field such that the drift current dominated over the diffusion term and the theoretical models [8,9,10], which were formulated to explain the results obtained from these experiments, essentially considered the samples to be infinite in extent and assumed that the generation took place at one point only in the bulk. This implies the collected photocurrent and photoluminescence signals will differ considerably from that predicted by the early theories.

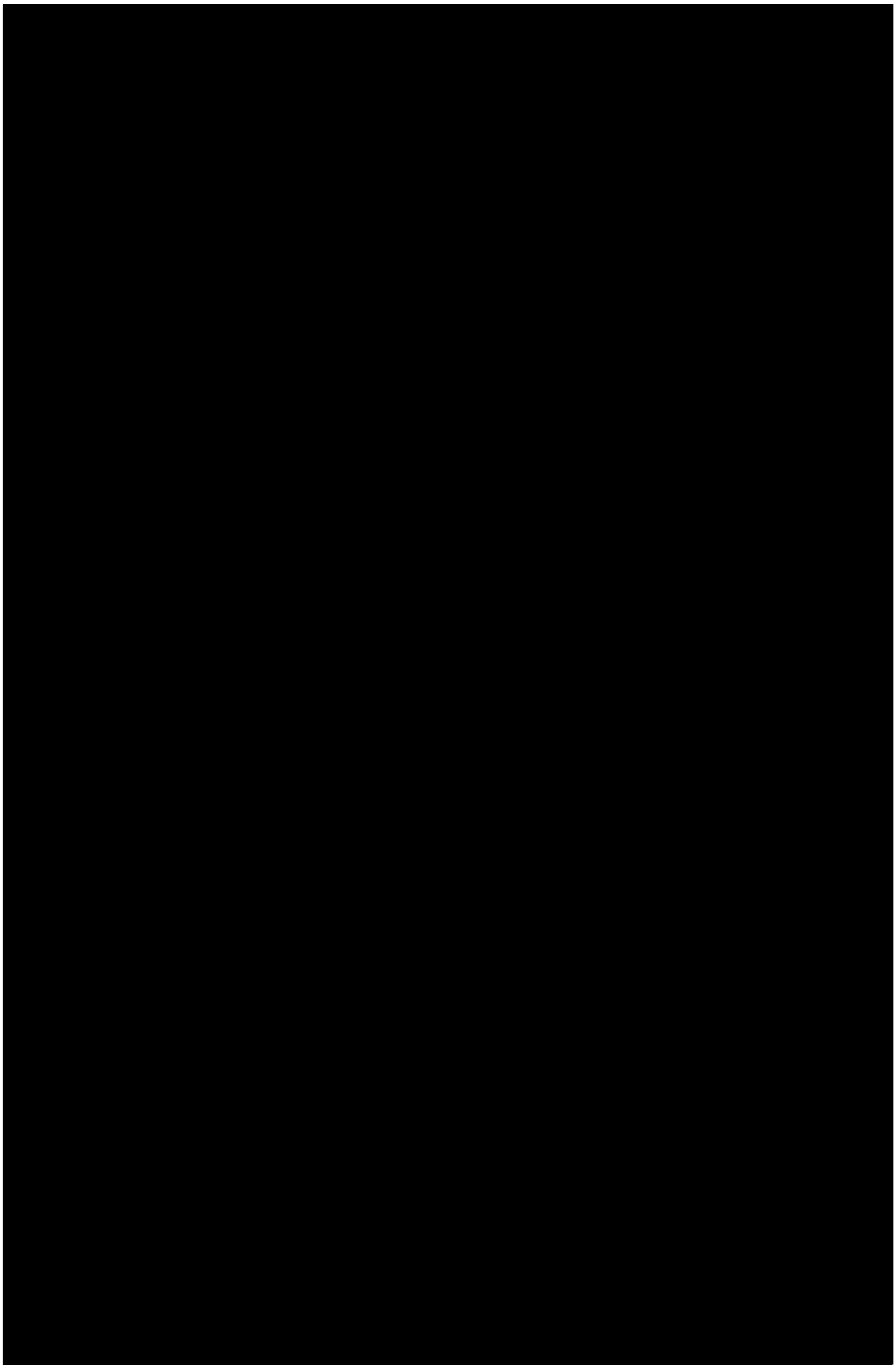

Figure 1.1. A comparison of EBIC (top) and OBIC (bottom) images of a silicon bipolar transistor. Electrically active defects can be clearly seen as the dark lines on both images, and it is clear that the resolution and contrast for both techniques is similar [reproduced from reference 22].

For this reason, and owing to the increased use of scanning optical microscopes in the OBIC and PL modes to characterize semiconductor devices, it has become neccesary to have a new model which accurately describes the formation of the beam induced current and photoluminescence images of semiconducting samples due to a monochromatic light beam focussed on the sample surface. This thesis attempts to explain the formation of optical beam induced current and photoluminescence signals by modelling the interaction of the finely focussed light beam with various semiconductor geometries and devices. All the cases treated are where the diffusion current dominates over the drift current, since it is assumed that any electric fields that are applied to the device are confined to the regions of the p-n junctions. We start, in Chapter 2, by applying the SOM to semiconductor device examination and characterization and demonstrate the various forms of imaging that are possible, this Chapter provides the motivation for the rest of the thesis which is dedicated to explaining the various imaging modes in a mathematically consistent form. In Chapter 3 a model is presented which predicts the form the excess minority carrier distribution generated in a semi-infinite semiconductor due to a highly convergent light beam focussed on the sample surface and demonstrates how, once the minority carrier distribution is known, it is possible to predict the imaging properties when electrically active defects are imaged in the OBIC and PL examination techniques. The formation of beam induced currents is considered in Chapters 4 and 5. In Chapter 4 it is assumed that the generation rate of electron hole pairs due to the light beam is a constant in time and, as such, only the steady state case is analysed resulting in various methods being suggested for the measurement of the minority carrier diffusion length. Chapter 5 then deals with the formation of beam induced currents due to a time varying focussed light beam and includes suggestions for the measurement of the minority carrier lifetime, as well as a time dependent theory for optical beam induced current defect imaging.

Since this thesis is concerned with *scanning* microscopy we consider, in Chapter 6, what effect moving the exciting beam can have on the form of the induced minority carrier distribution and hence the beam induced current for various device geometries. It is then shown, also in Chapter 6, how the *contrast* obtained as an electrically active defect is imaged in the OBIC technique can be effected by the scan speed. The photoluminescence signal generated from a semi-infinite semiconductor due to a time varying focussed light beam is considered in Chapter 7, where methods are suggested for measuring the minority carrier lifetime in unprocessed semiconductor wafers. Finally, Chapter 8 presents an overview of the general results of the work and the conclusions as well as suggestions for future work on the subject.

CHAPTER 2:

SCANNING OPTICAL MICROSCOPY OF SEMICONDUCTORS

An extremely versitile and useful laboratory tool is the conventional microscope which is essentially a parallel processing system where the whole object is imaged simultaneously. However it is possible to increase the versitility of the conventional microscope still futher by relaxing the parallel processing criteria to the limit where only one point of the object is imaged at a time. Clearly in order to build up an image of the whole object we now have to *scan* the object relative to the illumination system to build a point-by-point image of the sample [1].

A schematic representation of a typical scanning optical microscope, working in reflection, is given in Figure (2.1) where it is shown how both the reflected light and OBIC images can be obtained, it should be noted here that it is, of course, also possible to operate the system in transmission. The main features shown, which are common to all scanning optical microscopes, are a light source focussed onto the sample surface via an objective lens, an x-y scanning system which scans the sample with respect to the stationary light beam and a photosensitive detector, such as a photodiode, which is used to convert the optical signal into an electronic one such that various forms of image processing may be performed by use of a computer.† Using a scanning system of this kind, where the beam is stationary and the object scanned, it is possible to produce high quality reflected light images such as the one shown in Figure (2.2). Here we are imaging the surface a D-MOS device using red light from a HeNe laser. A low magnification image is shown to illustrate that there is no loss of resolution or contrast across the image field due to the mechnical scanning.

As well as producing simple reflected light images, such as the one shown in Figure (2.2), we can also use the *confocal* mode [1] of the SOM to produce optical sectioning and improved resolution images. The confocal system is identical to the system shown in Figure (2.1) except that it employs an axial point detector, in the form of a pinhole placed in front of a large area detector, such that light is only collected from a very

† It should be noted that it is also possible to build a scanning optical microscope where the beam is scanned relative to a stationary object, however specimen scanning is used here since the optics are simpler and the image quality is, in general, superior [1].

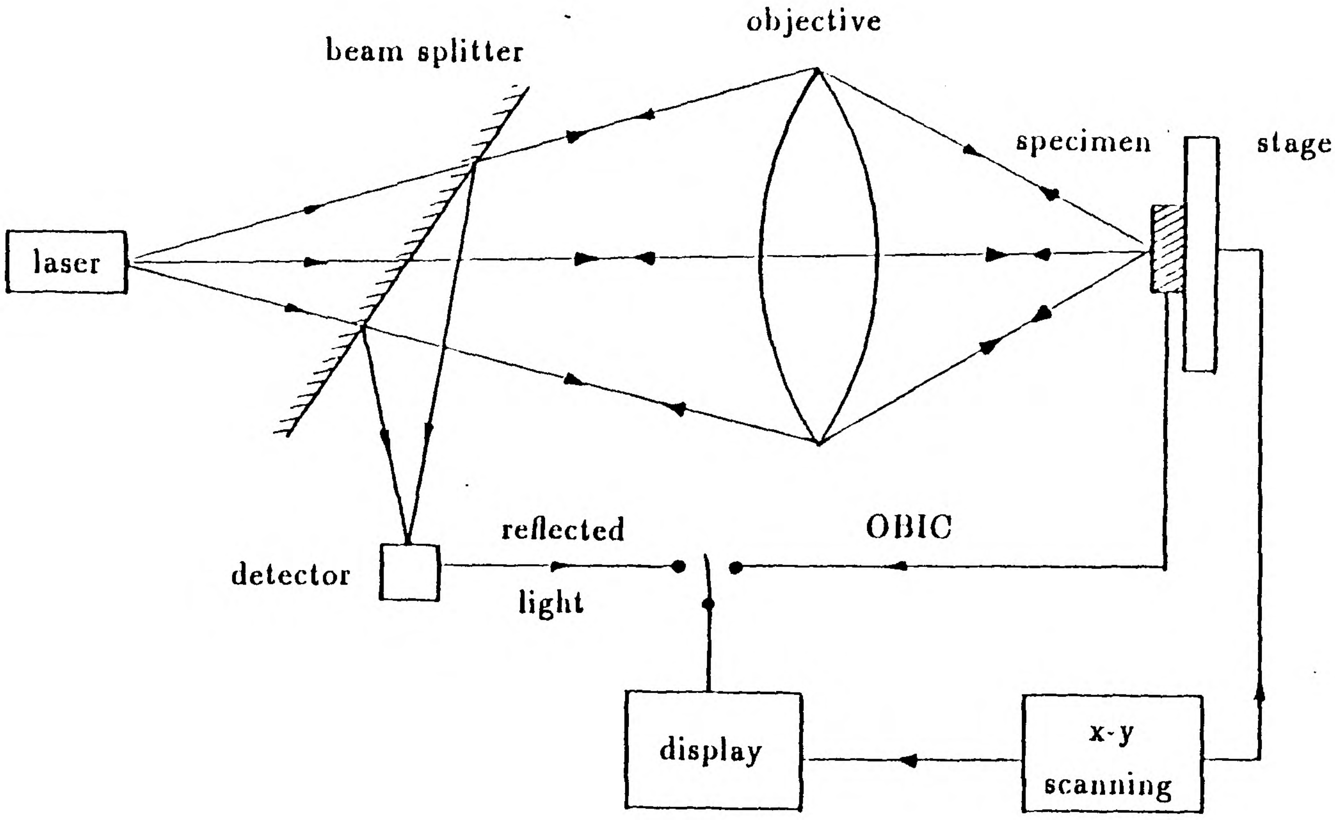

Figure 2.1. A schematic representation of a typical scanning optical microscope operating in reflection. Here the scanning is achieved by scanning the object relative to the stationary light beam.

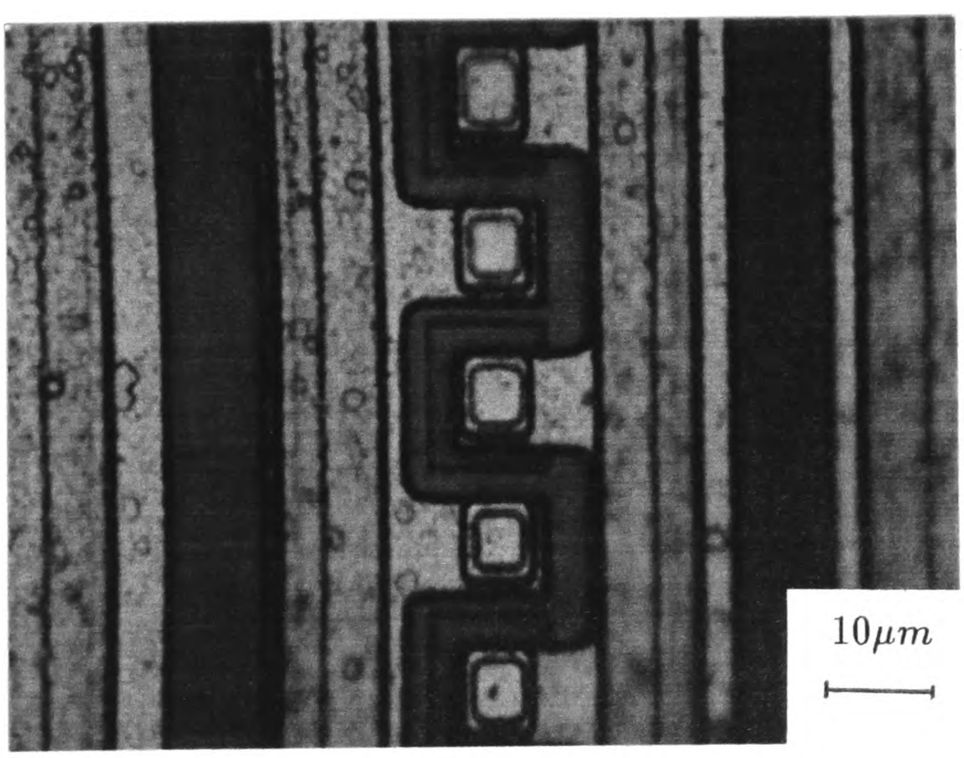

Figure 2.2. A low magnification reflected light image of a D-MOS device obtained in a scanning optical microscope such as the one shown schematically in Figure (2.1). It is clear that the resolution and contrast are good across the whole image field.

small region of the object. The origin of the depth discrimination in the confocal system is shown in Figure (2.3) where it is clear that only light from the focal plane is admitted through the pinhole and hence forms an image in the dector plane. With a confocal system of this kind it is possible to build-up an isometric surface plot of an object by taking images at a series of focus positions and summing them electronically. An isometric image of the D-MOS device, shown in reflection in Figure (2.2), was produced in this way and is shown in Figure (2.4).

If we specialize to the case when the object is a semiconductor we can, as well as using a photodiode to build an image using the reflected or transmitted light, use the Optical Beam Induced Current (OBIC) technique. Here we essentially use the object itself as a detector to build an image of the current induced by the scanning light beam in the sample [2]. As an example of this technique we consider the high voltage power diode a schematic cross-section of which is shown in Figure (2.5). The structure is essentially a simple p-n junction but with the addition of some p-type guard rings diffused around the central p-well. The purpose of these rings is to increase the break down voltage by preventing the depletion layer from spreading along the surface. Using the OBIC technique it is possible to "image" the depletion region spreading as a reverse bias is applied to the device and, in Figure (2.6), we show a series of OBIC line scans across the device together with a series of combinations of reflected light and OBIC images. The OBIC line scans are shown on the left hand side of Figure (2.6) starting from zero bias where the depletion region between the p-well and n-substrate is visible as the peak in the OBIC signal. As the reverse bias is increased it is clear that the depletion region spreads until, at a value of one hundred volts, the first p-ring is engulfed, as the reverse bias is increased further other rings become visible in the OBIC mode until eventually all the rings are included.

The OBIC imaging shown in Figure (2.6) is faily low magnification since the object is a large power diode, however it is also possible to produce high magnification OBIC images of defects in semiconductors. Figure (2.7) shows a typical high resolution OBIC image of a BFY 51 silicon bipolar transistor where dislocations are clearly visible as the dark lines.

From Figures (2.6) and (2.7) it is clear that the OBIC method is very useful for investigating *current* flow in semiconductor devices, however the technique is limited by the need for external contacts to be made to the sample to measure the current. This means that it is difficult to investigate the properties of unprocessed wafers where no contacts are present.

It is possible to produce *temporary* contacts by use of either a liquid electrolyte [3]

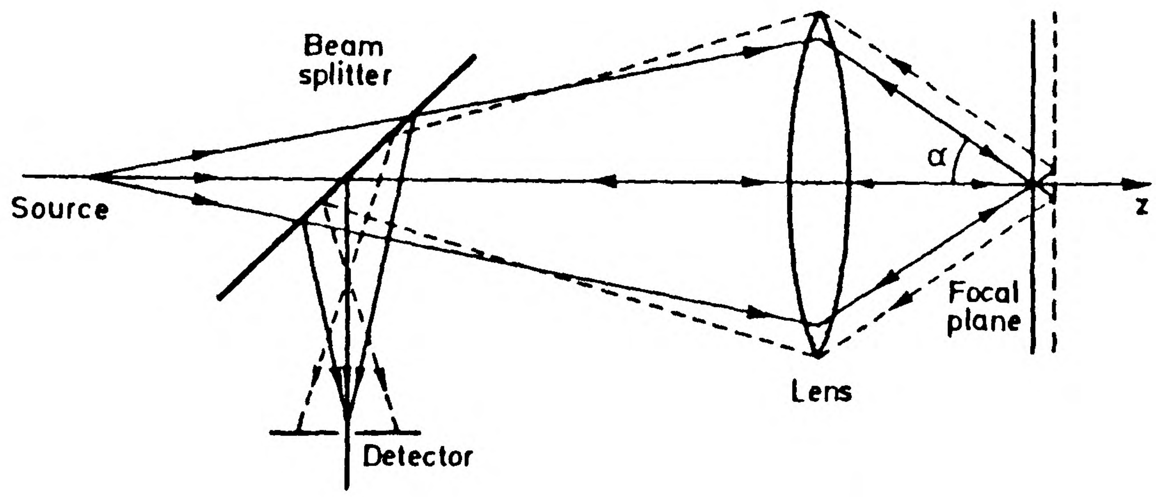

Figure 2.3. A schematic representation of a confocal scanning optical microscope showing the pinhole in front of the detector and the origin of the depth discrimination.

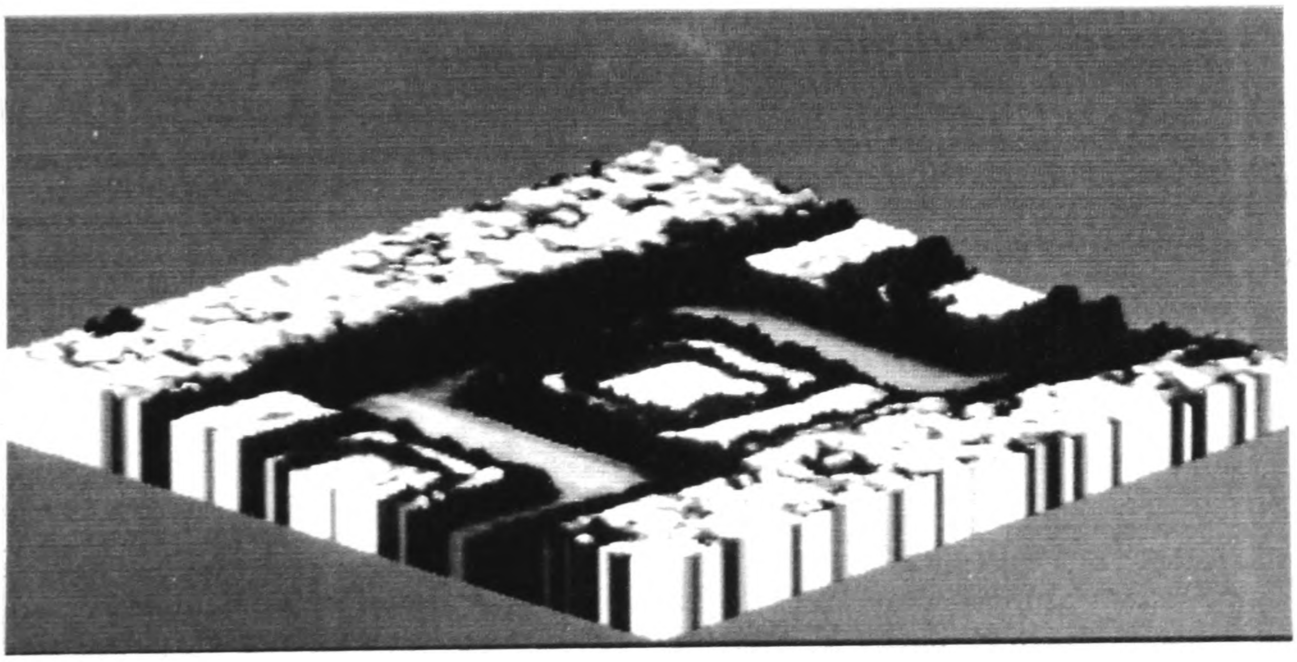

Figure 2.4. An isometric image which enables the surface topography of the D-MOS device, shown in reflected light in Figure (2.2), to easily visualised.

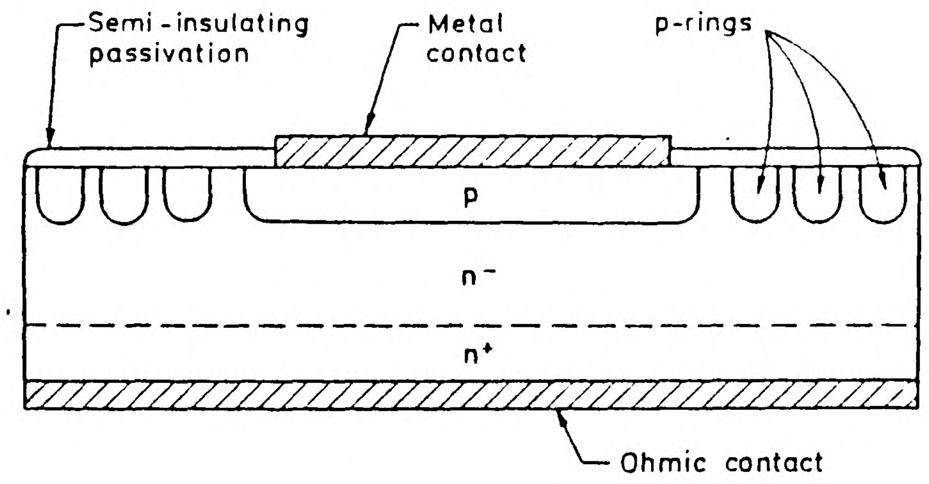

Figure 2.5. A schematic cross-section of a power diode showing the position of the p-type guard rings.

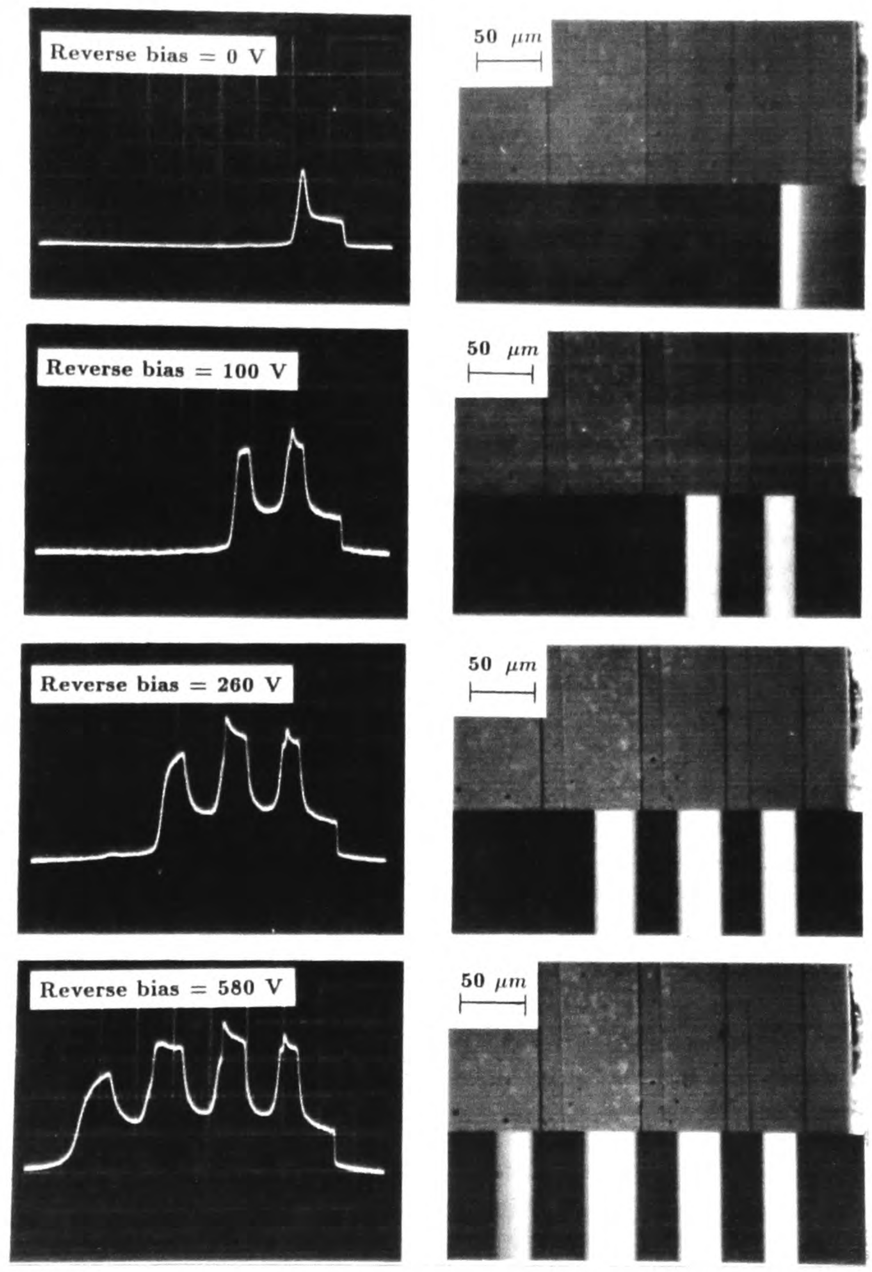

Figure 2.6. The spreading of the depletion region in the power diode which is shown schematically in Figure (2.5). The photographs on the right hand side show the reflected light images above the corresponding OBIC images and the traces on the left hand side show OBIC line scans across the device as the reverse bias is increased.

Figure 2.7. A high resolution OBIC image of a silicon bipolar transistor showing dislocations [Supplied by Dr. D. K. Hamilton].

(as discussed further in Chapters 4 and 5) or a metal grid placed in contact with the surface, or to use another noncontact method such as a capacitive detection system [4] where a plate is placed close to the sample surface and the capacitance of the system measured as the exciting beam scans the device. However, one simpler method is the *photoluminescence* technique [5,6] as described in the introduction of Chapter 1. The only drawback here is that a radiative transition is required such that the photoluminescence signal can be produced. Assuming such a transition is present it is possible to produce high resolution images of the electrical properties of the sample by collecting the photoluminescence in either reflection or transmition. Figure (2.8) shows a pair of photoluminescence images of InP obtained by using a red HeNe laser ($\lambda = 0.632\mu m$) to provide the excitation. The photoluminescence signal was of wavelength $\lambda \sim 0.9\mu m$ and the images where obtained in transmission, using suitable filters to block the exciting wavelength, at room temperature using a silicon detector. Figure (2.8a) is a low magnification image and Figure (2.8b) is a higher magnification image of the same part of the specimen. The dark and light bands that are clearly visible in Figure (2.8a) are due to doping variations in the InP sample giving rise to differences in the photoluminescence efficency, and the dark spots that can be seen in both Figures (2.8a) and (2.8b) are dislocations penetrating into the sample. From Figures (2.7) and (2.8) it is clear that the resolution obtainable in both the OBIC and PL techniques are comparable, which is interesting since in one case (OBIC) we measure an induced current and in the other we are simply measuring an emitted light intensity.

It is clear from the *qualitative* description given of OBIC and PL so far in this Chapter that both techniques can be extremely useful for investigating the electrical properties of semiconductors. However, in order to exploit the techniques to the full we would also like to be able to use them for *quantitative* investigations of the electrical properties. Clearly to do this we require a good physical model which explains the formation of OBIC and PL images such as those shown in Figures (2.7) and (2.8). Therefore in the following Chapters both the formation of the OBIC and PL signals is considered and it is shown how the SOM may be used not only as a qualitative tool but also to extract measurements of semiconductor material parameters.

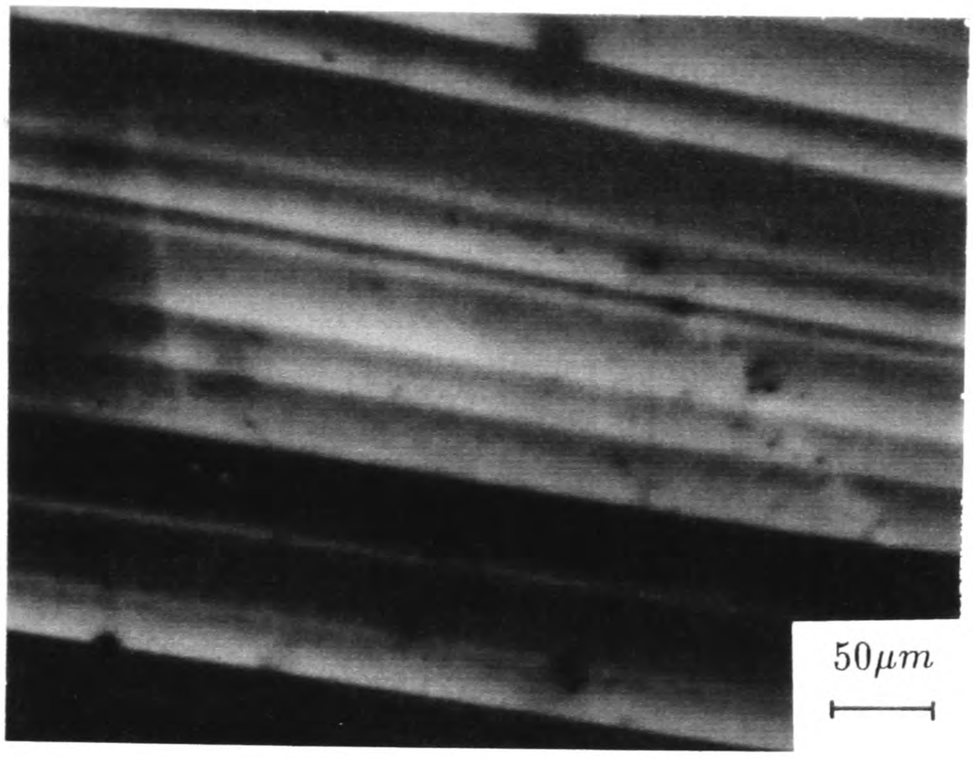

(a)

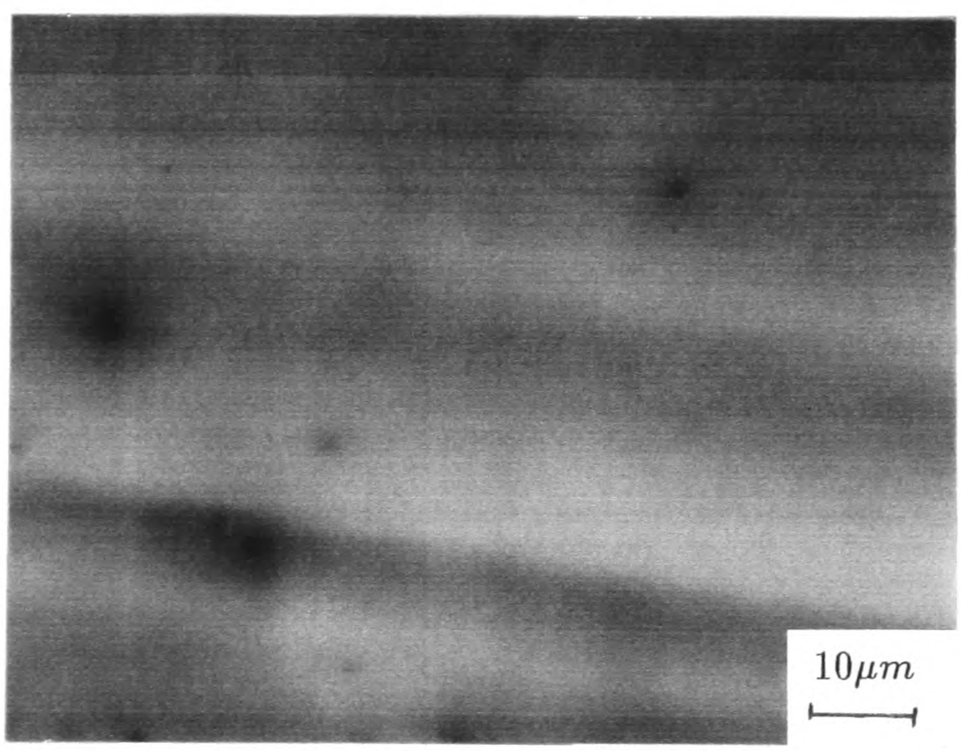

(b)

Figure 2.8. Transmission scanning photoluminescence images of InP, obtained at room temperature, showing doping variations (the dark and light bands) and defects (the dark spots), (a) is a low magnification image and (b) is a higher magnification image of the same part of the sample.

CHAPTER 3:
INJECTED MINORITY CARRIER DISTRIBUTION

3.0 Introduction

In order to extract meaningful results from data produced in beam induced current investigations of semiconductors it is clearly necessary to have a good physical model for the generation of the excess carriers by the beam, since it is these excess carriers that constitute the current and are ultimately responsible for the resolution in defect imaging applications. Most early analyses [1,2] assumed that the generation of the excess carriers took place at one point either on, or just below, the surface of the semiconductor. Van Roosbroeck gave an analysis deriving the continuity equation [3] for the excess carriers injected into the semiconductor, and later the Green's function [4] for the semi-infinite media case, which agreed with the earlier work by Bryan [5] on the equivalent heat conduction problem. However, once the Green's function is known there still remains the problem of representing the source term which, for beam induced carrier problems, is proportional to the incident beam intensity within the semiconductor. For the case of an electron beam this is difficult to model since the primary electron beam tends to spread out under the surface of the semiconductor into a rather pear shaped region [6]. For this reason the generation function is usually approximated by a sphere at some depth into the semiconductor [7], the depth of the centre of the sphere representing the penetration depth of the primary electron beam.

In the optical case the generation function is somewhat easier to approximate as either; simply a point on the surface [8,9], corresponding to strong absorption, an array of point sources decaying exponentially into the semiconductor [10,11,12], representing a narrow beam, or, to try and take account of the incident beam width, a Gaussian lateral profile is sometimes introduced and used in conjuction with an exponentially decaying axial term [13]. However, even the decaying Gaussian generation function is only an approximation to the true light intensity [14] within the semiconductor due to light focussed onto the surface via a high numerical objective lens, as is the case in the scanning optical microscope.

In this Chapter the steady state minority carrier distribution injected into a semi-infinite semiconductor by a highly convergent focussed light beam is calculated. The method of calculation exploits the radial symmetry of the problem by introducing the Hankel transform with respect to the radial coordinate, and uses the associated convolution theorem to give an expression for the transform of the generation function. The minority carrier distribution is calculated for various values of objective lens numerical aperture and the effects of surface recombination velocity and minority carrier diffusion length are also studied. As an example of a use for the minority carrier distribution applications to the OBIC mode of the scanning optical microscope are considered where the imaging of electrically active defects is modelled showing how the resolution of the technique depends on, amongst other things, the numerical aperture of the objective lens. Photoluminescence studies of a defect in a semi-infinite semiconductor are also considered as an example and again it is shown how the resolution of the technique depends explicitly on the numerical aperture of the objective lens. Finally, the full expressions obtained for the minority carrier distribution due to focussed light excitation are compared to those obtained when the much simpler decaying Gaussian approximation is used.

3.1 The Induced Minority Carrier Distribution

In this section the induced minority carrier distribution in a semi-infinite semiconductor is calculated. Initially a general expression for the distribution due to an arbitrary radially symmetric generation function is found, the analysis is then specialised to the case of focussed light excitation such that the generation function $g(r, z)$ can be written as [14]

$$g(v,u) = g_0 A \exp\left(-\alpha_u u\right) \left| \int_0^1 J_0(v\rho) \exp\left(-\frac{iu\rho^2}{2}\right) \exp\left(-\frac{\beta u\rho^2}{2}\right) \rho \, d\rho \right|^2, \tag{3.1}$$

where v and u are normalised optical coordinates [15] given by,

$$v = \left(\frac{2\pi}{\lambda}\right) r \sin\theta \qquad u = \left(\frac{2\pi}{\lambda}\right) z \sin^2\theta. \tag{3.2}$$

Here λ is the wavelength, $\sin\theta$ the numerical aperture of the objective lens, β is related to α, the intensity absorption coefficient via $2k\beta = \alpha$ with k being the wavenumber, ρ is a radial variable in the objective pupil plane, g_0 is a constant taking into account surface reflectivity and quantum efficiency, r and z are radial and axial coordinates respectively and α_u is the normalised intensity absorption coefficient,

$$\alpha_u = \left(\frac{\alpha\lambda}{2\pi}\right) \sin^2\theta. \tag{3.3}$$

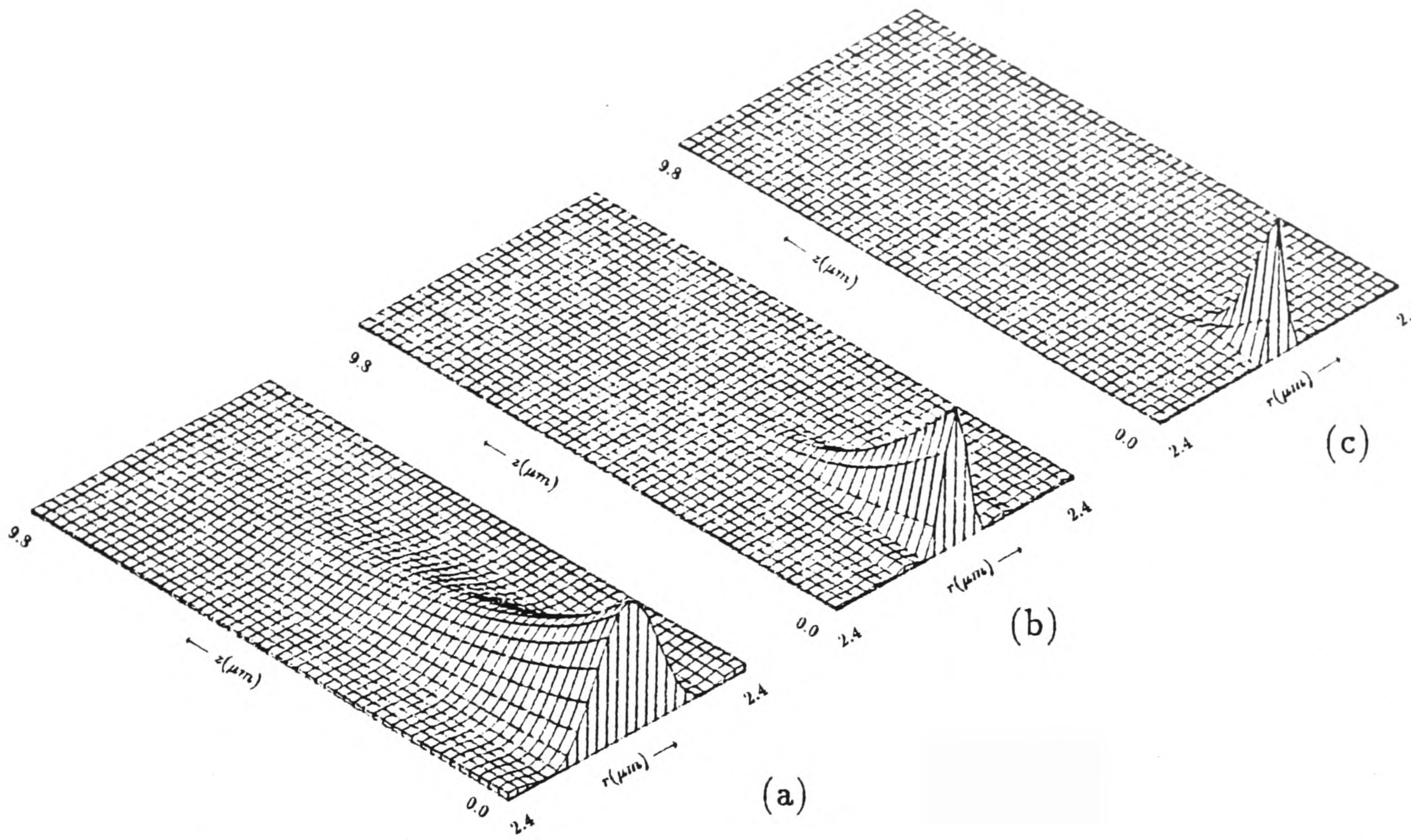

Figure 3.1. The intensity of red light in silicon for values of numerical aperture of (a) $\sin\theta = 0.2$, (b) $\sin\theta = 0.5$ and (c) $\sin\theta = 0.9$.

The premultiplying factor A is a normalisation constant given by

$$A = \frac{\alpha k^2 \sin^4\theta}{2\pi \ln\left[1 + \frac{\sin^2\theta}{2}\right]}, \tag{3.4}$$

chosen such that,

$$2\pi \int_0^\infty \int_0^\infty g(r,z)\, r dr dz = g_0. \tag{3.5}$$

Isometric surface plots of the light intensity within the semiconductor, as given by Equation (3.1), are shown for a selection of numerical apertures in Figure (3.1), the parameters chosen are consistent with red light incident on the surface of silicon ($\lambda = 0.632\mu m$ and $\alpha = 0.4\mu m^{-1}$).

Assuming the semiconducting sample in question is n-type and bounded by the $z = 0$ plane, the distribution of minority carriers (holes in this case) $\Delta p(r,z)$, induced by the focussed light beam can be found by solution of the steady state diffusion equation. For the case of linear recombination and low injection, such that the addition of the excess carriers does not significantly effect the background conductivity, the diffusion equation can be written as [3],

$$\nabla^2 \Delta p(r,z) - \frac{\Delta p(r,z)}{L^2} = -\frac{1}{D} g(r,z) \tag{3.6}$$

where D is the diffusion constant and L the minority carrier diffusion length.† The boundary conditions on the injected carrier distribution can be taken as

$$\frac{\partial}{\partial z}\Delta p(r,z)\Big|_{z=0} = \frac{v_s}{D}\Delta p(r,z)\Big|_{z=0} \tag{3.7a}$$

and,

$$\Delta p(r,z)\big|_{z\to\infty} \to 0. \tag{3.7b}$$

Equation (3.7a) takes into account the increased recombination rate at the $z = 0$ surface, due to the presence of surface states, via a *surface recombination velocity*, v_s, [16] which ranges from zero, when there are no surface states present, to infinity when total recombination of all the excess carriers occurs at the surface. The boundary condition of Equation (3.7b) is used to ensure a bounded solution.

Since the generation function for focussed light is naturally written in the *optical* coordinates (v,u) and the diffusion equation in the *cylindrical* coordinates (r,z) it is important at this point to choose one set of coordinates and work with them throughout. Most of the manipulation involves the generation function and so it is best to choose the optical coordinates v and u which, from Equation (3.2), can be defined as

$$v = ar, \qquad \text{and}, \qquad u = bz \tag{3.8}$$

with $a = (2\pi/\lambda)\sin\theta$ and $b = (2\pi/\lambda)\sin^2\theta$. The diffusion equation can now be written in the optical coordinate system as,

$$a^2\frac{1}{v}\frac{\partial}{\partial v}\left(v\frac{\partial}{\partial v}\Delta p(v,u)\right) + b^2\frac{\partial^2}{\partial u^2}\Delta p(v,u) - \frac{\Delta p(v,u)}{L^2} = -\frac{1}{D}g(v,u), \tag{3.9}$$

with the boundary conditions becoming,

$$\frac{\partial}{\partial u}\Delta p(v,u)\Big|_{u=0} = s\Delta p(v,u)\Big|_{u=0}, \tag{3.10a}$$

and,

$$\Delta p(v,u)\big|_{u\to\infty} \to 0, \tag{3.10b}$$

where $s = v_s/bD$ is a normalised surface recombination velocity.

We require a solution to Equation (3.9) for a general generation term, $g(v,u)$, and so it is useful to adopt a Green's function [17] approach to the solution. The problem also has an obvious cylindrical symmetry which suggests that Equation (3.9) may be most easily solved by introducing the Hankel Transform [18 p.458] of $\Delta p(v,u)$ with respect to the radial coordinate v, defined as

$$\Delta\bar{p}(\nu,u) = \int_0^\infty \Delta p(v,u)J_0(\nu v)\,v\,dv \tag{3.11}$$

† It should be noted that an entirely analogous expression can be written for electrons in p-type material, although the low injection level condition is generally more restrictive [3].

where J_0 is a zero order Bessel function of the first kind. Under this transformation the diffusion equation becomes

$$\frac{\partial^2}{\partial u^2}\Delta\bar{p}(\nu,u) - \phi^2\Delta\bar{p}(\nu,u) = -\frac{1}{Db^2}\,\bar{g}(\nu,u), \tag{3.12}$$

where $\bar{g}(\nu,u)$ is the Hankel transform of the generation function and,

$$\phi^2 = a^2\nu^2/b^2 + 1/L^2b^2. \tag{3.13}$$

The boundary conditions of Equation (3.10) still apply but with $\Delta p(v,u)$ replaced by $\Delta\bar{p}(\nu,u)$ since the transformation acts purely on the radial coordinate. The Green's function for Equation (3.12) which satifies the boundary conditions is straightforward to find using standard techniques, and is given as [13]

$$G(\nu,u|u_0) = \frac{1}{\phi}\left\{e^{-\phi|u-u_0|} + \left(\frac{\phi-s}{\phi+s}\right)e^{-\phi(u+u_0)}\right\}, \tag{3.14}$$

and so the general solution to the transformed diffusion equation can be written,

$$\Delta\bar{p}(\nu,u) = -\frac{1}{Db^2}\int_0^\infty G(\nu,u|u_0)\bar{g}(\nu,u_0)\,du_0, \tag{3.15}$$

from which the induced carrier distribution can be found via the inverse Hankel transform as,

$$\Delta p(v,u) = -\frac{1}{Db^2}\int_0^\infty\int_0^\infty G(\nu,u|u_0)\bar{g}(\nu,u_0)J_0(\nu v)\,du_0\,\nu d\nu. \tag{3.16}$$

Equation (3.16) is a general expression for the induced carrier distribution in the semi-infinite sample for an arbitrary radially symmetric generation term $g(v,u)$.
Speciali~~s~~zing to the practically important case where the generation is due to a focussed light beam, the distribution may be found from Equation (3.16) and, since the form of the Green's function is well known, the problem reduces to finding an expression for the Hankel transform of the generation function $\bar{g}(\nu,u)$. It will be useful to re-write Equation (3.1) as,

$$\begin{aligned} g(v,u) &= g_0 A\exp\left(-\alpha_u u\right)\left|\int_0^1 J_0(v\rho)\exp\left(-\frac{iu\rho^2}{2}\right)\exp\left(-\frac{\beta u\rho^2}{2}\right)\rho\,d\rho\right|^2 \\ &= g_0 A\exp\left(-\alpha_u u\right)\left|\int_0^\infty P(\rho,u)J_0(v\rho)\rho d\rho\right|^2 \\ &= g_0 A\exp\left(-\alpha_u u\right)\left|h(v,u)\right|^2 \end{aligned} \tag{3.17}$$

where,

$$P(\rho,u) = \exp\left(-i\frac{u\rho^2}{2}\right)\exp\left(-\frac{\beta u\rho^2}{2}\right) \qquad \text{for} \qquad |\rho| \leq 1 \tag{3.18}$$

and,

$$h(v,u) = \int_0^{\infty} P(\nu,u)J_0(v\nu)\,\nu d\nu = \mathcal{H}\{P(\nu,u)\}, \tag{3.19}$$

here $\mathcal{H}$ represents the Hankel transform operator. Using Equation (3.17) for the generation function, the Hankel transform $\bar{g}(\nu,u)$ is given as,

$$\begin{aligned}\bar{g}(\nu,u) &= g_0 A \exp(-\alpha_u u) \int_0^{\infty} |h(v,u)|^2 J_0(\nu v)\, v dv \\ &= g_0 A \exp(-\alpha_u u)\, \mathcal{H}\left\{|h(v,u)|^2\right\} \\ &= g_0 A \exp(-\alpha_u u)\, \mathcal{H}\left\{h(v,u)\right\} \otimes \mathcal{H}\left\{h(v,u)^*\right\},\end{aligned}$$

that is,

$$\bar{g}(\nu,u) = g_0 A \exp(-\alpha_u u)\, P(\nu,u) \otimes P^*(\nu,u), \tag{3.20}$$

where $\otimes$ and $*$ represent the convolution operation and complex conjugate respectively. Now, using the convolution theorem for the Hankel transform [19 p.250], $\bar{g}(\nu,u)$ can be written,

$$\bar{g}(\nu,u) = g_0 A \exp(-\alpha_u u) \int_0^{\infty} \int_0^{2\pi} P(\rho_1,u)P^*(\rho_2,u)\, \rho_1 d\rho_1 d\phi \tag{3.21}$$

where the variables ρ_1, ρ_2, ν and ϕ are related via the cosine rule as

$$\rho_2^2 = \nu^2 + \rho_1^2 - 2\nu\rho_1 \cos\phi \qquad \text{for} \qquad |\rho_1|, |\rho_2| \le 1. \tag{3.22}$$

Equations (3.21) and (3.22) can be represented graphically as an integration over the region of overlap of the two circles, $\rho_1 = 1$ and $\rho_2 = 1$, whose centres are displaced by an amount ν, the transform variable. This is shown in Figure (3.2) where the relationship between the variables ρ_1, ρ_2 and ν can be visualized.

An expression for $\bar{g}(\nu,u)$ can now be written explicitly using the form of $P(\rho,u)$ from Equation (3.18) as

$$\bar{g}(\nu,u) = g_0 A \exp(-\alpha_u u) \int_{\mathrm{S}} \exp\left(-\frac{iu}{2}\left\{\rho_1^2 - \rho_2^2\right\}\right) \exp\left(-\frac{\beta u}{2}\left\{\rho_1^2 + \rho_2^2\right\}\right) d\mathrm{S}, \tag{3.23}$$

where the region S is defined as the overlap area between the two circles in Figure (3.2). The integrand in Equation (3.23) can be simplified by introducing a new coordinate system, centered on the region of overlap, as shown in Figure (3.3) from which it is clear that the coordinate systems (ρ_1, ρ_2) and (ρ, θ) are related by

$$\rho_1^2 = \rho^2 + \Delta^2 + 2\rho\Delta\cos\theta \tag{3.24a}$$

$$\rho_2^2 = \rho^2 + \Delta^2 - 2\rho\Delta\cos\theta \tag{3.24b}$$

which enables the exponents in Equation (3.24) to be re-written in the form,

$$\frac{\rho_1^2 + \rho_2^2}{2} = \rho^2 + \Delta^2, \qquad \text{and} \qquad \frac{\rho_1^2 - \rho_2^2}{2} = 2\rho\Delta\cos\theta, \tag{3.25}$$

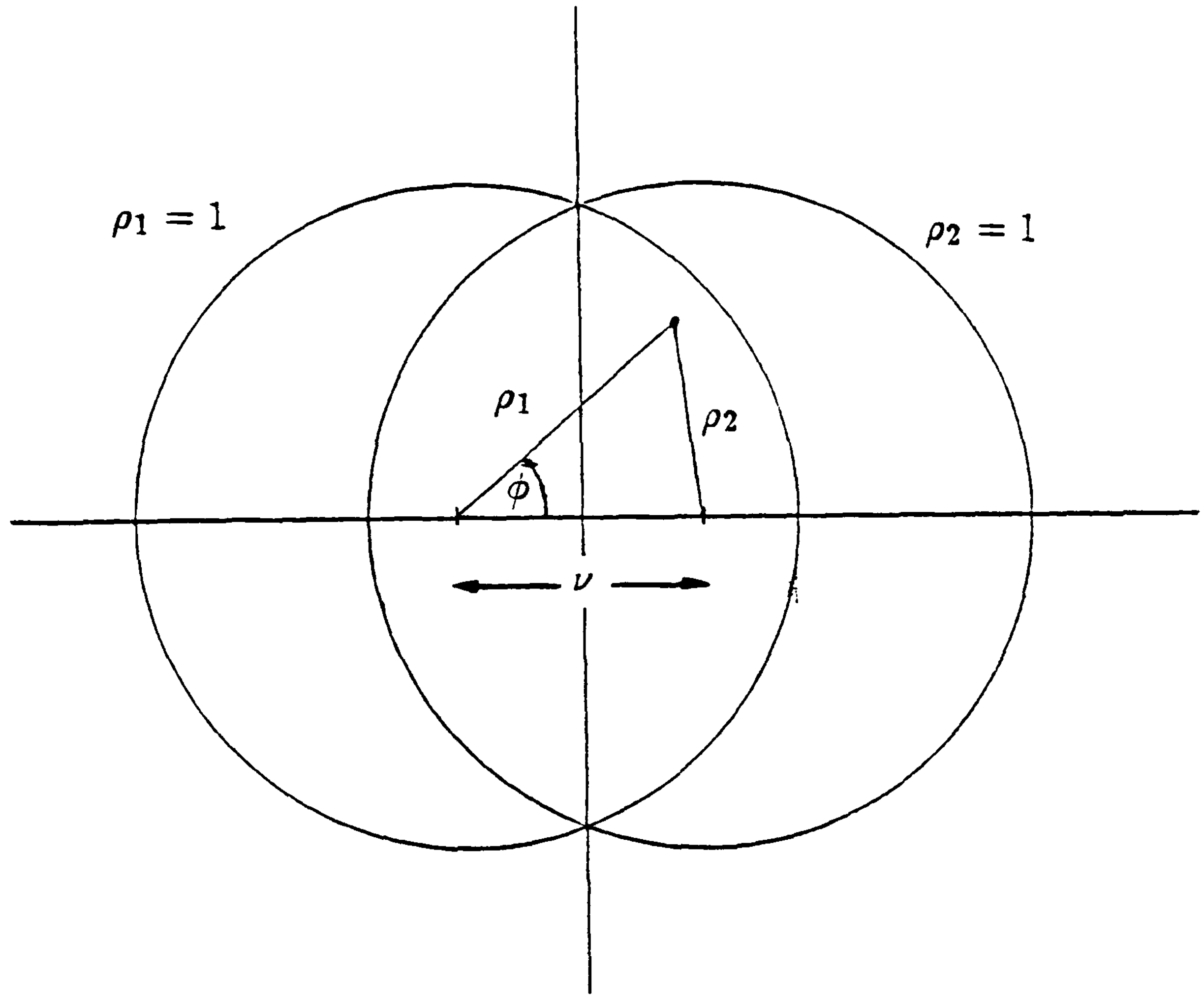

Figure 3.2. Graphical representation of the convolution $P(\rho, u) \otimes P^*(\rho, u)$. The region of integration in Equation (3.21) is given by the overlap of the $\rho_1 = 1$ and $\rho_2 = 1$ circles.

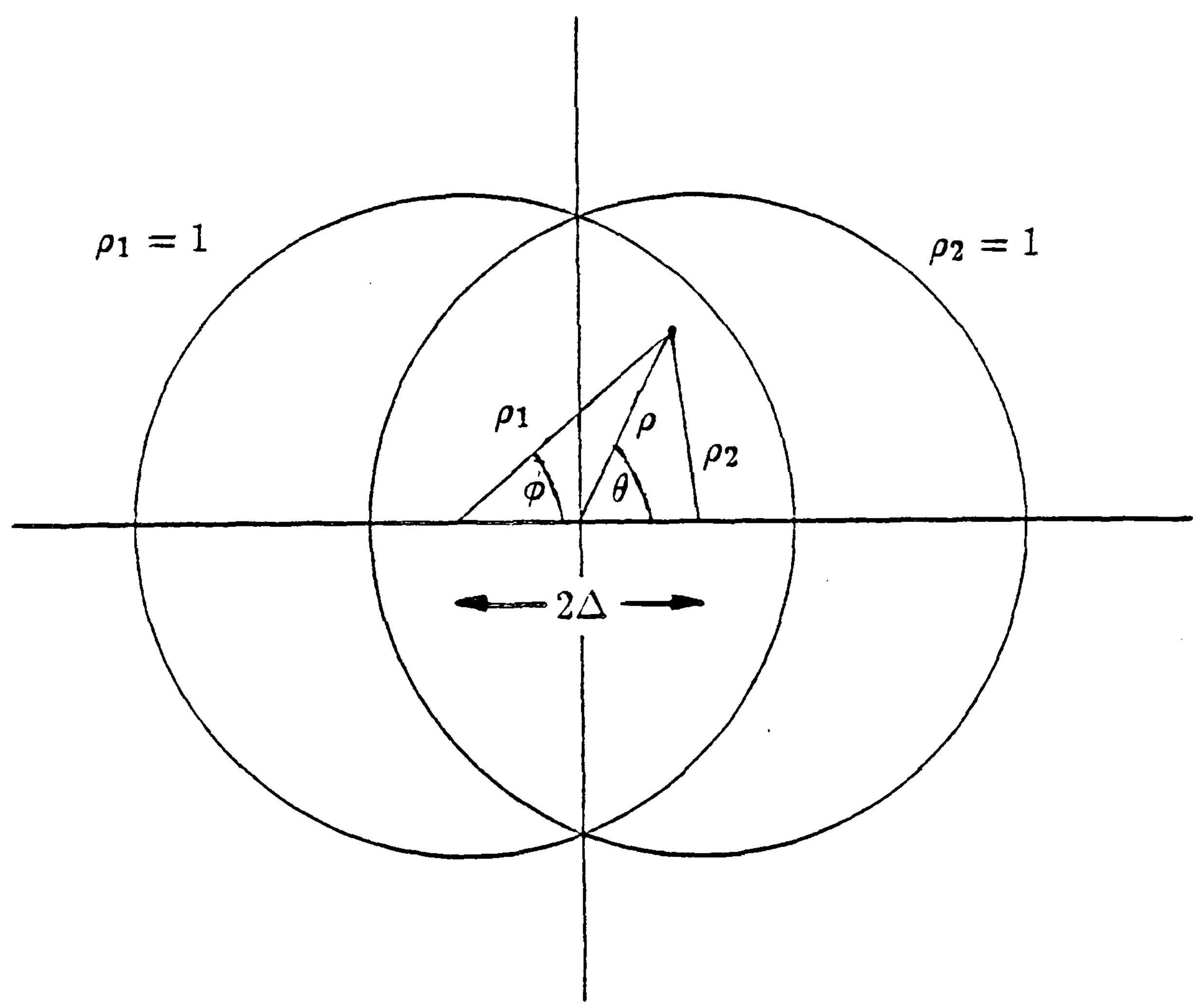

Figure 3.3. Definition of the coordinate system used for the evaluation of the surface integral in Equation (3.23).

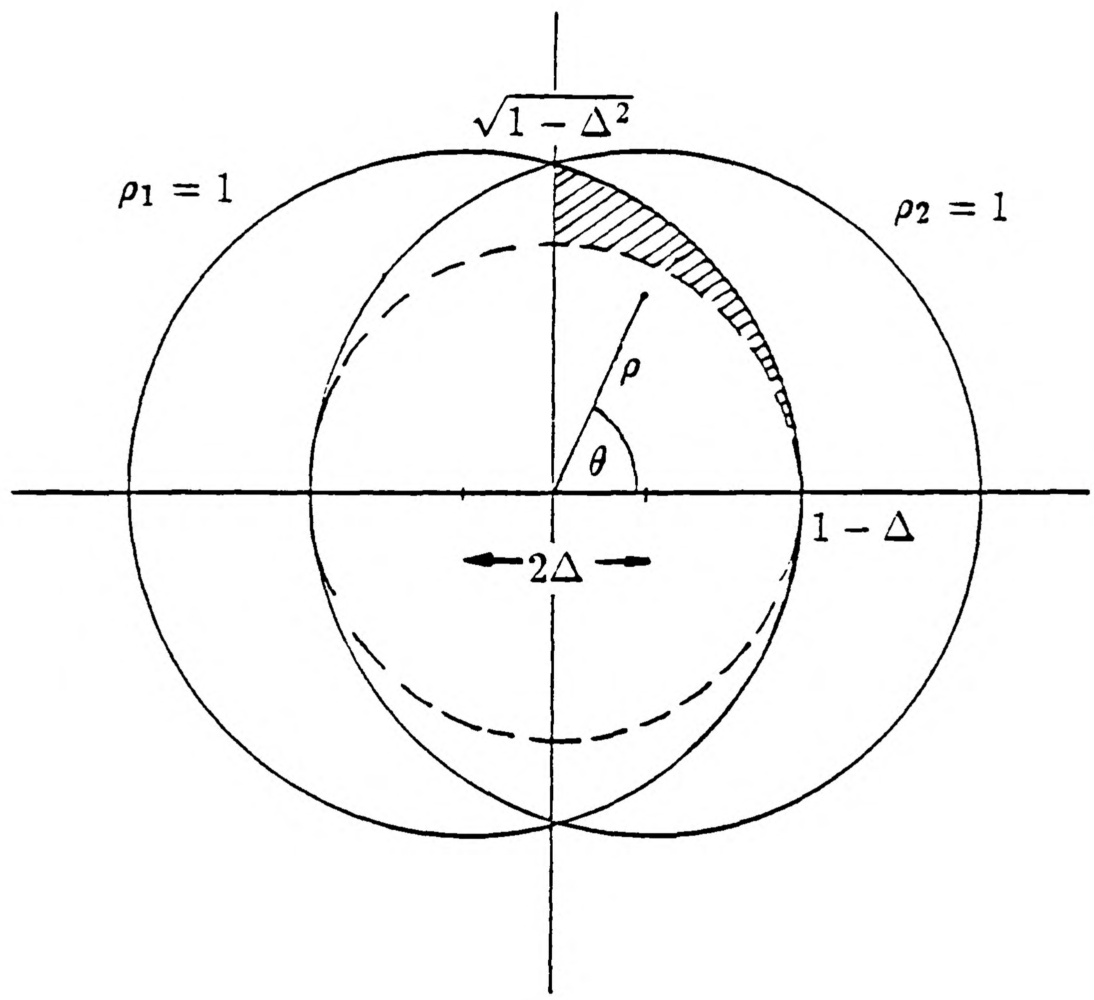

Figure 3.4. Splitting-up of the integration region in Equation (3.26) to simplify the surface integral

here the transform variable, ν, is related to Δ via $\nu = 2\Delta$ $\cancel{\nu = \Delta/2.}$ An expression for the Hankel transform of the generation function in the new coordinates (ρ, θ) now takes the form,

$$\bar{g}(\nu, u) = g_0 A \exp\left(-\alpha_u u\right) \exp\left(-u\beta\Delta^2\right) \int_{\mathbf{S}} \exp\left(-i2u\rho\Delta\cos\theta\right) \exp\left(-u\beta\rho^2\right) d\mathbf{S}. \quad (3.26)$$

Evaluation of the surface integral in Equation (3.26) can be further simplified by splitting-up the area to be integrated over (the circle overlap in Figure (3.3)) into a circle, given by $\rho = 1 - \Delta$, and four sectors such as the one shown shaded in Figure (3.4).

Evaluation of the integrals in ρ and θ over the regions shown in Figure (3.4) is now fairly straightforward and given in Appendix A, where the final expression obtained for the Hankel transform of the generation function is, from Equation (A11)

$$\bar{g}(\nu, u) = g_0 A \left\{ 2\pi \int_0^{1-\Delta} \exp\left(-\Lambda u\right) J_0(2u\Delta\rho)\, \rho d\rho \right.$$
$$\left. + \; 4 \int_{1-\Delta}^{\sqrt{1-\Delta^2}} \int_0^{\sin^{-1}(\lambda)} \exp\left(-\Lambda u\right) \cos(2u\Delta\rho\sin\theta)\, d\theta \rho d\rho \right\}, \quad (3.27)$$

where,

$$\Lambda = \alpha_u + \beta\,(\Delta^2 + \rho^2)\,, \qquad \text{and,} \qquad \lambda = \frac{1 - \rho^2 - \Delta^2}{2\rho\Delta}. \tag{3.28}$$

Before continuing to find the induced carrier distribution due to the focussed light generation term, it is interesting to consider the form of $\bar{g}(\nu, u)$, as given by Equation (3.27), and see how this differs from previous approximations where focussing effects have been ignored. For the cases where the generation term is taken as a point source on the surface [8,9] or a decaying series of point sources [10,11,12] the generation function can be written as separate functions of the radial and axial coordinates, such that,

$$g_a(v, u) = g_0 A_a V(v).U(u), \tag{3.29}$$

with A_a being a normalisation constant and where $U(u) = \delta(u)$ for the point source or, $U(u) = \exp(-\alpha_u u)$ for the decaying series of point sources, but for both $V(v) = \delta(v)/v$. Here δ is the Dirac-Delta function. So, for the above approximations the Hankel transform of the generation term has the form,

$$\bar{g}_a(\nu, u) = g_0 A_a\, U(u). \tag{3.30}$$

One obvious difference between the expressions for $\bar{g}$ is that in the focussed beam case, Equation (3.27), $\bar{g}(\nu, u)$ has a natural cut-off point in ν, namely,

$$\bar{g}(\nu, u) = 0 \qquad \text{for} \qquad \nu \geq 2, \tag{3.31}$$

since both the integrals in Equation (3.27) vanish for $\Delta \geq 1$. This is because the separation, $\nu = 2\Delta$, of the centres of the $\rho_1 = 1$ and $\rho_2 = 1$ circles in the convolution is greater than the sum of their radii, and so there is no overlap and hence the convolution is zero, whereas, for the approximations $\bar{g}_a$ is non-zero for $0 \leq \nu \leq \infty$.

We can investigate the form of the Hankel transform of the focussed beam generation function by looking at isometric surface plots, for various values of the numerical aperture, as shown in Figure (3.5). The Figure shows plots of the function $R(\nu, u)$ which is defined as,

$$R(\nu, u) = \frac{\bar{g}(\nu, u)}{g_0 \exp(-\alpha_u u)}, \tag{3.32}$$

since the $\exp(-\alpha_u u) = \exp(-\alpha z)$ is independent of the numerical aperture. The cut-off point in $\bar{g}(\nu, u)$ at $\nu = 2$ is clearly visible in each of the plots. It is interesting to note that $R(\nu, u)$ and hence $\bar{g}(\nu, u)$ decays more rapidly with depth into the semiconductor at high numerical aperture, this is a consequence of the increase in effective absorption with increasing numerical aperture, as can be seen from Figure (3.1)

We can now continue from Equation (3.27) and calculate the induced minority carrier distribution due to the incident focussed light beam. The Hankel transform of the

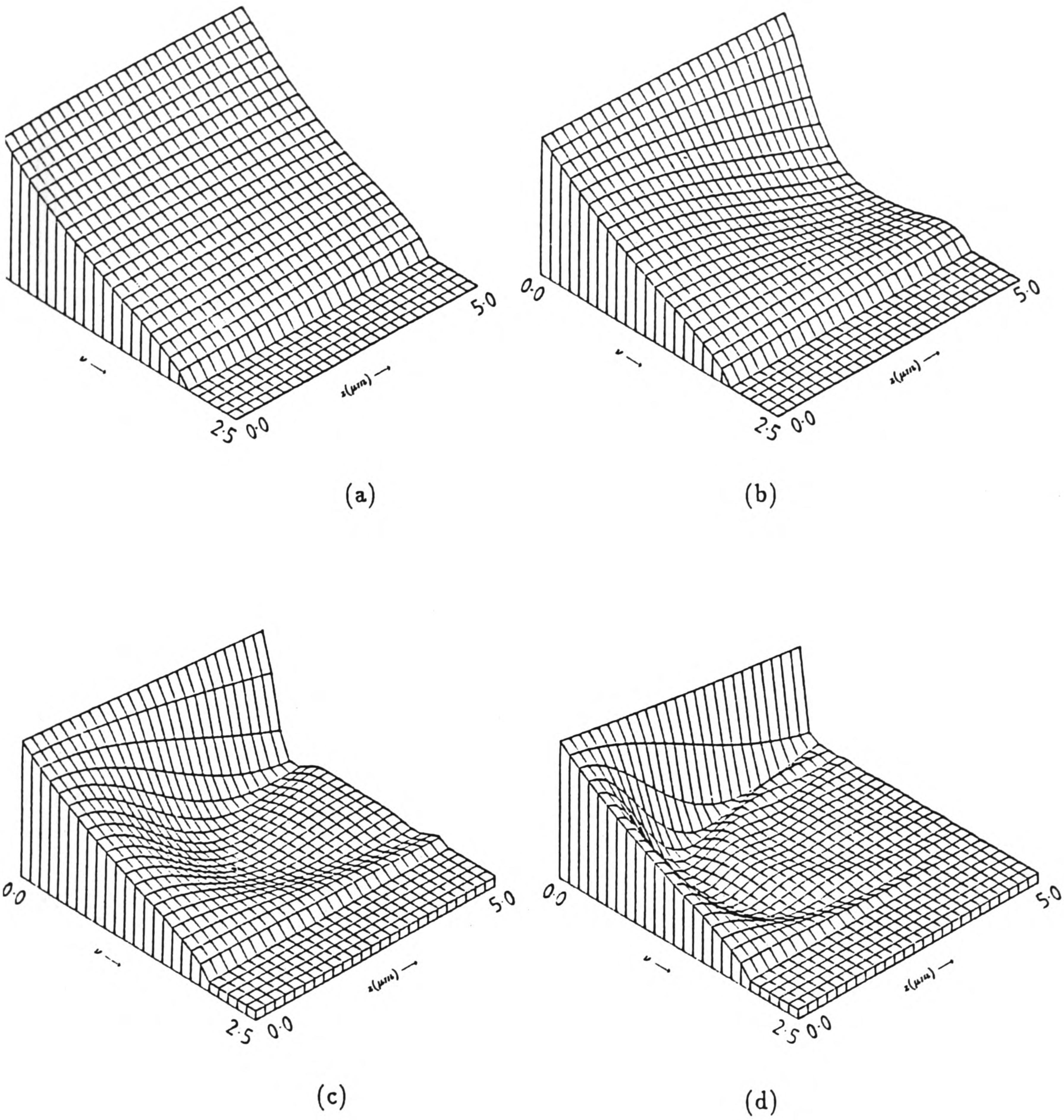

Figure 3.5. Isometric surface plots of the function $R(\nu, u)$ as defined in Equation (3.32). The case shown is for red light in silicon, where the intensity absorption coefficient $\alpha = 0.4\mu m^{-1}$, the wave number $k = 10\mu m^{-1}$, and for (a) numerical aperture $\sin\theta = 0.2$, (b) numerical aperture $\sin\theta = 0.4$, (c) numerical aperture $\sin\theta = 0.6$, and (d) numerical aperture $\sin\theta = 0.9$.

distribution can be found from Equation (3.15) where the Green's function $G(\nu, u|u_0)$ is given by Equation (3.14) and the source term $\bar{g}(\nu, u)$ from Equation (3.27). Folding the Green's function and source is fairly straightforward and given in Appendix B where it is shown, Equation (B8), that the final expression for the transformed minority carrier distribution, $\Delta\bar{p}(\nu, u)$, has the form

$$\Delta\bar{p}(\nu,u) = -\frac{g_0 A}{Db^2\phi}\Bigg\{\int_0^\infty \exp\left(-\phi|u-u_0|\right)\Bigg[2\pi\int_0^{1-\Delta}\exp\left(-\Lambda u_0\right)J_0(2\Delta\rho u_0)\rho\, d\rho$$
$$+4\int_{1-\Delta}^{\sqrt{1-\Delta^2}}\int_0^{\sin^{-1}(\lambda)}\exp\left(-u\rho^2\beta\right)\cos(2u\Delta\rho\sin\theta)\, d\theta\rho d\rho\Bigg]\, du_0$$
$$+\left(\frac{\phi-s}{\phi+s}\right)\exp(-\phi u)\Bigg[2\pi\int_0^{1-\Delta}\Gamma(\phi,\rho)\,\rho d\rho$$
$$+4\int_{1-\Delta}^{\sqrt{1-\Delta^2}}\tan^{-1}\left\{\frac{\tan(\sin^{-1}(\lambda))}{(\Lambda+\phi)\Gamma(\phi,\rho)}\right\}\Gamma(\phi,\rho)\,\rho d\rho\Bigg]\Bigg\}, \tag{3.33}$$

where

$$\Gamma(\phi,\rho) = \frac{1}{\sqrt{(\phi+\Lambda)^2+4\Delta^2\rho^2}}. \tag{3.34}$$

From Equation (3.33) it is possible to find the minority carrier distribution via the inverse Hankel transform as,

$$\Delta p(v,u) = \int_0^\infty \Delta\bar{p}(\nu,u)J_0(\nu v)\,\nu d\nu. \tag{3.35}$$

Unfortunately, it is not possible to express this result in any simple form, even in the special cases of zero or infinite surface recombination velocity or infinite diffusion length, however, it is possible to evaluate Equation (3.35) numerically.

A full discussion of the effects of all the parameters in Equation (3.35), namely; the absorption coefficient α, the diffusion length L, the surface recombination velocity v_s, the numerical aperture $\sin\theta$, and the wavelength of the incident light λ, on the form of the induced carrier distribution would be extremly lengthy due to the large number of combinations of parameters, and so the object here is to point out the main trends rather than give an exhaustive discription of all the details. The absorption coefficient α and wavelength λ are essentially fixed by the type of semicondu c tor in question and we will choose to consider red HeNe light ($\lambda = 632.8nm$), incident on the surface of silicon, for which it is known that the absorption coefficient $\alpha = 0.4\mu m^{-1}$ [20].

We are now left with the three parameters v_s, L and $\sin\theta$, the first two being properties of the semiconductor and the third of the illumination system. Figure (3.6) shows isometric surface plots of the induced minority carrier distribution, as given by Equation (3.35), for various values of the numerical aperture $\sin\theta$, and when $L = 5\mu m$ and $v_s/D = 1.0\mu m^{-1}$.

As would be expected the peak in the distribution is less well confined radially at low numerical apertures, since then the incident radiation is fairly well approximated by a plane wave, however, it is also clear that the distribution penetrates further into the semiconductor at low numerical apertures implying that the distribution is less well confined axially also.

The effect of the surface recombination velocity can be seen from Figure (3.7) where the minority carrier distribution from Equation (3.35) is plotted for the cases of $\sin\theta = 0.6$, $L = 5.0\mu m$ and $v_s \rightarrow 0$, $v_s/D = 1.0\mu m^{-1}$ and $v_s \rightarrow \infty$.

The surface plots in Figure (3.6) and (3.7) are useful to obtain a qualitative feel for the shape of the injected distribution but for quantitative investigations it is generally easier to consider axial and radial plots separately. Figure (3.8) shows the form of the on-axis distribution $\Delta p(0,z)$ as a function of depth into the semiconductor for various values of surface recombination velocity. It is important to note that for any non-zero value of v_s the distribution always peaks some distance below the semiconductor surface. This shift away from the surface is to be expected for a non-zero surface recombination velocity owing to the differential form of the boundary condition in Equation (3.7a) where v_s essentially defines the gradient of the carrier distribution at the surface. The effect of the minority carrier diffusion length is shown in Figure (3.9) where again the on axis distribution is plotted. The diffusion length appears to have a greater effect at low numerical apertures, although at values of $L \geq 10\mu m$ the distribution is fairly well approximated by the limiting case as $L \rightarrow \infty$, for all values of the surface recombination velocity and numerical aperture.

It is possible to investigate the radial behaviour of the distribution by looking at cross-sections at various depths into the semiconductor and, in Figure (3.10), we show radial sections through the distribution at depths of $z = 0.4\mu m$, $z = 1.0\mu m$ and $z = 2.0\mu m$ for the case when $\alpha = 0.4\mu m^{-1}$, $L = 5\mu m$ and $v_s/D = 1.0\mu m^{-1}$. It is interesting to note from Figure (3.10) that although at high numerical apertures, as can be seen from Figure (3.1), the light intensity in the semiconductor has side lobes there are no side lobes present in the carrier distribution, this is due to the diffusion and recombination mechanisms *smoothing* the carrier distribution.

Figure (3.10a) is as one might expect intuitively, that is the distribution is better confined for the cases of high numerical aperture, in Figures (3.10b) and (c) the same is true although the maximum does not occur at the highest numerical aperture. The

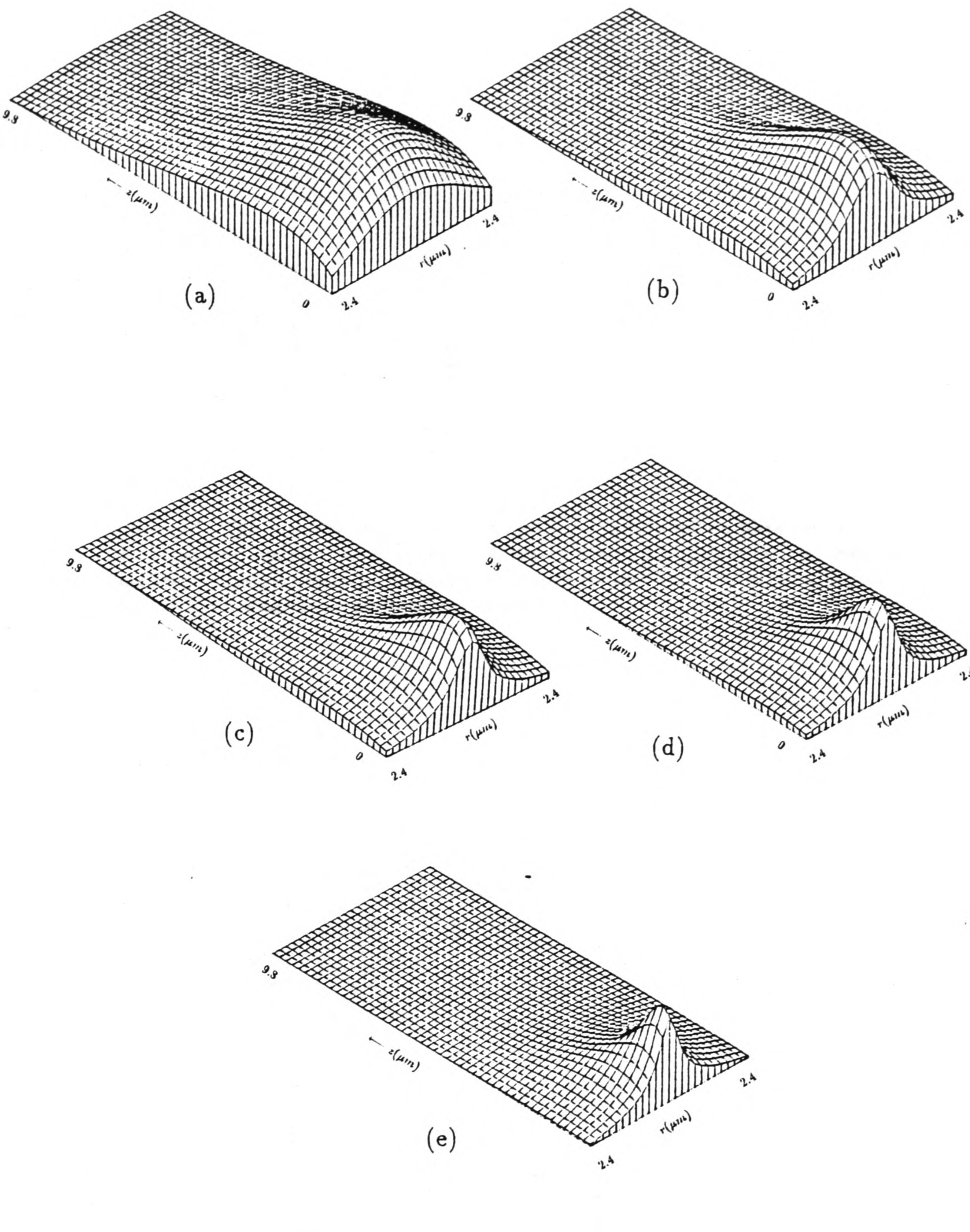

Figure 3.6. Surface plots of the minority carrier distribution $\Delta p(r, z)$ injected by red light focussed onto the surface of silicon having a bulk diffusion length $L = 5\mu m$ and a surface recombination velocity $v_s/D = 1.0\mu m^{-1}$, for objective lens numerical aperture, (a) $\sin\theta = 0.1$, (b) $\sin\theta = 0.3$, (c) $\sin\theta = 0.5$, (d) $\sin\theta = 0.7$, and (e) $\sin\theta = 0.9$.

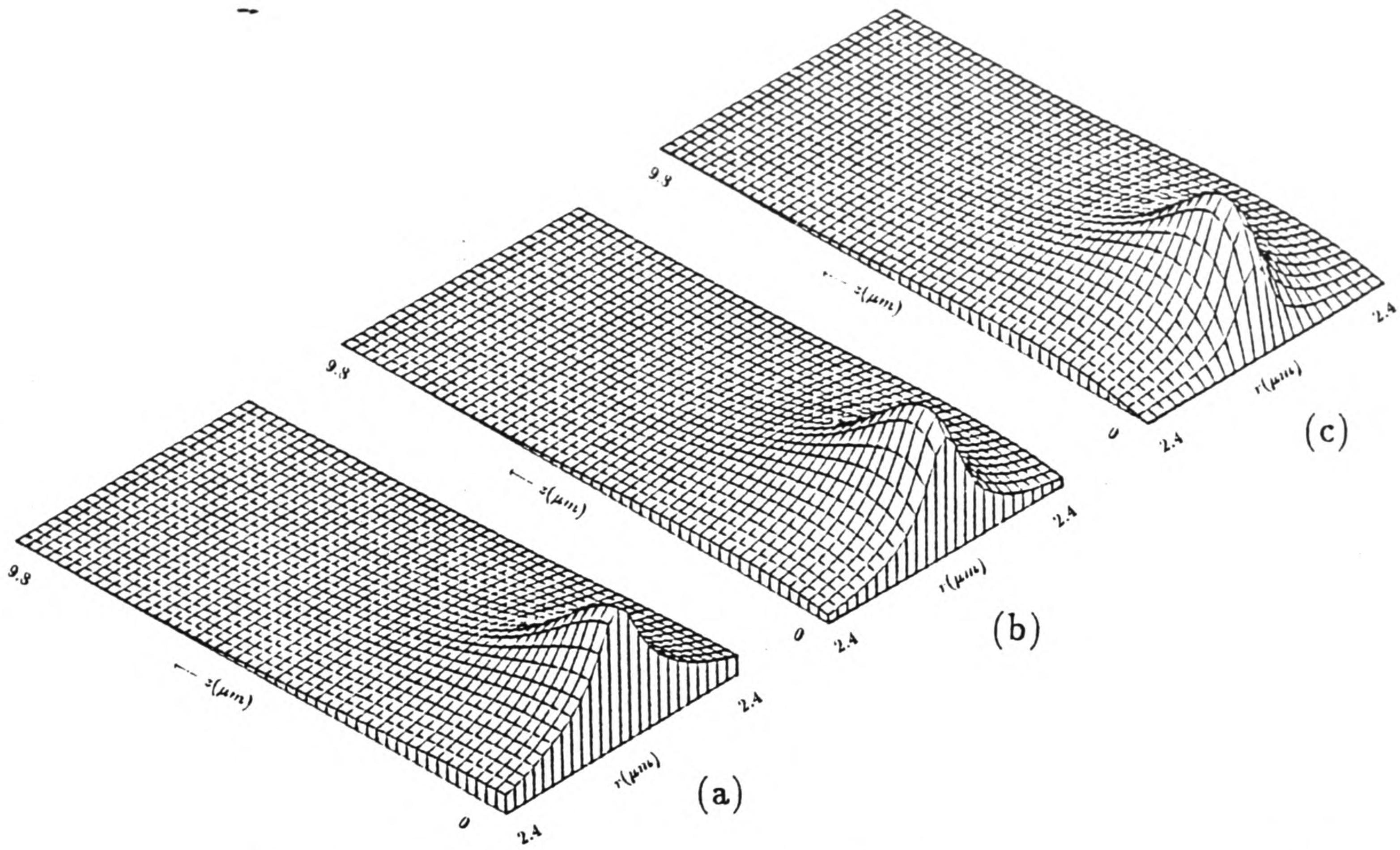

Figure 3.7. The minority carrier distribution for red light in silicon when the objective lens numerical aperture $\sin\theta = 0.6$, the diffusion length $L = 5.0\mu m$ and (a) zero surface recombination velocity, (b) a surface recombination velocity of $v_s/D = 1.0\mu m^{-1}$, and (c) infinite surface recombination velocity.

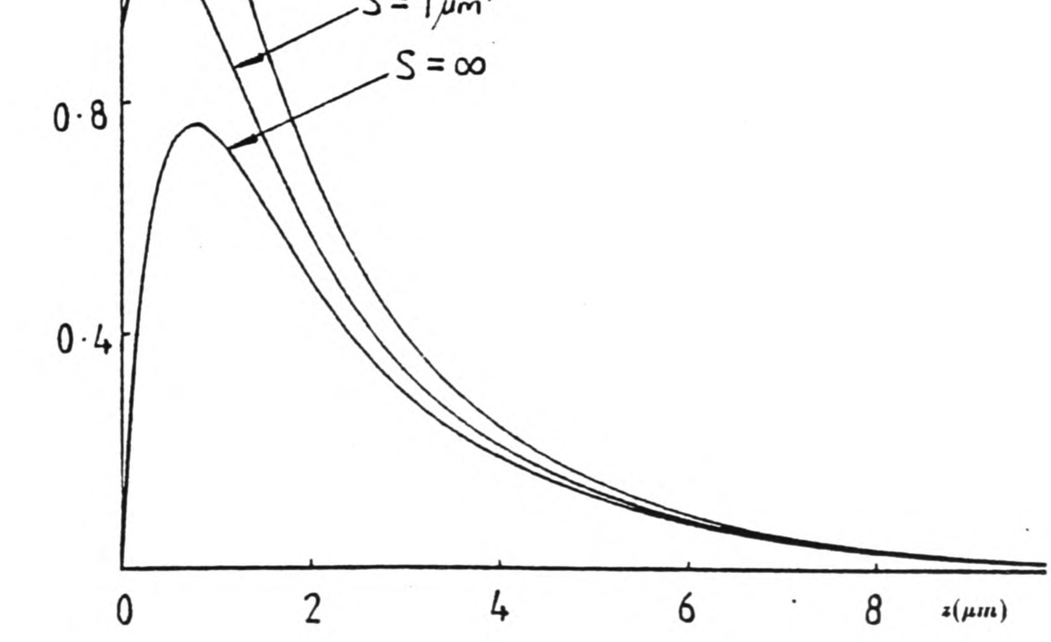

Figure 3.8. The on axis minority carrier distribution $\Delta p(0,z)$ for the case when $\alpha = 0.4\mu m^{-1}$, $L = 10\mu m$, $\sin\theta = 0.6$ and various values of surface recombination velocity.

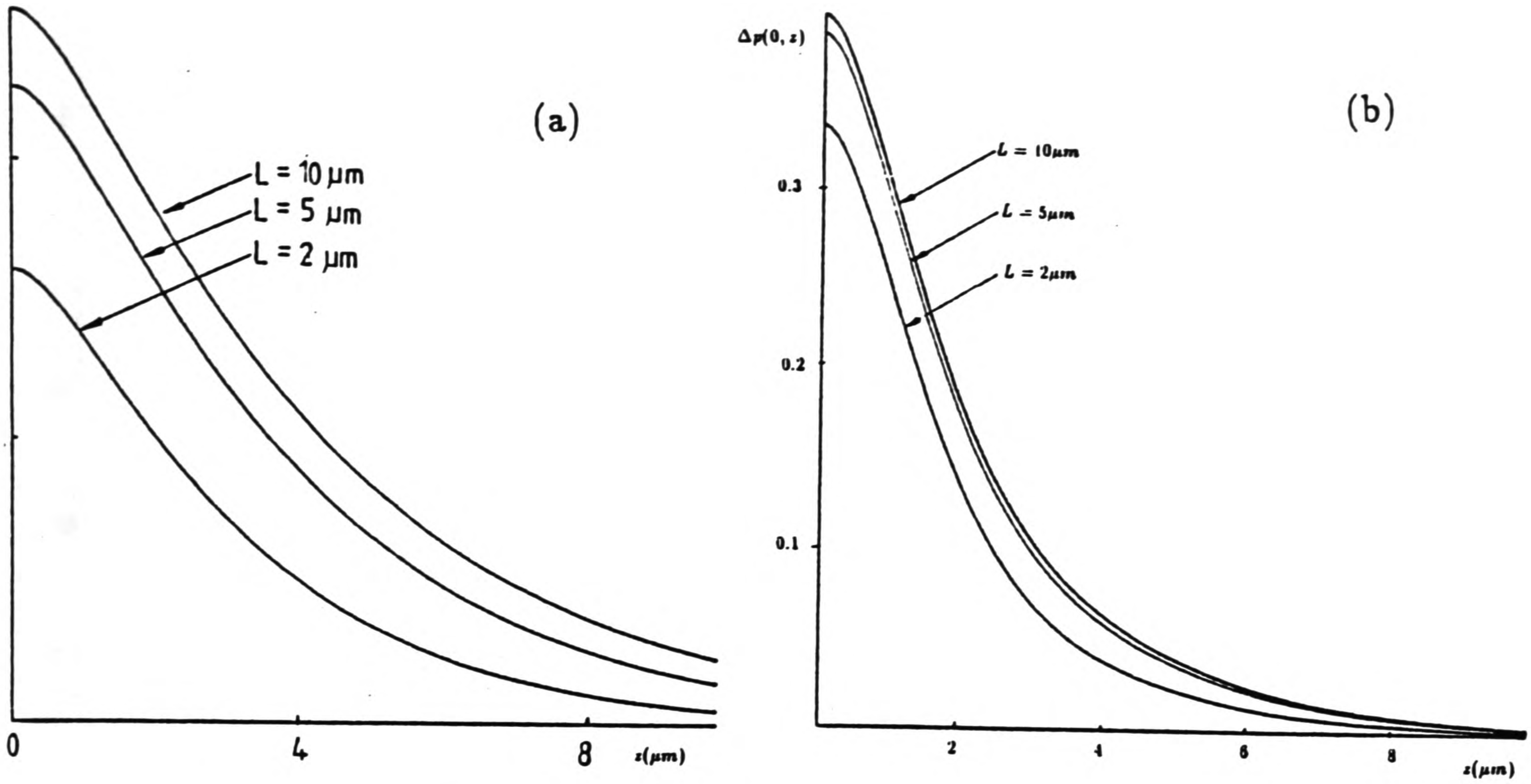

Figure 3.9. The on-axis carrier distribution for red light in silicon with zero surface recombination velocity for various values of diffusion length when the numerical aperture of the objective lens is (a) $\sin\theta = 0.2$, and (b) $\sin\theta = 0.6$.

reason for this can be seen from Figure (3.11) where on-axis plots are shown for an intermediate value of surface recombination velocity, $v_s/D = 1.0\mu m^{-1}$ and a diffusion length of $L = 5.0\mu m$. It is clear from Figure (3.11) that, for the high numerical apertures, the distribution decays more quickly into the semiconductor to the point where at a high value of, say $\sin\theta = 0.9$ most of the injected distribution is confined to a depth of less than about $3\mu m$.

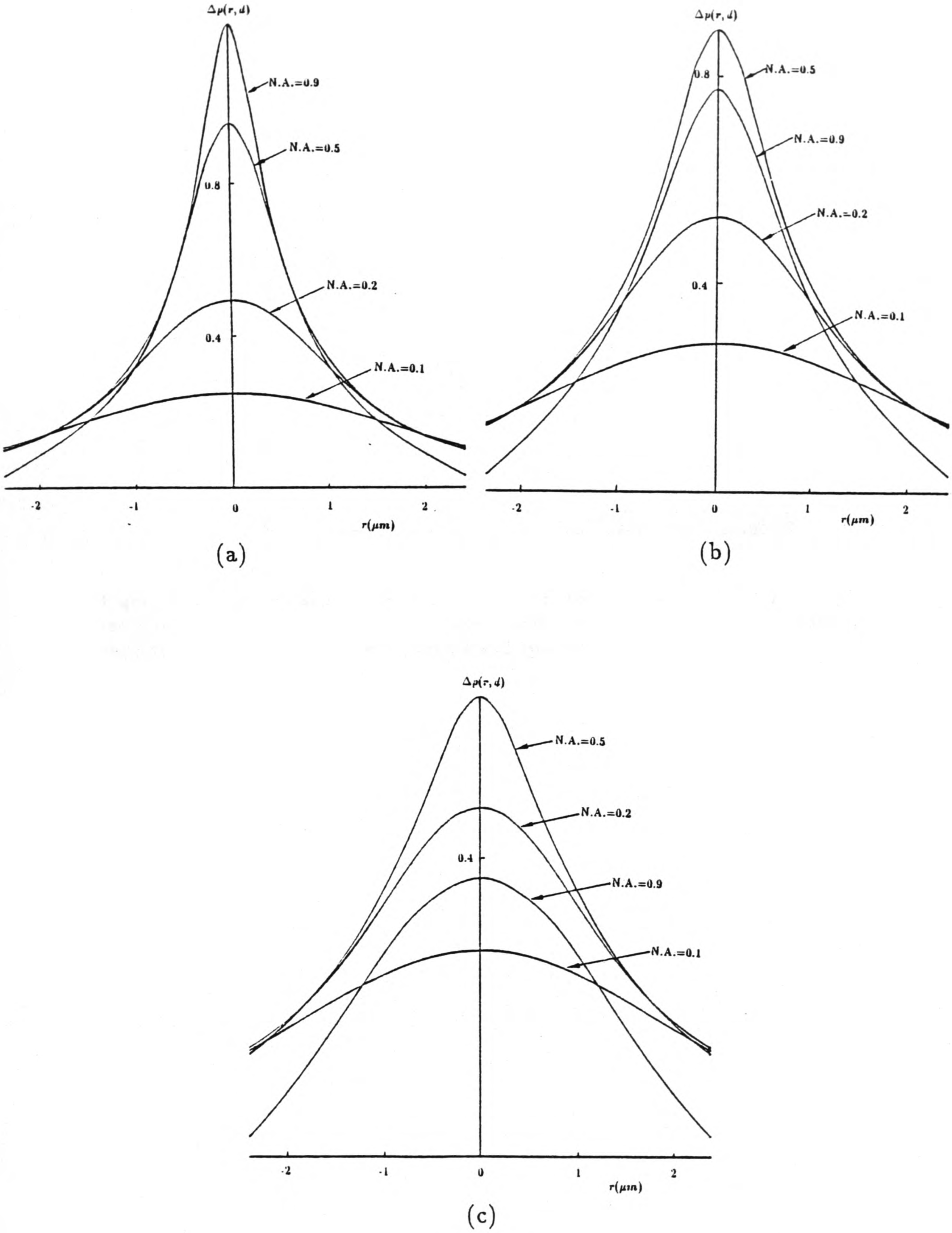

Figure 3.10. Radial sections through the minority carrier distribution for red light in silicon with a surface recombination velocity of $v_s/D = 1.0\mu m^{-1}$ and a diffusion length of $L = 5\mu m$ for section depths of (a) $z = 0.4\mu m$, (b) $z = 1.0\mu m$ and (c) $z = 2.0\mu m$.

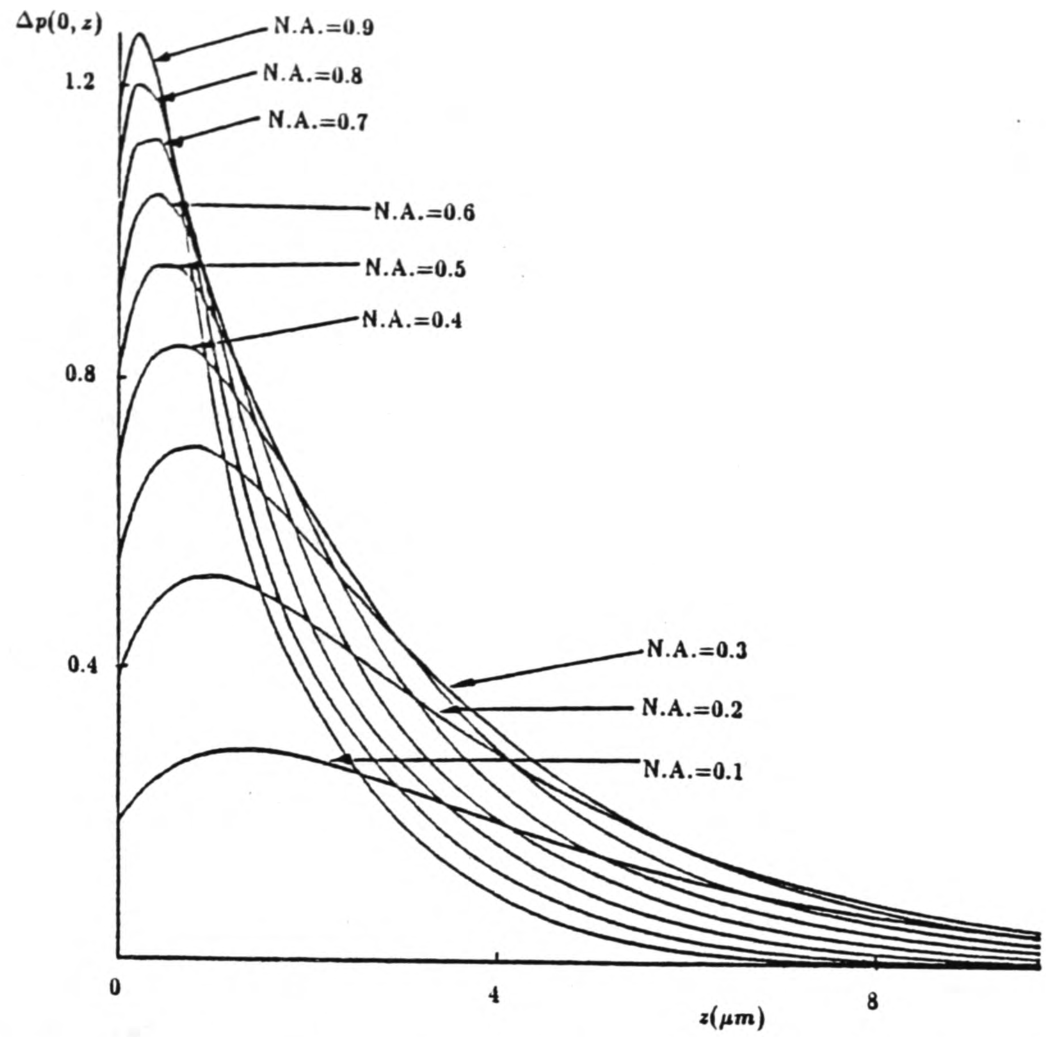

Figure 3.11. The on-axis carrier distribution for red light in silicon with a surface recombination velocity of $v_s/D = 1.0\mu m^{-1}$ and diffusion length of $L = 5.0\mu m$ for various values of the objective lens numerical aperture.

3.2 Information Depth

The decrease in peneration depth of the injected minority carrier distribution with increasing numerical aperture, as described above, can be investigated further by introducing the idea of an *information depth* [21,22]. As a somewhat arbitrary definition of information depth we can ask, what is the distance, d, that we must go into the semiconductor before we have sampled, say 90% of the photo induced carriers. That is, if we introduce the function,

$$\omega(z) = \int_0^\infty \Delta p(r,z)\, r dr, \tag{3.36}$$

the information depth, d is the solution of,

$$\int_0^d \omega(z)\, dz = 0.9 \int_0^\infty \omega(z)\, dz, \qquad 3.37)$$

or, equivalently

$$\int_d^\infty \omega(z)\, dz = 0.1 \int_0^\infty \omega(z)\, dz. \tag{3.38}$$

Defining $\Omega(d)$ such that,

$$\Omega(d) = \int_d^\infty \omega(z)\, dz = \int_d^\infty \int_0^\infty \Delta p(r,z)\, r dr dz, \tag{3.39}$$

the definition of the information depth can be written from Equation (3.38) as,

$$\Omega(d) = 0.1\Omega(0). \tag{3.40}$$

It is straightforward to calculate Ω, since we can expoit the radial symmetry, using

$$\int_d^\infty \int_0^\infty \Delta p(r,z)\, r dr dz = \int_d^\infty \Delta \bar{p}(0,z)\, dz, \tag{3.41}$$

and so we need only consider $\Delta\bar{p}(\nu, z)$, as given by Equation (3.33), in the much simplified form obtained as the transform variable $\nu \to 0$. It is possible to find $\Omega(0)$ and $\Omega(d)$ analyticaly as [21]

$$\Omega(0) = \frac{2g_0}{\ln(\mu)} \left\{ \ln(\mu) - \left(\frac{sL}{1+sL}\right) \ln\left(\frac{\mu\alpha L + 1}{\alpha L + 1}\right) \right\}, \tag{3.42}$$

and,

$$\begin{aligned} \Omega(d) = \frac{g_0}{\ln(\mu)} \Bigg[& \exp\left(-\frac{d}{L}\right) \left\{ \left(\frac{1-sL}{1+sL}\right) \ln\left(\frac{\mu\alpha L+1}{\alpha L+1}\right) \right. \\ & \left. + \ln\left(\frac{\mu\alpha L - 1}{\alpha L + 1}\right) + E_1\left[\left(\frac{\mu\alpha L - 1}{L}\right) d\right] \right\} \\ & + \exp\left(\frac{d}{L}\right) \left\{ E_1\left[\left(\frac{\alpha L+1}{L}\right) d\right] - E_1\left[\left(\frac{\mu\alpha L+1}{L}\right) d\right] \right\} \\ & + 2\left\{E_1(\alpha d) - E_1(\mu\alpha d)\right\} \Bigg], \end{aligned} \tag{3.43}$$

$$\text{where} \qquad \epsilon = \frac{\sin^2\theta}{4}, \qquad \text{and} \qquad \mu = (1+2\epsilon) = \left(1 + \frac{\sin^2\theta}{2}\right), \tag{3.44}$$

and E_1 is an exponential integral of the first kind [23 p.227].

The solution of Equation (3.40) as a function of numerical aperture is shown in Figure (3.12), again for red light in silicon such that $\alpha = 0.4\mu m^{-1}$, and for a diffusion length of $L = 5\mu m$. The two limiting cases of zero and infinite surface recombination velocity are shown although the general trend applies for any v_s.

In the limiting case of low numerical aperture, such that $\epsilon \to 0$, and $\mu \to 1$ Equations (3.43) and (3.42) simplify considerably to

$$\Omega(0) = (1 - \alpha L)(1 + \alpha L + sL), \tag{3.45}$$

and,

$$\Omega(d) = (1 + sL)\exp(-\alpha d) - \alpha L^2(\alpha + s)\exp\left(-\frac{d}{L}\right), \tag{3.46}$$

from which it is possible to put a lower limit on the information depth by considering the high absorption ($\alpha \to \infty$) limit. Taking this limit we find that the actual value of surface recombination velocity is unimportant and that we arrive at,

$$d \approx 2.3L, \tag{3.47}$$

which is in reasonable agreement with Figure (3.12) where $L = 5\mu m$. It should be noted that the factor 2.3 ($= \ln 10$) is of course somewhat arbitrary and depends on the choice of the 90% criterion, and for example, if we had chosen a 95% criterion then the lower bound on the information depth would have been $d \approx (\ln 20)L \approx 3L$.

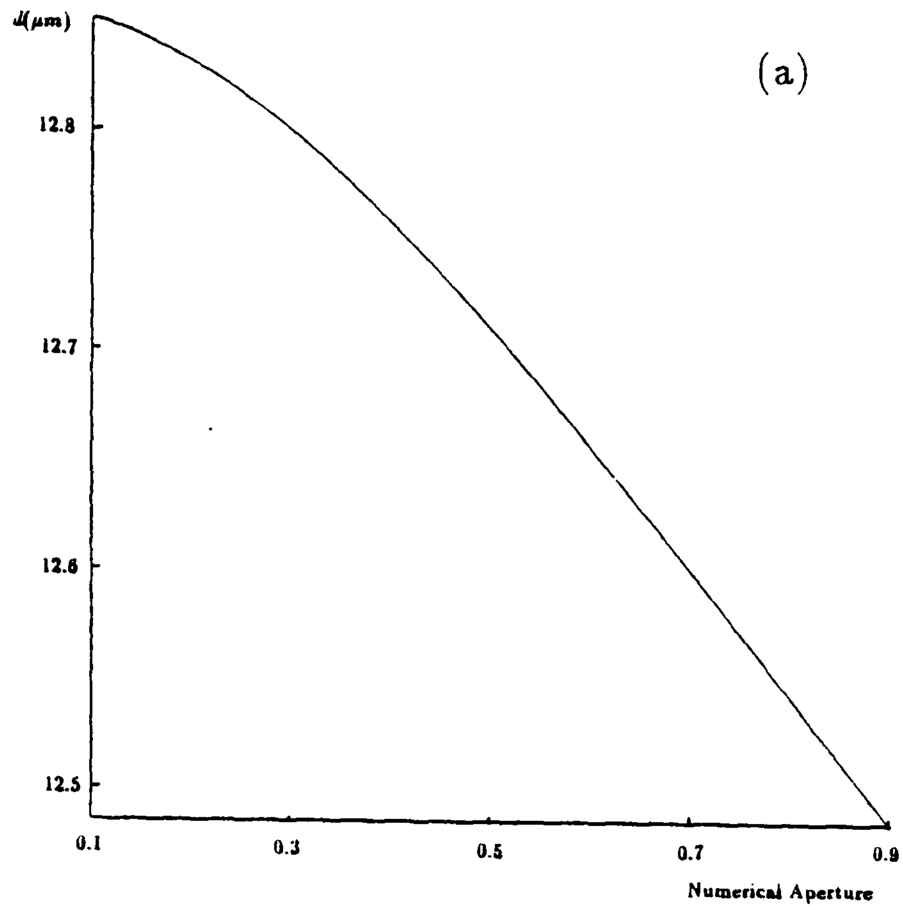

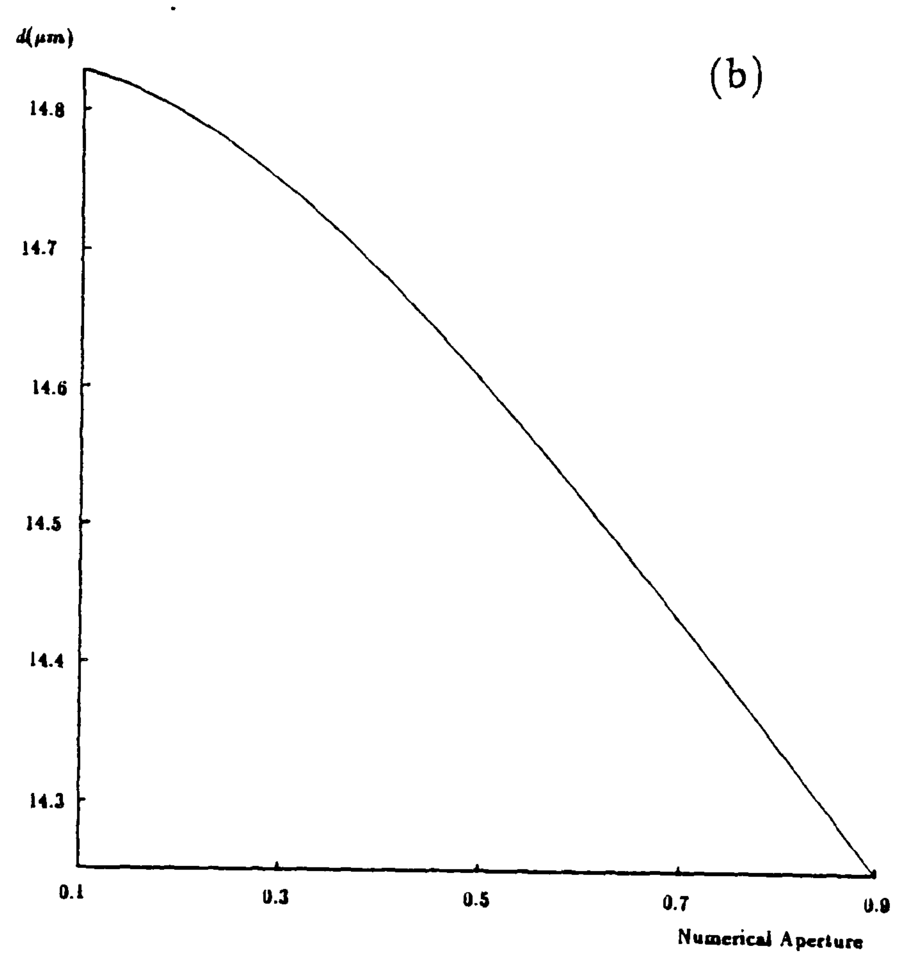

Figure 3.12. The information depth, d, as a function of numerical aperture for red light in silicon having a diffusion length $L = 5\mu m$ and (a) zero surface recombination velocity or, (b) infinite surface recombination velocity.

3.3 Uses for the minority carrier distribution

Having found the form of the induced minority carrier distribution due to a focussed light beam we can now demonstrate it's importance by considering the two practically important examples of (i) Optical Beam Induced Current (OBIC) imaging of defects and (ii) Photoluminescence (PL) imaging of defects.

Example (i): Optical Beam Induced Current Imaging of Electrically Active Defects

One of the main attractions of the beam induced current examination technique is the ability to image electrically active defects close to the semiconductor surface. However, it is clear that to use this technique with any degree of certainty it is neccessary to have a good physical model for the formation of the Optical Beam Induced Current image of the defect. Therfore in the following a defect, defined as a region of increased minority carrier recombination as shown in Figure (3.13), is introduced into the semi-infinite semiconductor and the OBIC contrast calculated as a function of the illuminating lens numerical aperture.

The presence of the defect can be taken into account by introducing a position dependant recombination term into the diffusion Equation such that [24,25,26]

$$\nabla^2 \Delta p(\mathbf{r}) - \frac{\Delta p(\mathbf{r})}{L^2} = -\frac{1}{D} g(\mathbf{r}) + \gamma(\mathbf{r}) u(\mathbf{r}) \Delta p(\mathbf{r}), \tag{3.48}$$

where $\gamma(\mathbf{r})$ is the defect distribution and $u(\mathbf{r})$ is a step function defined to be unity in the region, F, of the defect and zero elsewhere.

The presence of the defect modifies the minority carrier distribution $\Delta p(\mathbf{r})$ such that the solution to Equation (3.48) has to be written in the form of a Fredholm equation given by,

$$\Delta p(\mathbf{r}) = \frac{1}{D} \int_V g(\mathbf{r_0}) G(\mathbf{r}|\mathbf{r_0})\, d\mathbf{r_0} - \int_F \gamma(\mathbf{r_0}) \Delta p(\mathbf{r_0}) G(\mathbf{r}|\mathbf{r_0})\, d\mathbf{r_0}. \tag{3.49}$$

Since we expect the presence of the defect to make a small difference to the OBIC signal, and in fact it has been shown practically [27] that this *is* the case, it is plausible to approximate the solution of Equation (3.49) by a Neumann expansion [28] to first order, such that

$$\Delta p(\mathbf{r}) \approx \Delta p_1(\mathbf{r}) = \Delta p_0(\mathbf{r}) - \int_F \gamma(\mathbf{r_0}) \Delta p_0(\mathbf{r_0}) G(\mathbf{r}|\mathbf{r_0})\, d\mathbf{r_0}, \tag{3.50}$$

where $\Delta p_0(\mathbf{r})$ is the zero order Neumann term which is simply the solution in the absence of a defect as calculated in Section 3.1. However, in the OBIC examination

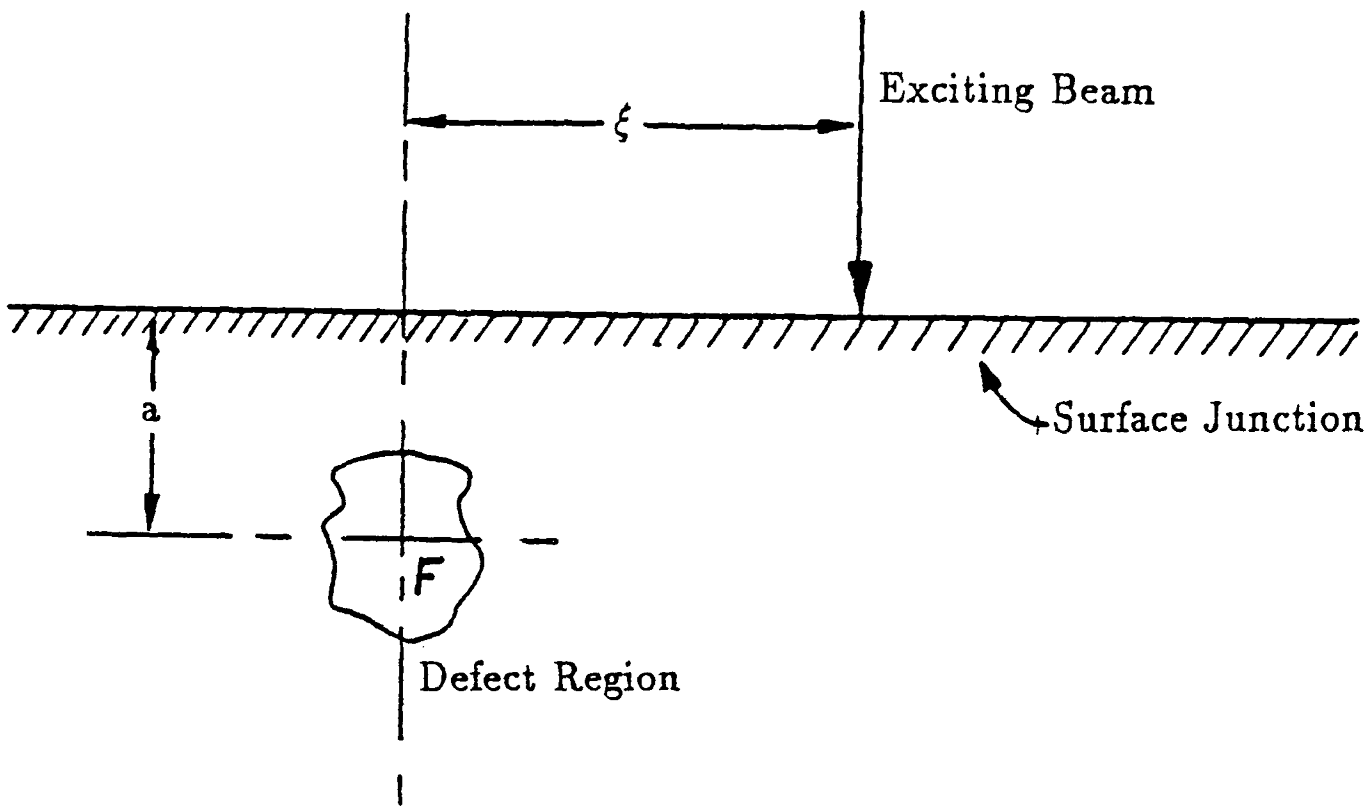

Figure 3.13. Schematic representation of an electrically active defect in a semi-infinte semiconductor.

technique it is the induced *current* that is measured and, if we choose to consider a Schottky barrier diode as shown in Figure (3.13) where the collecting junction is on the $z = 0$ surface, the diffusion current, I, can be found directly from the induced minority carrier distribution since,

$$I = qD \int_0^{2\pi} \int_0^{\infty} \frac{\partial}{\partial z} \Delta p(r,z)\Big|_{z=0} r dr d\theta. \tag{3.51}$$

Substituting $\Delta p(r,z)$ from Equation (3.50) into Equation (3.51) we see that

$$I = I_0 - I^*, \tag{3.52}$$

where I_0 is the diffusion current in the absence of the defect and I^* is the *decrease* in current due to the presence of the defect. From Equation (3.50) it is clear that

$$I_0 = 2\pi qD \int_0^{\infty} \frac{\partial}{\partial z} \Delta p_0(r,z)\big|_{z=0} r dr, \tag{3.53a}$$

and,

$$I^* = 2\pi qD \int_0^{\infty} \frac{\partial}{\partial z} \left\{ \int_F \gamma(\mathbf{r}_0) \Delta p_0(\mathbf{r}_0) G_\infty(\mathbf{r}|\mathbf{r}_0)\, d\mathbf{r}_0 \right\} \big|_{z=0} r dr. \tag{3.53b}$$

The ∞ subscript on the Green's function signifies that, due to the presence of the surface junction, the limiting value of $G(\mathbf{r}|\mathbf{r}_0)$ as the surface recombination velocity tends to infinity is to be taken. Considering I_0 first, and assuming the order of intergration and differentiation can be interchanged freely, we can use the radial symmetry to give

$$I_0 = 2\pi qD \frac{\partial}{\partial z} \Delta \bar{p}_0(0,z)\Big|_{z=0},$$

$$= 2\pi q \frac{\partial}{\partial z} \left\{ \int_0^\infty \bar{g}(0, z_0) G_\infty(0, z|z_0)\, dz_0 \right\} \Big|_{z=0}$$
$$= 2\pi q \int_0^\infty \bar{g}(0, z_0) \left\{ \frac{\partial}{\partial z} G_\infty(0, z|z_0) \Big|_{z=0} \right\} dz_0. \tag{3.54}$$

Turning to I^* we see that,

$$I^* = 2\pi q D \int_0^\infty \frac{\partial}{\partial z} \left\{ \int_F \gamma(\mathbf{r_0}) \Delta p_0(\mathbf{r_0}) G_\infty(\mathbf{r}|\mathbf{r_0})\, d\mathbf{r_0} \right\} \Big|_{z=0} r\,dr$$
$$= 2\pi q D \frac{\partial}{\partial z} \left\{ \int_F \gamma(\mathbf{r_0}) \Delta p_0(\mathbf{r_0}) \left[\int_0^\infty G_\infty(\mathbf{r}|\mathbf{r_0}) \right] r\,dr \right\} \Big|_{z=0} d\mathbf{r_0}. \tag{3.55}$$

Again exploiting the radial symmetry we have,

$$\int_0^\infty G_\infty(\mathbf{r}|\mathbf{r_0})\, r\,dr = G_\infty(0, z|z_0). \tag{3.56}$$

Also, if we choose to consider a *point* defect, we can write the defect distribution, $\gamma(\mathbf{r})$ as

$$\gamma(r, z) = \frac{\gamma_0}{2\pi} \frac{\delta(r - \xi)}{r} \delta(z - a), \tag{3.57}$$

where a is the depth and ξ is the radial position of the defect and γ_0 is the defect's strength. Equations (3.56) and (3.57) allow us to write I^* in the form,

$$I^* = \gamma_0 q D \left\{ \frac{\partial}{\partial z} G_\infty(0, z|a)\big|_{z=0} \right\} \Delta p_0(\xi, a). \tag{3.58}$$

We can now define a *contrast* function, $C_{\text{obic}}(\xi, a)$, as the ratio of I^* and I_0 such that, from Equations (3.54) and (3.58), we have,

$$C_{\text{obic}}(\xi, a) = \left\{ \frac{\gamma_0 D\, h(a)}{2\pi \int_0^\infty h(z_0) \bar{g}(0, z_0)\, dz_0} \right\} \Delta p_0(\xi, a), \tag{3.59}$$

where the function $h(z_0)$ is given as,

$$h(z_0) = \frac{\partial}{\partial z} G_\infty(0, z|z_0)\big|_{z=0}. \tag{3.60}$$

For the case of focussed light excitation, using the form of the generation function and Green's function from Section 3.1, it is straightforward to show that Equation (3.59) reduces to

$$C_{\text{obic}}(\xi, a) = \frac{\gamma_0}{g_0} \left\{ \frac{\ln\left[1 + \frac{\sin^2\theta}{2}\right]}{\ln\left[1 + \frac{\sin^2\theta\alpha L}{2(\alpha L + 1)}\right]} \exp\left(-\frac{a}{L}\right) \right\} \Delta p_0(\xi, a), \tag{3.61}$$

that is,

$$C_{\text{obic}}(\xi, a) = \Phi(\sin\theta, a)\, \Delta p_0(\xi, a). \tag{3.62}$$

From which it is clear that the contrast for a defect at a certain depth is directly proportional to the minority carrier distribution, and so it is straightforward to find $C_{\mathrm{obic}}(\xi, a)$ by use of the expression for $\Delta p(r, z)$ given in Section 3.1.

Figure (3.14) shows contrast plots as obtained from Equation (3.62) for three values of numerical aperture, and various values of diffusion length, for a defect at a depth of $a = 2\mu m$. Each of the plots follows the same trends and, in particular, it can be seen that the contrast curves have no side lobes, this is to be expected from the form of Equation (3.62) since the carrier distribution has no side lobes either. The relative unimportance of the diffusion length when imaging defects can also be seen from Figure (3.14) and notably for values of $L \geq 10\mu m$ the $L \to \infty$ approximation is adequate.

One important question to ask is how does the resolution of the OBIC technique depend on the numerical aperture of the objective lens. If we define the resolution as the half width of the contrast curves it is possible to investigate the effect of the numerical aperture for defects at various depths. In Figure (3.15) the resolution is plotted against numerical aperture for a low value of diffusion length $L = 2\mu m$, Figure (3.15a), and in the limit $L \to \infty$ Figure (3.15b). For a shallow defect where $a = 0.5\mu m$ the curves are as one would expect, that is the resolution increases with numerical aperture until a limit is reached at around $0.8\mu m$, although for deeper defects the curves quite are different. It is clear that the resolution goes through a maximum, that is the half width goes through a minimum, at an intermediate value of numerical aperture. This is an important point to note since when imaging defects which are not close to the surface it is clearly not always wise to use a high numerical aperture lens in the illumination system to obtain maximum resolution. Again it can be seen from Figure (3.15) that the diffusion length is relatively unimportant since the resolution predicted in both Figure (3.15a) and (3.15b) is, certainly for the shallow defects, very similar.

It should be noted here that, although we have only considered a point defect as a straightforward example, it is no more difficult to calculate the contrast due to *line* defects either parallel or perpendicular to the semiconductor by simply changing the form of the defect distibution, $\gamma(\mathbf{r})$.

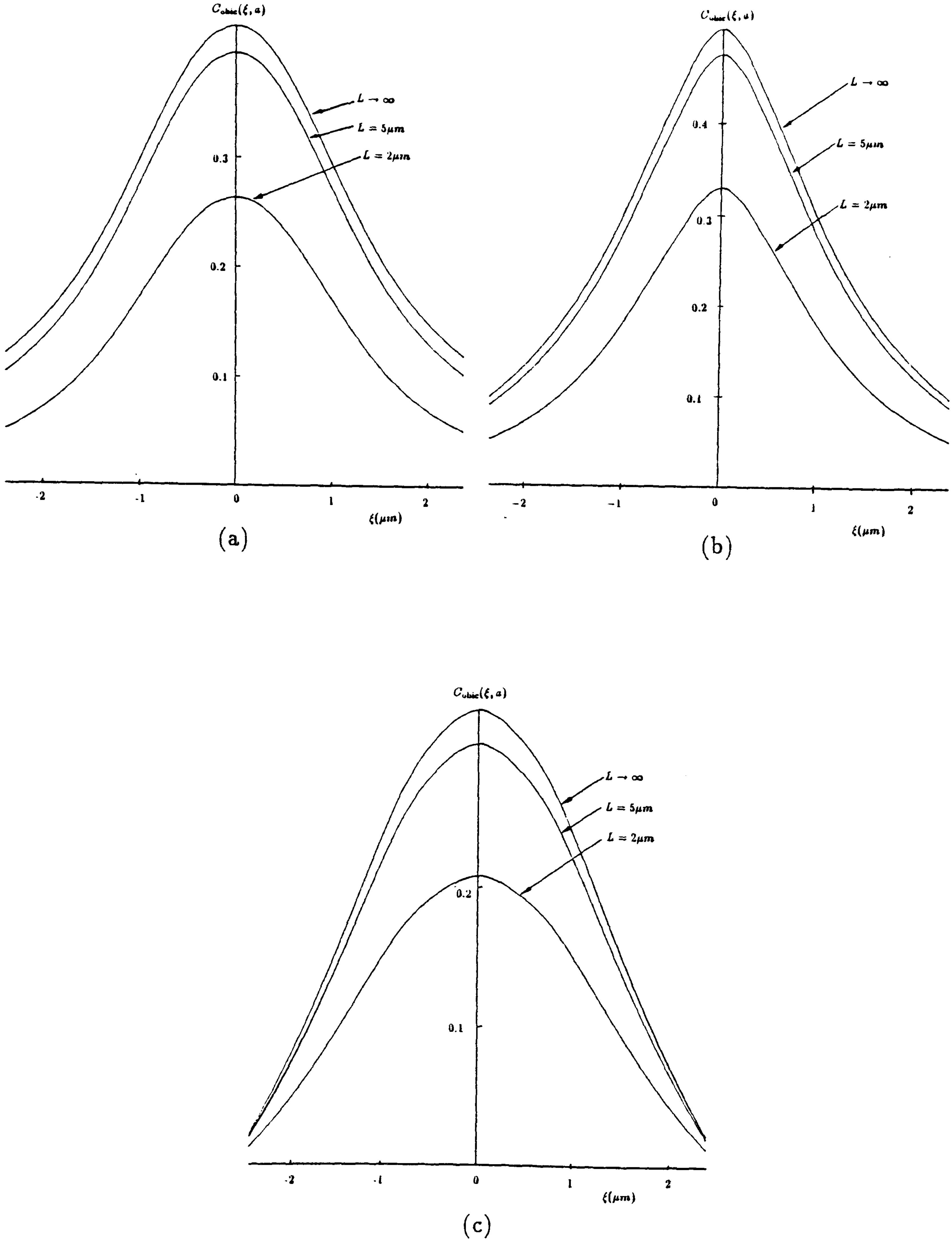

Figure 3.14. The contrast function for a point defect at a depth $a = 2\mu m$ in a silicon Schottky barrier of shallow p-n junction when illuminated with red light. The numerical aperture is taken as (a) $\sin\theta = 0.2$, (b) $\sin\theta = 0.6$ and, (c) $\sin\theta = 0.9$.

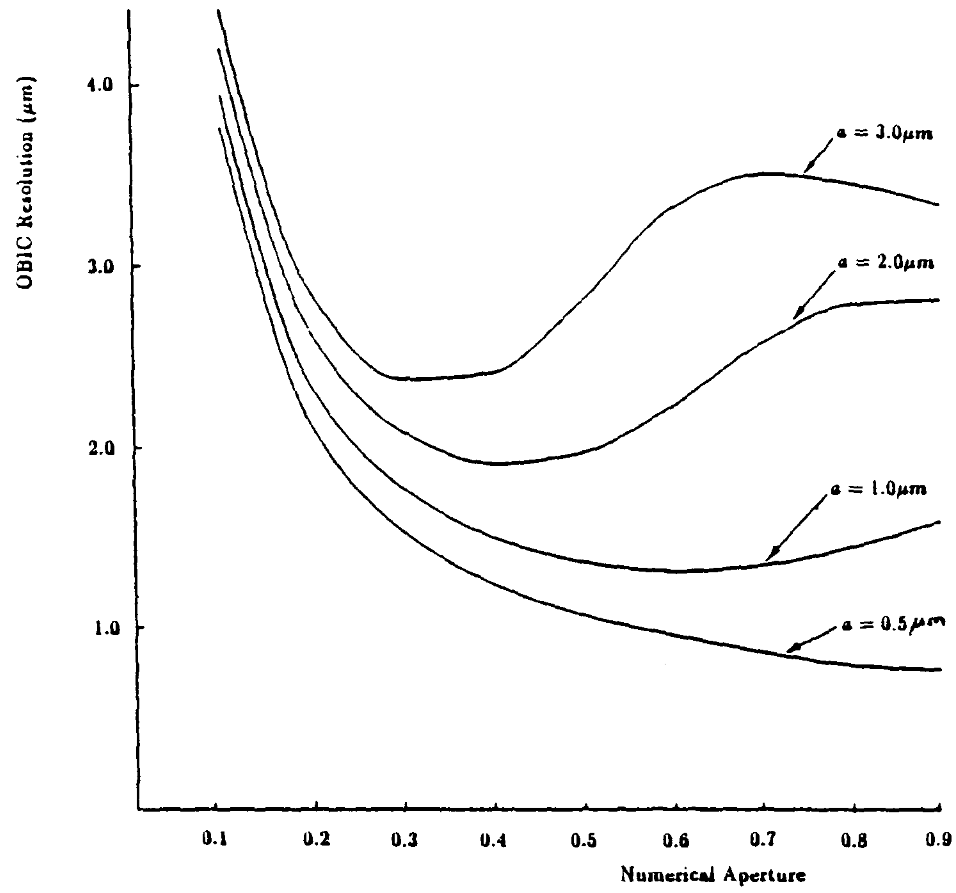

(a)

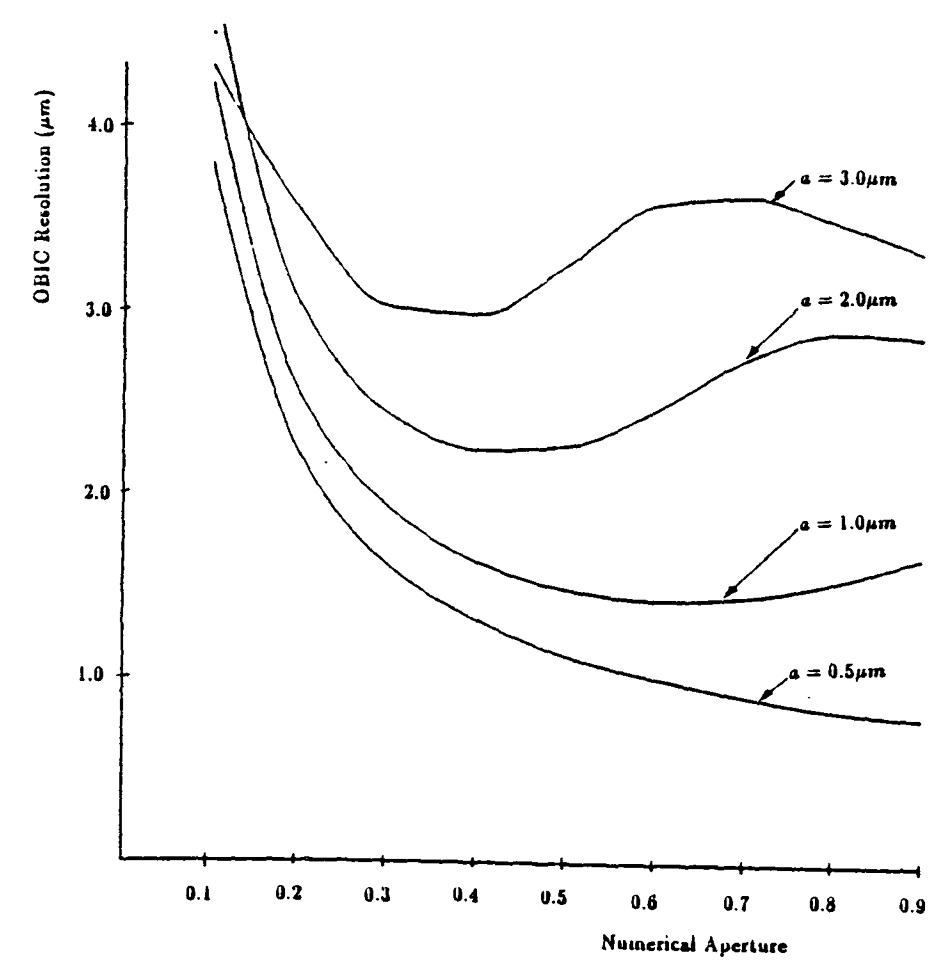

(b)

Figure 3.15. The resolution, defined as the half width of the contrast curves, for the OBIC imaging technique for various defect depths when $\alpha = 0.4\mu m^{-1}$, and (a) a diffusion length of $L = 2\mu m$ and (b) in the limit as $L \rightarrow \infty$.

Example (ii): Photoluminescence Imaging of Defects

Following on from the preceding example we now calculate the contrast obtained during photoluminescence studies of an electrically active defect. The photoluminescence signal, $\mathcal{P}$, can be expressed as [29,30,31],

$$\mathcal{P} = \int_{\mathbf{V}} A(z) \left(\frac{\tau}{\tau_r} \right) \Delta p(r,z)\, d\mathbf{V}, \tag{3.63}$$

where V is the semi-infinite volume of the material and the ratio of the total recombination rate to the radiative recombination rate, τ/τ_r, is the internal quantum efficiency of the material. The factor $A(z)$ represents the attenuation of the lumniscent light as it reaches the surface of the material and may be expressed as [32]

$$A(z) = \int_0^{\phi_c} \exp\left(-\frac{\alpha_l z}{\cos\phi} \right) \sin\phi\, d\phi, \tag{3.64}$$

here α_l is the absorption coefficient for the luminescencent radiation and ϕ_c is the critical angle at the semiconductor-air interface. It has been shown [33] that the critical angle is often sufficiently small such that $A(z)$ may be accurately described as $\exp(-\alpha_l z)$, although some authors neglect this term altogether [34]. For simplicity of calculation we will also ignore the internal absorbtion such that the photoluminescence signal can be written in the form,

$$\mathcal{P} \propto \int_0^\infty \int_0^\infty \Delta p(r,z)\, r dr dz. \tag{3.65}$$

Here $\Delta p(r,z)$ is simply the solution to the diffusion equation which has been modified to take account of the presence of the defect. Substituting the form of $\Delta p(r,z)$ from Equation (3.50) into Equation (3.65) gives

$$\mathcal{P} = \mathcal{P}_0 - \mathcal{P}^*, \tag{3.66}$$

where, similarly to the OBIC case, $\mathcal{P}_0$ represents the PL signal in the absence of the defect and $\mathcal{P}^*$ represents the *decrease* in PL due to the presence of the defect. Clearly it is possible to write $\mathcal{P}_0$ as,

$$\mathcal{P}_0 \propto \int_0^\infty \int_0^\infty \Delta p_0(r,z)\, r dr dz = \int_0^\infty \Delta p_0(0,z)\, dz, \tag{3.67}$$

and so,

$$\mathcal{P}_0 \propto \int_0^\infty \int_0^\infty \bar{g}(0,z_0) G(0,z|z_0)\, dz_0 dz, \tag{3.68}$$

such that,

$$\mathcal{P}_0 \propto \int_0^\infty \bar{g}(0,z_0) \left\{ \int_0^\infty G(0,z|z_0)\, dz \right\} dz_0. \tag{3.69}$$

Turning to $\mathcal{P}^*$ it is clear that, from Equation (3.50),

$$\mathcal{P}^* \propto \int_0^\infty \int_0^\infty \int_F \gamma(\mathbf{r_0})\Delta p_0(\mathbf{r_0})G(\mathbf{r}|\mathbf{r_0})\, d\mathbf{r_0} r dr dz, \tag{69}$$

which, by use of the Hankel transform, can be written,

$$\begin{aligned}\mathcal{P}^* &\propto \int_0^\infty \int_F \gamma(\mathbf{r_0})\Delta p_0(\mathbf{r_0})G(0,z|z_0)\, d\mathbf{r_0} dz \\ &\propto \int_F \gamma(\mathbf{r_0})\Delta p_0(\mathbf{r_0}) \left[\int_0^\infty G(0,z|z_0)\, dz\right] d\mathbf{r_0}.\end{aligned} \tag{3.70}$$

Speciali~~s~~zing to the case of a point defect at a depth a, as in the OBIC example, yields,

$$\mathcal{P}^* \propto \frac{\gamma_0}{2\pi}\left[\int_0^\infty G(0,z|a)\, dz\right] \Delta p_0(\xi, a). \tag{3.71}$$

The photoluminescence contrast, $C_{\text{pl}}(\xi, a)$, can be defined in an analogous way to the OBIC contrast as the ratio of $\mathcal{P}^*$ to $\mathcal{P}_0$, and as such has the form,

$$C_{\text{pl}}(\xi, a) = \left\{\frac{\gamma_0 f(a)}{2\pi \int_0^\infty f(z_0)\bar{g}(0, z_0)\, dz_0}\right\} \Delta p_0(\xi, a), \tag{3.72}$$

where $f(z_0) = \int_0^\infty G(0,z|z_0)\, dz$. For the case of focussed light excitation Equation (3.72) reduces to,

$$C_{\text{pl}}(\xi, a) = \frac{\gamma_0}{g_0} \frac{\left\{1 - \left(\frac{sL}{1+sL}\right)e^{-a/L}\right\}}{\left\{1 - \left(\frac{sL}{1+sL}\right)\frac{\ln\left[1+\frac{\sin^2\theta\alpha L}{2(\alpha L+1)}\right]}{\ln\left[1+\frac{\sin^2\theta}{2}\right]}\right\}} \Delta p_0(\xi, a), \tag{3.73a}$$

that is,

$$C_{\text{pl}}(\xi, a) = \Theta(\sin\theta, a)\, \Delta p_0(\xi, a). \tag{3.73b}$$

Again it is clear that the contrast function is directly proportional to the minority carrier distribution in the absence of a defect, $\Delta p_0(r, z)$, and so straightforward to calculate from Equation (3.35).

As an example of the form of Equation (3.73) Figure (3.16) shows the form of $C_{\text{pl}}(\xi, a)$ for a defect at a depth of $a = 2\mu m$ in gallium arsenide when the numerical aperture of the objective lens $\sin\theta = 0.6$ and the wavelength ~~incident~~ of the incident light is $\lambda = 752nm$. Figure (3.16a) is for the case when the surface recombination velocity $v_s/D \to 0$, and (3.16b) is for when $v_s/D \to \infty$. From the contrast curves it can be seen that the photoluminescence technique follows the same trends as the OBIC method described in the previous example, as would be expected since the expressions for the contrast functions in both cases differ only in their pre-multiplying factors. Again we can define the resolution to be the half width of the contrast curves and Figure (3.17)

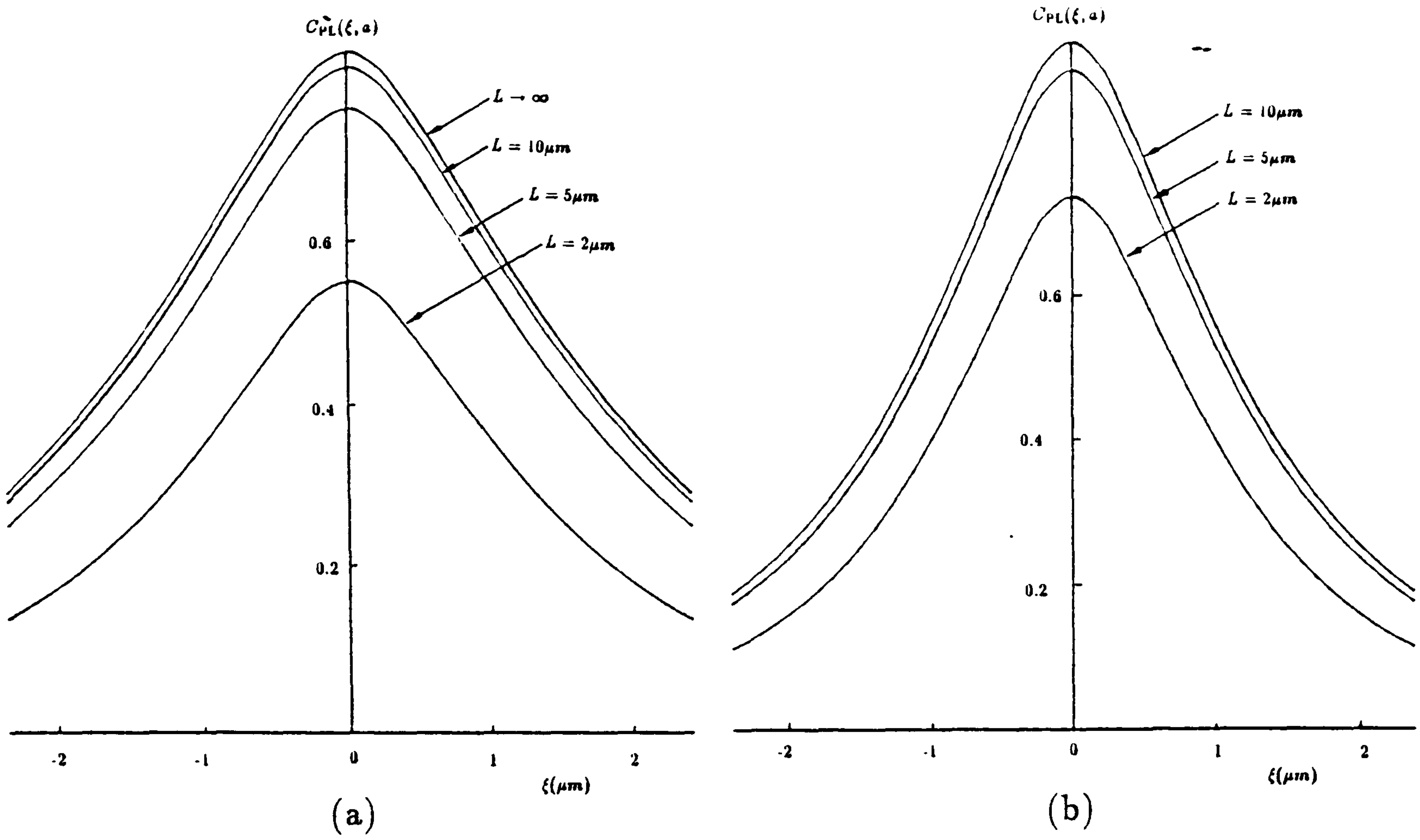

Figure 3.16. Plots of the photoluminescence contrast, for various diffusion lengths, for a point defect at a depth of $a = 2\mu m$ in a GaAs sample when illuminated with infra red light of wavelength $\lambda = 752nm$. The numerical aperture of the illuminating lens is $\sin\theta = 0.6$ and the surface recombination velocity is taken as (a) $v_s/D \to 0$, and (b) $v_s/D \to \infty$.

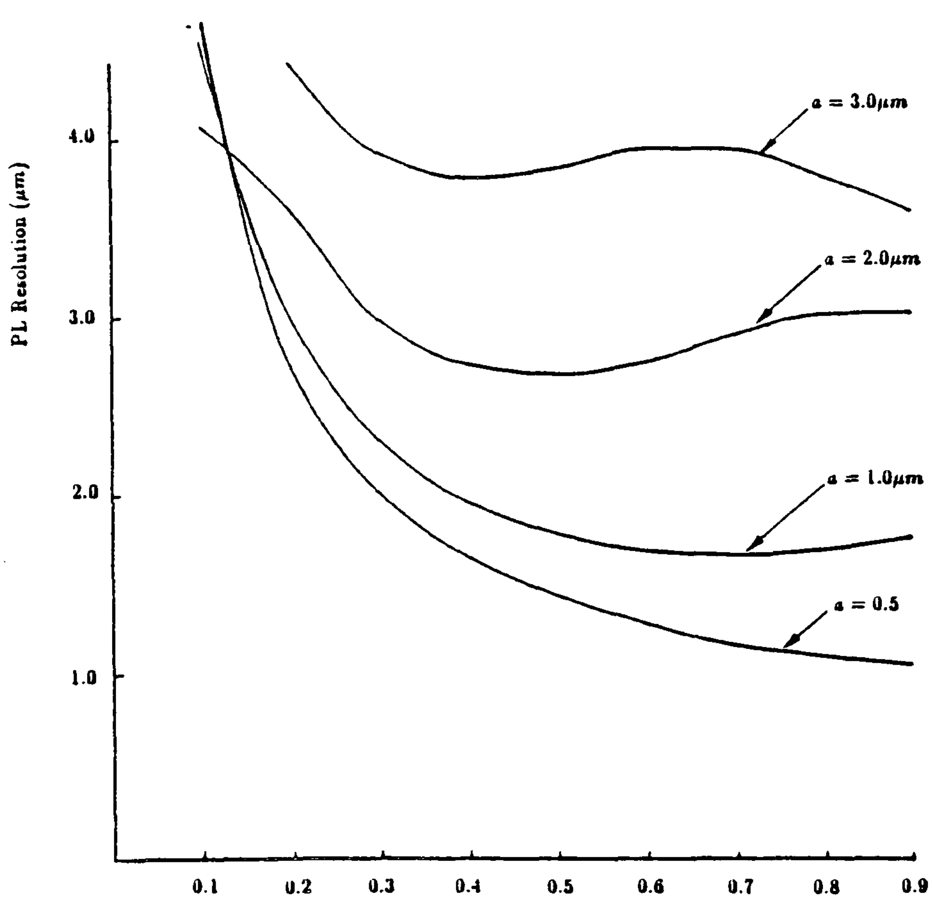

Figure 3.17. The resolution of the photoluminescence technique for the case when GaAs is illuminated with infra red light of wavelength $\lambda = 752nm$ such that $\alpha = 1.0\mu m^{-1}$. The diffusion length is taken as $L = 5\mu m$, the surface recombination velocity is $v_s/D = 1.0\mu m^{-1}$ and various defect depths are considered.

shows that the photoluminescence resolution varies in the same way with numerical aperture as does the OBIC resolution. That is, for defects more than, say, a micron from the surface the resolution goes through a maximum at an intermiediate value of numerical aperture, although the maximum resolution for the PL technique is seen to be about $1.1\mu m$ whereas in the OBIC example the maximum resolution was about $0.8\mu m$.

3.4 Approximate Theories

The calculation of the induced minority carrier distribution $\Delta p(r,z)$ as described in Section 3.1 is rather involved and time consuming. For this reason it is interesting to ask if there are any realistic approximations which can be used to simplify the analysis whilst still predicting the correct trends. The awkwardness of the problem stems from the complicated form of the generation function $g(r,z)$ and so it is this term to which we will seek an approximation.

In the *absence* of absorption ($\alpha_u \to 0$) the light intensity distribution in the focal plane can be written [35 p255] in the form,

$$g(v,0)\Big|_{\alpha_u \to 0} = A_1 \left[\frac{2J_1(v)}{v}\right]^2, \tag{3.74}$$

where J_1 is a Bessel function of the first kind and order one, and A_1 is a normalisation constant. If we assume that the rate at which the light is absorpted is purely proportional to the light intensity, the axial form of $g(v,u)$ can be approximated by a simple exponential decay with a decay length (in optical coordinates) of $1/\alpha_u$. This means that we can approximate the generation function by,

$$g(v,u) = A_2 \exp\left(-\alpha_u u\right) \left[\frac{2J_1(v)}{v}\right]^2. \tag{3.75}$$

The generation term in Equation (3.75) can be further simplified by noting that a Gaussian can be fitted, to a good accuracy, to the Bessel function by choosing the Gaussian half width c_v, correctly. If we make this further approximation it is possible to write the generation term in a much simplified form as

$$g(v,u) = \frac{g_0 \alpha_u a^2 b}{\pi c_v^2} \exp\left(-\alpha_u u\right) \exp\left(-\frac{v^2}{c_v^2}\right), \tag{3.76}$$

where the normalised Gaussian half width $c_v = 1.93$ for the best fit [25], and can be related to the *actual* Gaussian half width c, via,

$$c = \left(\frac{\lambda c_v}{2\pi}\right) \frac{1}{\sin\theta}. \tag{3.77}$$

The approximation given in Equation (3.76) will be refered to as the *decaying Gaussian approximation*, and Equation (3.77) gives us a way to choose the Gaussian half width, c, appropriate to a numerical aperture $\sin\theta$. A further simplification of the decaying Gaussian approximation can be found by assuming that the Gaussian half width is small compared to the diffusion length, since then we obtain,

$$g(v,u) = \frac{g_0 \alpha_u a^2 b}{2\pi} \frac{\delta(v)}{v} \exp\left(-\alpha_u u\right), \tag{3.78}$$

where $\delta(v)$ is the Dirac-delta function. Equation (3.78) will be refered to from now on as the *decaying point source approximation.* The induced carrier distribution in the decaying Gaussian approximation can now be calculated from the general expression given in Equation (3.16) which yields [13],

$$\Delta p(v,u) = \frac{g_0 \alpha_u a^2}{2\pi D b} \int_0^\infty \left\{ \exp(-\alpha_u u) - \left(\frac{\alpha_u + s}{\phi + s}\right) \exp(-\phi u) \right\} \frac{\exp(-\nu^2 c_v^2/4)}{(\phi^2 - \alpha_u^2)} J_0(\nu v)\, \nu d\nu. \quad (3.79)$$

Use has been made of Weber's first exponential integral [36 p.393],

$$\int_0^\infty \exp\left(-p^2 x^2\right) J_0(qx)\, x dx = \frac{1}{2p^2} \exp\left(\frac{-q^2}{4p^2}\right), \quad (3.80)$$

to calculate the Hankel transform of $g(v,u)$. The carrier distribution in the decaying point source approximation follows directly from Equation (3.79) by taking the limit as $c_v \to 0$. Unfortunately it is not possible to express Equation (3.79) in terms of known functions, although it is straightforward to evaluate numerically.

Figure (3.18) shows isometric surface plots, obtained from Equation (3.79), for the case when $\alpha = 0.4\mu m^{-1}$, $L = 5\mu m$, a Gaussian half width $c = 0.32\mu m$ which, from Equation (3.77), corresponds to a numerical aperture of $\sin\theta \approx 0.6$ and three values of surface recombination velocity. The carrier distribution due to the simple decaying point source approximation is shown in Figure (3.19), again for the case when $\alpha = 0.4\mu m^{-1}$, $L = 5\mu m$ and for three values of the surface recombination velocity.

It is clear from Figures (3.18) and (3.19) that both the approximations follow the same trends as given by the full theory and so we can see that Equation (3.79) provides a resonable approximation to the induced carrier distribution although tends to over estimate the depth of penetration of the excess carriers.

Again, it is easier to compare the focussed theory and Gaussian approximation by considering axial and radial sections through the distributions separately. Figure (3.20) shows on-axis comparisons for a high numerical aperture of $\sin\theta = 0.6\mu m$, Figure (3.20a), and a low numerical aperture of $\sin\theta = 0.2$, Figure (3.20b), when $\alpha = 0.4\mu m^{-1}$ and $L = 10\mu m$. The Gaussian half widths were chosen using Equation (3.77) to be $c = 0.32\mu m$ and $c = 0.97\mu m$ respectively. The fit at high numerical aperture is seen to be fairly poor where the Gaussian approximation over estimates the penetration depth considerably for all the values of surface recombination velocity, although at low numerical aperture the fit is excellent with the Gaussian approximation following the focussed theory at all values of surface recombination velocity.

In Figure (3.21) we give a comparison of radial sections through the distributions at different depths again for the case when $\alpha = 0.4\mu m^{-1}$, $L = 10\mu m$ and $v_s/D = 1.0\mu m$.

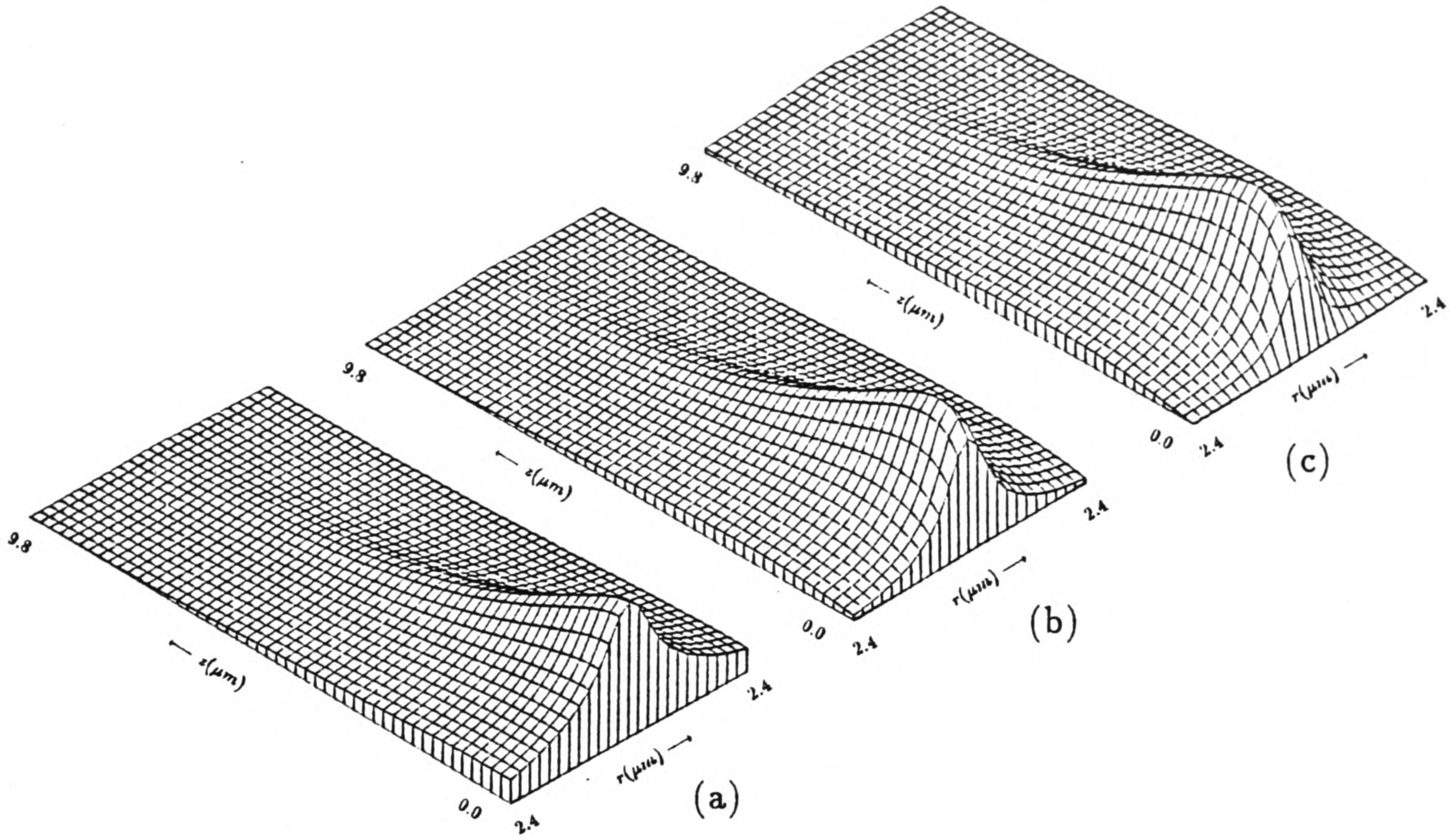

Figure 3.18. The minority carrier distribution $\Delta p(r, z)$ obtained from the decaying Gaussian approximation of Equation (3.79) for the case when $\alpha = 0.4\mu m^{-1}$, $L = 5\mu m$, $c = 0.32\mu m$ and a surface recombination velocity of (a) $v_s \rightarrow 0$, (b) $v_s/D = 1.0\mu m^{-1}$ and (c) $v_s \rightarrow \infty$.

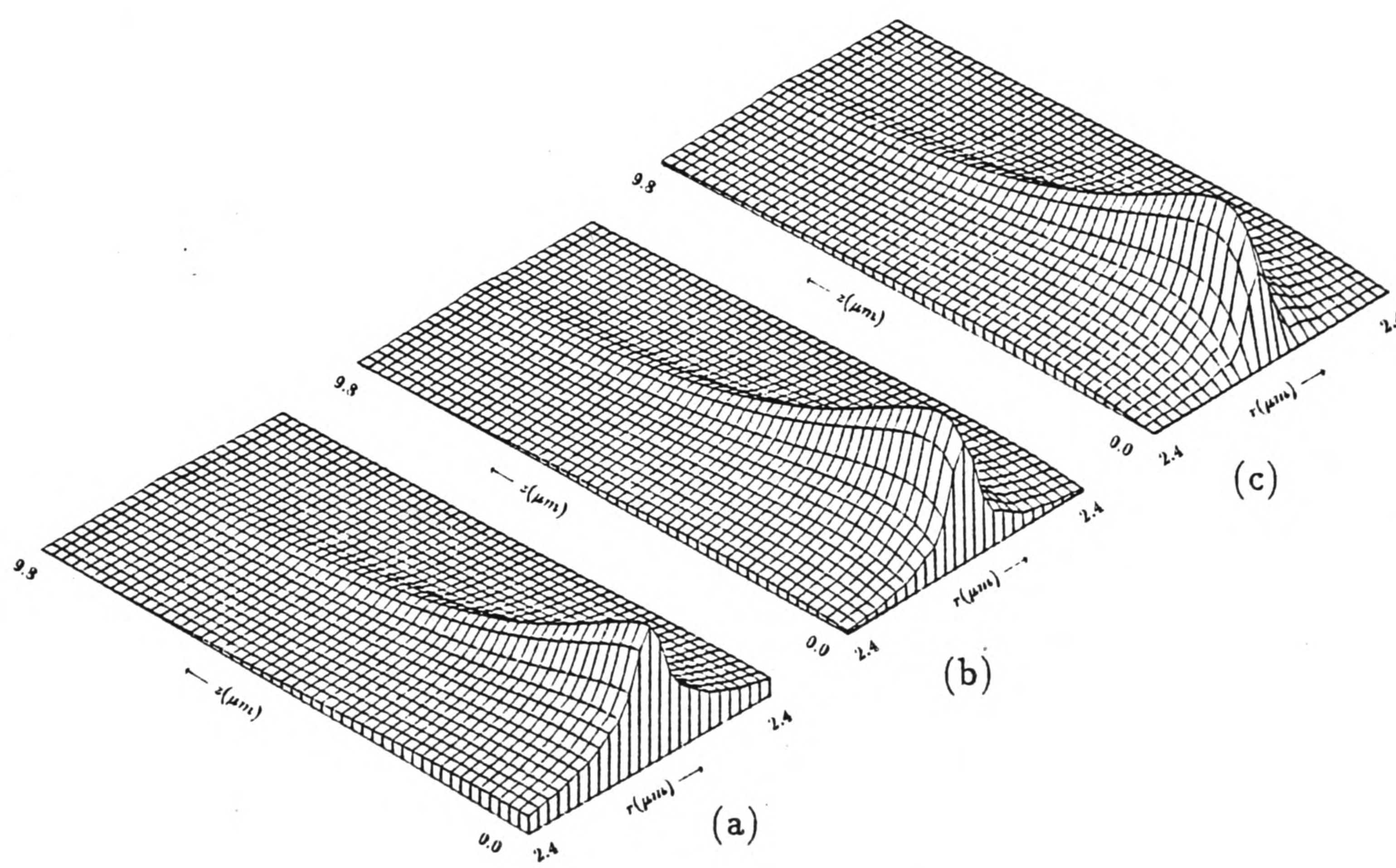

Figure 3.19. The minority carrier distribution $\Delta p(r, z)$ obtained from the decaying point source approximation for the case when $\alpha = 0.4\mu m^{-1}$, $L = 5\mu m$ and a surface recombination velocity of (a) $v_s \rightarrow 0$, (b) $v_s/D = 1.0\mu m^{-1}$ and (c) $v_s \rightarrow \infty$.

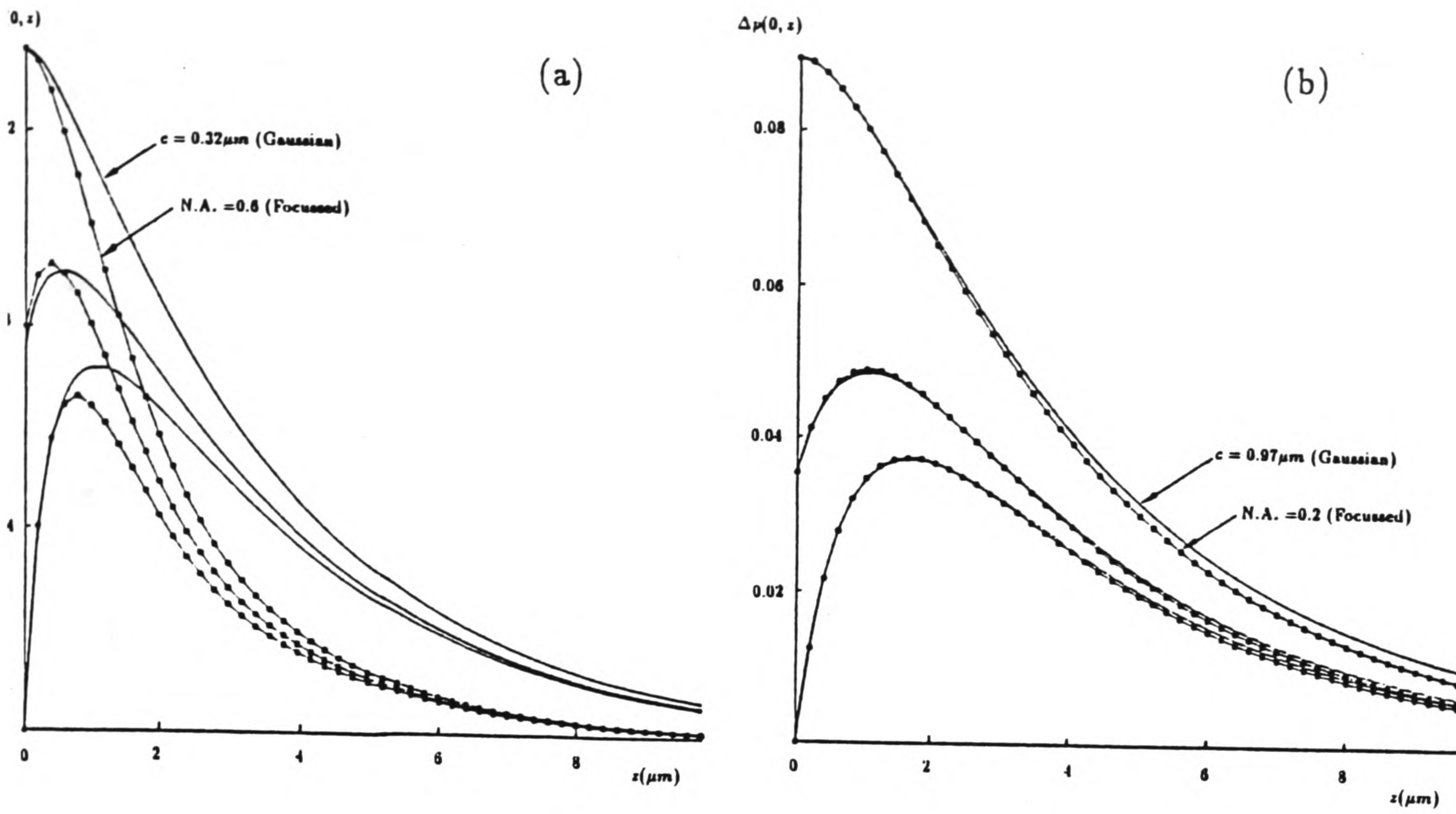

Figure 3.20. Comparisons of the on-axis carrier distribution produced from the focussed beam theory and the decaying Gaussian approximation for the case when $\alpha = 0.4\mu m^{-1}$, $L = 10\mu m$ and $v_s/D \rightarrow 0$, $v_s/D = 1.0\mu m^{-1}$ and $v_s/D \rightarrow \infty$. (a) is for a high numerical aperture of $\sin\theta = 0.6$ and Gaussian width of $c = 0.32\mu m$ and (b) is for a low numerical aperture of $\sin\theta = 0.2$ and Gaussian width of $c = 0.97\mu m$.

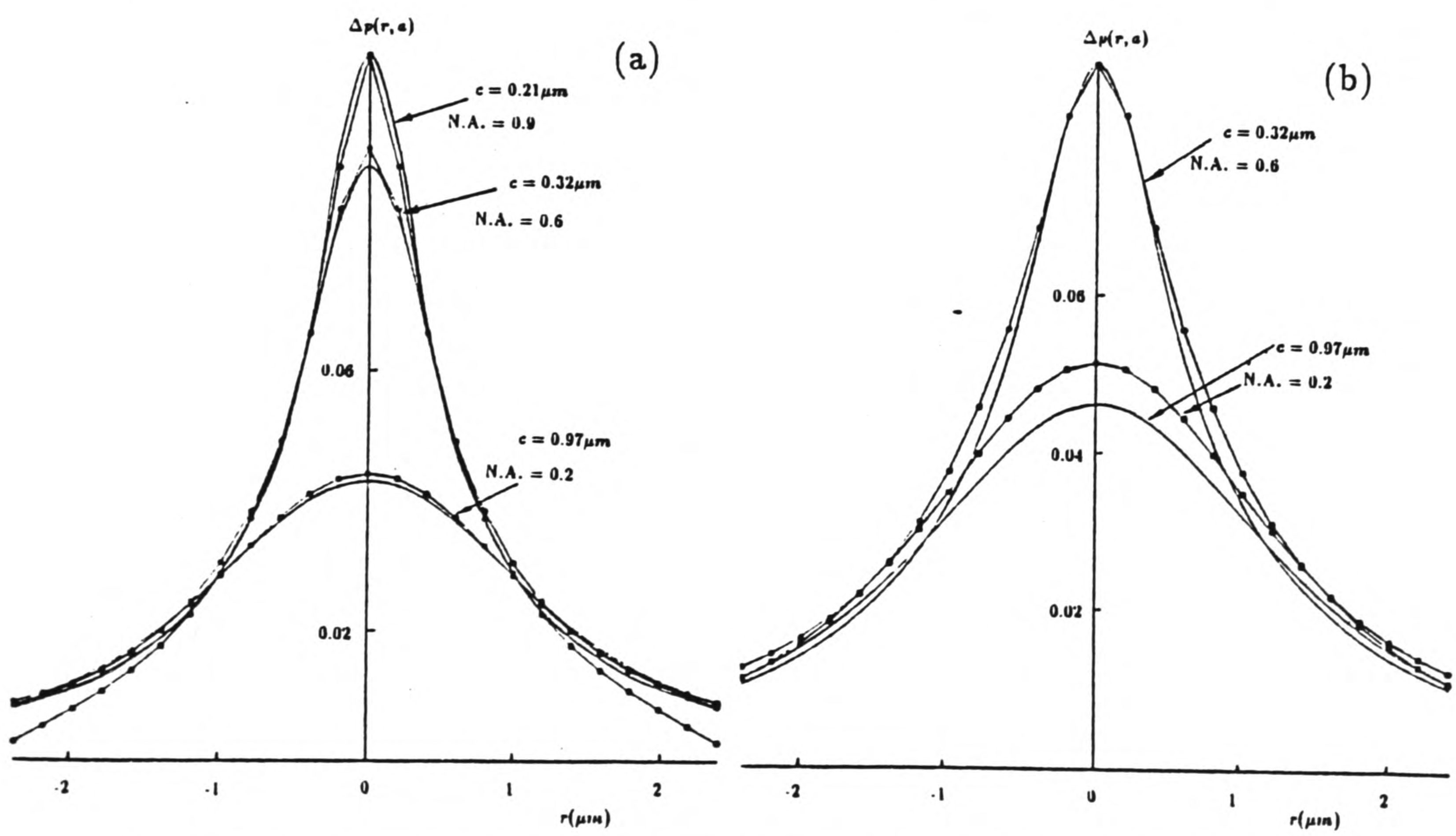

Figure 3.21. Comparisons of radial sections through the minority carrier distribution as predicted by the focussed and Gaussian theories when $\alpha = 0.4\mu m^{-1}$, $L = 10\mu m$ and $v_s/D = 1.0\mu m^{-1}$. (a) is for a section depth of $z = 0.4\mu m$ and values of numerical aperture of $\sin\theta = 0.2$, $\sin\theta = 0.6$ and $\sin\theta = 0.9$ with associated half widths of $c = 0.97\mu m$, $c = 0.32\mu m$ and $c = 0.21\mu m$ respectively and (b) for a section depth of $z = 1.0\mu m$ and numerical apertures of $\sin\theta = 0.2$ and $\sin\theta = 0.6$.

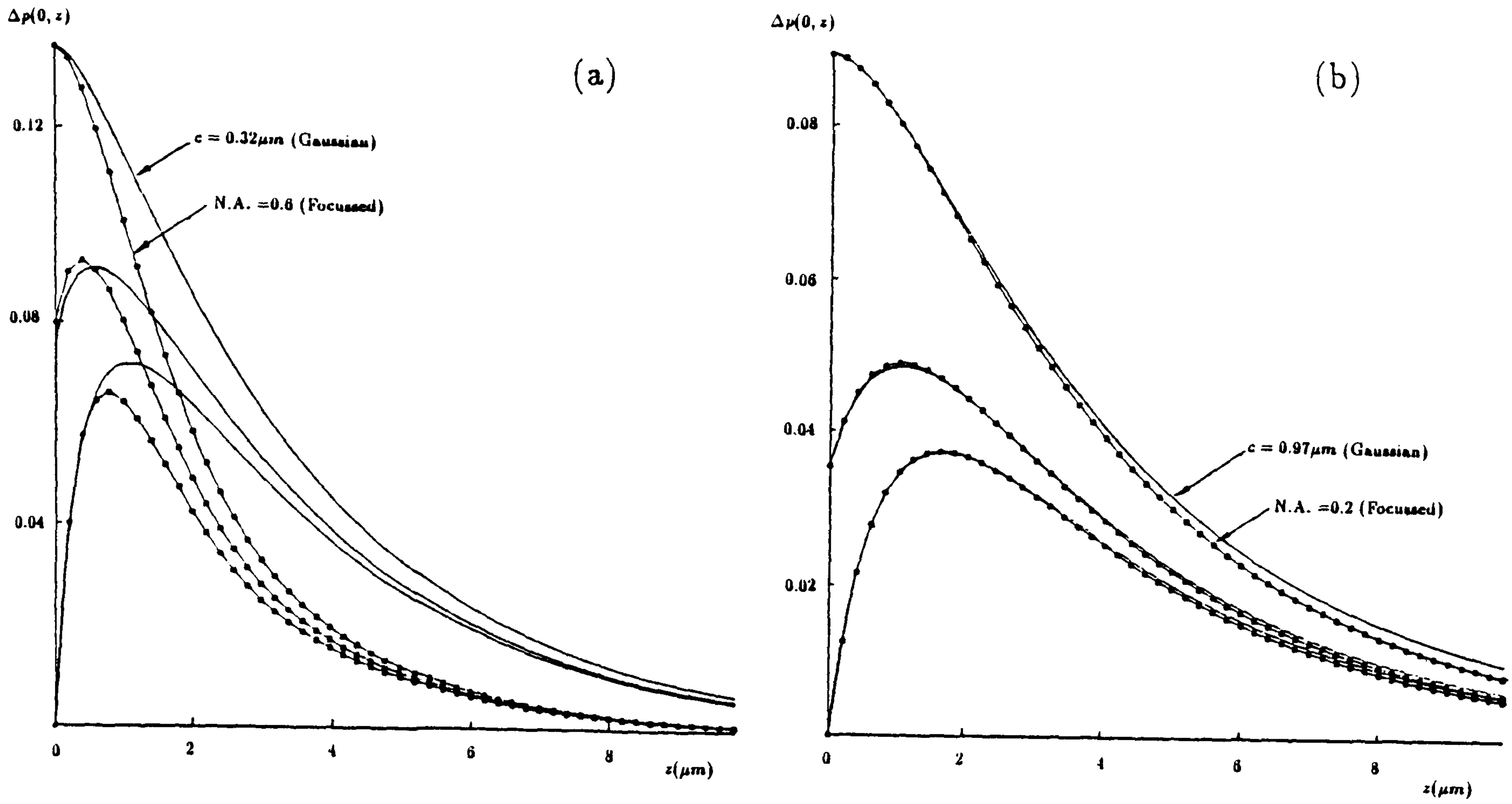

Figure 3.20. Comparisons of the on-axis carrier distribution produced from the focussed beam theory and the decaying Gaussian approximation for the case when $\alpha = 0.4\mu m^{-1}$, $L = 10\mu m$ and $v_s/D \rightarrow 0$, $v_s/D = 1.0\mu m^{-1}$ and $v_s/D \rightarrow \infty$. (a) is for a high numerical aperture of $\sin\theta = 0.6$ and Gaussian width of $c = 0.32\mu m$ and (b) is for a low numerical aperture of $\sin\theta = 0.2$ and Gaussian width of $c = 0.97\mu m$.

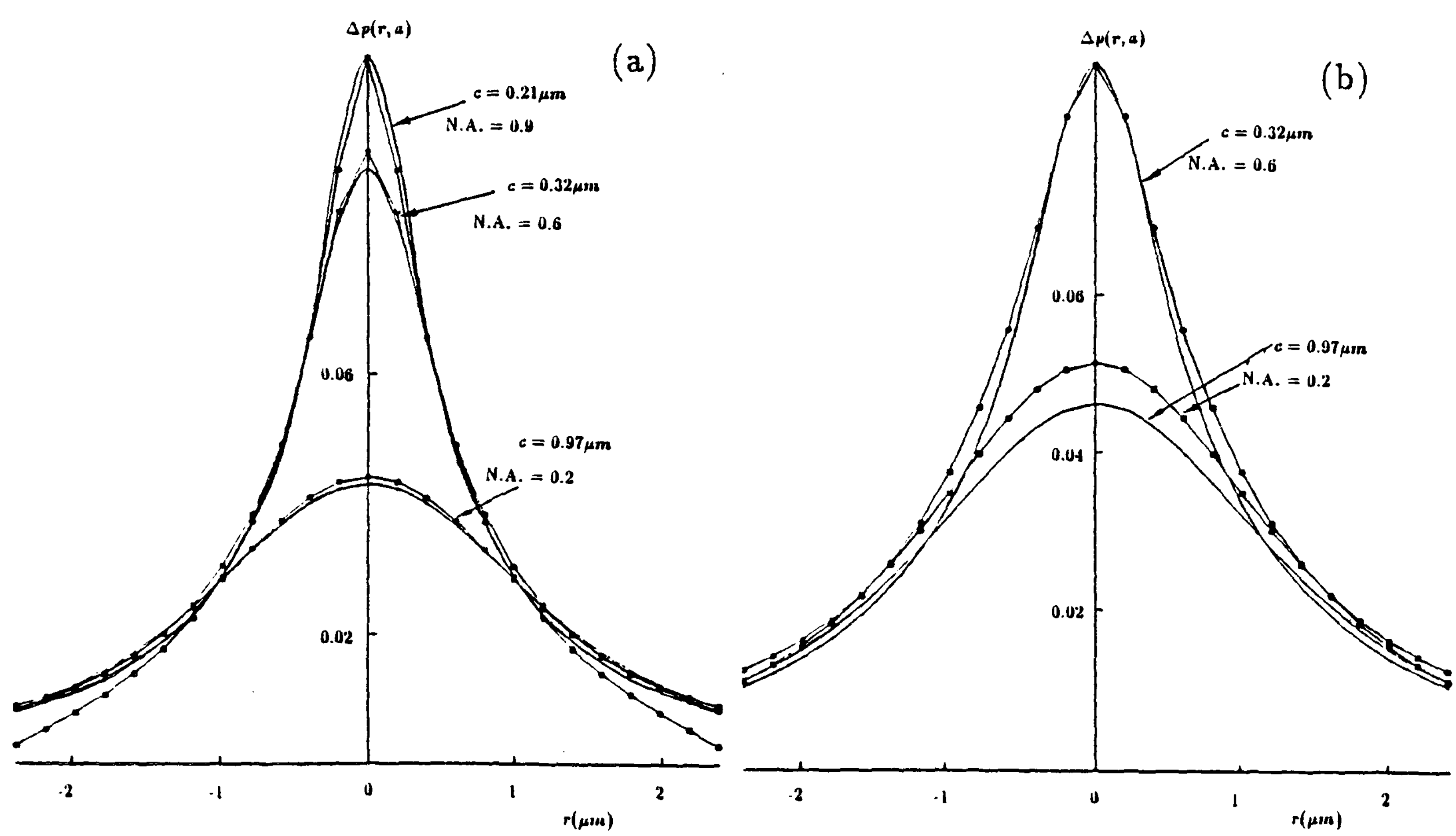

Figure 3.21. Comparisons of radial sections through the minority carrier distribution as predicted by the focussed and Gaussian theories when $\alpha = 0.4\mu m^{-1}$, $L = 10\mu m$ and $v_s/D = 1.0\mu m^{-1}$. (a) is for a section depth of $z = 0.4\mu m$ and values of numerical aperture of $\sin\theta = 0.2$, $\sin\theta = 0.6$ and $\sin\theta = 0.9$ with associated half widths of $c = 0.97\mu m$, $c = 0.32\mu m$ and $c = 0.21\mu m$ respectively and (b) for a section depth of $z = 1.0\mu m$ and numerical apertures of $\sin\theta = 0.2$ and $\sin\theta = 0.6$.

Figure (3.21a) shows the section at a depth of $z = 0.4\mu m$ for three values of numerical aperture and associated Gaussian half widths, and Figure (3.21b) at a depth of $z = 1.0\mu m$ for two values of numerical aperture.

It is clear from Figure (3.21) that the agreement is better at shallow depths for all values of numerical aperture, although for all depths it is seen that the shape of the focussed beam distribution is very well approximated by the Gaussian. This good agreement means that, in situations where a low numerical aperture lens is used, the simple decaying Gaussian theory can be used with confidence, this applies to the imaging of defects in OBIC and PL as well as the use of induced currents for the measurement of material parameters. Better agreement should be expected for the radial sections since Equation (3.77), from which the Gaussian half width is chosen, was found by comparing the radial forms of the light distribution within the semiconductor as predicted by the focussed and Gaussian theories.

In order to produce better agreement for the axial plots it is neccesary to extend the assumption of a simple exponential decay for the light intensity within the semiconductor. This can be done by considering the on-axis form of the light distribution within the material since then we have, from Equation (3.1),

$$g(0,z) = \frac{4A'g_0}{k^2\sin^4\theta(1+(\alpha/2k)^2)} \frac{\exp\left[-\alpha(1+\frac{\sin^2\theta}{4})z\right]}{z^2} \left\{\sin^2\left(\frac{k\sin^2\theta}{4}z\right) + \sinh^2\left(\frac{\alpha\sin^2\theta}{8}z\right)\right\}, \quad (3.81)$$

where A' is a normalisation constant. If we expand the *sin* and *sinh* functions for small arguments Equation (3.81) simplifies to

$$g(0,z) = \frac{A'g_0}{4}\exp\left\{-\alpha\left(1+\frac{\sin^2\theta}{4}\right)z\right\}. \quad (3.82)$$

It is interesting to note that Equation (3.82) still predicts a simple exponential decay for the light intensity within the semiconductor, although with an *effective absorption coefficient* which is a function of the numerical aperture, $\sin\theta$, given by

$$\alpha_{\text{eff}} = \left(1+\frac{\sin^2\theta}{4}\right)\alpha. \quad (3.83)$$

From Equation (3.83) it is clear that the effective absorption coefficient increases with increasing numerical aperture, as required to correct for the over estimation of the penetration depth by the Gaussian approximation, and in Figure (3.22) a comparison between the axial carrier distributions produced using α and α_{eff} for the absorption coefficients is given.

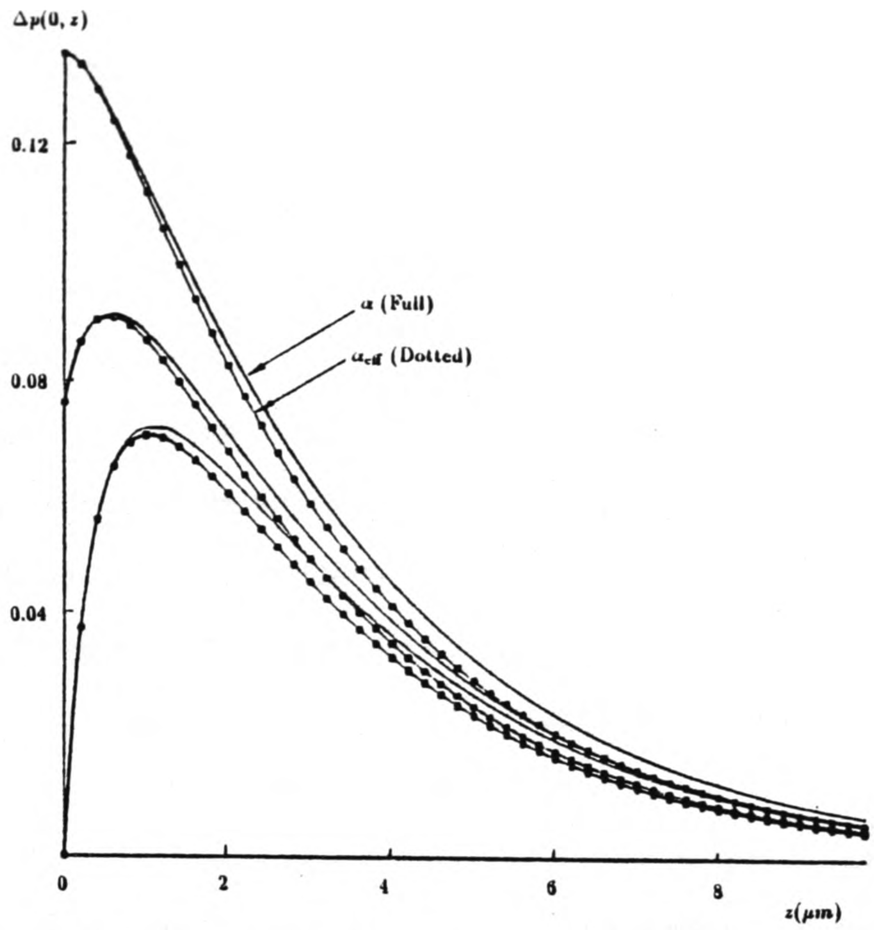

Figure 3.22. A comparison of axial sections through the minority carrier distribution given by using either α (the full lines) or α_{eff} (the dotted lines) for the absorption coefficient. The case shown is for when $\alpha = 0.4\mu m^{-1}$, $L = 5.0\mu m$, three values of surface recombination velocity and a numerical aperture of $\sin\theta = 0.6$ which gives, from Equations (3.77) and (3.83), values for c and α_{eff} of $c = 0.32\mu m$ and $\alpha_{\mathrm{eff}} = 0.436\mu m^{-1}$.

It is clear by comparing Figure (3.22) and Figure (3.20) that using α_{eff} gives a closer fit to the focussed beam curves although at high numerical apertures there is still a significant difference.

3.5 Conclusions

The excess minority carrier distribution induced in a semi-infinite semiconductor due to a highly convergent focussed light beam has been calculated. It has been shown how the induced distribution is a strong function of the numerical aperture of the objective lens through which the incident light is focussed, as well as depending on the material parameters of the semiconductor.

The calculated minority carrier distribution was used to model the imaging of electrically active defects, in both the Optical Beam Induced Current mode of the Scanning Optical Microscope, and in Photoluminescence techniques. It was shown that the resolution of both techniques exhibits a strong dependence on the numerical aperture of the illumination system, and that optimum resolution is not neccesarily achieved by using a lens with a high value of numerical aperture.

Finally, approximations to the focussed beam theory where considered where it was shown that, by choosing the Gaussian half-width correctly, a decaying Gaussian function could be used to produce an acceptable approximation to the actual induced minority carrier distribution at low numerical apertures. A new expression for the axial form of the generation function, which uses an effective absorption coefficient which is a function of the numerical aperture, was also suggested with a view to compensating for the over estimation of the penetration depth in both the decaying Gaussian and simple point source approximations.

CHAPTER 4:

STEADY STATE BEAM INDUCED CURRENTS

4.0 Introduction

The measurement of material parameters, such as minority carrier lifetime and surface recombination velocity, is of great interest to semiconductor process and design engineers. There are various methods for measuring the minority carrier lifetime based on the use of optical pulses [1], although the spatial resolution of the techniques is frequently poor due to the large area excitation. The bulk minority carrier diffusion length and surface recombination velocity may be found by an analysis of the transient capacitance of a MOS structure [2], although again the spatial resolution is limited by the size of the device, and information is only collected from a depth set by the depletion layer width. However, an Optical Beam Induced Current based technique, using the Scanning Optical Microscope, would be preferable to these methods since it would allow discrete, point-by-point lifetime measurements to be made [3,4,5]. In general, a method based on the use of the SOM will allow spatial inhomogenieties in a semiconductor's electrical properties to be observed with a resolution related to the half-width of the injected carrier distribution as was discussed in Chapter 3.

The most convenient way to investigate the minority carrier distribution is, in general, via the short circuit current obtained when the photoinduced excess carriers recombine at a rectifying contact such as a metalic point probe [6,7,8], a metal-semiconductor interface or p-n junction [9]. For the case of a large metal-semiconductor contact or p-n junction, and in the absence of any applied electric fields, this short circuit current is a diffusion current generated by the diffusion of the excess minority carriers across the depletion region. If we know the excess minority carrier distribution $\Delta p(r,z)$, and again consider an n-type semiconductor as in Chapter 3, we can write the diffusion current, I_{diff}, as

$$I_{\text{diff}} = qD \int_{\text{S}} \frac{\partial}{\partial n} \Delta p(r,z)\Big|_{\text{junction}} d\text{S}, \tag{4.1}$$

where S is the surface of the rectifying contact or junction and n is the normal to the surface.

In this Chapter the short circuit Optical Beam Induced Current (OBIC) is calculated for planar device geometries, that is, geometries where the rectifying junction is parallel to the semiconductor surface (taken as the $z = 0$ plane), in these cases use can be made of the cylindrical symmetry by introducing the Hankel Transform, as in Chapter 3, Equation (3.35), since then the carrier distribution can be written,

$$\Delta p(r,z) = \int_0^\infty \Delta\bar{p}(\nu,z) J_0(\nu r)\,\nu d\nu, \tag{4.2}$$

substitution of which into Equation (4.1) yields,

$$I_{\text{diff}} = qD \int_0^\infty \int_0^{2\pi} \int_0^\infty \frac{\partial}{\partial z}\{\Delta\bar{p}(\nu,z)\}\Big|_{z=\text{junction}} J_0(\nu r)\,\nu d\nu d\theta r dr. \tag{4.3}$$

Performing the integrations, noting that $\int_0^\infty J_0(\nu r)\,r dr = \delta(\nu)/\nu$, where $\delta(\nu)$ is the Dirac-Delta function, allows us to write Equation (4.3) in a much simplified form as,

$$I_{\text{diff}} = 2\pi qD \frac{\partial}{\partial z}\Delta\bar{p}(0,z)\Big|_{z=\text{junction}} \tag{4.4}$$

and so the surface integral in Equation (4.1) has been reduced to a differential which is, in general, easier to evaluate. It is straightforward to calculate $\Delta\bar{p}(0,z)$, that is the Hankel transform of the minority carrier distribution in the limit as the transform variable, ν, tends to zero, since it is simply the solution of the one dimensional diffusion equation,

$$\frac{\partial^2}{\partial z^2}\Delta\bar{p}(0,z) - \frac{\Delta\bar{p}(0,z)}{L^2} = -\frac{1}{D}\bar{g}(0,z), \tag{4.5}$$

where $\bar{g}(\nu,z)$ is the Hankel transform of the generation function as calculated in Chapter 3.

By using this symmetry exploiting method it is shown how it is possible to obtain analytic expressions for the induced current due to both decaying Gaussian and Focussed light generation terms. The calculations are performed for both shallow p-n junctions or Schottky barrier diodes, and deep planar p-n junctions.

4.1 Beam Induced Current in a Planar Junction

We begin by considering the simple p-n junction geometry of Figure (4.1) and calculate the junction photocurrent due to the photo-induced minority carriers. The surface of the semiconductor is characterized by a surface recombination velocity v_s and the metallurgical junction depth is taken as h_0, such that collection of the photo-induced carriers takes place at a depth, $z = h_0 - w$, where w is the depletion layer width.

The solution of the one dimensional diffusion equation given in Equation (4.5) is subject to the transformed boundary conditions which, for this geometry, can be written,

$$\frac{\partial}{\partial z}\Delta\bar{p}(0,z)\Big|_{z=0} = \frac{v_s}{D}\,\Delta\bar{p}(0,z)\Big|_{z=0} \tag{4.6}$$

and,

$$\Delta\bar{p}(0,z)\Big|_{z=h_0-w} = 0, \tag{4.7}$$

since the transformation acts purely on the radial coordinate. Equation (4.7) merely states that the induced carriers are collected at the depletion edge which occurs at a depth of $z = h_0 - w$ into the sample. A convenient method of solution of the problem is via a Green's function approach similar to Chapter 3. It is fairly straightforward to find the Green's function to the diffusion equation, subject to the boundary conditions of Equations (4.6) and (4.7), by standard techniques [10] which give [11],

$$G(0,z|z_0) = \frac{L}{2\left[1+\left(\frac{1-sL}{1+sL}\right)e^{-2h/L}\right]}\left\{e^{-|z-z_0|/L} + \left(\frac{1-sL}{1+sL}\right)e^{-(z+z_0)/L} - e^{-2h/L}\left(e^{(z+z_0)/L} + \left(\frac{1-sL}{1+sL}\right)e^{|z-z_0|/L}\right)\right\}, \tag{4.8}$$

where $s = v_s/D$ is a normalised surface recombination velocity and $h = h_0 - w$. Note that the Green's function given in Equation (4.8) reduces to the Green's function of Chapter 3 in the limit as $h \to \infty$, as one would expect, since then we are simply considering the semi-infinite media.

Folding the Green's function with the source term, $\bar{g}(0,\nu)$, gives an expression for the transformed minority carrier distribution as,

$$\Delta\bar{p}(0,z) = -\frac{1}{D}\int_0^h G(0,z|z_0)\bar{g}(0,z_0)\,dz_0. \tag{4.9}$$

Substituting Equation (4.9) into the expression for the diffusion current given in Equation (4.4) yields [11], assuming that the order of integration and differen~~c~~tiation can be interchanged freely,

$$I_{\text{diff}} = -2\pi q\int_0^h \left\{\frac{\cosh(z_0/L) + sL\sinh(z_0/L)}{\cosh(h/L) + sL\sinh(h/L)}\right\}\bar{g}(0,z_0)\,dz_0. \tag{4.10}$$

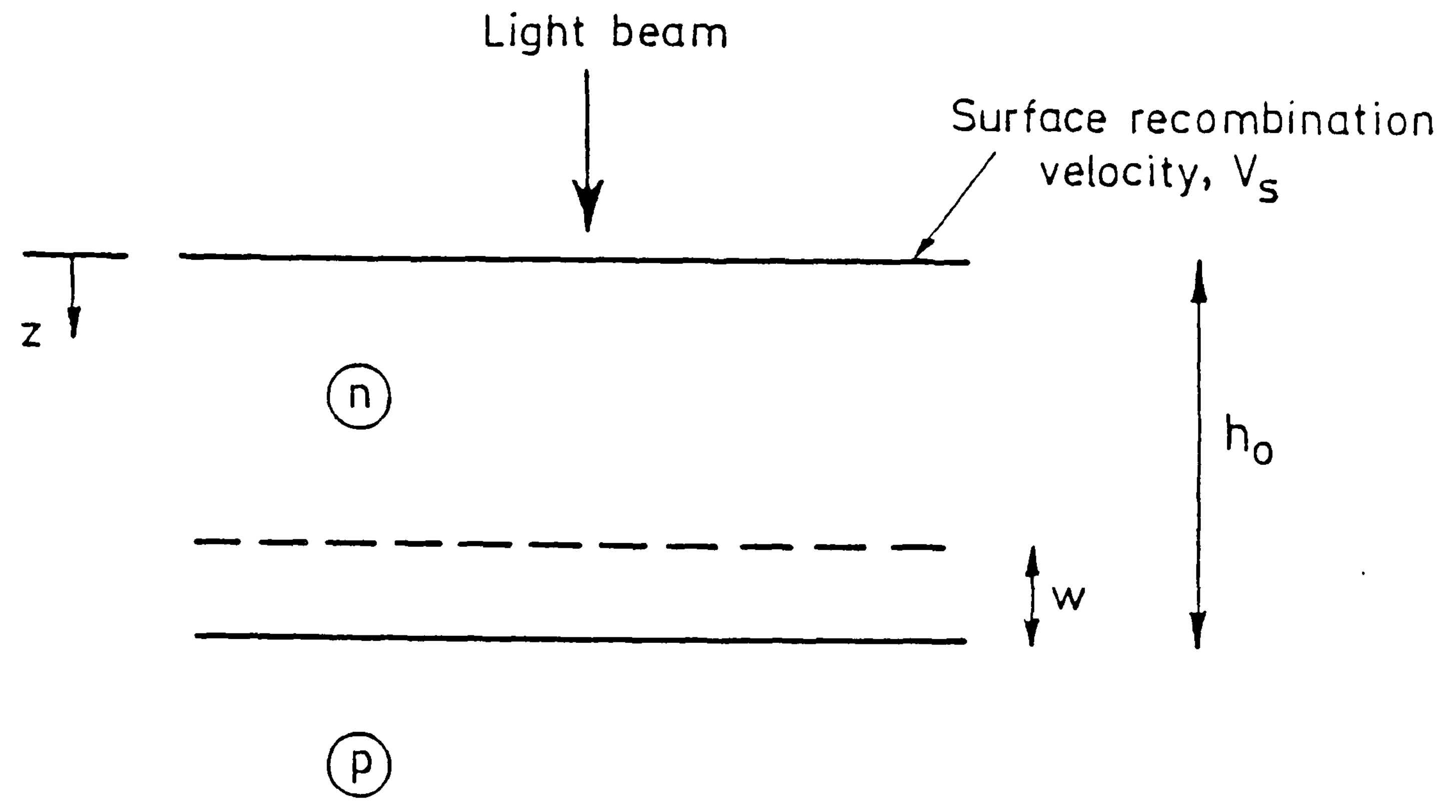

Figure 4.1. Schematic diagram of the planar p-n junction geometry

Equation (4.10) is a general expression for the diffusion current collected by a planar p-n junction, at a depth h, due to an arbitrary generation function.

In order to model the experiments where an exciting beam is used to inject carriers into a semiconductor we must add an extra current term to Equation (4.10). The extra term is to take account of the carriers that are generated within the depletion region by the incident beam, these carriers are immediately swept away by the built-in field to constitute a current. Assuming a quantum efficiency of unity for the process, which is realistic [12], the extra current term, I_{dep}, which we will call the *depletion region current* is given as,

$$I_{\text{dep}} = 2\pi \int_{h}^{h_0} \int_{0}^{\infty} g(r,z)\, r dr dz, \tag{4.11}$$

from which the total beam induced current, I, can be calculated via

$$I = I_{\text{diff}} + I_{\text{dep}}. \tag{4.12}$$

So far we have been completely general in choice of the generation function, $g(r,z)$, and hence in the form of $\bar{g}(0,z)$. Most analyses to date have considered the generation function to be an exponentially decaying array of point sources within the material [13,14,15] or else, to model the situation more closely, a Gaussian lateral profile is sometimes introduced [16,17]. However, as was shown in Chapter 3, both of these approximations predict minority carrier distributions considerably different from that predicted by the focussed beam generation term and, as such, it can be expected that the form of the photocurrents may differ considerably. For this reason we extend the previous analyses by considering focussed light to be the exciting beam. From Chapter 3, Equation (3.20), we know the form of the Hankel transform of the generation function in the limit, $\nu \to 0$, is

$$\bar{g}(0,z) = g_0 A \exp(-\alpha z) \int_0^{\infty} |h(v,z)|^2 \, v dv, \tag{4.13}$$

that is,

$$\bar{g}(0,z) = g_0 A \exp(-\alpha z) \int_0^{\infty} |P(\rho,z)|^2 \, \rho d\rho. \tag{4.14}$$

Equation (4.14) follows from Equation (4.13) by use of Rayleigh's Theorem [18 p.250], A is the normalisation constant given in Equation (3.4) and $P(\rho, z)$ is the Hankel transform of $h(\nu, z)$ as in Chapter 3. Using the form of $P(\rho, z)$ from Equation (3.18) gives,

$$\bar{g}(0,z) = \frac{g_0}{2\pi \ln(\mu)} \left\{ \frac{\exp(-\alpha z) - \exp(-\alpha\mu z)}{z} \right\}, \tag{4.15}$$

where, as in Chapter 3, $\mu = (1 + 2\epsilon)$, $\epsilon = (\sin^2\theta)/4$ and $\sin\theta$ is the numerical aperture of the objective lens. Substituting Equation (4.15) into the general expression for I_{diff} in Equation (4.10) gives an *analytical* expression for the diffusion current as [11],

$$\begin{aligned} I_{\text{diff}} = & \frac{-q g_0}{\ln(\mu)\left[e^{h/L} + \left(\frac{1-sL}{1+sL}\right) e^{-h/L}\right]} \left\{ E_1\left[(\alpha\mu L - 1)\frac{h}{L}\right] - E_1\left[(\alpha L - 1)\frac{h}{L}\right] \right. \\ & + \left(\frac{1-sL}{1+sL}\right)\left(E_1\left[(\alpha\mu L + 1)\frac{h}{L}\right] - E_1\left[(\alpha L + 1)\frac{h}{L}\right] - E_1\left[(\alpha L - 1)\frac{h}{L}\right]\right) \\ & \left. \frac{1}{1+sL}\left(\ln\left[\frac{\alpha^2\mu^2L^2 - 1}{\alpha^2L^2 + 1}\right] + sL\ln\left[\frac{\alpha\mu L - 1}{\alpha\mu L + 1}\frac{\alpha L + 1}{\alpha L - 1}\right]\right)\right\}, \end{aligned} \tag{4.16}$$

where E_1 is an exponential integral of order one [19 p.227]. If a reverse bias is now applied to the device the depletion layer will increase in width, such that h can be replaced in Equation (4.16) by $h = h_0 - w$, where w is the voltage dependent depletion width [20 p.74], and is proportional to the square root of the applied bias for an abrupt junction or the cube root for a linearly graded junction.

Figure (4.2) shows the variation of the logarithm of the diffusion current as a function of depletion layer width for the case when red light, of wavelength $\lambda = 0.6328\mu m$, is focussed through a lens with a numerical aperture of $\sin\theta = 0.5$ onto silicon, such that the intensity absorbtion coefficient is $\alpha = 0.4\mu m^{-1}$ [21]. The metalurgical junction depth is taken as $h_0 = 17\mu m$ and the minority carrier diffusion length as $L = 10\mu m$. It can be seen from Figure (4.2) that the logarithm of the diffusion current varies linearly with the depletion width, although the gradient of the plots is a function of

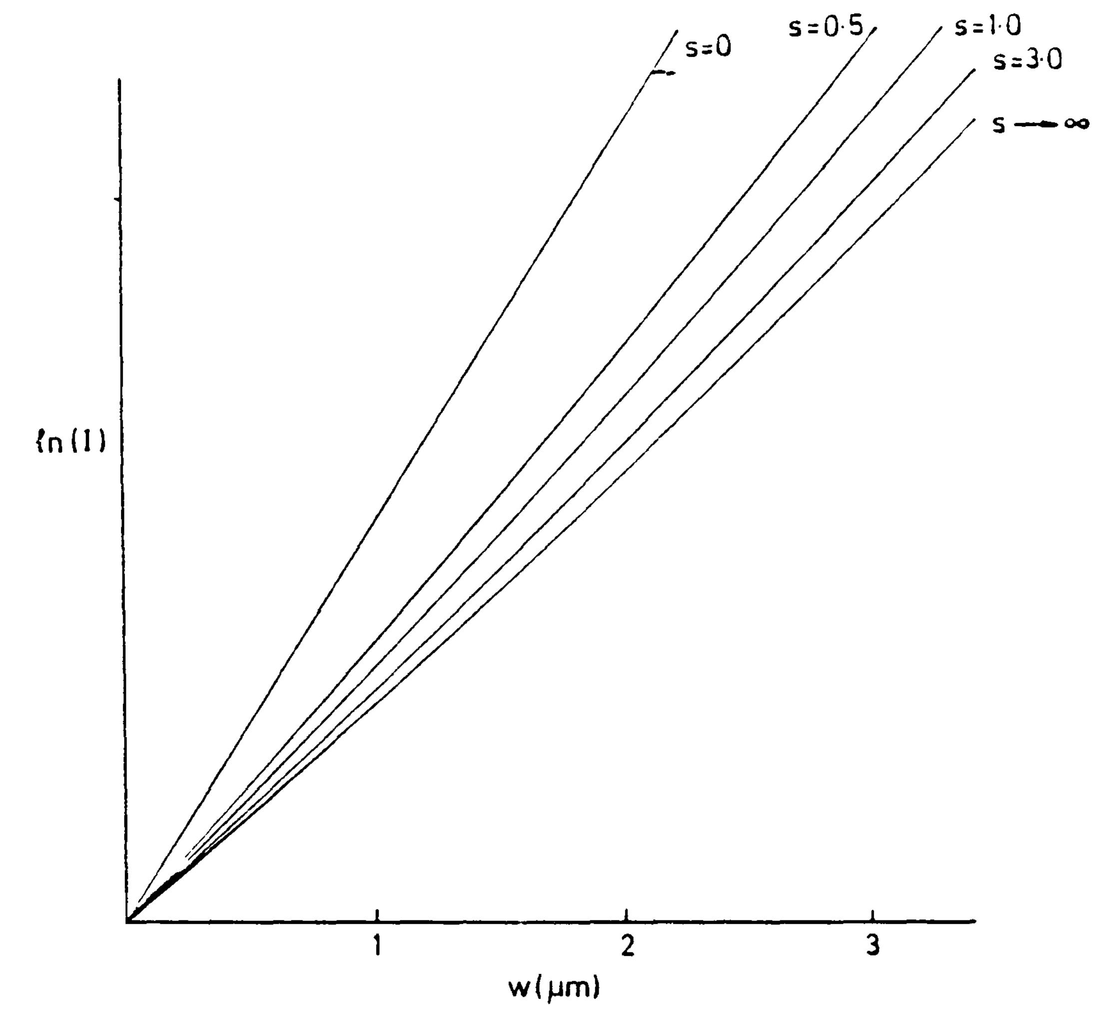

Figure 4.2. The diffusion current, as a function of depletion layer width, collected at a planar p-n junction at a depth of $h_0 = 17\mu m$ due to red light, $\lambda = 0.6328\mu m$, focussed onto silicon, $\alpha = 0.4\mu m^{-1}$, with a diffusion length of $L = 10\mu m$ for various values of surface recombination velocity, $v_s/D/\mu m^{-1}$.

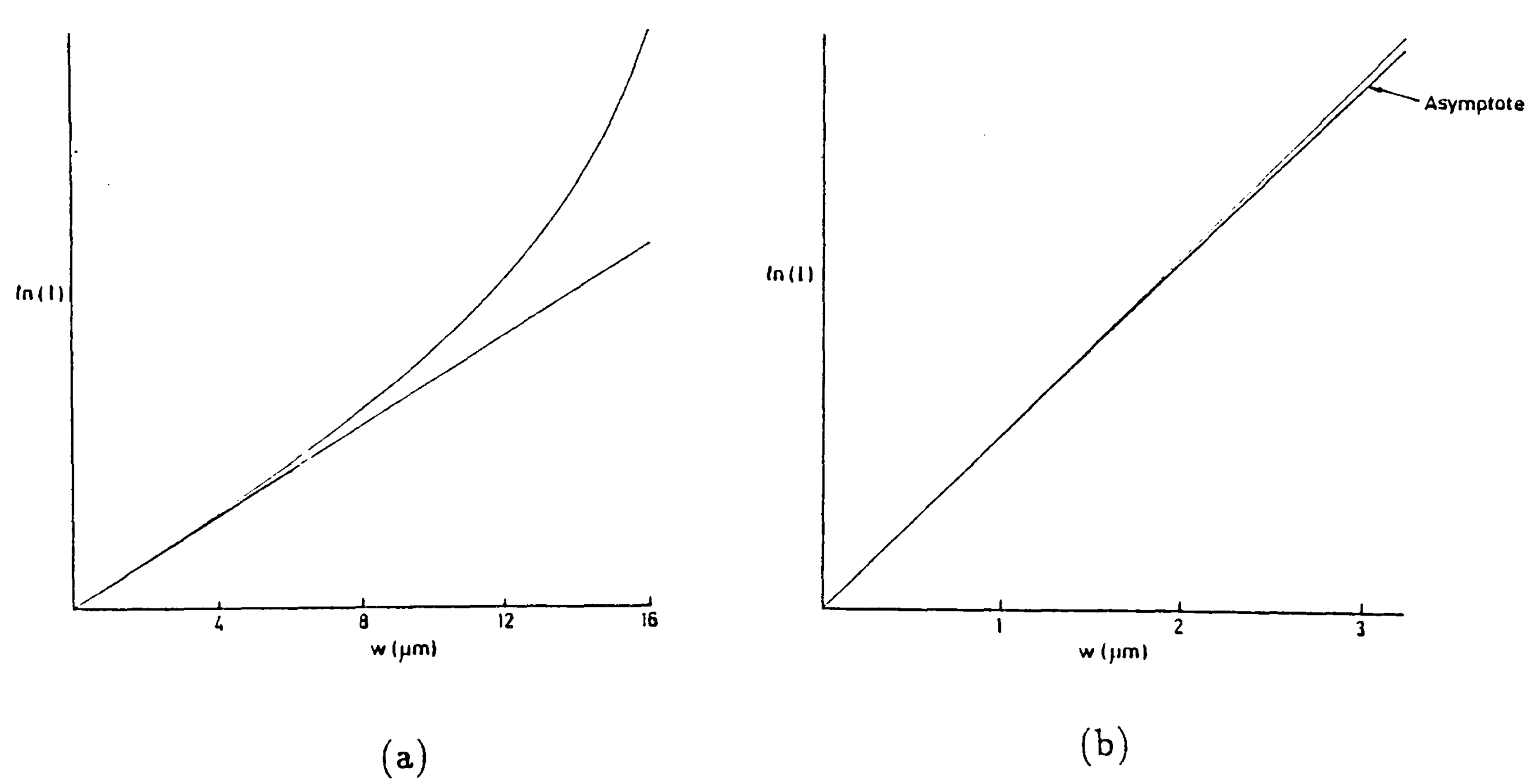

Figure 4.3. The logarithm of the diffusion current collected by a planar p-n junction of depth $h_0 = 17\mu m$ when $v_s/D = 1.0\mu m^{-1}$ and $L = 10\mu m$. The straight line asymptote is given by Equation (4.16), (a) is for a large range in w and (b) is for a small range.

surface recombination velocity. The values that have been choosen for the various parameters are typical of high-voltage power transistors and, since the junction is relatively deep compared to the absorption depth of the light, it is resonable to assume that the diffusion current will dominate over the depletion region current and so Figure (4.2) can be taken to represent the total current collected at the junction.

If the junction is known to be deep, then it is reasonable to assume that the value of the integral in Equation (4.10) is not very sensitive to the upper limit, and as such we may let this tend to infinity. ‡ This allows us to evaluate the integral to produce an expression which is much simpler than that given in Equation (4.16) and can be written,

$$I_{\text{diff}} \sim \frac{-qg_0 f(\alpha, s, L, \sin\theta)}{[\cosh(h/L) + sL\sinh(h/L)]}. \tag{4.17}$$

If the junction current is plotted on a logarithmic scale it is clear that the precise form of the function $f(\alpha, s, L, \sin\theta)$ is unimportant,† and since f is the only term that is a function of the exciting beam shape (given by the numerical aperture $\sin\theta$) we can see that for deep junctions the form of the generation function is unimportant, as would be expected due to the *"averaging out"* by the diffusion process. However, the gradient of the "$\ln(I_{\text{diff}})$.vs.w" curve is still a function of the surface recombination velocity. It is interesting to see if there are any approximations that can be made to the full expression of Equation (4.16) such that it is possible to find an analytic expression for the way in which this gradient varies with v_s. The rate of change of the general expression for the current, given in Equation (4.16), with the depletion width, w, can be found in the limit of $w \to 0$ as,

$$\frac{\partial}{\partial w}\ln(I_{\text{diff}})\bigg|_{w\to 0} = \frac{1}{L}\left\{\frac{\tanh(h/L) + sL}{1 + sL\tanh(h/L)}\right\}, \tag{4.18}$$

denoting this gradient by $m(s)$ we can construct a straight line approximation as,

$$\ln(I_{\text{diff}}) \sim m(s)\cdot w. \tag{4.19}$$

Figure (4.3) shows a comparison between the approximations of Equation (4.17) and Equation (4.19) for two different ranges of the depletion width w.

It is clear that the straight line asymptote of Equation (4.19) is a good approximation for low values of the depletion width w, and in these situations we can see that, from

‡ Physicaly this means that the generation term $g(r,z)$ has decayed sufficiently by $z = h$ such that it is permisible to ignore the generation of carriers at any depth greater than $z = h$, and, since $g(r,z)$ essentially decays as $\exp(-\alpha z)$ the condition can be written $\exp(-\alpha h) \ll 1$ which is clearly the case when $\alpha = 0.4\mu m^{-1}$ and $h = 17\mu m$.

† It should be noted that f is straightforward to calculate and can be found from [11]

Equation (4.18), the gradient, $m(s)$, varies from

$$m(0) = \frac{1}{L}\tanh(h/L), \tag{4.20}$$

for zero surface recombination velocity, to

$$m(\infty) = \frac{1}{L}\coth(h/L), \tag{4.21}$$

for infinite surface recombination velocity. This gives us a fairly straightforward way to find an approximate value for the diffusion length L, assuming that the relative size of the surface recombination velocity is known, (that is whether $v_s \to 0$ or $v_s \to \infty$). Since, knowing the gradient, m, it is simply a matter of solving the relevant transcendental equation, given by either Equation (4.20) or (4.21), for the diffusion length.

Of course, the expressions become even simpler if the ratio of the junction depth to diffusion length is such that

$$\cosh\left(\frac{h}{L}\right) \sim \sinh\left(\frac{h}{L}\right) \sim \frac{1}{2}\exp\left(\frac{h}{L}\right), \tag{4.22}$$

since then Equation (4.17) can be further simplified to give,

$$I_{\text{diff}} \sim \frac{-2qg_0 f(\alpha, s, L, \sin\theta)}{(1+sL)} \cdot \exp\left(-\frac{h}{L}\right), \tag{4.23}$$

and now a plot of the logarithm of the junction current against the depletion width, w, yields a straight line of gradient $1/L$, since $h = h_0 - w$. The beauty of the situation is that the surface recombination velocity does not enter into the interpretation of the results, and so techniques proposed by Engström *et al* [13], to detect resistivity and lifetime variations, may be used with confidence. However, it must be stressed that, without a good deal of *a priori* knowledge about the device under test, one cannot be sure that Equation (4.23) rather than Equation (4.17) or (4.16) applies.

An experiment was performed, using a Scanning Optical Microscope, to investigate the variation of the photocurrent with applied bias for a planar device such as that modelled above. The device was of the deep junction type with the metalurgical junction being $500\mu m$ below the semiconductor surface, and the doping on one side of the junction was much greater than on the other, meaning that the abrupt one-sided approximation could be used to relate the depletion width to the applied reverse bias.

A schematic cross-section of the device is shown in Figure (4.4), the connections to measure the photocurrent where made to the metal annulus on the top and the ohmic contact on the back. The photocurrent was of the order of μA's and so straightforward to measure using a Kiethley ammeter, the applied bias varied from $60V$ to $500V$ producing a change in the depletion width, w, from $36\mu m$ to $105\mu m$. The results are shown in Figure (4.5) where it is clear that the $\ln(I).vs.w$ curve is linear.

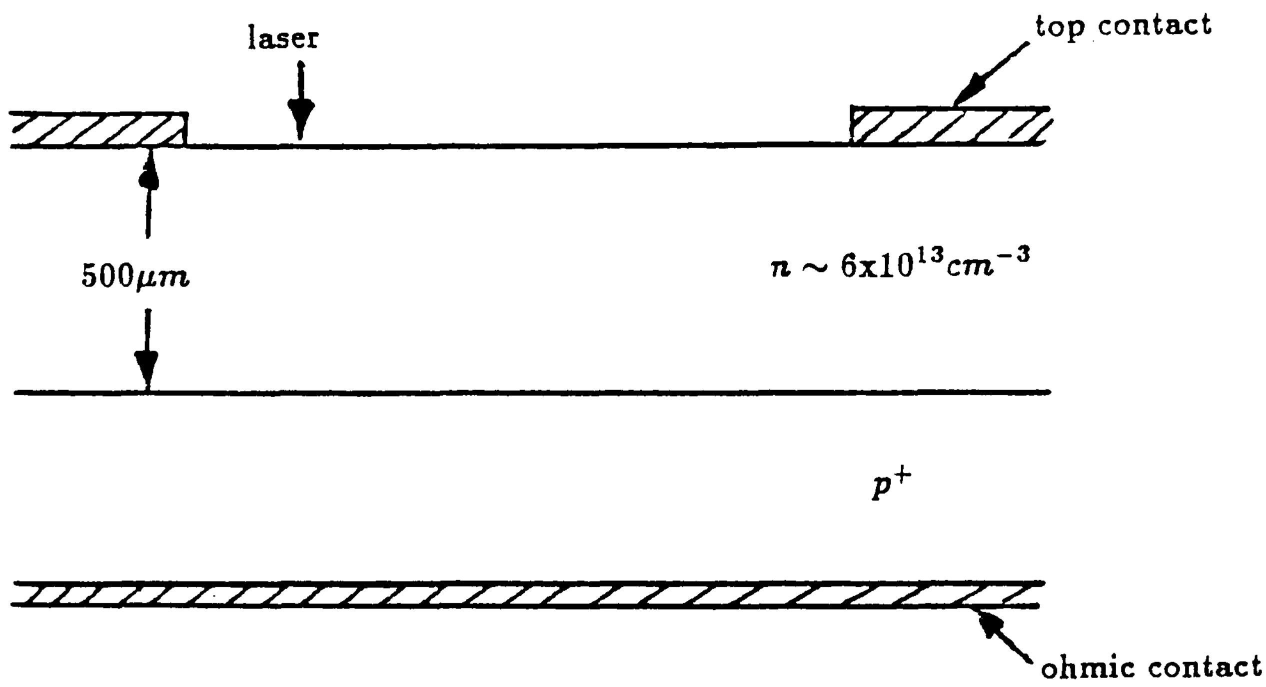

Figure 4.4. Schematic cross-section of the planar p-n junction used to investigate the dependance of the photocurrent on applied bias.

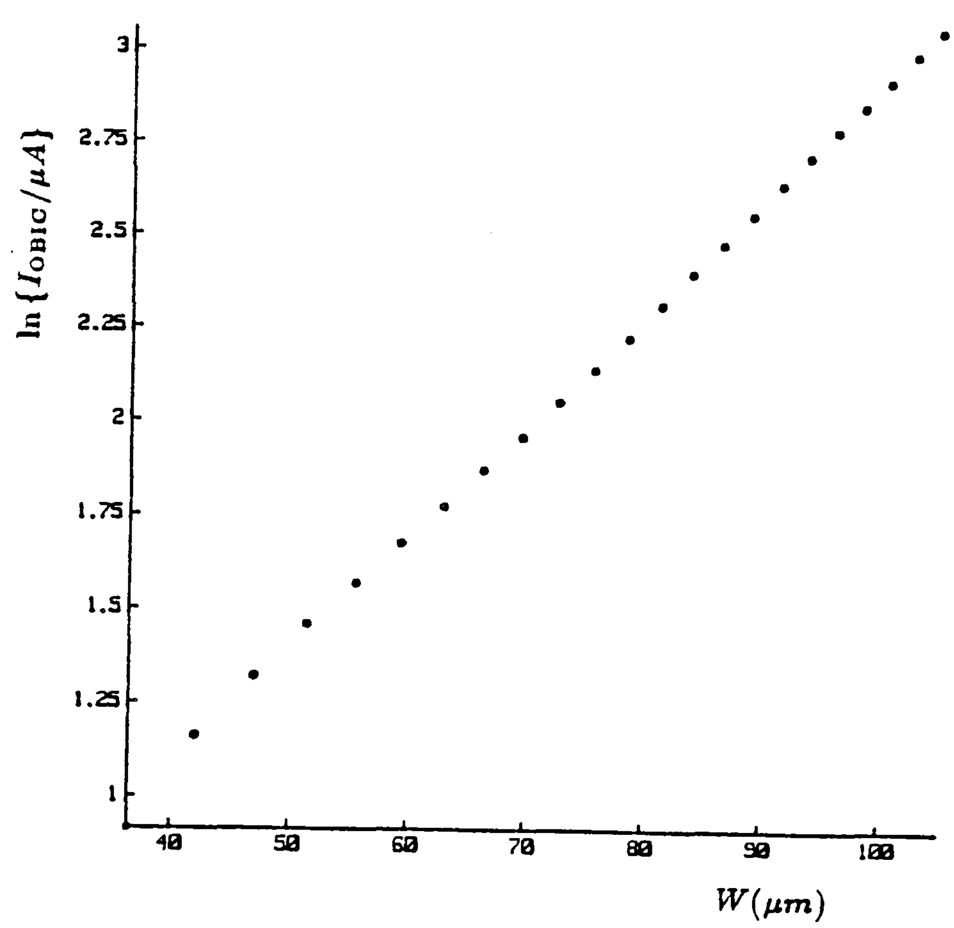

Figure 4.5. The experimental results obtained as the photocurrent was measured as a function of the applied bias for the device shown schematically in Figure (4.4).

Since the metalurgical junction is deep in the device being investigated it is safe to assume that Equation (4.23) can be used to obtain the diffusion length as the recipricle of the gradient in Figure (4.5). Using this method a value for the diffusion length of

$$L = 33\mu m \tag{4.24}$$

was obtained.

4.2 Beam Induced Current in a Finite Thickness Schottky Barrier

It is clear from the previous section that any attempt to extract information on a quantitative basis from beam induced current studies of planar p-n junctions is plagued by the need to know values for the surface recombination velocity and metalurgical junction depth. One way around this difficulty is to use a Schottky barrier diode [20 p.245] for the experiments, as then, owing to the fact that the collecting junction is on the surface, the surface recombination velocity is known to be infinite and the junction depth to be zero. A schematic diagram of the device to be modelled is shown in Figure (4.6) where, as in the planar p-n junction case the depletion layer width is taken as w, and now the *back* surface is characterized by a surface recombination velocity v_{bs}.

We choose to model a device of finite thickness, d, as the most general case, although in practice it is often safe to assume that the device is of semi-infinite extent if $d/L \gg 1$. The current induced in the device by the light beam can be found from Equation (4.4), since the device geometry also exhibits cylindrical symmetry. The transformed carrier distribution, $\Delta\bar{p}(0,z)$, can again be found from the one dimensional diffusion equation given in Equation (4.5), although this time the boundary conditions on the solution are,

$$\Delta\bar{p}(0,z)|_{z=w} = 0, \tag{4.25}$$

and,

$$\frac{\partial}{\partial z}\Delta\bar{p}(0,z)\bigg|_{z=d} = \frac{v_{bs}}{D}\Delta\bar{p}(0,z)\bigg|_{z=d}, \tag{4.26}$$

which merely state that the charge collection takes place at the edge of the depletion region, $z = w$, and that the device has a thickness $z = d$. The approach to the solution is the same as the previous section and Chapter 3, that is, to find the Green's function and fold it with the source term. The Green's function, $G(0,z|z_0)$, is fairly straightforward to find and the derivation, which is a good example of how most of the Green's functions used in this thesis were found, is given in Appendix C where it is shown that,

$$G(0,z|z_0) = \frac{L}{2\left[e^{-2d/L} + \left(\frac{1-s_bL}{1+s_bL}\right)e^{-2w/L}\right]}\left\{e^{-2d/L}\left\{e^{-2w/L}e^{(z+z_0)/L} - e^{|z-z_0|/L}\right\}\right.$$
$$\left. + \left(\frac{1-s_bL}{1+s_bL}\right)\left\{e^{-2w/L}e^{-|z-z_0|/L} - e^{-(z+z_0)/L}\right\}\right\}, \tag{4.27}$$

where $s_b = v_{bs}/D$ is the normalised back surface recombination velocity.

Folding the Green's function of Equation (4.27) and source, $\bar{g}(0,z)$, and substituting into the expression for the diffusion current in Equation (4.4) gives the general

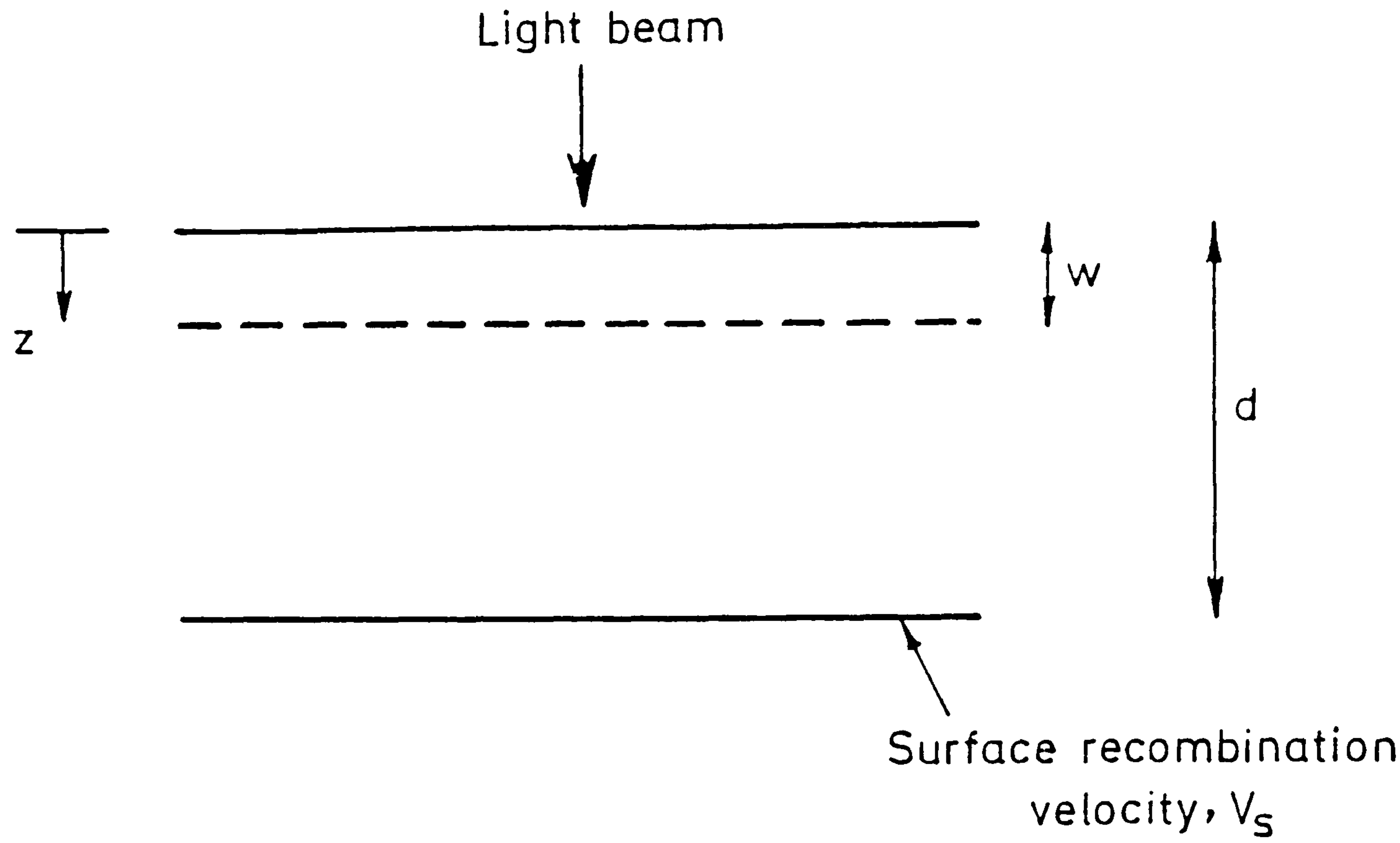

Figure 4.6. A schematic diagram of the finite thickness Schottky barrier diode geometry.

expression for the diffusion current as,

$$I_{\text{diff}} = -2\pi q \int_w^d \exp\left(-\frac{z_0 - w}{L}\right) \left\{ \frac{\exp(2z_0/L) + \Gamma \exp(2d/L)}{\exp(2w/L) + \Gamma \exp(2d/L)} \right\} \bar{g}(0, z_0)\, dz_0, \qquad (4.28)$$

where the effect of the back surface recombination velocity is taken into account by the variable Γ which is given by

$$\Gamma = \left(\frac{1 - s_b L}{1 + s_b L}\right), \qquad (4.29)$$

and may vary between 1, for $s_b \to 0$, and -1, for $s_b \to \infty$. Again specializing to the case of focussed light excitation, where $\bar{g}(0, z)$ is given by Equation (4.15), it is routine to find an *analytic* expression for the diffusion current as,

$$\begin{aligned} I_{\text{diff}} = \frac{-qg_0}{\ln(\mu)\left[e^{-(d-w)/L} + \Gamma e^{(d-w)/L}\right]} \cdot \\ \Bigg(e^{-d/L} \Bigg\{ E_1\left[(\alpha\mu L - 1)\frac{w}{L}\right] - E_1\left[(\alpha\mu L - 1)\frac{d}{L}\right] \\ + E_1\left[(\alpha L - 1)\frac{d}{L}\right] - E_1\left[(\alpha L - 1)\frac{w}{L}\right] \Bigg\} \\ + \quad \Gamma e^{d/L} \Bigg\{ E_1\left[(\alpha\mu L + 1)\frac{w}{L}\right] - E_1\left[(\alpha\mu L + 1)\frac{d}{L}\right] \\ + E_1\left[(\alpha L + 1)\frac{d}{L}\right] - E_1\left[(\alpha L + 1)\frac{w}{L}\right] \Bigg\} \Bigg). \end{aligned} \qquad (4.30)$$

Since the junction is on the surface in this geometry we cannot neglect the contribution of the *depletion region* term to the total current, this can be found, in the unity quantum efficiency approximation, as

$$\begin{aligned} I_{\text{dep}} &= 2\pi q \int_0^w \int_0^\infty g(r,z)\, r dr dz \\ &= 2\pi q \int_0^w \bar{g}(0,z)\, dz, \end{aligned} \tag{4.31}$$

which is found to be,

$$I_{\text{dep}} = \frac{q g_0}{\ln(\mu)} \Big(\ln(\mu) + E_1(\alpha\mu w) - E_1(\alpha w) \Big). \tag{4.32}$$

The condition of the back surface is only important in structures that are thin compared to the diffusion length, and it is clear that it is only the diffusion current term that is affected, via the parameter Γ. In Figure (4.7) the diffusion current is shown as a function of the depletion region thickness, w/d, for the two extremes of back surface recombination velocity, $v_{bs} \to 0$ and $v_{bs} \to \infty$, that is $\Gamma \to 1$ and $\Gamma \to -1$ respectively. Figure (4.7a) is for a relatively small diffusion length of $L = 3\mu m$ and a thin device with $d = 6\mu m$, whereas Figure (4.7b) is for a long diffusion length of $L = 10\mu m$ and a thick device where $d = 20\mu m$.

It is clear from Figure (4.7) that the effect of the back surface is more important for the thinner device, even though the ratio of thickness to diffusion length is the same in each case. In Figure (4.8) the increase in *total* current (the sum of the diffusion and depletion terms) is shown as a function of depletion width for the case where the back surface is important, that is, for parameters as in Figure (4.7a).

The results can be illustrated further by considering a thick device where the state of the back surface is unimportant. This situation can be modelled by letting $d \to \infty$ in Equation (4.30) which yields a much simplified form for the *normalised* total current, I_{norm}, as,

$$\begin{aligned} I_{\text{norm}} &= \frac{I(w)}{I(\infty)} \\ &= \frac{1}{\ln(\mu)} \Big\{ \ln(\mu) + E_1(\alpha\mu w) - E_1(\alpha w) \\ &\qquad - e^{w/L} \Big(E_1 \Big[(\alpha\mu L + 1)\frac{w}{L} \Big] - E_1 \Big[(\alpha L + 1)\frac{w}{L} \Big] \Big) \Big\}. \end{aligned} \tag{4.33}$$

Equation (4.33) is plotted, as a function of the depletion width, in Figure (4.9) for a selection of diffusion lengths, where it can be seen that for sufficiently high reverse bias, that is large depletion layer widths, all the carriers are collected.

The limiting cases of $L \to \infty$ and $L \to 0$ are shown in Figure (4.9), it is easy to show that analytic expressions for these limits follow directly from Equation (4.33) as,

$$I_{\text{norm}}\big|_{L\to\infty} \to 1, \tag{4.34}$$

$$I_{\text{norm}}\big|_{L\to 0} \to 1 + \frac{E_1(\alpha\mu w) - E_1(\alpha w)}{\ln(\mu)}. \tag{4.35}$$

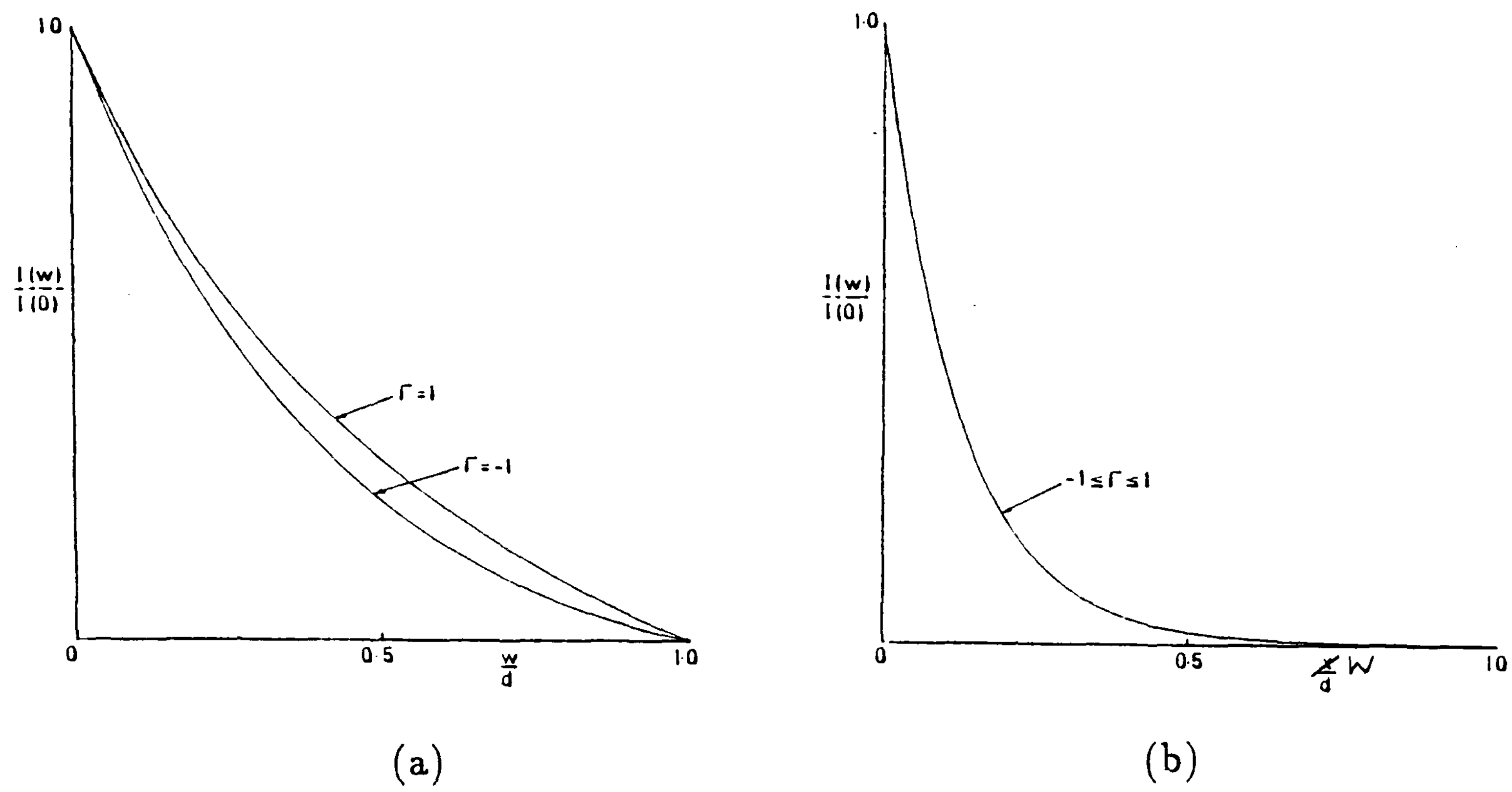

Figure 4.7. The normalised diffusion current collected by a finite thickness silicon Schottky barrier due to red light, such that $\alpha = 0.4\mu m^{-1}$, focussed through a lens with a numerical aperture of $\sin\theta = 0.6$. (a) is for the case when the thickness of the device, $d = 6\mu m$ and diffusion length, $L = 3\mu m$, and (b) for the case of a device thickness $d = 20\mu m$ and diffusion length $L = 10\mu m$.

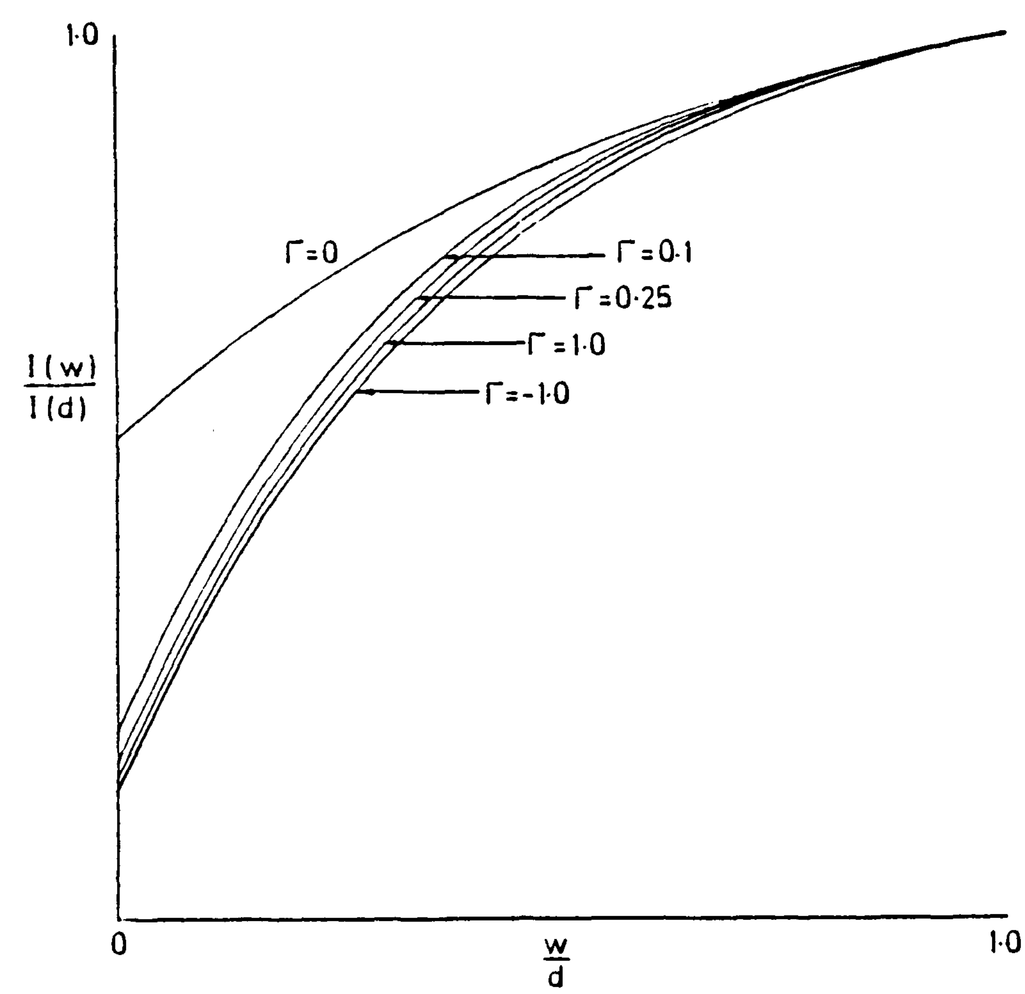

Figure 4.8. The normalized total photocurrent for red light focussed onto the surface of a silicon Schottky barrier as a function of depletion region width, for various values of back surface recombination given by the parameter Γ. The case shown is for when $d = 6\mu m$, $L = 3\mu m$, $\alpha = 0.4\mu m^{-1}$ and $\sin\theta = 0.6$.

The effect of the numerical aperture on the total photocurrent is shown in Figure (4.10), again for red light in silicon. The low numerical aperture curves can be reproduced by approximating the generation term by the decaying Gaussian approximation of Chapter 3, or by taking the limit of Equation (4.33) as $\sin\theta \to 0$, since in both cases the Hankel transform of generation term takes the form,

$$\bar{g}(0,z) = \frac{\alpha g_0}{2\pi}\exp(-\alpha z). \tag{4.36}$$

Extending the analysis, to include this limit for completeness, gives an expression for the total current in a finite thickness Schottky in the low numerical aperture limit as,

$$I = qg_0\left[1 - e^{-\alpha d}\right] + \frac{\alpha L q g_0}{(\alpha L - 1)\left[e^{-(d-w)/L} + \Gamma e^{(d-w)/L}\right]}$$
$$\left\{\left(1 + \left(\frac{\alpha L - 1}{\alpha L + 1}\right)\Gamma\right)e^{-\alpha d} + \left(\frac{\alpha L - 1}{\alpha L + 1}\right)e^{-(\alpha L+1)\frac{w}{L}}\left[e^{-d/L} + \Gamma e^{d/L}\right]\right\}. \tag{4.37}$$

A disadvantage of using the Schottky barrier technique to measure the minority carrier diffusion length, by monitoring the total photocurrent as a function of applied reverse bias, is that it is difficult to present the results in a simple " straight line" form, as can be seen from Figures (4.9) and (4.10), and so some simple curve fitting is required, however, there are great advantages.

The main attraction of the Schottky geometry is the removal of the uncertainties in both surface recombination velocity and junction depth that occur in the planar junction situations. Other attractions of the Schottky barrier method are based on the use of electrolytic liquids to form the rectifying surface contact, since then it is also possible to produce a *temporary* Schottky barrier on the surface of a silicon wafer by use of a noncontaminating electrolyte [5]. This allows diffusion length measurements to be made on a wafer before and after processing and so gives a method of process control which is easily automated. As well as being used as a nondestructive method of diffusion length measurement it is also possible to *map* the diffusion length variations through the bulk of a semiconducting sample by simply replacing the noncontaminating electrolyte with one that etches silicon. Finally, it should be noted that, if we choose to combine the measurement of the photocurrent with scanning, any variations in w, the depletion layer width, due to perhaps doping inhomogenieties will manifest themselves by a change in the photocurrent [5,13].

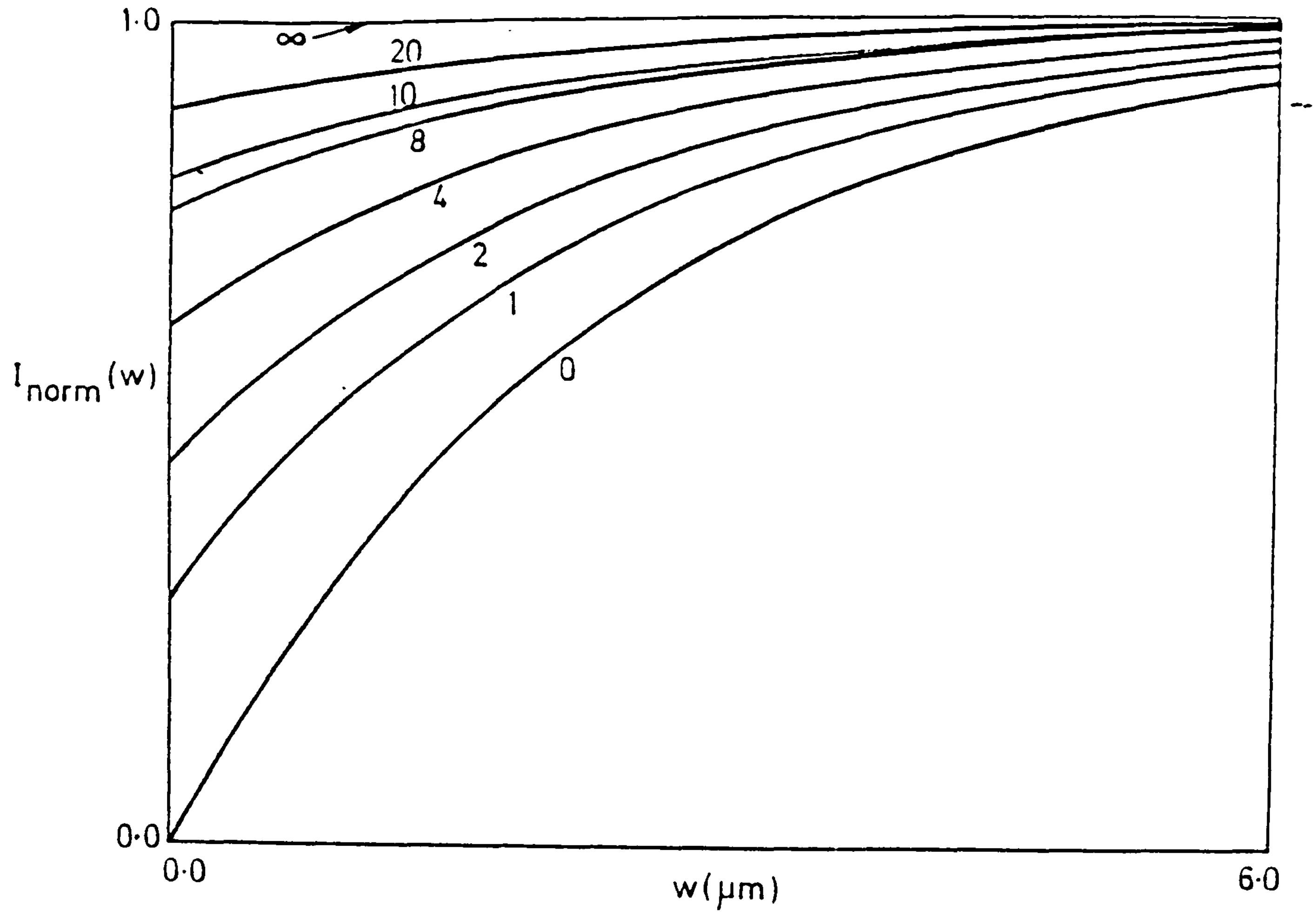

Figure 4.9. The normalized total photocurrent collected by a semi-infinite silicon Schottky barrier when illuminated with red light, such that $\alpha = 0.4\mu m^{-1}$ and $\lambda = 0.6328\mu m$, via a lens with a numerical aperture of $\sin\theta = 0.5$, as a function of depletion layer width.

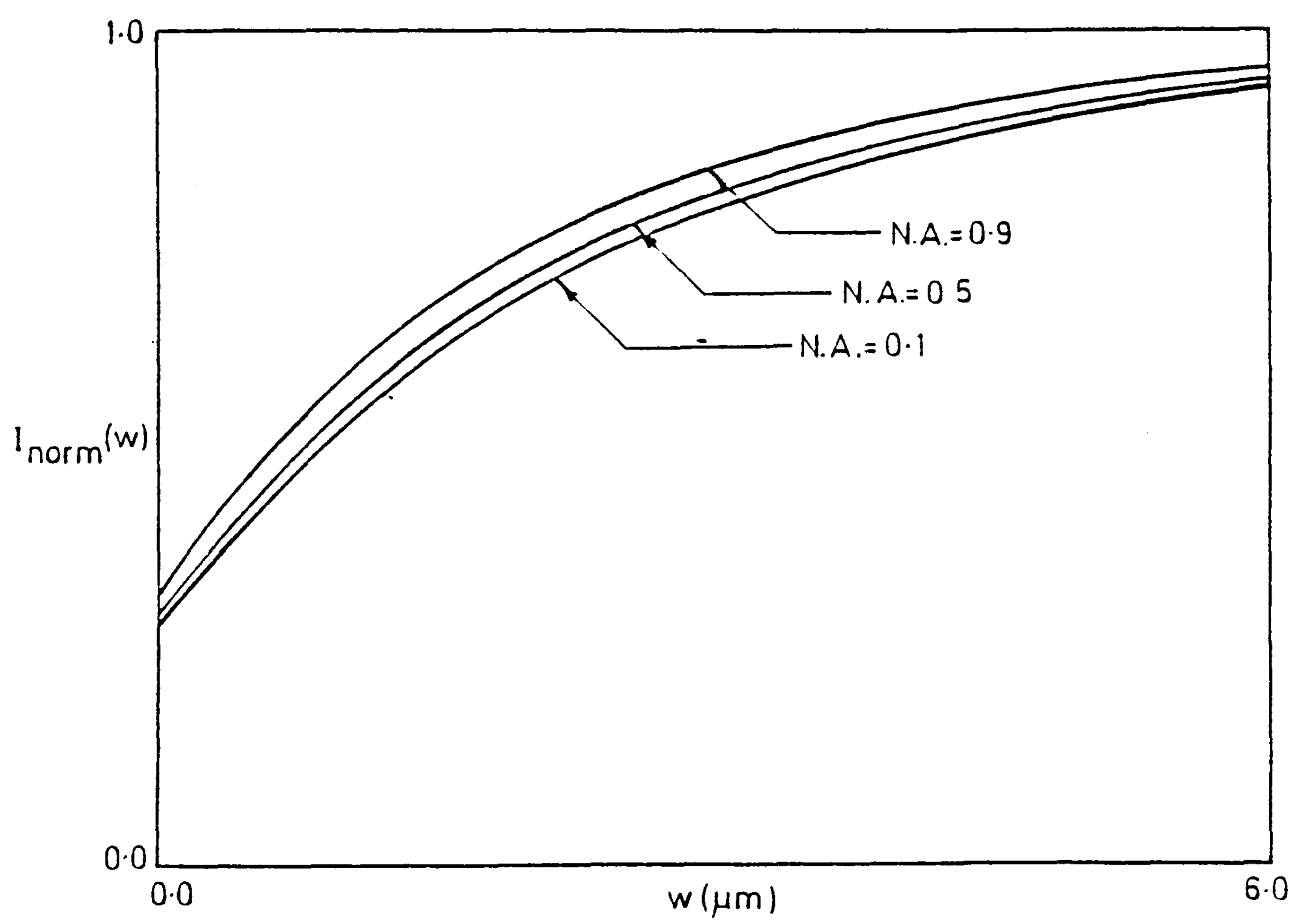

Figure 4.10. The normalized total current in a semi-infinite Schottky barrier as a function of depletion layer width for the case when $L = 1.0\mu m$ and $\alpha = 0.4\mu m^{-1}$ and for various values of numerical aperture.

4.3 Conclusions

General expressions for the current induced in both planar p-n junctions and finite thickness Schottky barriers due to an arbitrary, radially symmetric, exciting beam have been derived. The results were specialised to the case where light from a high numerical aperture lens provided the excitation.

It was shown that, in general, it is only possible to measure the minority carrier diffusion length by use of the planar junction geometry if the values for the surface recombination velocity and metalurgical junction depth are known. However, it was also shown that if the junction is deep the diffusion length can be found *without* knowledge of the surface recombination velocity.

The use of the Schottky barrier geometry to measure the minority carrier diffusion length is preferable owing to the removal of the uncertainty in the surface recombination velocity, although some simple curve fitting is required to extract the results.

CHAPTER 5:

TIME DEPENDENT BEAM INDUCED CURRENTS

5.0 Introduction

So far in this thesis steady state beam induced effects have been considered. In Chapter 3 the form of the *steady state* minority carrier distribution was found and in Chapter 4 *steady state* beam induced currents were calculated where it was shown that the measurement of the photocurrent in a Schottky barrier or planar p-n junction, as a function of reverse bias, could lead to a measurement of the diffusion length. One of the main reasons for wanting to measure the diffusion length, L, is to extract a value of the minority carrier lifetime, τ, which is related to the diffusion length via

$$\tau = \frac{L^2}{D}, \tag{5.1}$$

with D being the diffusion coefficient, since it is τ, *not* L which is frequently used by semiconductor device designers to characterize, amongst other things, the device gain and switching speed.

One obvious problem arises here: what is the value for the diffusion coefficient, D ? This problem can be overcome by realizing that we are essentially trying to measure a property, τ, which has the dimensions of time and is intimately related to the transient behaviour of the semiconductor, and yet we are using data collected in steady state experiments where all transient effects are ignored. Another slightly more subtle point, of which we must be aware, is that the vast majority of beam induced current experiments are performed in a *scanning* optical microscope where the exciting beam and the specimen are in relative motion. This means that each part of the semiconductor under examination "sees" a short burst of excitation, the length of which is related to the speed of scanning, which is in some ways analogous to a large sample of semiconductor being illuminated over it's whole surface with a short burst of light. In this rough analogy it would appear obvious that time dependent effects would have to be considered, and as such it is clear that in scanning systems we should strictly consider the time dependent form of the photocurrent which, in the limit of very slow scanning, reproduces the steady state results found in the previous Chapters. The special case where the scan speed is constant in magnitude and direction is considered in Chapter 6 which deals explicitly with scan speed effects.

Therefore, in this Chapter the time dependent beam induced minority carrier distribution, $\Delta p(r,z,t)$, is calculated from the time dependent diffusion equation which is written, [1] again for holes injected into an n-type sample,

$$D\nabla^2\Delta p(r,z,t) - \frac{\Delta p(r,z,t)}{\tau} + g(r,z)\cdot f(t) = \frac{\partial}{\partial t}\Delta p(r,z,t), \tag{5.2}$$

where we have assumed that the generation fuction can be represented as separate functions of space, $g(r,z)$, and time, $f(t)$.

In the following the solution to Equation (5.2) is found for an arbitrary form of temporal generation function and general, radially symmetric, spatial generation function. The spatial form of the generation function is then specialized to the practically important case of a focussed light beam and the minority carrier distribution is used to calculate the induced photocurrent, as a function of time, for various forms of the temporal generation function, $f(t)$. It is also shown how the minority carrier lifetime may be measured directly *without* a knowledge of the diffusion coefficient.

Finally, the contrast obtained as an electrically active defect, in a semi-infinite Schottky barrier, is imaged in the beam induced current mode of the scanning optical microscope is calculated. It is then shown how, by taking measurements at sufficiently short times after carrier injection and before the diffusion process has time to dominate, the resolution of the OBIC method may be increased.

5.1 Time Dependent Induced Carrier Distribution

Since we have choosen to consider a semi-infinite Schottky barrier the boundary conditions on the solution to Equation (5.2) are given as,

$$\Delta p(r,z,t)\Big|_{z=0} = 0, \qquad \text{and}, \qquad \Delta p(r,z,t)\Big|_{z=\infty} = 0, \tag{5.3}$$

where it has been assumed that the depletion width is small compared to the diffusion length such that the charge collection takes place at $z = 0$. The problem has cylindrical symmetry and so may be simplified by introducing the Hankel transform of the carrier distribution, $\Delta\bar{p}(\nu,z,t)$, as used in Chapter 3 and 4, this reduces Equation (5.2) to a partial differencial equation in two variables,

$$D\frac{\partial^2}{\partial z^2}\Delta\bar{p}(\nu,z,t) - D\phi^2\Delta\bar{p}(\nu,z,t) + \bar{g}(\nu,z)\cdot f(t) = \frac{\partial}{\partial t}\Delta\bar{p}(\nu,z,t), \tag{5.4}$$

where ϕ is as defined in Chapter 3, Equation (3.13). Equation (5.4) may be further simplified by introducing the function $\Delta\bar{P}(\nu,z,t)$ defined as,

$$\Delta\bar{P}(\nu,z,t) = \exp\left(D\phi^2 t\right)\Delta\bar{p}(\nu,z,t), \tag{5.5}$$

since then we have,

$$D\frac{\partial^2}{\partial z^2}\Delta\bar{P}(\nu,z,t) + \bar{g}(\nu,z)\cdot f(t)\cdot\exp\left(D\phi^2 t\right) = \frac{\partial}{\partial t}\Delta\bar{P}(\nu,z,t). \tag{5.6}$$

This partial differential equation can be reduced to a one dimensional equation by introducing the Laplace transform of $\Delta\bar{P}(\nu,z,t)$ via,

$$\mathcal{L}\left[\Delta\bar{P}(\nu,z,t)\right] = \Delta\mathcal{P}(\nu,z,p) = \int_0^\infty \Delta\bar{P}(\nu,z,t)\exp(-pt)\,dt, \tag{5.7}$$

with $\mathcal{L}$ denoting the Laplace transform operator. Assuming the initial boundary condition $\Delta p(r,z,0) = 0$ we can now write Equation (5.6) in the form,

$$\frac{\partial^2}{\partial z^2}\Delta\mathcal{P}(\nu,z,p) - q^2\Delta\mathcal{P}(\nu,z,p) = -\frac{1}{D}\bar{g}(\nu,z)\mathcal{F}(p - D\phi^2), \tag{5.8}$$

with $q = \sqrt{p/D}$ and $\mathcal{F}(p) = \mathcal{L}[f(t)]$.

The Green's function to Equation (5.8) is straightforward to find [2,3,4] and is given as,†

$$G(\nu,z|z_0,p) = \frac{1}{2q}\Big\{\exp[-q|z-z_0|] - \exp[-q(z+z_0)]\Big\}, \tag{5.9}$$

whence the general solution to Equation (5.8) can be written,

$$\Delta\mathcal{P}(\nu,z,p) = \frac{1}{D}\mathcal{F}(p - D\phi^2)\int_0^\infty \bar{g}(\nu,z_0)G(\nu,z|z_0,p)\,dz_0. \tag{5.10}$$

† This is simply the Green's function found in Appendix C for the finite thickess Schottky barrier evaluated in the limit as the thickness, $d \to \infty$, the depletion width, $w \to 0$ and with $1/L^2$ replaced by q^2.

The general form of the induced minority carrier distribution may be found via the inverse Laplace transformation of Equation (5.10), the use of Equation (5.5) and the inverse Hankel transformation.‡

To give an example of the type of solution predicted by Equation (5.10) we can consider the illumination to be from a low numerical aperture lens since then, using the results of Chapter 3, the spatial generation function, $g(r,z)$ may be represented by the decaying Gaussian given in Equation (3.76), which means that the Hankel transform, $\bar{g}(\nu,z)$, is also a decaying Gaussian as can be seen from Equation (3.80). The simplest form for the temporal generation function is a Delta function since then we have,

$$\mathcal{F}(p - D\phi^2) = 1, \tag{5.11}$$

and Equation (5.10) may be written simply as,

$$\Delta\mathcal{P}(\nu,z,p) = \frac{\alpha g_0}{2\pi(p-\alpha^2 D^2)} \exp(-\nu^2 c^2/4)\Big\{\exp(-\alpha z) - \exp(-qz)\Big\}. \tag{5.12}$$

From Equation (5.12) it is routine, using the inverse Laplace transformations tabulated in Carslaw and Jeager [5], to write the minority carrier distribution as,

$$\begin{aligned}\Delta p(r,z,t) =& \frac{\alpha g_0}{2D(c^2+2Dt)} \exp\left\{-(1-\alpha^2 D\tau)\frac{t}{\tau}\right\} \exp\left\{-\frac{r^2}{c^2+2Dt}\right\}\cdot \\ & \exp(-\alpha z)\left\{\operatorname{erfc}\left(\alpha\sqrt{Dt} - \frac{z}{2\sqrt{Dt}}\right) - \operatorname{erfc}\left(\alpha\sqrt{Dt} + \frac{z}{2\sqrt{Dt}}\right)\right\},\end{aligned} \tag{5.13}$$

where erfc is an error function complement [6]. Figure (5.1) shows contour plots of Equation (5.13) for various normalised times, t/τ, after injection for the case when $\alpha L = 0.4$ and $cL = 0.05$.

From Figure (5.1) it is clear that the region of maximum carrier concentration becomes more diffuse and spreads deeper into the bulk with time, this is an important point to note when OBIC or photoluminescence results are taken as a function of time, since it is clear that the resolution and section being imaged are functions of time after carrier injection.

‡ The method used here is an example of the repeated transform approach used classically in the solution of the heat conduction equation see, for example, [5 p.464].

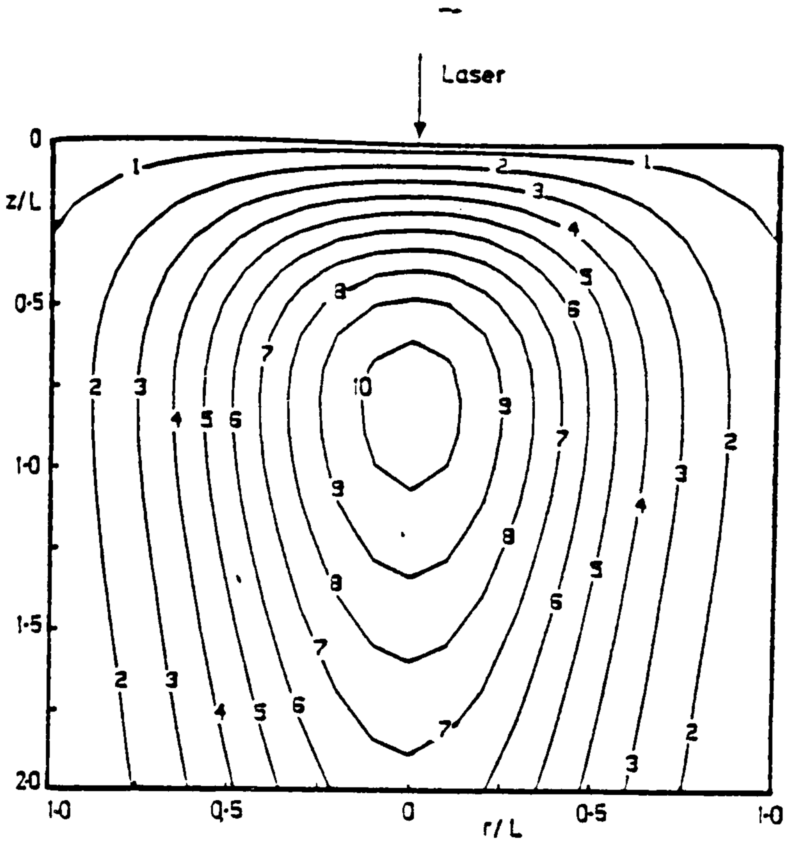

(a)

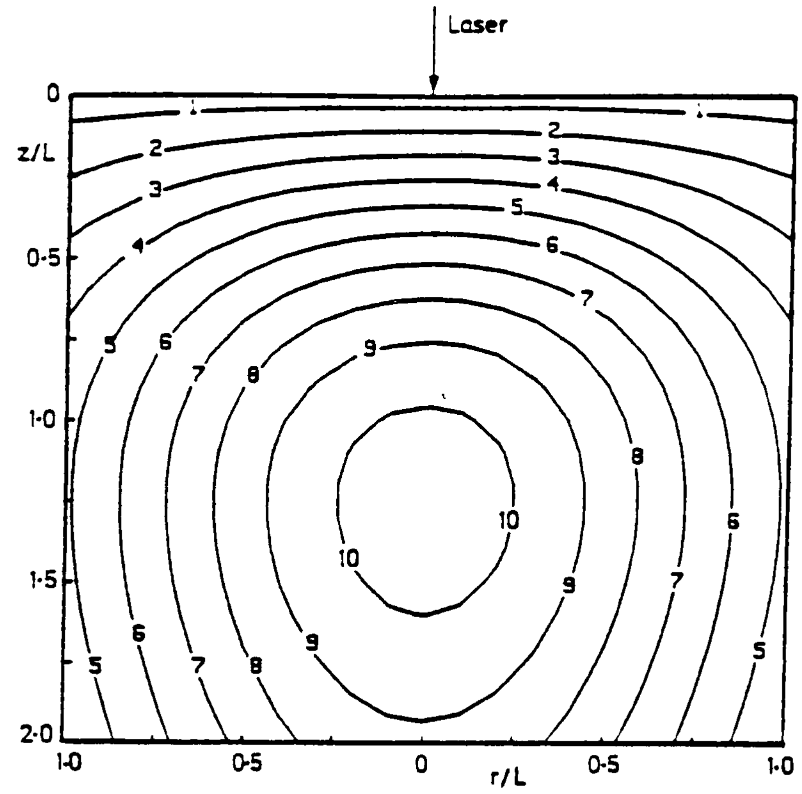

(b)

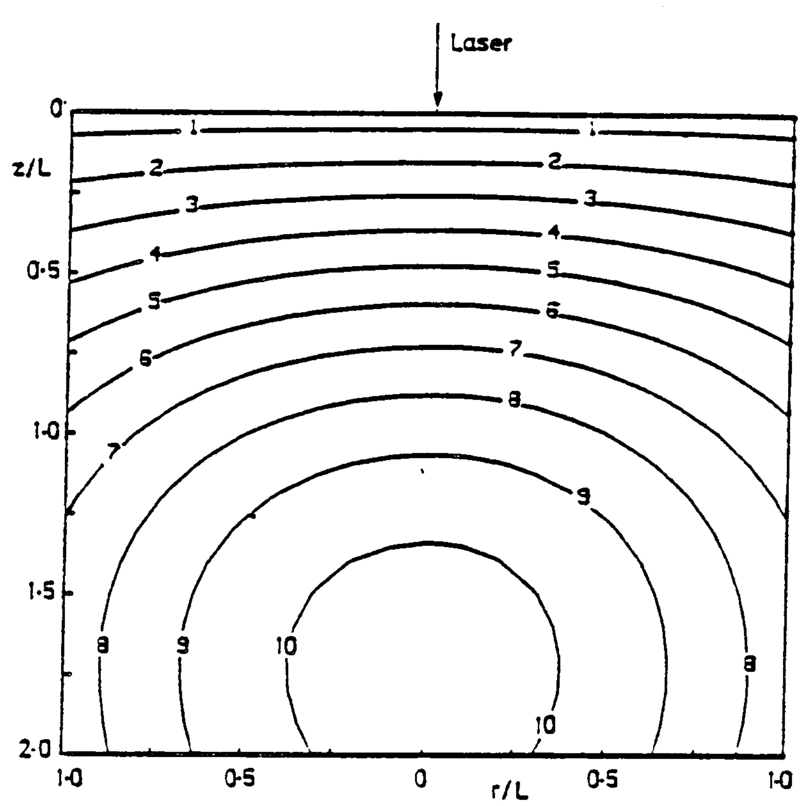

(c)

Figure 5.1. Contour plots of the minority carrier distribution injected into a semi-infinite silicon Schottky barrier by a short pulse of red light from a low numerical aperture lens, such that $\alpha L = 0.4$ and $cL = 0.05$. (a) Corresponds to the distribution 0.1τ after injection, (b) corresponds to the distribution 0.3τ after injection and (c) corresponds to the distribution 0.7τ after injection. The contour numbering is such that a high contour number represents a high carrier concentration and is normalised such that contour ten in (a) represents unity with the contour spacing being 0.105, in (b) contour ten represents 0.19 and the spacing is 0.02 and finally in (c) contour ten is 0.033 with spacing of 0.004.

5.2 Time Dependent Information Depth

The change in peneration depth as a function of time after carrier injection can be investigated further by introducing a *time dependent information depth* [7] which is the time dependent equivalent of the steady state information depth introduced in Chapter 3. Following the definitions of Chapter 3 we can define the time dependent information depth as the distance, $d(t)$, into the semiconductor at which 90% of the photoinduced carriers have been sampled, and so introducing the function

$$\omega(z,t) = \int_0^\infty \Delta p(r,z,t)\, r dr = \Delta\bar{p}(0,z,t), \tag{5.14}$$

the information depth is given as the solution to,

$$\Omega(d,t) = 0.1\Omega(0,t), \tag{5.15}$$

where, similarly to Chapter 3,

$$\Omega(d,t) = \int_d^\infty \omega(z,t)\, dz = \int_d^\infty \Delta\bar{p}(0,z,t)\, dz. \tag{5.16}$$

The calculation of the function $\Omega(d,t)$ for a semi-infinite semiconductor with arbitrary surface recombination velocity is fairly straightforward, although rather lengthy, and yields an analytic result [7], however, the solution of Equation (5.16) has to be found numerically. Figure (5.2) shows the time evolution of the information depth for the limiting cases of zero and infinite surface recombination velocity.

It is clear from Figure (5.2) that the time taken to reach the steady state is slightly less for low values of surface recombination velocity, however we see that a greater depth of the specimen is probed for higher recombination velocities. This is a result of our definition of information depth and the fact that for non-zero values of surface recombination velocity the induced minority carrier distribution always peaks some distance below the semiconductor surface [2 and Chapter 3]. It is interesting to note from Figure (5.2) that a high absorption limit to the information depth appears to exist at large values of time. This is just as we would expect from the *steady state* information depth as found in Chapter 3 where it was shown that, in the limit as $\alpha \rightarrow \infty$, $d \sim 2.3L$ independent of surface recombination velocity. The same is predicted from the time dependent theory in the large t limit, as it must.

Figure (5.3) shows the variation of the information depth as a function of time for various surface recombination velocities, where it is clear that the state of the surface of the device does not have a great effect on the depth of the sample being probed.

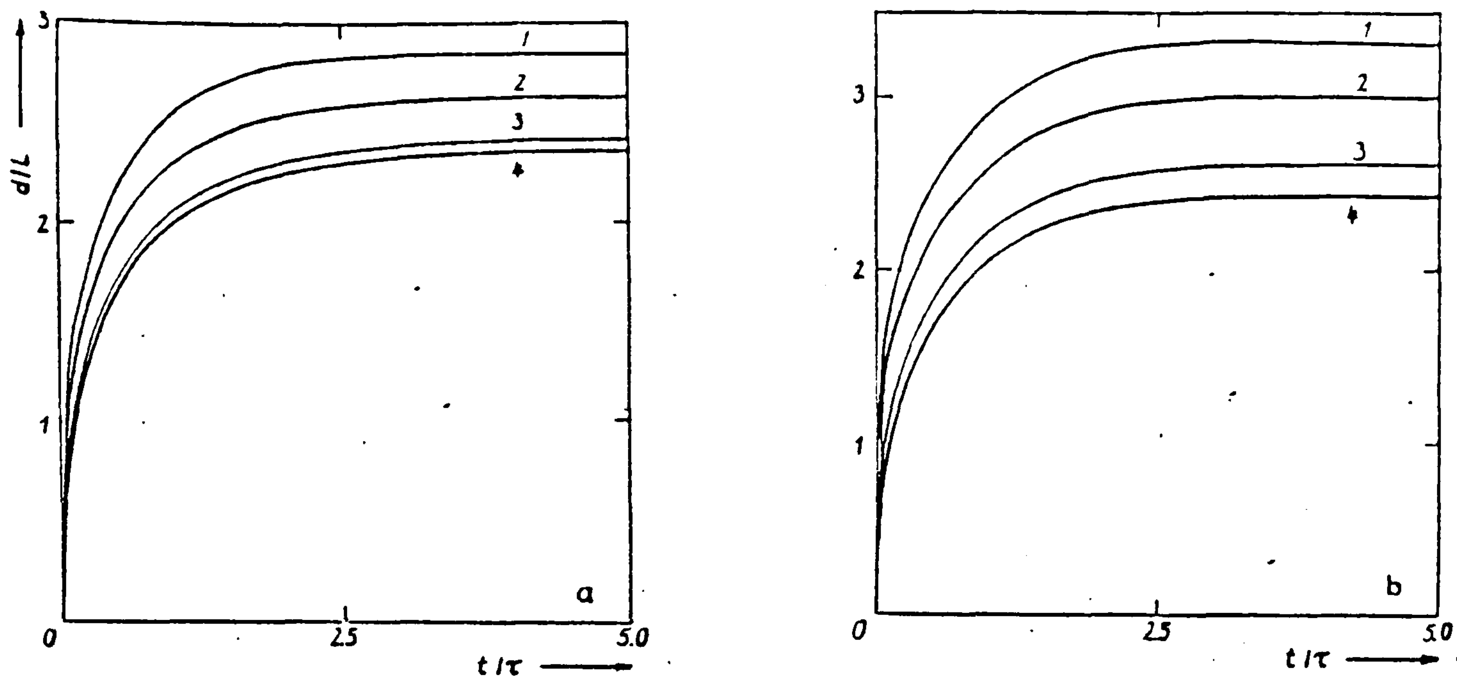

(a) (b)

Figure 5.2. The time evolution of the information depth for the cases of (a) zero surface recombination velocity and (b) infinite surface recombination velocity. The curves shown are for different values of absorption coefficient, α, such that (1) represents $\alpha L = 1.5$, (2) represents $\alpha L = 2.0$, (3) represents $\alpha L = 4.0$ and (4) is the limit in which $\alpha \rightarrow \infty$.

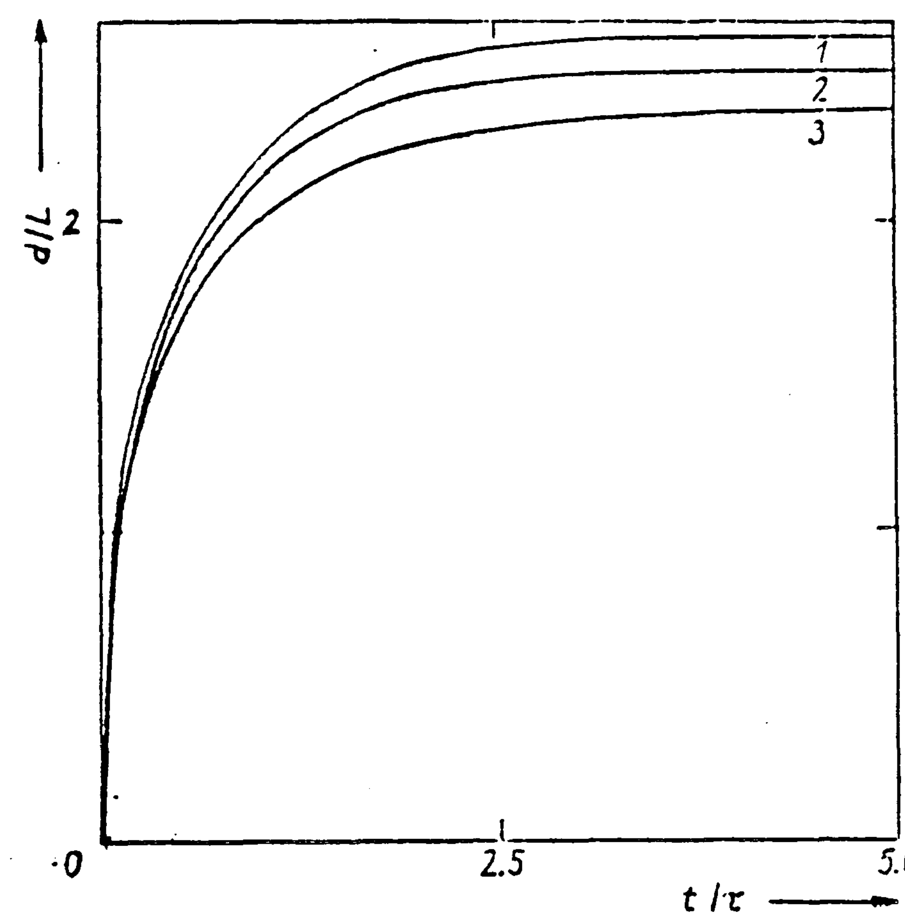

Figure 5.3. The time evolution of the information depth for the case when $\alpha L = 4.0$ and three values of surface recombination velocity, (1) is for $v_s \rightarrow \infty$, (2) for $v_s/D = 5.0\mu m^{-1}$ and (3) for $v_s \rightarrow 0$.

5.3 Time Dependent Beam Induced Current In a Schottky Barrier

Returning to the case of the semi-infinite Schottky barrier considered in Section 5.1 we now calculate the photo-induced junction current as a function of time. The diffusion current, $I_{\text{diff}}(t)$, collected at the surface junction can be written in an analogous form to the steady case as,

$$I_{\text{diff}}(t) = 2\pi q_e D \frac{\partial}{\partial z} \Delta\bar{p}(0,z,t)\bigg|_{z=0} \tag{5.17}$$

where q_e is the electric charge unit. Now, we can write an expression for $\Delta\bar{p}(0,z,t)$, using the substitution of Equation (5.5) and the Laplace transformation of Equation (5.7), as,

$$\Delta\bar{p}(0,z,t) = \exp(-t/\tau)\mathcal{L}^{-1}\left[\Delta\mathcal{P}(0,z,p)\right], \tag{5.18}$$

where $\mathcal{L}^{-1}$ represents the inverse Laplace transformation, and so a general expression for the time dependent diffusion current may be written, using Equation (5.10), in the form,

$$I_{\text{diff}}(t) = 2\pi q_e \exp(-t/\tau)\frac{\partial}{\partial z}\left\{\mathcal{L}^{-1}\left[\mathcal{F}\left(p-\frac{1}{\tau}\right)\int_0^\infty \bar{g}(0,z_0)G(0,z|z_0,p)\,dz_0\right]\right\}\bigg|_{z=0}. \tag{5.19}$$

Using the form of the Green's function in Equation (5.9) this expression for the diffusion current may be readily simplified to,

$$I_{\text{diff}}(t) = 2\pi q_e \exp(-t/\tau)\int_0^\infty \mathcal{L}^{-1}\left\{\exp(-qz_0)\mathcal{F}\left(p-\frac{1}{\tau}\right)\right\}\bar{g}(0,z_0)\,dz_0. \tag{5.20}$$

Equation (5.20) is a general expression from which the beam induced diffusion current collected by a semi-infinite Schottky barrier due to arbitrary spatial and temporal generation functions may be found. Speciali~~s~~zing to the case of light focussed through a high numerical aperture lens we know that the Hankel transform of the generation function, in the $\nu \to 0$ limit, is given by Equation (4.15) which, upon substitution into Equation (5.20) gives an expression for the diffusion current as,

$$I_{\text{diff}}(t) = \frac{q_e g_0}{\ln(\mu)}\exp(-t/\tau)\int_0^\infty \mathcal{L}^{-1}\left[\exp(-qz_0)\mathcal{F}\left(p-\frac{1}{\tau}\right)\right] \left\{\frac{\exp(-\alpha z_0)-\exp(-\alpha\mu z_0)}{z_0}\right\}dz_0. \tag{5.21}$$

The form of the solution predicted by Equation (5.21) can now be demonstrated by considering various forms for the temporal generation function $f(t)$. In the following examples we consider the three important cases of; (i) Delta Function Excitation, (ii) Step and Finite Pulse Excitation, and finally, (iii) Harmonic Excitation.

Example (i): Delta Function Excitation

For the case of a pulse whose duration is short compared to the lifetime we have,

$$f(t) = \delta(t), \tag{5.22}$$

which gives $\mathcal{F}(p - 1/\tau) = 1$, substitution into Equation (5.21), performing the inverse Laplace transformation and the integration yields [7],

$$I_{\text{diff}}(t) = \frac{q_e g_0}{2\ln(\mu)} \frac{\exp(-t/\tau)}{t} \Big\{ \exp(\alpha^2 Dt)\text{erfc}(\alpha\sqrt{Dt}) - \exp(\alpha^2\mu^2 Dt)\text{erfc}(\alpha\mu\sqrt{Dt}) \Big\}. \tag{5.23}$$

In the low numerical aperture limit, $\mu \to 1$, Equation (5.23) takes the form,

$$I_{\text{diff}}(t) = q_e g_0 \alpha \sqrt{\frac{D}{\pi t}} \exp(-t/\tau) \Big\{ 1 - \alpha\sqrt{\pi Dt} \exp(\alpha^2 Dt)\text{erfc}(\alpha\sqrt{Dt}) \Big\}. \tag{5.24}$$

Plots of Equations (5.23) and (5.24) are given in Figure (5.4) for various values of the absorption coefficient α.

It is clear form Figure (5.4) that the current versus time plots appear to straighten-out for large values of time and, as such, it is interesting to look at the large time expansion of Equation (5.24) or (5.23). Expanding the error function complements using [6],

$$\text{erfc}(x) \sim \frac{\exp(-x^2)}{\sqrt{\pi}x} \left(1 - \frac{1}{2x^2} + \cdots \right) \tag{5.25}$$

we obtain from, Equation (5.23),

$$I_{\text{diff}}(t) \sim \frac{q_e g_0 (\mu - 1)}{2\alpha\sqrt{\pi D}\mu \ln(\mu)} \cdot \frac{\exp(-t/\tau)}{t^{3/2}}, \tag{5.26}$$

and expanding Equation (5.24) gives,

$$I_{\text{diff}}(t) \sim \frac{q_e g_0}{2\alpha\sqrt{\pi D}} \cdot \frac{\exp(-t/\tau)}{t^{3/2}}, \tag{5.27}$$

from which it is clear that the temporal behaviour of the large t expansion of the diffusion current does not depend on the form of the spatial generation function. This suggests a method for the measurement of the minority carrier lifetime, τ, since at sufficiently long times after injection a plot of $\ln[t^{3/2} I_{\text{diff}}(t)]$ against t will yield a straight line whose slope is $-1/\tau$, independent of the absorption coefficient and the form of the spatial generation function. ‡

‡ This is an important point to note since one might, at first sight, expect the current to vary simply as $I(t) \propto \exp(-t/\tau)$, the use of which would lead to an error in the measured lifetime.

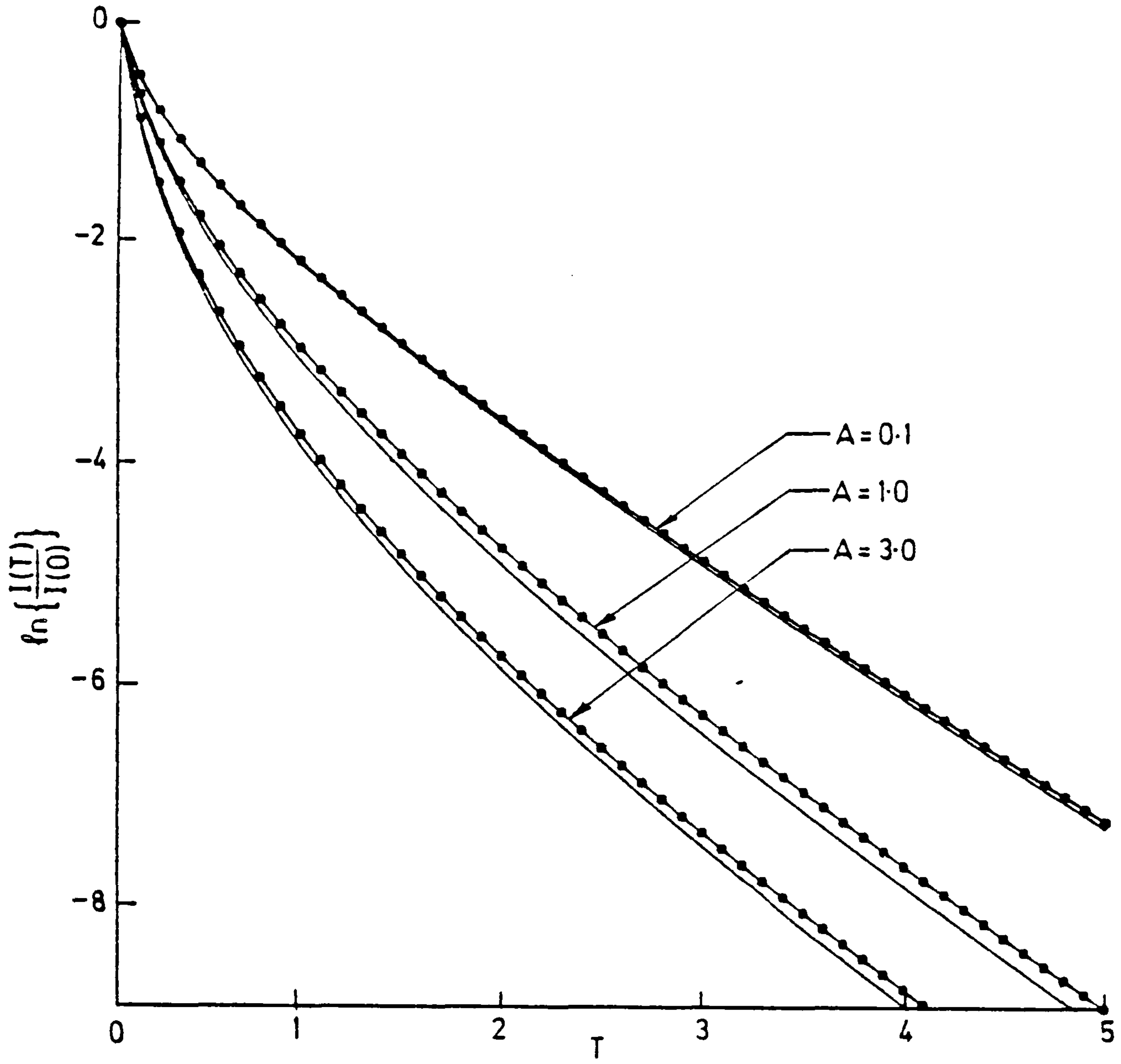

Figure 5.4. The photocurrent induced in a semi-infinite Schottky barrier by a short light pulse as a function of time after carrier injection. The curves shown are for three values of absorption coefficient, $\alpha L = 0.1$, $\alpha L = 1.0$ and $\alpha L = 3.0$. The dotted lines represent the low numerical aperture approximation given in Equation (5.~~27~~ 34) and the full lines are from the full theory of Equation (5.~~26~~ 33) with a numerical aperture of $\sin\theta = 0.6$.

Example (ii): Step and Finite Pulse Excitation

We now move on to consider the form of the junction current due to a unit step in the incident light intensity where $f(t)$ is given by,

$$f(t) = \begin{cases} 0, & t \leq 0 \\ 1, & t > 0. \end{cases} \tag{5.28}$$

For this case we have,

$$\mathcal{F}\left(p - \frac{1}{\tau}\right) = \frac{1}{p - \frac{1}{\tau}}, \tag{5.29}$$

which upon substitution into Equation (5.21) yields an expression for the diffusion current as,

$$I_{\text{diff}}(t) = \frac{q_e g_0}{\ln(\mu)} \int_0^\infty \left\{ \exp(-z_0/L)\text{erfc}\left[\frac{z_0}{2\sqrt{Dt}} - \sqrt{\frac{t}{\tau}}\right] + \exp(z_0/L)\text{erfc}\left[\frac{z_0}{2\sqrt{Dt}} + \sqrt{\frac{t}{\tau}}\right]\right\} \left(\frac{\exp(-\alpha z_0) - \exp(-\alpha\mu z_0)}{z_0}\right) dz_0, \tag{5.30}$$

for the case of low numerical aperture Equation (5.30) reduces to,

$$I_{\text{diff}}(t) = \frac{q_e g_0}{(\alpha^2 L^2 - 1)} \left\{ \alpha L \left(1 - \exp(-t/\tau)\exp(\alpha^2 D t)\text{erfc}\left[\alpha\sqrt{Dt}\right]\right) - \text{erfc}\left[\sqrt{\frac{t}{\tau}}\right]\right\}. \tag{5.31}$$

Again the effect of the numerical aperture on the form of the current versus time plots is found to be small, and so we show in Figure (5.5) the rise in diffusion current due to excitation via a low numerical aperture lens.

It is clear that the current rise time is less for the higher values of absorption coefficient, this is to be expected since at high absorption most of the photo-induced carriers are generated close to the surface and hence in the vicinity of the surface junction.

It is now possible to calculate the form of the junction current if the laser is suddenly turned off after the steady state has been reached. The steady state beam induced signal, in the low numerical aperture limit, can be readily found by letting $t \to \infty$ in Equation (5.31), this gives,

$$I_{\text{dc}} = \frac{q_e g_0 \alpha L}{(\alpha L + 1)}, \tag{5.32}$$

which is in agreement with previous steady state analyses [8]. The current decay after the beam is switched off may then be written as,

$$I_{\text{off}}(t) = 1 - \frac{I_{\text{on}}(t)}{I_{\text{dc}}}, \tag{5.33}$$

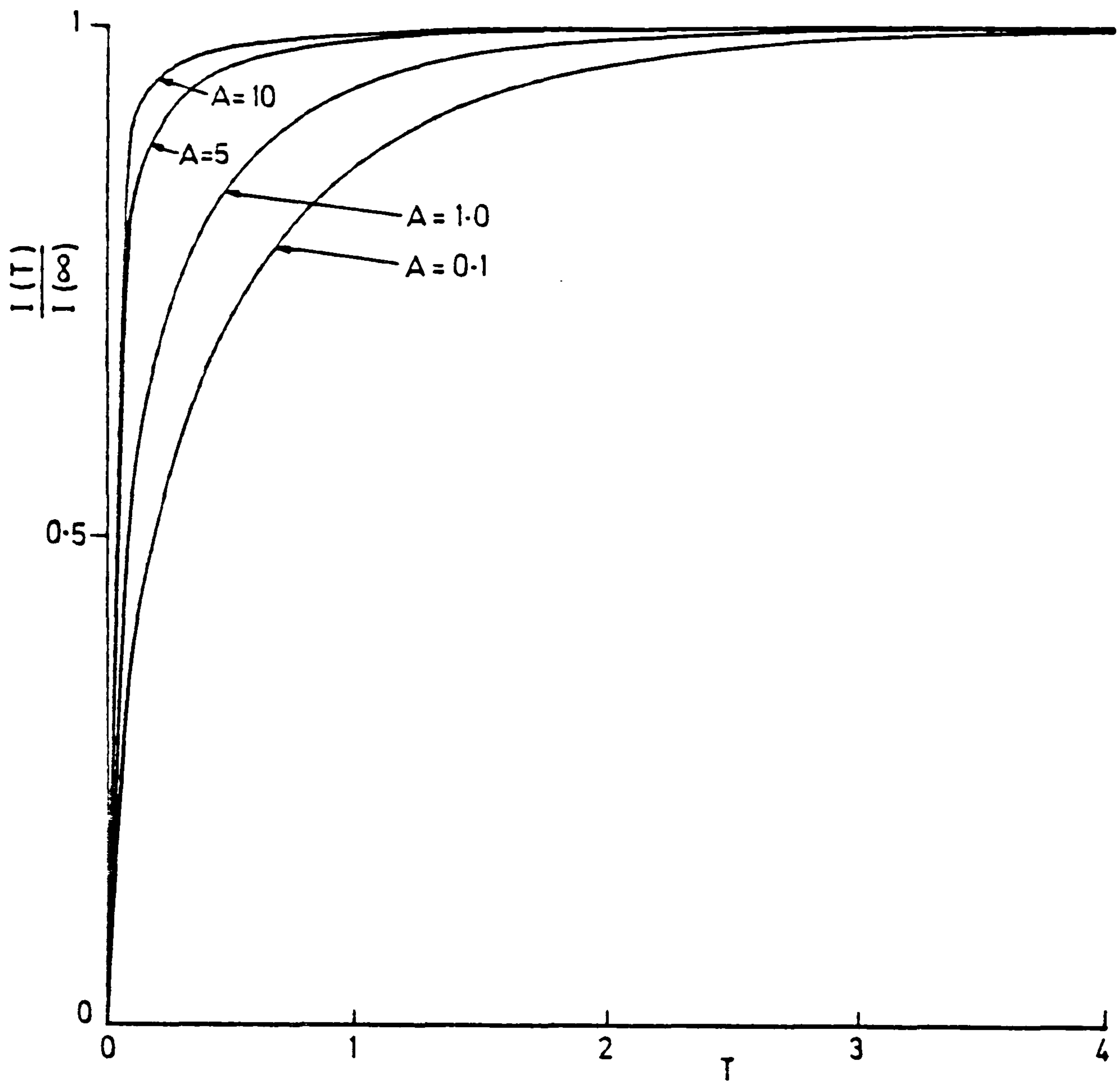

Figure 5.5. The rise in the diffusion current immediately after turning on the light beam. The curves are for various values of the absorption, that is $\alpha L = 10.0$, $\alpha L = 5.0$, $\alpha L = 1.0$ and $\alpha L = 0.1$.

where I_{on} is given by Equation (5.31) and t now represents the time following the switching off of the beam.

Plots of Equation (5.33) are shown in Figure (5.6), where a straightline asymptote appears to exist at large values of time, and so once again it is interesting to look at the large time expansion of Equation (5.33). Expanding the error function complements as before we obtain,

$$I_{\text{off}}(t) \sim \frac{q_e g_0(\alpha^2 L^2 - 1)}{2\sqrt{\pi}\alpha^2 L^2} \cdot \frac{\exp(-t/\tau)}{t^{3/2}}, \tag{5.34}$$

which has the same temporal behaviour as the large t expansion obtained for the delta function excitation in Equation (5.27). This is to be expected physically since the excitation mechanism should have no effect on the rate of minority carrier recombination, and so the same conclusions apply with regards to lifetime measurement, that is, a plot of $\ln[t^{3/2} I_{\text{diff}}(t)]$ against t will yield a straight line whose slope is $-1/\tau$.

For completeness we show in Figure (5.7) the form of the diffusion current against time for a finite length pulse in the low numerical aperture limit. This is most easilly modelled mathematically by summing two equal and opposite step functions separated appropriately in time.

It is clear from Figure (5.7) that the current rise and fall times exhibit the same dependence on absorption coefficient as in the step function case.

Example (iii): Harmonic Excitation

A form of excitation which may be easier to produce practically than the delta or step functions of examples (i) and (ii) is an harmonic modulation of the light intensity. In this case we can model $f(t)$ as,

$$f(t) = \exp(i\omega t), \tag{5.35}$$

where $i = \sqrt{-1}$ and ω is the modulation frequency, since we are only interested in the modulus and phase of the junction current and not the actual amplitude.† For this form of temporal excitation we have that,

$$\mathcal{F}\left(p - \frac{1}{\tau}\right) = \frac{1}{p - \left(\frac{1+i\omega\tau}{\tau}\right)}, \tag{5.36}$$

substitution of which into Equation (5.21) yields the junction current as,

$$\begin{aligned} I_{\text{diff}}(t) = & \frac{q_e g_0}{2\ln(\mu)} \exp(i\omega t) \int_0^\infty \left\{ \exp(-\bar{\omega} z_0/L) \operatorname{erfc}\left[\frac{z_0}{2\sqrt{Dt}} - \bar{\omega}\sqrt{\frac{t}{\tau}}\right] \right. \\ & \left. + \exp(\bar{\omega} z_0/L) \operatorname{erfc}\left[\frac{z_0}{2\sqrt{Dt}} + \bar{\omega}\sqrt{\frac{t}{\tau}}\right] \right\} \left(\frac{\exp(-\alpha z_0) - \exp(-\alpha\mu z_0)}{z_0}\right) dz_0, \end{aligned} \tag{5.37}$$

where $\bar{\omega} = \sqrt{1 + i\omega\tau}$.

Equation (5.37) includes the transient behaviour due to the excitation beginning at $t = 0$; we are interested in the steady state limit of Equation (5.37) which may be found by letting $t \to \infty$ giving,

$$I_{\text{diff}}(t) = \frac{q_e g_0}{\ln(\mu)} \exp(i\omega t) \ln\left[\frac{\alpha\mu L + \bar{\omega}}{\alpha L + \bar{\omega}}\right]. \tag{5.38}$$

For the limiting case of excitation via a low numerical aperture lens Equation (5.38) reduces to,

$$I_{\text{diff}}(t) = \frac{q_e g_0 \alpha L}{(\alpha L + \bar{\omega})} \exp(i\omega t). \tag{5.39}$$

It should be noted here that Equations (5.39) and (5.38) could have been found by substituting $f(t) = \exp(i\omega t)$ into the diffusion equation and looking for solutions of the form $\Delta p(r, z, t) = \Delta p(r, z)\exp(i\omega t)$, or by taking the Fourier transform of the diffusion equation with respect to time. However, we decided to stay with the Laplace transformation here since it is a more general method giving both the transient and steady state solutions.

---

† If we were interested in the amplitude it would be easy to extend the results of this section by simply replacing $f(t)$ with $1 + \exp(i\omega t)$, or by simply adding the solution of the steady state problem to the one found with $\exp(i\omega t)$ as the source term since the problem is linear.

Figure (5.8) shows plots of the modulus of the junction current, as given by Equations (5.38) and (5.39), as a function of frequency for various absorption coeficients. It is clear that the focussing of the beam has a greater effect at higher absorption coefficients and that the modulus of the junction current dies away rapidly with increasing modulation frequency. The phase of the junction current is shown in Figure (5.9), again as a function of frequency, for various values of the absorption coefficient.

Figure (5.9) indicates an alternative method for measuring the minority carrier lifetime, assuming the absorption coefficient is known, since it is possible to choose some phase shift and note the excitation frequency ω, at which this phase shift occurs for a given sample, then by simply reading on the plot the value of $\omega\tau$ and hence τ could be found. This technique has the advantage that it is steady state, and so a better signal to noise ratio may be expected than in the photocurrent decay methods discussed previously.

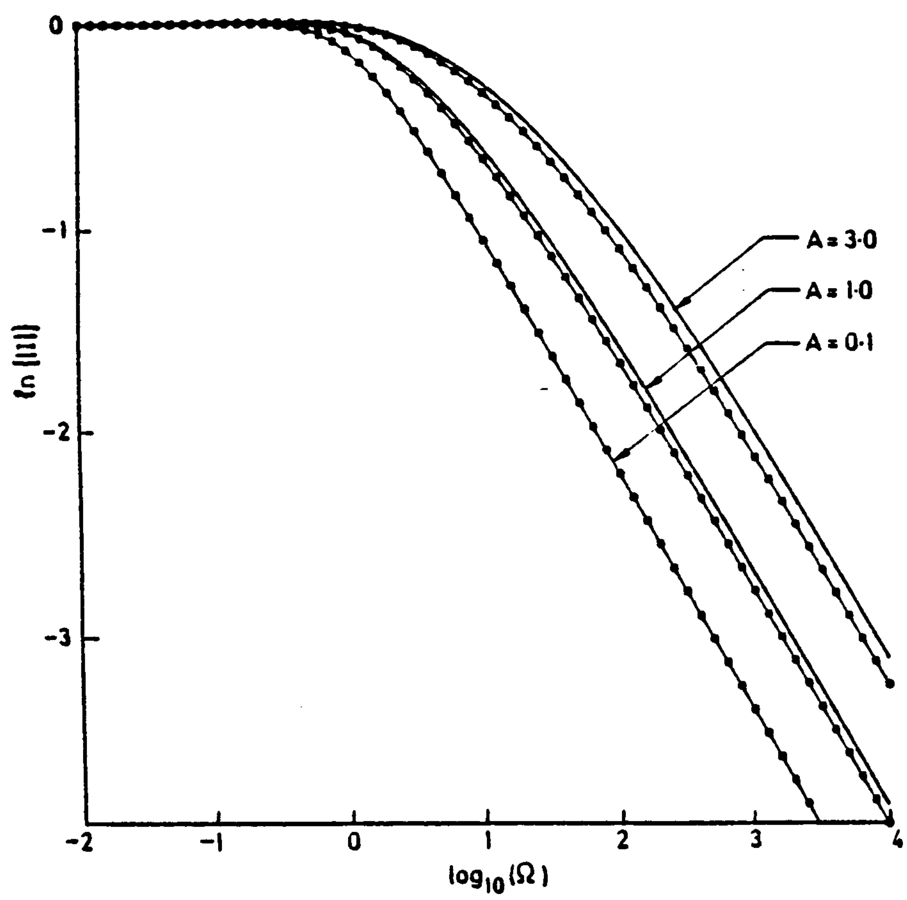

Figure 5.8. The logarithm of the modulus of the junction current as a function of laser modulation frequency. The dotted curves represent the low numerical aperture approximation of Equation (5.39), the curves are labelled for values of the absorption coefficient, $\alpha L = 0.1$, $\alpha L = 1.0$ and $\alpha L = 3.0$.

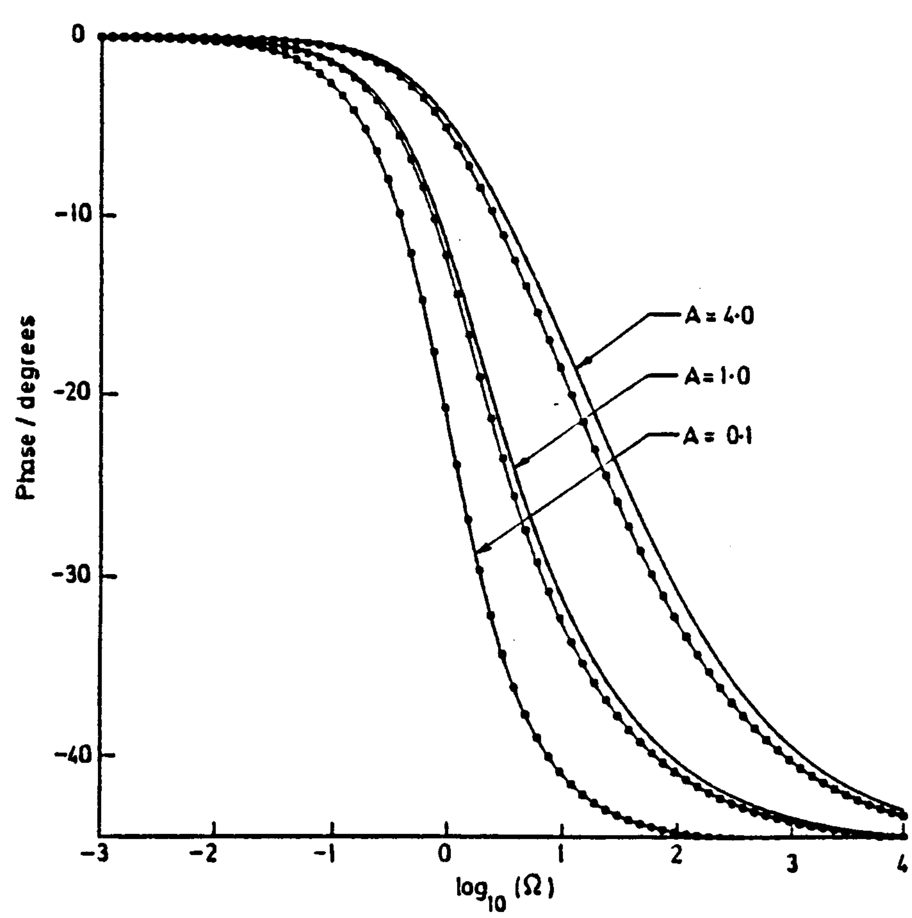

Figure 5.9. The phase shift between the junction current and the excitation as a function of modulation frequency. The dotted curves represent the low numerical aperture approximation of Equation (5.39) and the plots shown are for absorption coefficient values of $\alpha L = 0.1$, $\alpha L = 1.0$ and $\alpha L = 4.0$.

5.4 Time Dependent Defect Imaging

In Chapters 2 and 3 it was shown how the increased recombination rate at an electrically active defect in a semiconducting sample leads to a decrease in the beam induced current, and enables the defect to be *imaged* in the OBIC mode of the scanning optical microscope. The analysis in Chapter 3 given was purely for the steady state case. Here the analysis of defect imaging is extended to include time dependence, resulting in expressions for the contrast as a function of time, for arbitrary spatial and temporal generation functions. Step function excitation is considered as an example for the temporal generation function since we may assume that this represents the sudden increase in beam intensity seen by each part of the semiconductor as the beam scans the specimen.

The analysis is very similar to Chapter 3 except that the starting equation is the *time dependent* diffusion equation as opposed to the steady state diffusion equation. The presence of the defect is taken into account by introducing an extra, position dependent, recombination term into the diffusion equation giving,

$$D\nabla^2\Delta p(\mathbf{r},t) - \frac{\Delta p(\mathbf{r},t)}{\tau} + g(\mathbf{r})\cdot f(t) = \frac{\partial}{\partial t}\Delta p(\mathbf{r},t) + D\,\gamma(\mathbf{r})u(\mathbf{r})\Delta p(\mathbf{r},t), \qquad (5.40)$$

where $\gamma(\mathbf{r})$ is the defect distribution and $u(\mathbf{r})$ is a step function as in Chapter 3. The presence of the defect destroys the cylindrical symmetry that existed in the calculation of the minority carrier distribution and the induced junction current, and so we are unable to use the Hankel transform. However, we can follow a similar approach to section 5.1 and make the substitution,

$$\Delta P(\mathbf{r},t) = \exp(t/\tau)\Delta p(\mathbf{r},t), \qquad (5.41)$$

which means that Equation (5.40) simpifies to,

$$D\nabla^2\Delta P(\mathbf{r},t) + g(\mathbf{r})\cdot f(t)\exp(t/\tau) = \frac{\partial}{\partial t}\Delta P(\mathbf{r},t) + D\,\gamma(\mathbf{r})u(\mathbf{r})\Delta P(\mathbf{r},t), \qquad (5.42)$$

from which the time dependence can be illiminated by use of the Laplace transformation, $\Delta\mathcal{P}(\mathbf{r},p)$, of $\Delta P(\mathbf{r},t)$ as defined in Equation (5.7) giving,

$$\frac{\partial^2}{\partial z^2}\Delta\mathcal{P}(\mathbf{r},p) - q^2\Delta\mathcal{P}(\mathbf{r},p) = -\frac{1}{D}g(\mathbf{r})\mathcal{F}\left(p-\frac{1}{\tau}\right) + \gamma(\mathbf{r})u(\mathbf{r})\Delta\mathcal{P}(\mathbf{r},p) \qquad (5.43)$$

here $q = \sqrt{p/D}$ as before. If we choose to consider a semi-infinite Schottky barrier, as in the previous sections, the Green's function to Equation (5.43) is given by the three dimensional equivalent to Equation (5.9), which is [3,5,9],

$$G(\mathbf{r}|\mathbf{r_0},p) = \frac{1}{4\pi}\left\{\frac{\exp(-qR_1)}{R_1} - \frac{\exp(-qR_2)}{R_2}\right\}, \qquad (5.44)$$

where $R_{1,2} = \sqrt{(x-x_0)^2 + (y-y_0)^2 + (z \mp z_0)^2}$. The solution to Equation (5.43) can now be written directly as,

$$\Delta\mathcal{P}(\mathbf{r},p) = \frac{1}{D}\mathcal{F}\left(p - \frac{1}{\tau}\right)\int_V g(\mathbf{r_0})G(\mathbf{r}|\mathbf{r_0},p)\,d\mathbf{r_0} - \int_F \gamma(\mathbf{r_0})\Delta\mathcal{P}(\mathbf{r_0},p)G(\mathbf{r}|\mathbf{r_0},p)\,d\mathbf{r_0}. \tag{5.45}$$

It is clear that Equation (5.45) is a Fredholm equation similar to that obtained in the steady state analysis, and so here we make the same approximation as in Chapter 3 by assuming that the solution to Equation (5.45) can be written as a Neumann expansion to first order such that,

$$\Delta\mathcal{P}(\mathbf{r},p) \approx \Delta\mathcal{P}_1(\mathbf{r},p) = \Delta\mathcal{P}_0(\mathbf{r},p) - \int_F \gamma(\mathbf{r_0})\Delta\mathcal{P}_0(\mathbf{r_0},p)G(\mathbf{r}|\mathbf{r_0},p)\,d\mathbf{r_0}, \tag{5.46}$$

where $\Delta\mathcal{P}_0(\mathbf{r},p)$ is the zero order Neumann term or the solution in the absence of a defect. The minority carrier distribution in the presence of the defect can now be found by taking the inverse Laplace transformation of Equation (5.46) and applying the coordinate transformation of Equation (5.41).

We are interested in the diffusion current collected by the surface junction, which is given by the integral over the surface of the *gradient* of the carrier distribution, as defined in Equation (4.1), which may be written in the cartesian coordinate system as,

$$I(t) = q_e D \int_{-\infty}^{\infty}\int_{-\infty}^{\infty} \frac{\partial}{\partial z}\Delta p(\mathbf{r},t)\Big|_{z=0} dx\,dy, \tag{5.47}$$

that is,

$$I(t) = q_e D \exp(-t/\tau)\int_{-\infty}^{\infty}\int_{-\infty}^{\infty} \frac{\partial}{\partial z}\left\{\mathcal{L}^{-1}\left[\Delta\mathcal{P}(\mathbf{r},p)\right]\right\}\Big|_{z=0} dx\,dy. \tag{5.48}$$

From the form of $\Delta\mathcal{P}(\mathbf{r},p)$ in Equation (5.46) it is clear that the current will have two terms, as in the steady state case, that is,

$$I(t) = I_0(t) - I^*(t), \tag{5.49}$$

with,

$$I_0(t) = q_e \exp(-t/\tau)\int_V \mathcal{L}^{-1}\left[\exp(-qz_0)\mathcal{F}\left(p - \frac{1}{\tau}\right)\right] g(\mathbf{r_0})\,d\mathbf{r_0}, \tag{5.50}$$

and,

$$I^*(t) = q_e D \exp(-t/\tau)\int_F \mathcal{L}^{-1}\left[\exp(-qz)\Delta\mathcal{P}_0(\mathbf{r},p)\right]\gamma(\mathbf{r})\,d\mathbf{r}, \tag{5.51}$$

where use has been made of the form of the Green's function given in Equation (5.44). The time dependent contrast function, $C(t)$, can now be defined in an analogous way to the steady state contrast function as,

$$C(t) = \frac{I^*(t)}{I_0(t)}. \tag{5.52}$$

So far we have been completely general about the form of the spatial and temporal generation functions; we shall now specialize to the case of a point defect, such that the defect distribution, $\gamma(\mathbf{r})$, is simply a Dirac-delta function, illuminated by light from a low numerical aperture lens, such that the spatial generation function, $g(\mathbf{r})$, is given by the decaying Gaussian approximation of Chapter 3. Substitution into Equations (5.50) and (5.51) then yields,

$$I_0(t) = \alpha q_e g_0 \exp(-t/\tau) \int_0^\infty \mathcal{L}^{-1}\left[\exp(-q z_0)\mathcal{F}\left(p - \frac{1}{\tau}\right)\right] \exp(-\alpha z_0)\, dz_0, \tag{5.53}$$

and,

$$I^*(\xi, t) = \frac{\alpha q_e g_0 \gamma_0}{\pi c^2} \exp(-t/\tau) \exp(-\xi^2/c^2) \int_0^\infty \int_0^\infty \exp(-\alpha z_0) \exp(-r_0^2/c^2) I_0\left(\frac{2\xi r_0}{c^2}\right)$$
$$\left[\mathcal{L}^{-1}\left\{\frac{\exp(-q\lambda_1)}{\lambda_1} - \frac{\exp(-q\lambda_2)}{\lambda_2}\right\} \exp(-qd)\mathcal{F}\left(p - \frac{1}{\tau}\right)\right] r_0 dr_0 dz_0, \tag{5.54}$$

where $\lambda_{1,2} = \sqrt{r_0^2 + (d \mp z_0)^2}$, and I_0 is a modified Bessel function of the first kind and zero order [6]. A scan coordinate, ξ, has been introduced in Equation (5.54) giving the separation of the beam and defect and d is the depth of the point defect below the semiconductor surface.

We can now specailize further by choosing the temporal form of the generation function, $f(t)$; if we choose this to be a step function as in example (ii) of section 5.3 the expressions for I_0 and I^* take the form,

$$I_0(t) = \frac{q_e g_0 \alpha}{(\alpha^2 L^2 - 1)} \left\{\alpha L \left(1 - \exp(-t/\tau) \exp(\alpha^2 D t) \mathrm{erfc}\left[\alpha\sqrt{Dt}\right]\right) - \mathrm{erfc}\left[\sqrt{\frac{t}{\tau}}\right]\right\} \tag{5.55}$$

and,

$$I^*(\xi, t) = \frac{\alpha q_e g_0 \gamma_0}{\pi c^2} \exp(-\xi^2/c^2) \int_0^\infty \int_0^\infty r_0 dr_0 dz_0 \exp(-\alpha z_0) \exp(-r_0^2/c^2) I_0\left(\frac{2\xi r_0}{c^2}\right)$$
$$\left[\exp(-d/L)\left\{\frac{\exp(-\lambda_1/L)}{\lambda_1}\mathrm{erfc}\left[\frac{d+\lambda_1}{2\sqrt{Dt}} - \sqrt{\frac{t}{\tau}}\right] - \frac{\exp(-\lambda_2/L)}{\lambda_2}\mathrm{erfc}\left[\frac{d+\lambda_2}{2\sqrt{Dt}} - \sqrt{\frac{t}{\tau}}\right]\right\}\right.$$
$$\left. + \exp(d/L)\left\{\frac{\exp(-\lambda_1/L)}{\lambda_1}\mathrm{erfc}\left[\frac{d+\lambda_1}{2\sqrt{Dt}} + \sqrt{\frac{t}{\tau}}\right] - \frac{\exp(-\lambda_2/L)}{\lambda_2}\mathrm{erfc}\left[\frac{d+\lambda_2}{2\sqrt{Dt}} + \sqrt{\frac{t}{\tau}}\right]\right\}\right]. \tag{5.56}$$

Note that Equation (5.55) is the same as obtained in Equation (5.31), this is to be expected since $I_0(t)$ is simply the junction current in the absence of a defect, as calulated by use of the Hankel transform, in Section 5.3, example (ii). It is clear from Equations (5.55) and Equation(5.56) that there is no simple way in which the contrast can be related to the carrier distribution, as was possible in the steady state case, however it is straightforward to evaluate the contrast numerically.

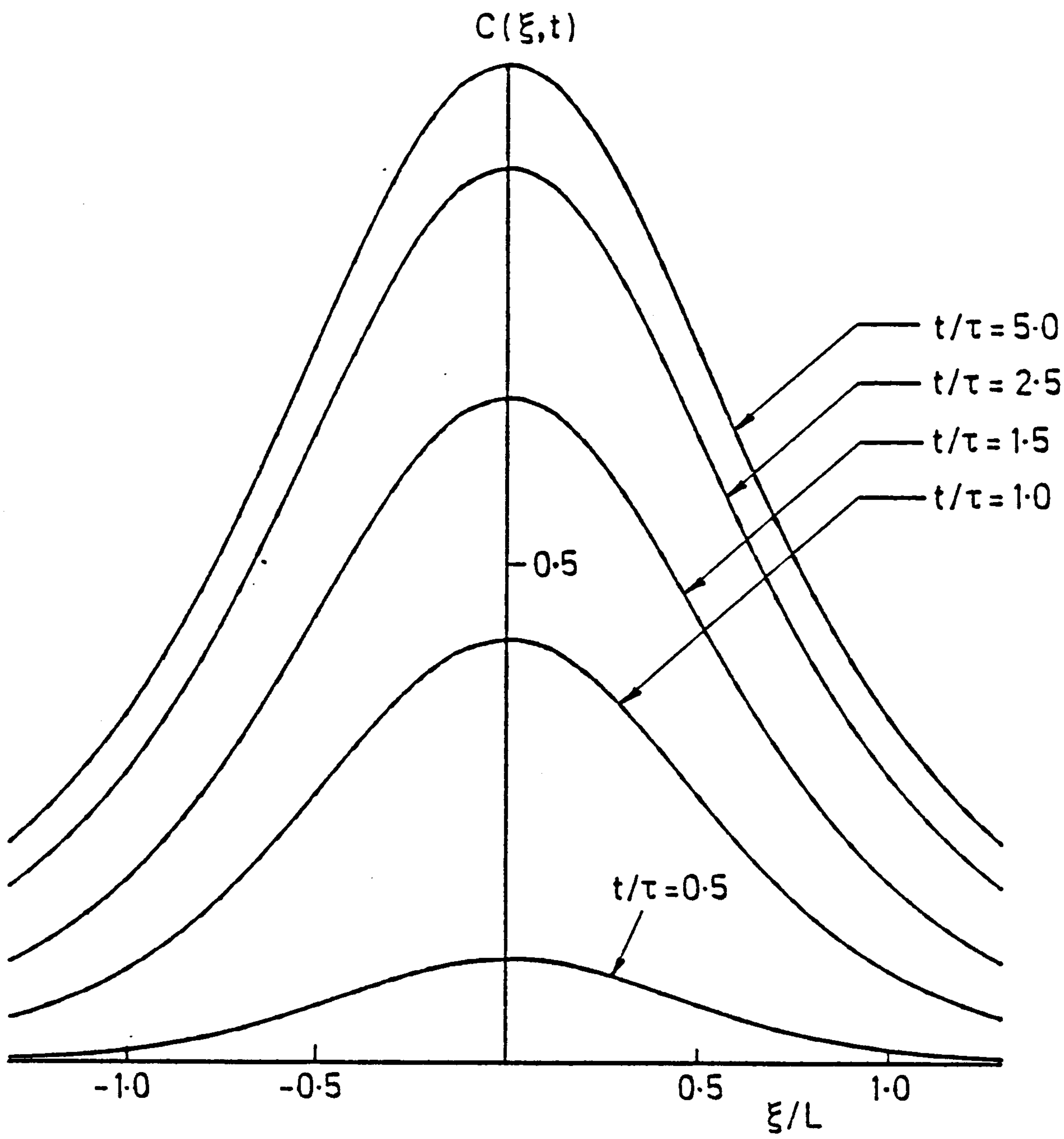

Figure 5.10. The contrast, as a function of probe position, for a point defect located $d = 2L$ below the surface of a semi-infinite Schottky barrier when $\alpha L = 0.4$ and $c = 0.5L$. The curves shown are for various times after the light beam is switched on and are normalised such that the curve obtained for $t/\tau = 5.0$ is unity directly above the defect, that is at $\xi = 0$.

Figure (5.10) shows the form of the contrast curves obtained from Equations (5.52), (5.55) and (5.56) for various times after beam switch-on. The case shown is for when $\alpha L = 0.4$, $c = 0.5L$ and a defect depth of $d = 2L$.

The curve given by $t = 5\tau$ is identical to that obtained by the previous steady state theories [10,11], this is interesting since we can now obtain a measure for the time after which the steady state theories begin to become applicable. In Figure (5.11) the variation of contrast as a function of time is shown in the form of a surface plot which gives a good "feel" for the way in which the contrast builds up to it's steady state limit, Figure (5.11a) shows the surface plot for a defect at a depth of $d = L$, and Figure (5.11b) for a defect depth $d = 3L$.

It is clear from Figure (5.11) that the steady state contrast is reached after a greater time for a deep defect. This is an important point to note when using scanning systems to image electrically active defects since, if the scan speed is too high, the system does not have sufficient time to reach it's steady state limit and a reduced contrast signal results [10 and Chapter 6]. The halfwidth of the contrast curves in Figure (5.11) also varies with time and, since this halfwidth is related to the resolution of the defect imaging system, it follows that the resolution is a function of time after beam switch on. Figure (5.12) shows the variation of the half width with time, from which it can be seen that at short times after beam switch on the resolution is considerably better than that obtained in the steady state limit.

This suggests a way of obtaining improved resolution when imaging defects, since if a beam chopper was to used to switch the beam on and off and images collected only at small times after carrier injection an improved resolution image could be obtained. The main drawback to this technique is that at small times after carrier injection the maximum contrast is somewhat less than it's steady state value, which can be seen clearly from Figure (5.13) where the maximum contrast, $C(0,t)$, is shown as a function of time.

Figure (5.13) shows that for a deep defect at, say, $d = 3L$ the contrast can take up to six lifetimes to reach it's maximum steady state value, whereas for a shallow defect where $d = L$ the rise time is of the order three lifetimes. This implies that in order to use the method described above to increase the resolution of the OBIC technique, and still obtain an adequate signal to noise ratio, some form of contrast enhancement system may be required.

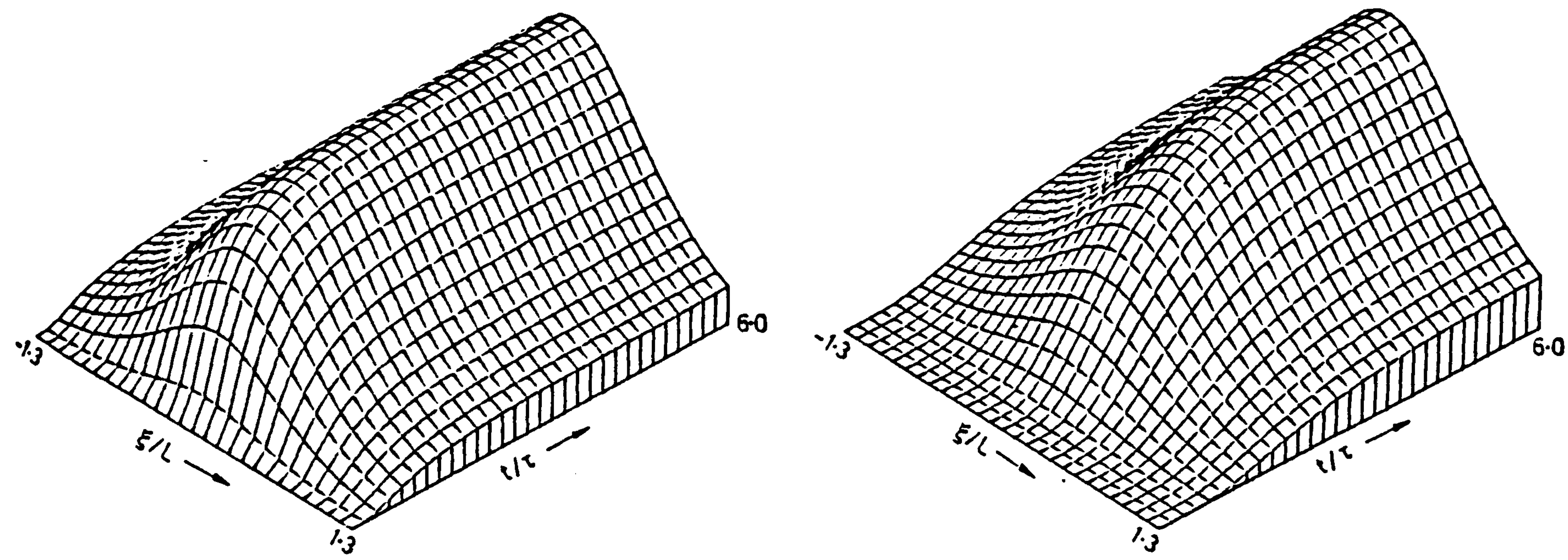

(a) (b)

Figure 5.11. Isometric surface plots showing the evolution of the contrast as a function with time after beam switch on for a point defect in a semi-infinite Schottky barrier when $\alpha L = 0.4$, $c = 0.5L$ and defect depths of (a) $d = L$ and (b) $d = 3L$.

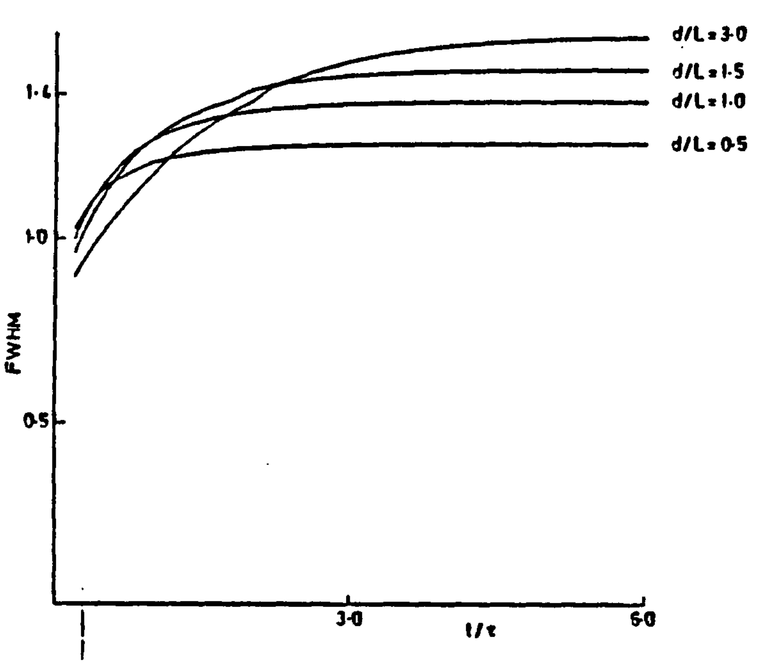

Figure 5.12. The variation of the half width of the contrast function as a function of time after the light beam is turned on. The curves shown are for various values of defect depth and for the case when $\alpha L = 0.4$ and $c = 0.5L$.

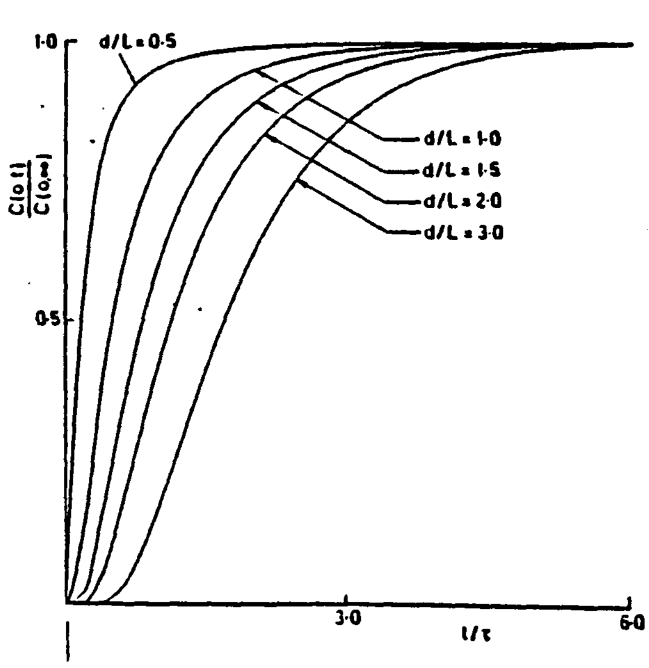

Figure 5.13. The variation of the maximum contrast $C(0,t)$ as a function of time after carrier injection for the case when $\alpha L = 0.4$ and $c = 0.5L$. The curves are shown for various defect depths and are normalised to unity at the steady state.

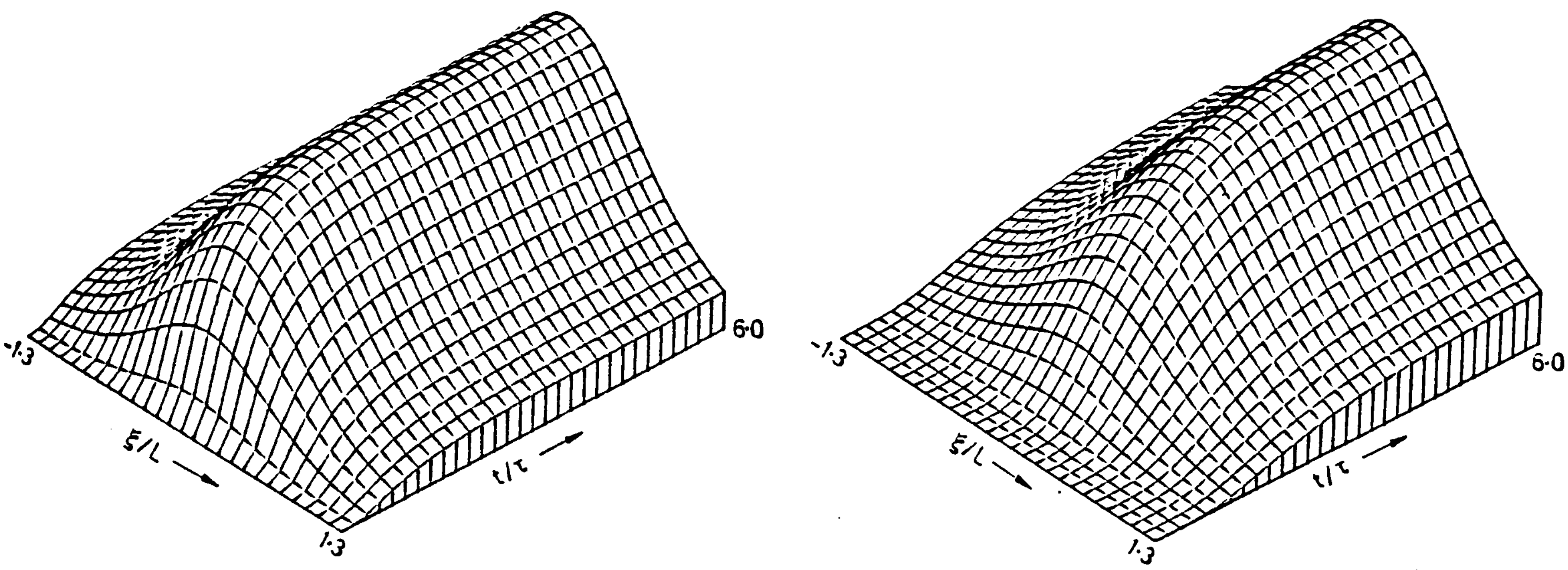

(a) (b)

Figure 5.11. Isometric surface plots showing the evolution of the contrast as a function with time after beam switch on for a point defect in a semi-infinite Schottky barrier when $\alpha L = 0.4$, $c = 0.5L$ and defect depths of (a) $d = L$ and (b) $d = 3L$.

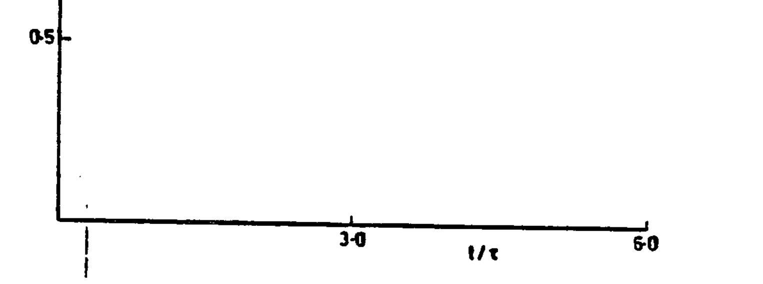

Figure 5.12. The variation of the half width of the contrast function as a function of time after the light beam is turned on. The curves shown are for various values of defect depth and for the case when $\alpha L = 0.4$ and $c = 0.5L$.

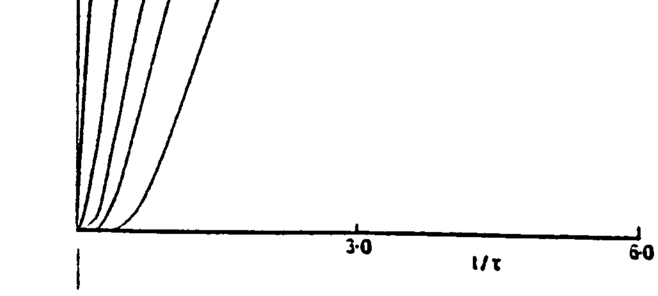

Figure 5.13. The variation of the maximum contrast $C(0, t)$ as a function of time after carrier injection for the case when $\alpha L = 0.4$ and $c = 0.5L$. The curves are shown for various defect depths and are normalised to unity at the steady state.

5.5 Conclusions

General expressions have been derived which give the time dependent induced minority carrier distribution and photocurrent in a semi-infinite Schottky barrier diode due to focussed light excitation. It was shown that the effects of beam focussing did not greatly effect the form of the junction current. Two methods for measuring the minority carrier lifetime have been suggested; one in which the photocurrent decay is measured after excitation with a short light pulse, and another where the phase shift between the junction current and sinusiodal excitation is monitored. It was shown that neither of the techniques suggested rely on having an accurate knowledge of the spatial form of the generation function, and so the simpler decaying Gaussian or decaying point source approximations of Chapter 3 can often be reliably used to model the focussed light excitation.

A parameter termed the *time dependent information depth* was introduced and defined as the depth, d, within which the majority (set as 90%) of the photoinduced minority carriers exist. The variation of the information depth as a function of time after beam "switch-on" has been considered, and it was shown that at high absorption in the steady state limit a lower bound can be put on d of $d = 2.3L$, where L is the minority carrier diffusion length, which is in good agreement with previous work [7 and Chapter 3].

General expressions which give the OBIC contrast obtained due to the presence of a defect in a semi-infinite Schottky barrier diode when illuminated with a time varying light beam were also derived. It was shown that the resolution of the OBIC technique is a function of time after beam switch-on and that, by taking data at specific times, an improved resolution OBIC image may be produced. The special case of laser excitation has been considered, although it should be noted that the general trends apply equally well to the electron beam case.

CHAPTER 6: SCAN SPEED EFFECTS

6.0 Introduction

The use of scanning optical or electron microscopes in semiconductor device characterization is now a well accepted technique, with various device goemmetries being used to yield information about the semiconducting sample under test [1,2,3]. One common device configuration is shown in Figure (6.1) where the electron or light beam induced carriers are injected some distance, ξ, away from a p-n junction located in the $x = 0$ plane. The induced junction current is then measured as a function of scan position and attempts are made to extract material parameters, such as the minority carrier lifetime or diffusion length, from the data [4,5,6,7].

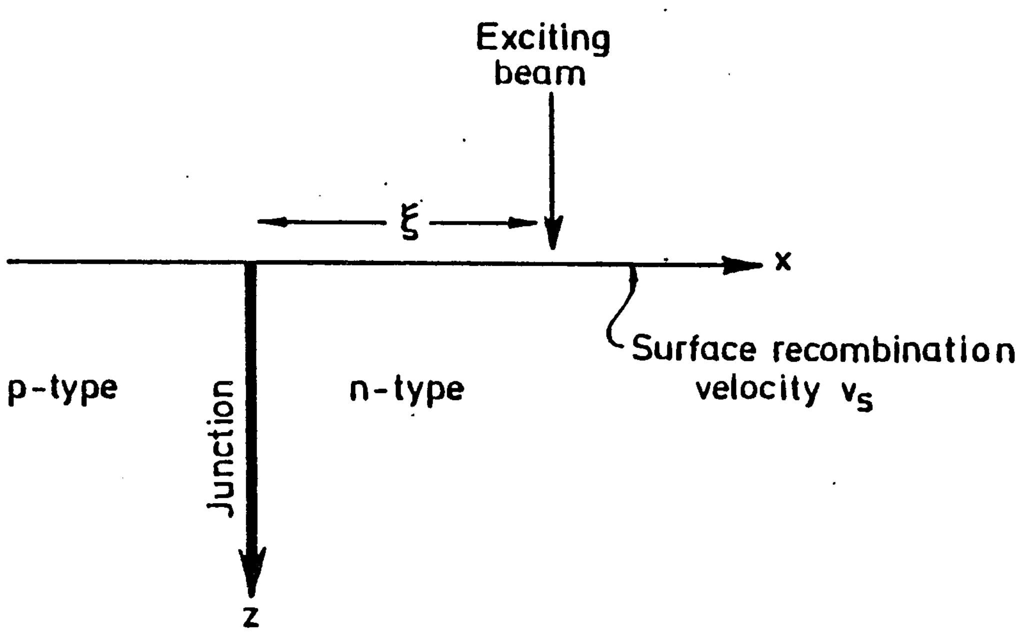

Figure 6.1. Schematic representation of a p-n juction which is perpendicular to the semiconductor surface.

Early analyses [4] neglected the role of the surface recombination velocity and merely assumed that the current, $I(\xi)$, varied with the junction-beam separation, ξ, as

$$I(\xi) = I_0 \exp(-\xi/L), \tag{6.1}$$

where L is the minority carrier diffusion length. The effect of the surface recombination velocity, v_s, was taken into account by Van Roosbroeck [8] who gave the Green's function for a semi-infinite medium bounded by a surface characterized by the recombination velocity. Van Roosbroeck's analysis reproduced the results first formulated by Bryan [9,10], and later others [11,12], for the equivalent heat conduction problem [13 p.358]. Specialisation to the cases where electrons or light constitute the exciting beam were given by Berz and Kuiken [5] and Hu and Drowley [6] respectively. All of these analyses essentially demostrated that the surface recombination velocity plays an important role in determining the form of the detected current versus scan position curve near the collecting junction, and that it is not until $\xi \gg L$ that the shape becomes independent of v_s, following an exponential form, allowing the diffusion length to be obtained from the decay rate.

However, the vast majority of these measurements are taken in *scanning* instruments but none of the analyses consider the speed at which the exciting beam is scanned across the specimen surface and the effect this might have on the collected current. Indeed the only mention of scan speed effects, to our knowledge, was given in 1954 by Adams [14]. DiStefano [15] necessarily includes scan speed effects in the analysis of the capacitive detection scheme in his scanning surface photo-voltage system, although this is quite different from the situations that we are considering here. The neglect of the scan speed is perfectly resonable at low scanning rates, however we have noticed scan speed dependent effects when examining power transistors in our scanning optical microscope and, as more real time imaging systems are developed, it becomes increasingly important to understand how the scan speed can effect the *magnitude* of the beam induced current, as well as the *shape* of the beam induced current line scan across the surface of a device. The scan speed can also be important in systems where a photographic record of an image is made by using a much slower scan speed than for ordinary examination since it is possible for the images to differ considerably in detail. We should note here that scan speeds of $250m/sec$ can be realised with TV rate scanning in scanning optical microscopes using rotating mirror wheels or acoustic optic deflectors [16].

In the following, therefore, we will analyse the form of the junction current, as a function of the scan velocity, obtained by scanning a light beam across the p-n geomettry shown in Figure (6.1). We then extend the analysis and consider the form of the junction current, as a function of scan velocity, for the semi-infinite Schottky barrier geometry of Chapters 4 and 5, and show that, as well as affecting the magnitude of the beam induced current, the scan speed can also modify the form of the contrast curves obtained when an electrically active defect close to the surface is scanned over. Finally, the results of an experimental investigation into the effects of scan speed on beam induced currents are presented.

6.1 Analysis for Perpendicular Junctions

The beam induced junction current for the geometry shown in Figure (6.1) can be found via the injected minority carrier distribution, $\Delta p(\mathbf{r},t)$, as in previous Chapters. Although here the problem has no radial symmetry and so a cartesian coordinate system is used, in which the time dependent diffusion equation can be written,

$$D\nabla^2\Delta p(x,y,z,t) - \frac{\Delta p(x,y,z,t)}{\tau} + g_{\rm v}(x,y,z,t) = \frac{\partial}{\partial t}\Delta p(x,y,z,t), \qquad (6.2)$$

where $g_{\rm v}(x,y,z,t)$ represents the generation function due to the *moving* beam. The boundary conditions for the geometry of Figure (6.1) can be written,

$$D\frac{\partial}{\partial z}\Delta p(x,y,z,t)\Big|_{z=0} = v_s\Delta p(x,y,z,t)\Big|_{z=0} \qquad (6.3)$$

and,

$$\Delta p(x,y,z,t)\Big|_{x=0} = 0, \qquad (6.4)$$

where Equation (6.3) characterizes the surface at $z = 0$ by introducing a surface recombination velocity, v_s, and Equation (6.4) takes account of the p-n junction in the $x = 0$ plane. Initially we shall find the solution for the semi-infinite media and hence ignore the boundary condition given in Equation (6.4). As in the previous Chapters we shall adopt a Green's function approach to the problem, so that the time dependent Green's function, $G(x|x_0,y|y_0,z|z_0,t|t_0)$, is given by the solution of,

$$D\nabla^2 G(x|x_0,y|y_0,z|z_0,t|t_0) - \frac{G(x|x_0,y|y_0,z|z_0,t|t_0)}{\tau} + \delta(x-x_0)\delta(y-y_0)\delta(z-z_0)\delta(t-t_0) = \frac{\partial}{\partial t}G(x|x_0,y|y_0,z|z_0,t|t_0), \qquad (6.5)$$

where the point source is taken to be located at (x_0,y_0,z_0,t_0). Equation (6.5) is simply that solved by Bryan [9] and others (e.g., [8,11,12]) and has a solution, which satisfies the boundary condition in Equation (6.3), given by

$$G(x|x_0,y|y_0,z|z_0,t|t_0) = \frac{\exp(-(t-t_0)/\tau)}{[4\pi D(t-t_0)]^{3/2}}\exp\left[-\frac{(x-x_0)^2+(y-y_0)^2}{4D(t-t_0)}\right] \left\{\exp\left[-\frac{(z-z_0)^2}{4D(t-t_0)}\right] + \exp\left[-\frac{(z+z_0)^2}{4D(t-t_0)}\right] - \frac{2S}{L}\int_0^\infty \exp\left(-\frac{S\rho}{L}\right)\exp\left[-\frac{(z+z_0+\rho)^2}{4D(t-t_0)}\right]d\rho\right\}, \qquad (6.6)$$

where S is a normalised surface recombination velocity given by , $S = v_s/v_D$ with v_D being the diffusion velocity, defined as $v_D = L/\tau$, and L is the diffusion length.† The

† Note that this definition differs from the normalised surface recombination velocity s, used in the previous Chapters, by the factor L, that is $S = sL$. Here the surface recombination velocity is normalised with respect to the diffusion velocity, v_D, to avoid confusion since later in this Chapter we also normalise the scan velocity with respect to v_D.

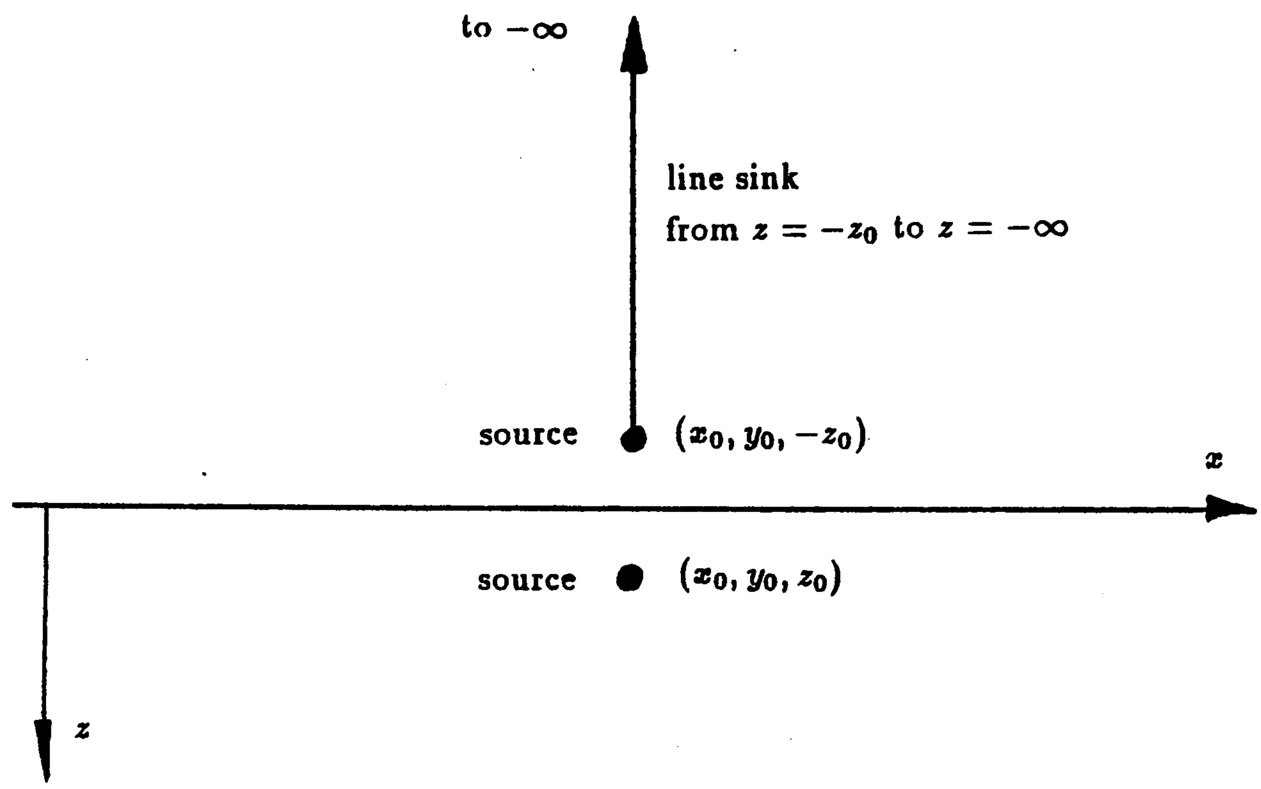

Figure 6.2. A graphical representation of the Green's function for the semi-infinite media, given in Equation (6.6), showing the two point sources at (x_0, y_0, z_0) and $(x_0, y_0, -z_0)$ and the line sink extending form $z = -z_0$ to $z = -\infty$.

Green's function in Equation (6.6) can be represented physically in terms of a *source* and *sink* distribution, as commonly used in electrostatic and heat conduction problems [13 p.255]. The *source* and *sink* distribution is shown schematicaly in Figure (6.2).

The first term in the large "curly" brackets in Equation (6.6) represents the source term at (x_0, y_0, z_0), the second term represents the image source, reflected in the $z = 0$ surface, at $(x_0, y_0, -z_0)$, and the third term can be thought of as representing a line *sink*‡ extending from $z = -z_0$ to $z = -\infty$. The total strength of the line sink is a function of the surface recombination velocity such that, in the special case of zero surface recombination velocity, the source and sink distribution reduces to a *source* at (x_0, y_0, z_0) together with an image *source* at $(x_0, y_0, -z_0)$, and conversely, in the case of infinite surface recombination velocity the ditribution reduces to a *source* at (x_0, y_0, z_0) and an image *sink* at $(x_0, y_0, -z_0)$.

The effect of moving the beam at some velocity, v, can now be taken into account by introducing a moving source term relating the space and time variables. Such that, if we choose to scan in the positive x direction, the point of injection (x_0, y_0, z_0, t_0) becomes $(x_0 + v[t - t_0], y_0, z_0, t_0)$. The time dependent Green's function, due to the moving

‡ **A *sink* as used here simply means a source whose strength is negative.**

source, can then be found from Equation (6.6) via this coordinate transformation as,

$$G(x|x_0 + v[t - t_0], y|y_0, z|z_0, t|t_0). \tag{6.7}$$

If we assume that the beam intensity is constant in time, and not effected by the scanning, the temporal form of the generation function can be taken as a constant of strength unity and so, if we begin scanning at $t = 0$, the scan speed dependent Green's function at time t is given as the integral of Equation (6.7) from $t_0 = 0$ to $t_0 = t$, that is,

$$G_v(x|x_0, y|y_0, z|z_0, t) = \int_0^t G(x|x_0 + v[t - t_0], y|y_0, z|z_0, t|t_0)\, dt_0. \tag{6.8}$$

The steady state form of the *scan speed dependent* Green's function can then be found by simply letting the upper limit of the integral in Equation (6.8) tend to ∞, giving

$$G_v(x|x_0, y|y_0, z|z_0) = \int_0^\infty G(x|x_0 + v[t - t_0], y|y_0, z|z_0, t|t_0)\Big|_{t\to\infty} dt_0. \tag{6.9}$$

Using the form of the time dependent Green's function in Equation (6.6) it is straightforward to evaluate Equation (6.9) using the result [17],

$$\int_0^\infty \exp\left[-\left(t + \frac{a^2}{4t}\right)\right] = 2\sqrt{\pi}\,\frac{\exp(-a)}{a}, \tag{6.10}$$

to give,

$$\begin{aligned} G_v(x|x_0, y|y_0, z|z_0) = \frac{1}{4\pi D} \exp\left(\nu\frac{(x - x_0)}{L}\right) & \left\{ \frac{\exp\left[-\sqrt{(x-x_0)^2 + (y-y_0)^2 + (z-z_0)^2}/\mu L\right]}{\sqrt{(x-x_0)^2 + (y-y_0)^2 + (z-z_0)^2}} \right. \\ & + \frac{\exp\left[-\sqrt{(x-x_0)^2 + (y-y_0)^2 + (z+z_0)^2}/\mu L\right]}{\sqrt{(x-x_0)^2 + (y-y_0)^2 + (z+z_0)^2}} \\ & \left. - \frac{2S}{L}\int_0^\infty \exp\left(-\frac{S\rho}{L}\right) \frac{\exp\left[-\sqrt{(x-x_0)^2 + (y-y_0)^2 + (z+z_0+\rho)^2}/\mu L\right]}{\sqrt{(x-x_0)^2 + (y-y_0)^2 + (z+z_0+\rho)^2}}\, d\rho \right\}. \end{aligned} \tag{6.11}$$

where ν is a normalised scan velocity given as $\nu = v/2v_D$ and $\mu = (1 + \nu^2)^{-1/2}$. Equation (6.11) is the *steady state, scan speed dependent* Green's function for the semi-infinite media. It is clear that by letting the scan velocity $v \to 0$ in Equation (6.11) we return to the steady state Green's function given previously [8].

Using the form of Equation (6.11) it is now possible to calculate the scan speed dependent induced minority carrier distribution, $\Delta p_v(x, y, z)$, due to the scanning light beam. Assuming that the width of the exciting beam is small compared to the diffusion length, the generation function, $g(x,y,z)$, is given from Equation (3.76) in the limit as the Gaussian beam width, c, tends to zero that is*

$$g(x,y,z) = \alpha g_0 \, \delta(x-\xi)\delta(y)\exp(-\alpha z), \tag{6.12}$$

where α is the intensity absorption coefficient, and the scan position is given by ξ as in Figure (6.1). We can fold the Green's function of Equation (6.11) with this source term by noting that the integral in Equation (6.11) represents, as is shown in Figure (6.2), a line sink extending from $z = -z_0$ to $z \to -\infty$, which can be thought of as a continuous series of point sinks of strengths $(2S/L)\exp\left[-S(\rho - z_0)/L\right]$ for $\rho > z_0$. Thus, integrating one these of sinks against the source term given in Equation (6.12) gives,

$$\begin{aligned} -\frac{2S\alpha g_0}{L}\exp\left(-\frac{S\rho}{L}\right)\int_0^{\rho}\exp(-\alpha z_0)\exp\left(\frac{Sz_0}{L}\right)dz_0 \\ = -\frac{2S\alpha g_0}{(S-\alpha L)}\left[\exp(-\alpha\rho) - \exp\left(-\frac{S\rho}{L}\right)\right]. \end{aligned} \tag{6.13}$$

Equation (6.13) gives an expression for the strength of the image sink distribution as a function of the sink position ρ. The full expression for the induced minority carrier distribution in the semi-infinite media is given from Equations (6.11), (6.12) and (6.13) as

$$\begin{aligned} \Delta p_v(x,y,z) =& \frac{\alpha g_0}{4\pi D}\exp\left[\frac{\nu(x-\xi)}{L}\right] \\ & \left\{\int_0^{\infty}\exp(-\alpha z_0)\frac{\exp\left[-\sqrt{(x-\xi)^2+(y-y_0)^2+(z-z_0)^2}/\mu L\right]}{\sqrt{(x-\xi)^2+(y-y_0)^2+(z-z_0)^2}}dz_0\right. \\ & + \int_0^{\infty}\exp(-\alpha z_0)\frac{\exp\left[-\sqrt{(x-\xi)^2+(y-y_0)^2+(z+z_0)^2}/\mu L\right]}{\sqrt{(x-\xi)^2+(y-y_0)^2+(z+z_0)^2}}dz_0 \\ & - \frac{2S}{(S-\alpha L)}\int_0^{\infty}\left(\exp(-\alpha\rho) - \exp\left(-\frac{S\rho}{L}\right)\right) \\ & \left.\frac{\exp\left[-\sqrt{(x-\xi)^2+(y-y_0)^2+(z+\rho)^2}/\mu L\right]}{\sqrt{(x-\xi)^2+(y-y_0)^2+(z+\rho)^2}}d\rho\right\}. \end{aligned} \tag{6.14}$$

Now, we wish to model the p-n junction geometry shown in Figure (6.1) and so we must take account of the presence of the junction at $x = 0$. This can be done, again by use of the method of images, by introducing a *sink* distribution at $(-\xi, y_0, z_0)$ corresponding

This is simply the decaying point source approximation as discussed in Chapter 3, see Chapter 3 references [10,11,12].

to the *source* distribution at (ξ, y_0, z_0), given in Equation (6.14). The distribution introduced at $(-\xi, y_0.z_0)$ has to be a sink to ensure that the induced minority carrier distribution is zero in the $x = 0$ plane, such that the boundary condition of Equation (6.4) is satisfied. This sink distribution, $\Delta p'_{\mathrm{v}}(x,y,z)$, can be written simply as

$$\Delta p'_{\mathrm{v}}(x,y,z) = -\Delta p_{-\mathrm{v}}(x,y,z)\Big|_{\xi \to -\xi} \tag{6.15}$$

where it should be noted that the sink has a *negative* scan velocity since it is the mirror image, in the $x = 0$ plane, of the source term which has a *positive* scan velocity. The full expression for the induced minority carrier distribution, $\Delta P_{\mathrm{v}}(x,y,z)$, for the geometry of Figure (6.1) can now be written directly as

$$\Delta P_{\mathrm{v}}(x,y,z) = \Delta p_{\mathrm{v}}(x,y,z) + \Delta p'_{\mathrm{v}}(x,y,z). \tag{6.16}$$

It is straightforward to evaluate Equation (6.16) numerically and Figure (6.3) shows isometric surface plots of the injected minority carrier distribution, $\Delta P_{\mathrm{v}}(x,y,z)$, for the case when $\alpha = 0.4\mu m^{-1}$, $L = 5.0\mu m$ and $S \to 0$ in the low scan speed limit of $v \to 0$.

The surface plots as shown in Figure (6.3) are useful to obtain a "feel" for the shape of distribution, and, for example, it can be seen from the plots that the boundary condition of zero carriers at the $x = 0$ junction is satisfied. However, to see the effect of the scan speed it is easier to consider contour plots as shown in Figure (6.4). Figure (6.4a) shows the injected distribution for a scan velocity of $v = +2v_D$, that is scanning away from the junction at $x = 0$, and Figure (6.4b) is for a scan velocity of $v = -2v_D$. It is clear from Figure (6.4) that the carriers tend to bunch up in front of the advancing probe and leave a rather spread out distribution in it's wake.

We are now in a position to calculate the diffusion current collected by the p-n junction in the $x = 0$ plane which is given, as a function of scan position and velocity, as

$$I(\xi) = qD \int_{-\infty}^{\infty} \int_{0}^{\infty} \frac{\partial}{\partial x} \Delta P_{\mathrm{v}}(x,y,z)\Big|_{x=0} dz dy. \tag{6.17}$$

Using the form of $\Delta p_{\mathrm{v}}(x,y,z)$ in Equation (6.14) we can perform the y integral using the relationship [18]

$$\int_{-\infty}^{\infty} \frac{\exp\left[-\sqrt{b^2+y^2}/\mu L\right]}{\sqrt{b^2+y^2}}\, dy = 2K_0\left(\frac{b}{L}\right), \tag{6.18}$$

where K_0 is a modified Bessel function of the second kind and zero order. Using this together with the Bessel function relationship [18],

$$\frac{dK_0(x)}{dx} = -K_1(x), \tag{6.19}$$

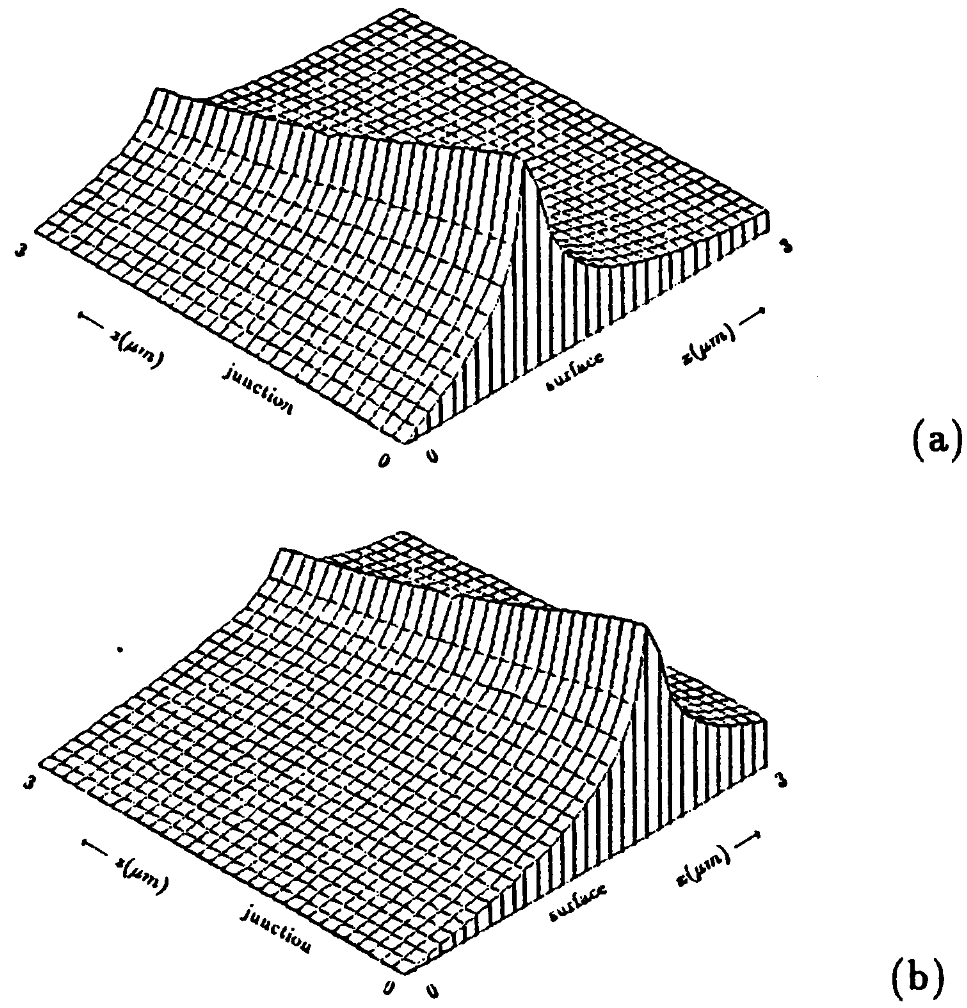

Figure 6.3. Isometric surface plots of the induced minority carrier distribution in the region of a p-n junction for the low scan speed limit and when $\alpha = 0.4\mu m^{-1}$, $L = 5.0\mu m$, $S \rightarrow 0$ and (a) $\xi = 1.0\mu m$ and (b) $\xi = 2.0\mu m$.

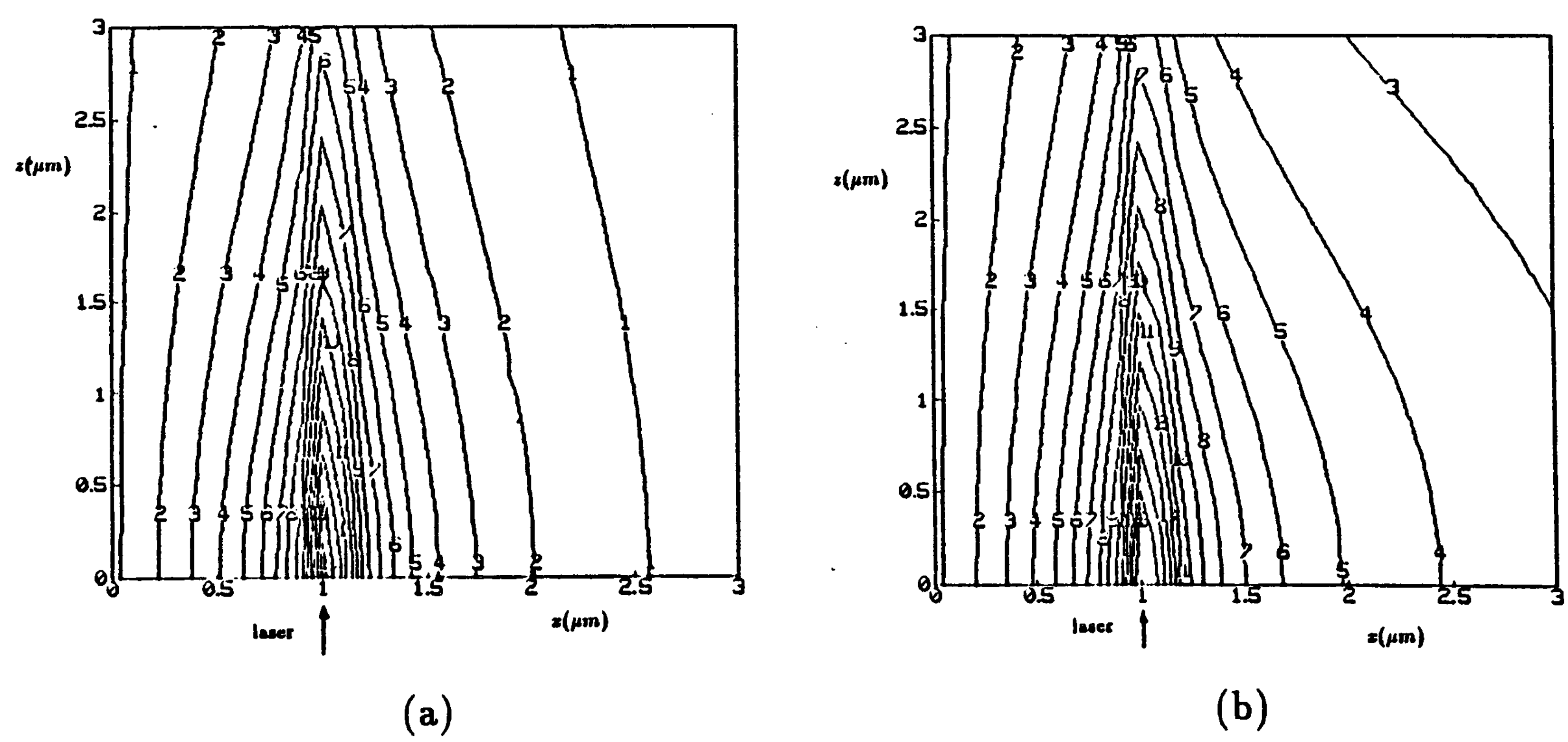

Figure 6.4. Contour plots of the induced minority carrier distribution for the case when $\alpha = 0.4\mu m^{-1}$, $L = 5.0\mu m$, $S \rightarrow 0$ and (a) a scan velocity of $v = +2v_D$ and (b) $v = -2v_D$. The contour numbering is such that a high contour number corresponds to a high carrier concentration and the contours are the same in (a) and (b).

where K_1 is a modified Bessel function of the second kind and of order one, the junction current can be written,

$$\begin{aligned}
I(\xi) = \frac{\alpha q g_0}{\pi\mu D L}\exp\left(-\frac{\nu\xi}{L}\right)\Bigg\{\Bigg[\int_0^\infty\int_0^\infty \exp(-\alpha z_0)\Bigg\{&\frac{K_1\left[\sqrt{\xi^2+(z-z_0)^2}/\mu L\right]}{\sqrt{\xi^2+(z-z_0)^2}} \\
&+\frac{K_1\left[\sqrt{\xi^2+(z+z_0)^2}/\mu L\right]}{\sqrt{\xi^2+(z+z_0)^2}}\Bigg\}\,dz_0dz \\
-\frac{2S\xi}{(S-\alpha L)}\int_0^\infty\int_0^\infty\left[\exp(-\alpha\rho)-\exp\left(-\frac{S\rho}{L}\right)\right]&\frac{K_1\left[\sqrt{\xi^2+(z+\rho)^2}/\mu L\right]}{\sqrt{\xi^2+(z+\rho)^2}}\,d\rho dz\Bigg] \\
-\nu\mu\Bigg[\int_0^\infty\int_0^\infty\exp(-\alpha z_0)\Big\{&K_0\left[\sqrt{\xi^2+(z-z_0)^2}/\mu L\right] \\
&+K_0\left[\sqrt{\xi^2+(z+z_0)^2}/\mu L\right]\Big\}\,dz_0dz \\
-\frac{2S}{(S-\alpha L)}\int_0^\infty\int_0^\infty\left[\exp(-\alpha\rho)-\exp\left(-\frac{S\rho}{L}\right)\right]&K_0\left[\sqrt{\xi^2+(z+\rho)^2}/\mu L\right]\,d\rho dz\Bigg]\Bigg\}
\end{aligned} \tag{6.20}$$

This rather complicated result can be simplified by reducing the double integrals to single integrals by integrating by parts using,

$$\begin{aligned}
&\int_0^\infty\int_0^\infty f(\xi,z\pm z_0)\exp(-\alpha z_0)\,dz_0dz \\
&\qquad = \frac{1}{\alpha}\int_0^\infty f(\xi,z)\,dz \mp \frac{1}{\alpha}\int_0^\infty f(\xi,z_0)\exp(-\alpha z_0)\,dz_0
\end{aligned} \tag{6.21}$$

where,

$$f(\xi,z\pm z_0) = \frac{K_1\left[\sqrt{\xi^2+(z\pm z_0)^2}/\mu L\right]}{\sqrt{\xi^2+(z\pm z_0)^2}} \qquad \text{or,} \qquad K_0\left[\sqrt{\xi^2+(z\pm z_0)^2}/\mu L\right]. \tag{6.22}$$

In Equation (6.21) we have used the symmetry in z and z_0 which allows us to write,

$$\frac{\partial}{\partial z_0}f(\xi,z\pm z_0) = \pm\frac{\partial}{\partial z}f(\xi,z\pm z_0). \tag{6.23}$$

This enables Equation (6.20) to be simplified considerably, and yields the final expression for the scan speed dependent induced junction current as,

$$\begin{aligned}
I(\xi) = \frac{2qg_0}{\pi L(S-\alpha L)}\exp\left(-\frac{\nu\xi}{L}\right)\int_0^\infty&\left\{S\exp(-\alpha\rho)-\alpha L\exp\left(-\frac{S\rho}{L}\right)\right\} \\
&\left\{\xi\frac{K_1\left[\sqrt{\xi^2+\rho^2}/\mu L\right]}{\sqrt{\xi^2+\rho^2}} - \mu\nu K_0\left[\sqrt{\xi^2+\rho^2}/\mu L\right]\right\}d\rho,
\end{aligned} \tag{6.24}$$

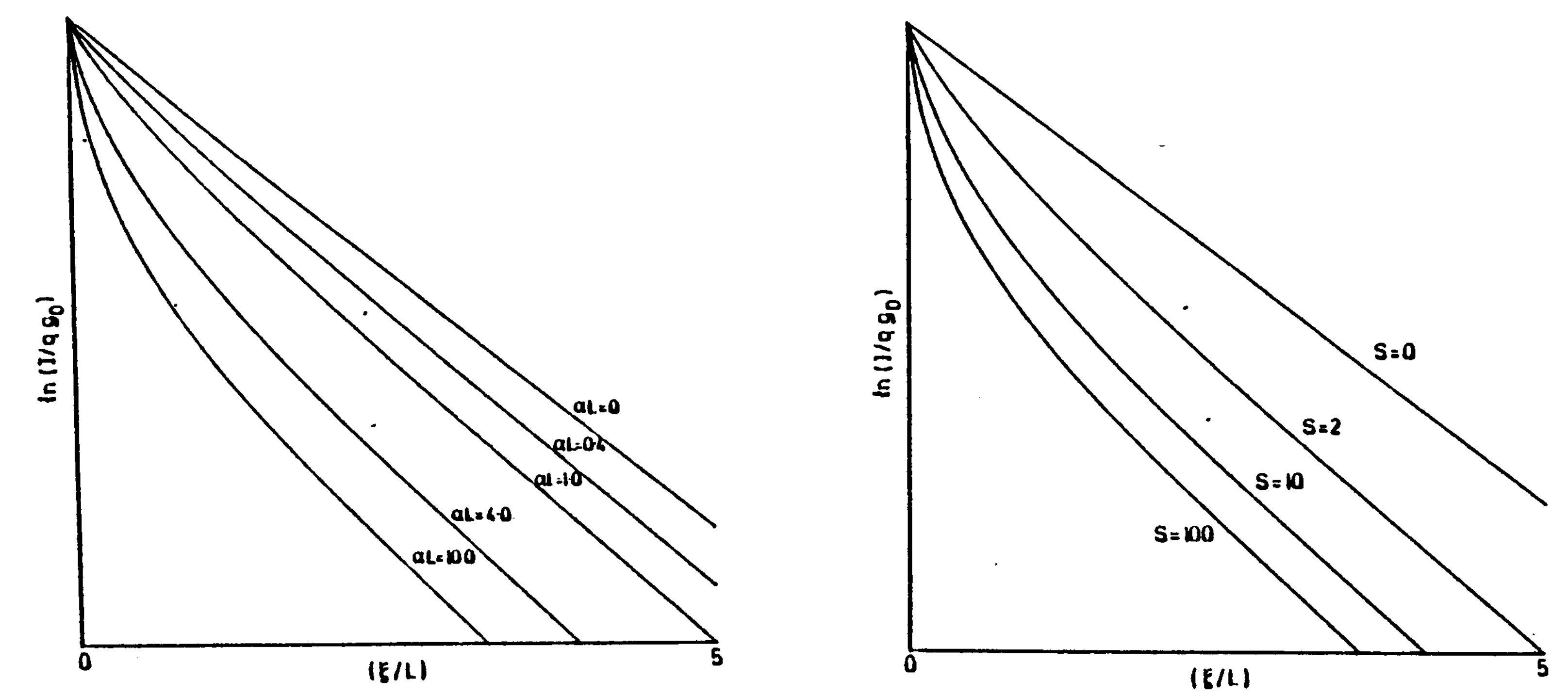

(a) (b)

Figure 6.5. The logarithm of the junction current induced by the scanning light spot as a function of junction-beam separation for the case of low scan speed and when (a) $S = 100$ and various values of the absorption coefficient, and (b) $\alpha L = 10.0$ and various values of the surface recombination velocity.

which reduces, in the low scan speed limit of $v \to 0$, to the expression previously derived by Hu and Drowley [6].

Equation (6.24) is straightforward to evaluate numerically and, before we discuss the scan-speed effects, it will be useful to consider the roles of attenuation, α, and surface recombination velocity, S. Figures (6.5a) and (6.5b) show, for the slow scan speed limit ($v \to 0$), that for increasing attenuation or recombination velocity the greater is the initial curvature of the $\ln[I_0(\xi)]$ versus position curve, and hence inacurracy in the simple $I(\xi) \sim \exp(-\xi/L)$ approximation.

The special case of either $S \to 0$ or $\alpha \to 0$ is of interest since the expression for the current in Equation (6.24) can then be reduced to

$$I(\xi) = \frac{2qg_0}{\pi L} \exp\left(-\frac{\nu\xi}{L}\right) \int_0^\infty \left\{ \xi \frac{K_1\left[\sqrt{\xi^2+\rho^2}/\mu L\right]}{\sqrt{\xi^2+\rho^2}} - \mu\nu K_0\left[\sqrt{\xi^2+\rho^2}/\mu L\right] \right\} d\rho, \qquad (6.25)$$

which may be dramatically simplified by use of the Sonine formula [18 p.417] to give,

$$I(\xi) = qg_0\mu(1-\mu\nu)\exp\left(-\frac{\xi}{L_{\text{eff}}}\right), \qquad (6.26)$$

where,

$$\frac{1}{L_{\text{eff}}} = \frac{1}{L}\left[\frac{1}{\mu} - \nu\right]$$

that is,

$$\frac{1}{L_{\text{eff}}} = \frac{1}{L}\left[\sqrt{1+\nu^2} - \nu\right]. \tag{6.27}$$

It is clear that in this case the current response is indeed of the exponential decay form, but that the "effective" diffusion length, L_{eff} is a function of both the scan speed and scan *direction* (that is, the sign of v). By taking the two extreme values of the effective diffusion length, that is the values obtained when scanning towards and away from the junction, we obtain two equations from which both the values of the diffusion coefficient, D, and lifetime, τ, can be found independently. By simple algebra we find that,

$$D = \frac{v}{(1/L_2 - 1/L_1)} \tag{6.28a}$$

and,

$$\tau = \frac{(L_1 - L_2)}{v}, \tag{6.28b}$$

where L_1 and L_2 are the values of the effective diffusion length when scanning away from and towards the junction, that is, v *positive* and *negative* respectively. The actual diffusion length is then given simply as $L = \sqrt{L_1 L_2}$. Equations (6.28a) and (6.28b) agree with those quoted by Adam [14] and illustrate an advantage of situations where the scan speed is important, since usually we have two unkowns in the diffusion equation, D and τ, and by being able to vary the scan speed, if only in direction, we have two simultaneous equations from which D and τ can be obtained independently. This is illustrated in Figure (6.6) where the effect of the scan direction on the systems response is shown when the surface recombination velocity is zero.

The relatively straightforward way of obtaining D and τ outlined above does not, of course, apply in general for nonzero S. In these more general cases the full expression of Equation (6.24) must be used and more sophisticated curve fitting routines are needed. Figures (6.7a) and (6.7b) illustrate the form of the response which will be obtained for two values of the surface recombination velocity and attenuation coefficient. It is interesting to note just how much of an effect the scan speed can have in certain circumstances.

The size and direction of the scan velocity also determines the value of the junction current, $I(\xi)$, when the beam is directly over the junction, that is $\xi = 0$, since then the current is given, from Equation (6.24) as,

$$I(0) = qg_0\mu\left[1 - \frac{2\nu}{\pi L(S-\alpha L)}\int_0^\infty \left\{S\exp(-\alpha\rho) - \alpha L\exp\left(-\frac{S\rho}{L}\right)\right\} K_0\left(\frac{\rho}{\mu L}\right)\,d\rho\right], \tag{6.29}$$

which can be further simplified by performing the integration [17] to give,

$$I(0) = qg_0\mu\left[1 - \frac{2\mu\nu}{\pi}\left(\frac{S\,h\{\alpha\mu L\} - \alpha L\,h\{\mu S\}}{s - \alpha L}\right)\right] \tag{6.30}$$

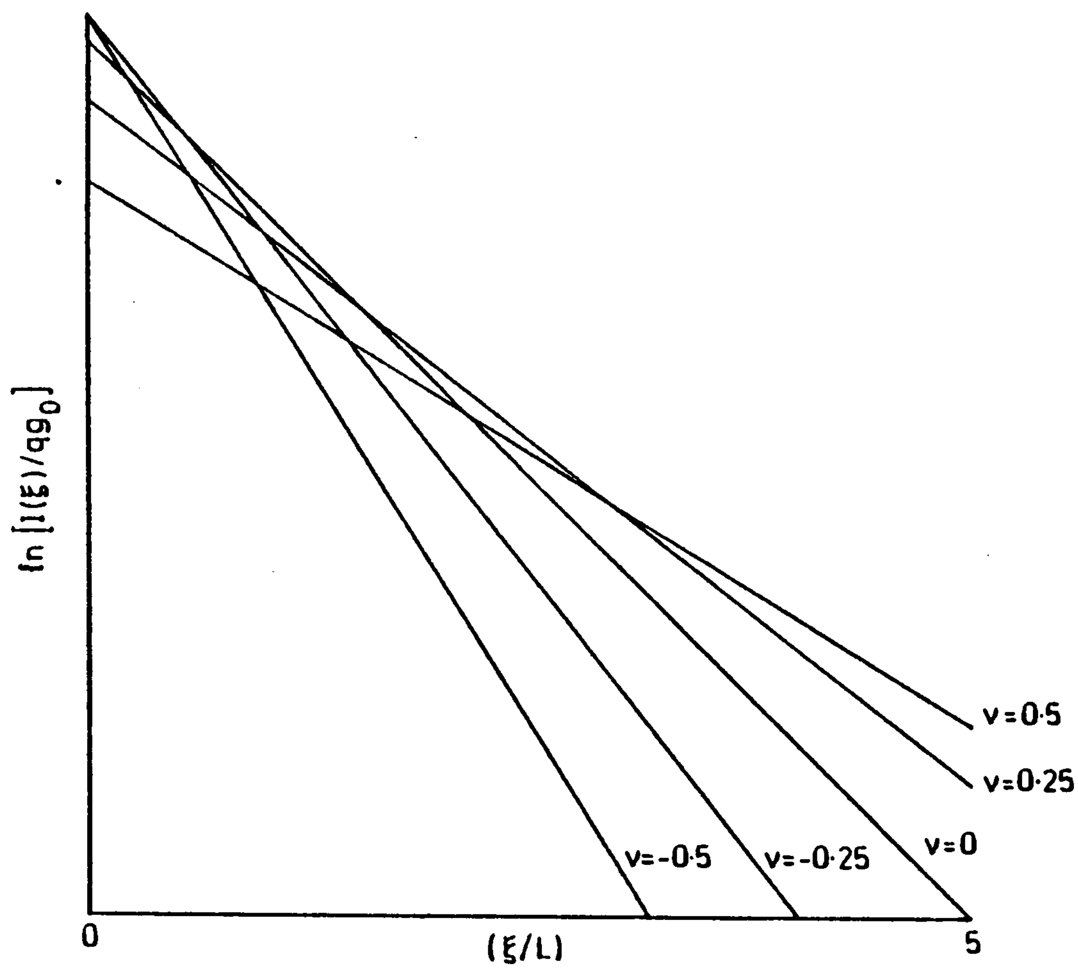

Figure 6.6. The logarithm of the photo-induced junction current as a function of beam-junction separation for various values of the normalised scan velocity, ν, and for the case when $S \rightarrow 0$.

Here the function h is defined as

$$h\{\beta\} = \begin{cases} \frac{\cos^{-1}(\beta)}{\sqrt{1-\beta^2}}, & \text{for } \beta < 1; \\ \frac{\ln\left(\beta+\sqrt{\beta^2-1}\right)}{\sqrt{\beta^2-1}} & \text{for } \beta > 1. \end{cases} \tag{6.31}$$

Equation (6.30) is plotted in Figure (6.8) where the asymmetry of the curves for negative and positive scan velocities is clearly visible. It should be noted that the curves in Figure (6.8) are normalised such that $I(0) = 1$ when the scan velocity is zero. In the special case of zero surface recombination velocity Equation (6.30) reduces to

$$I(0) = qg_0\mu(1 - \mu\nu), \tag{6.32}$$

which is plotted as the $S = 0$ curve in Figure (6.8a).

Far away from the junction, where $\xi \gg \mu L$, we may obtain an approximate expression for the rate at which the junction current decays with beam-junction separation, ξ, given in Equation (6.24), by exploiting the rate at which the Bessel functions decay as the argument increases. That is, since we are assuming $\xi \gg \mu L$ it follows that, when ρ is significantly greater than zero the argument of the Bessel functions will be very

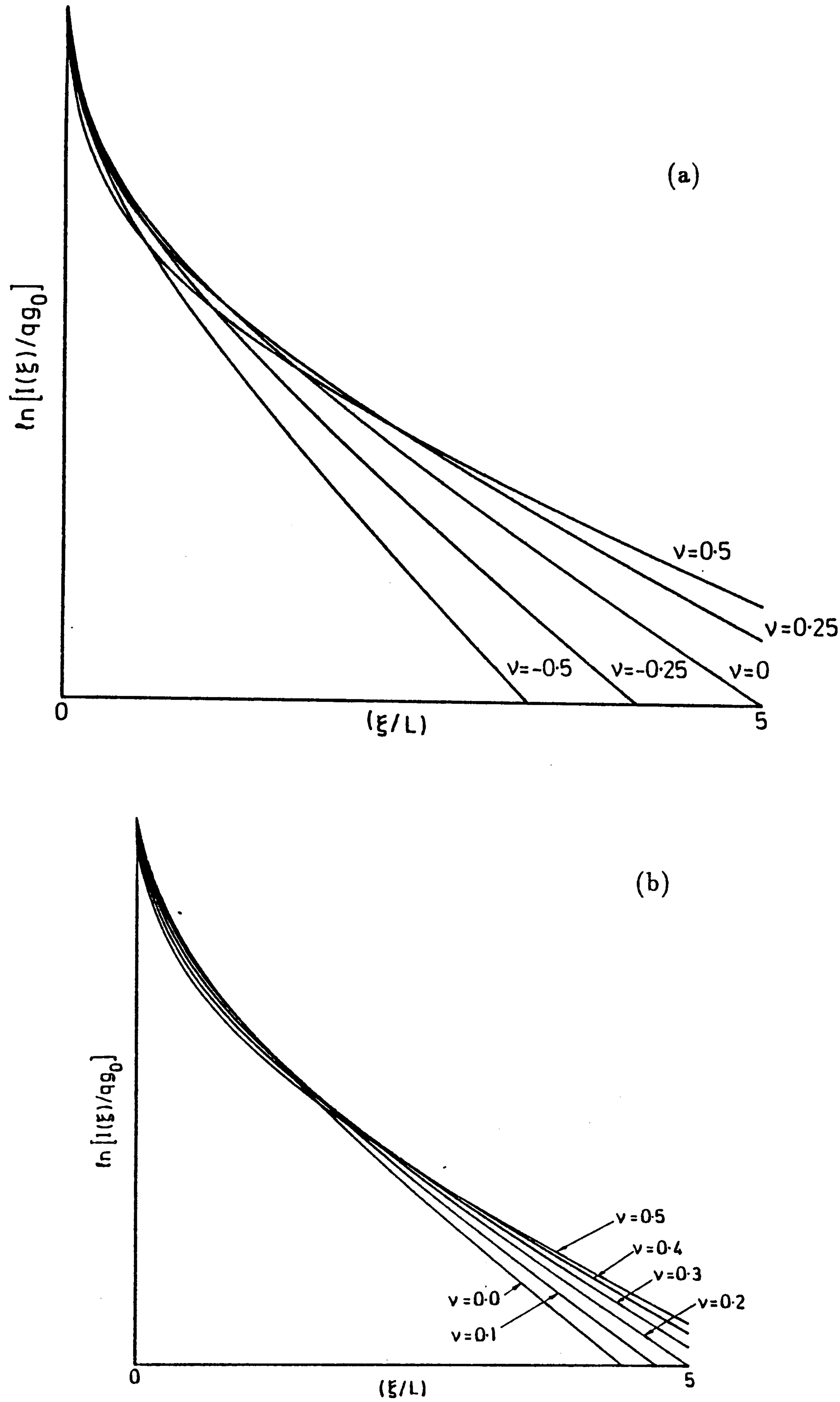

Figure 6.7. The logarithm of the junction current as a function of scan position and for various values of the normalised scan velocity when (a) $S = 10.0$ and $\alpha L = 10.0$ and (b) $S = 100.0$ and $\alpha L = 0.4$.

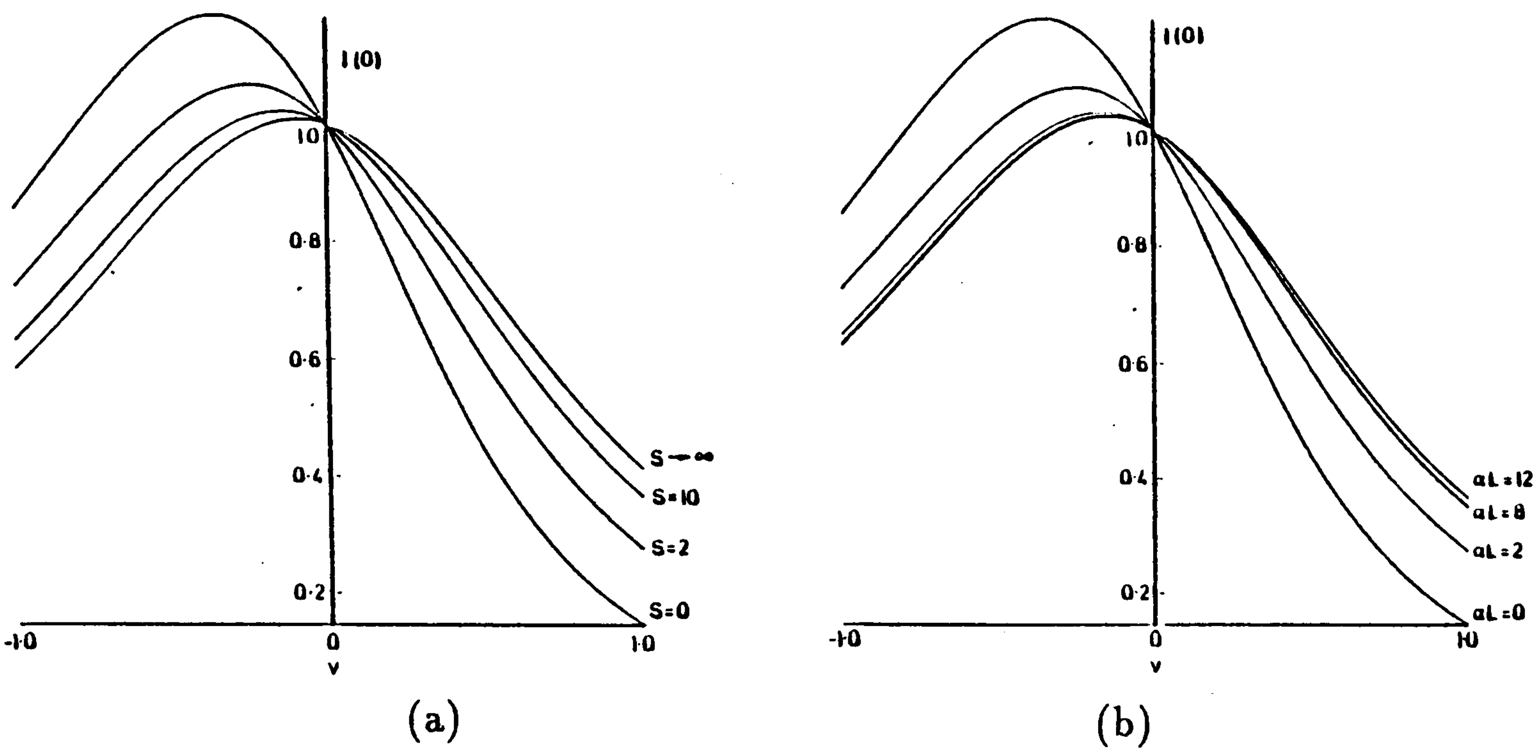

Figure 6.8. The variation of the junction current, $I(0)$, for zero beam-junction separation as a function of the normalised scan velocity ν. (a) is for various values of surface recombination velocity when $\alpha L = 12$, and (b) is for various values of the absorption coefficent when $S = 10.0$.

large, and so the integrand very small. In this case, for the Bessel functions to exist, we can make the approximation that $\sqrt{\xi^2 + \rho^2}/\mu L \sim \xi/\mu L$ which allows us to remove the Bessel functions from under the integration sign in Equation (6.24) and evaluate the resulting integral analytically to yield,

$$I(\xi) = \frac{2qg_0}{\pi L}\left(\frac{1}{\alpha L} + \frac{1}{S}\right)\exp\left(-\frac{\nu\xi}{L}\right)\left[K_1\left(\frac{\xi}{\mu L}\right) - \nu\mu K_0\left(\frac{\xi}{\mu L}\right)\right], \tag{6.33}$$

from which it is clear that the surface recombination velocity appears only as a premultiplying factor and so does *not* influence the shape of the $\ln\{I(\xi)\}$ .vs. ξ curve. If we now allow ξ to be sufficiently large such that we can make the additional approximation,

$$K_1\left(\frac{\xi}{\mu L}\right) \approx K_0\left(\frac{\xi}{\mu L}\right) \approx \sqrt{\frac{\pi\mu L}{2\xi}}\exp\left(-\frac{\xi}{\mu L}\right), \tag{6.34}$$

we can write Equation (6.33) as,

$$I(\xi) = qg_0(1 - \mu\nu)\sqrt{\frac{2L\mu}{\pi\xi}}\left(\frac{1}{\alpha L} + \frac{1}{S}\right)\exp\left(-\frac{\xi}{L_{\text{eff}}}\right), \tag{6.35}$$

where L_{eff} is given by Equation (6.27). This suggests that a plot of $\ln\left[\sqrt{\xi}\cdot I(\xi)\right]$ against ξ should be a straight line whose gradient is $1/L_{\text{eff}}$, and so if we are sufficiently far away from the junction we can use the technique described earlier to measure D and τ independently, without knowledge of the surface recombination velocity. The asymptotic expansions given in Equations (6.33) and (6.35) also suggest that in many cases it is better to plot $\ln\left[\sqrt{\xi}\cdot I(\xi)\right]$ rather than the more accepted $\ln\left[I(\xi)\right]$ when presenting results and measuring material parameters.

Figure (6.9) shows a typical plot, in the slow scan speed limit, where the Bessel function solution of Equation (6.33) is seen to be a very good approximation for $\xi/L \gg 1$. If we include scan speed effects we obtain curves as shown in Figure (6.10), again the Bessel function solution is the better overall approximation but, if we are able to take data sufficiently far from the junction, we see that the exponential approximation becomes resonably parallel to the full curve and hence a valid approximation.

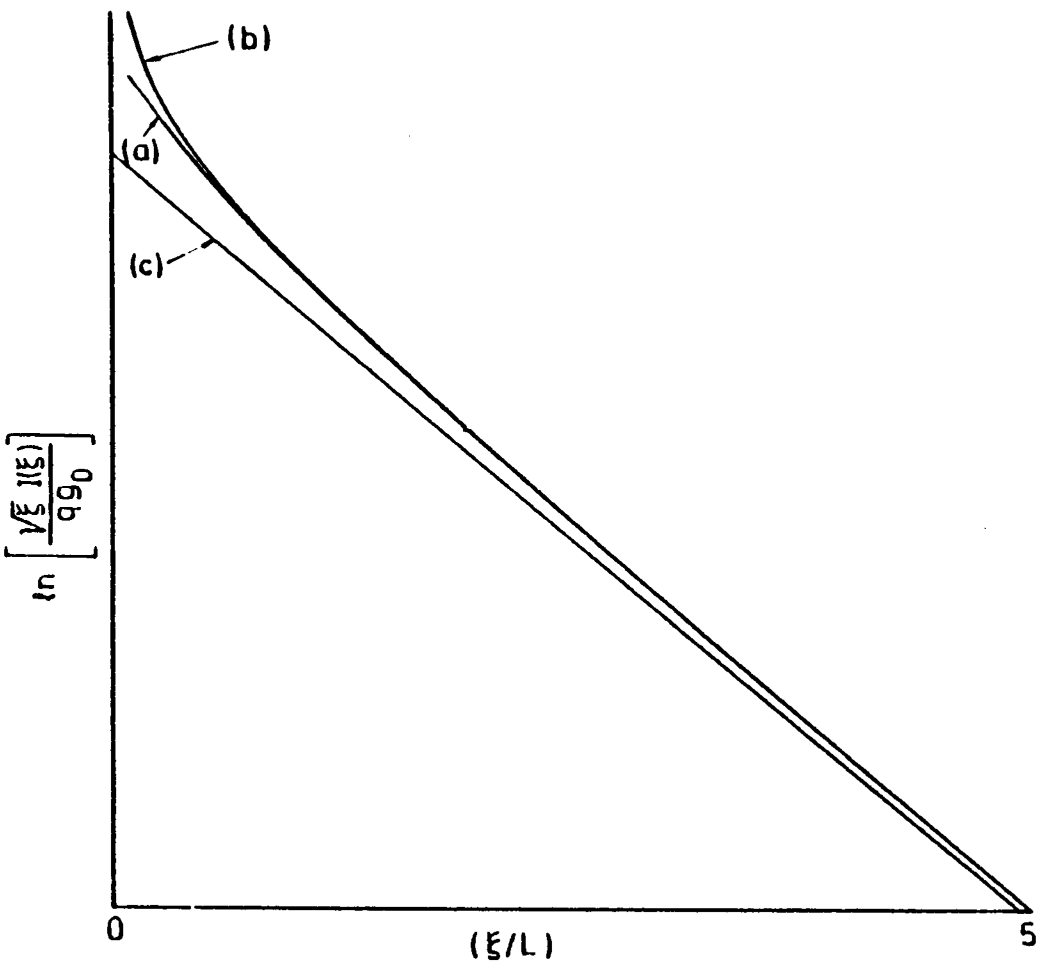

Figure 6.9. The logarithm of $\sqrt{\xi} \cdot I(\xi)$ as a function of ξ in the slow scan speed limit for the case when $S = 100$ and $\alpha L = 12$. Curve (a) is plotted from the full expression of Equation (6.24), curve (b) is the Bessel function approximation of Equation (6.33) and (c) is the exponential approximation of Equation (6.35).

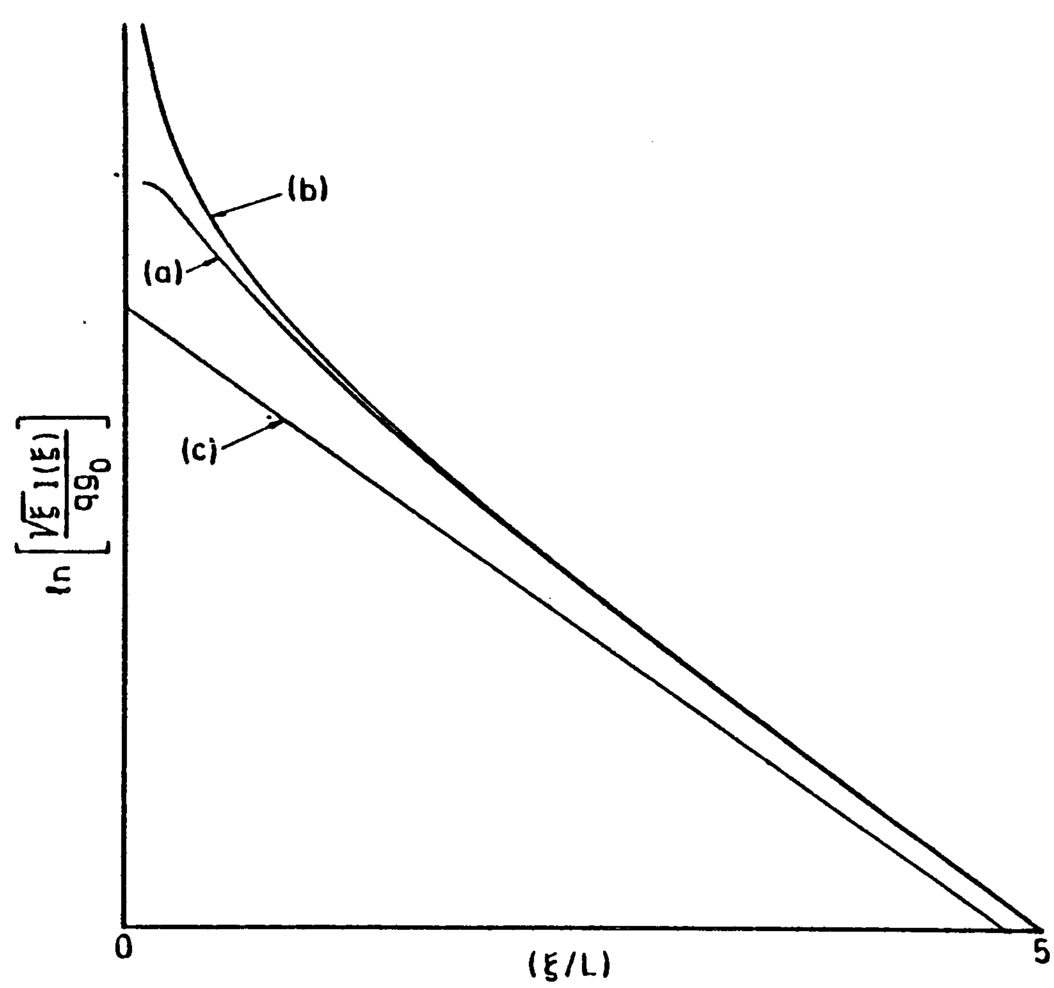

Figure 6.10. The logarithm of $\sqrt{\xi} \cdot I(\xi)$ as a function of ξ for the case when $S =$ 10.0, $\alpha L = 12.0$ and a normalised scan velocity of $\nu = 0.5$. Curve (a) is from the full expression of Equation (6.24), curve (b) is the Bessel function approximation of Equation (6.33) and (c) is the exponential approximation of Equation (6.35).

6.2 Analysis for Schottky Barrier Diodes

In the previous section the effect of the beam scan velocity on induced current measurements of semiconductors was condsidered and it was shown that, for the geometry of Figure (6.1), the rate of scanning could have a considerable effect on the form of the beam induced current. Another device which is often used for beam induced current measurements is the shallow p-n junction or Schottky barrier diode geometry, discussed in Chapters 4 and 5 in connection with steady state and time dependent beam induced current measurements. Therefore, in this section, we extend the methods of the previous section to include a scan speed dependent analysis [19] of a shallow p-n juction or Schottky barrier.

We can model the effect of the scan velocity in exactly the same way as for the perpendicular junction geometry, that is, beginning with the time dependent Green's function for the semi-infinite Schokkty barrier diode and introducing a source term moving with a velocity v. Following this technique gives the scan speed dependent Green's function, $G_v(x|x_0, y|y_0, z|z_0)$, for the Schottky barrier geometry as †

$$G_v(x|x_0, y|y_0, z|z_0) = \frac{\exp\left(\frac{\nu(x-x_0)}{L}\right)}{4\pi D}\left\{\frac{\exp\left[-\sqrt{(x-x_0)^2+(y-y_0)^2+(z-z_0)^2}/\mu L\right]}{\sqrt{(x-x_0)^2+(y-y_0)^2+(z-z_0)^2}}\right.$$
$$\left. - \frac{\exp\left[-\sqrt{(x-x_0)^2+(y-y_0)^2+(z+z_0)^2}/\mu L\right]}{\sqrt{(x-x_0)^2+(y-y_0)^2+(z+z_0)^2}}\right\}, \tag{6.36}$$

where μ and ν are as before. The scan speed dependent induced minority carrier distribution in the Schottky barrier can be found by folding Equation (6.36) with the source term. Since the form of the Green's function for this geometry is slightly simpler than in the perpendicular junction case we can use the more realistic decaying Gaussian approximation of Chapter 3, Equation (3.76), to represent the source term, rather than the decaying point source approximation as used in the previous section. Performing the integrations is straightforward, and a section, taken throught the resulting distribution in the $y = 0$ plane, is shown in the form of a contour plot in Figure (6.11).

It is clear from Figure (6.11) that, in both cases, the distribution peaks some distance below the surface, this is to be expected owing to the infinite surface recombination velocity [Chapter 3]. The main effect of the scan speed, however, is to produce an

† This is simply the Green's function of Equation (6.11) evaluated in the the limit as $S \to \infty$ since the recombination velocity at the surface junction is infinite.

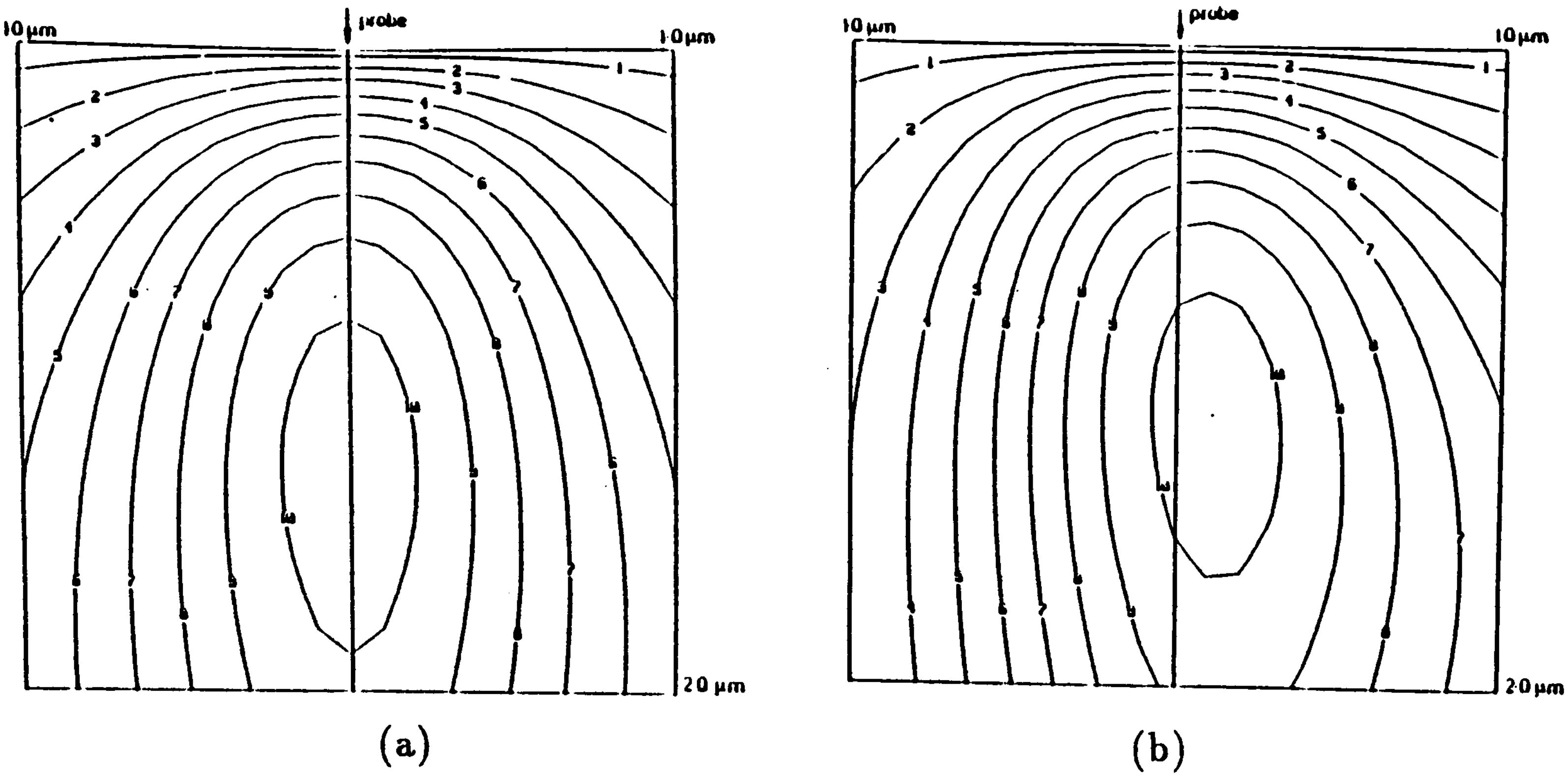

Figure 6.11. Contour plots of the photo-induced minority carrier distribution for the case when $\alpha = 0.4\mu m^{-1}$, $L = 10.0\mu m$ and a Gaussian half width of $c = 0.5\mu m$. The contour notation is such that a high contour number represents a high carrier distribution, (a) is for the low scan speed limit of $v \to 0$ and (b) is for a scan speed of $v/v_D = -1.0$ that is for the beam scanning from right to left.

asymmetric carrier distribution with the carriers tending to bunch up in front of the advancing probe and leave a rather more spread out cloud in its wake.

Having found the excess minority carrier distribution due to the scanning probe we are now in a position to calculate the beam induced diffusion current collected at the surface junction. A general expression for the diffusion current is given in Chapter 4, Equation (4.1), which in the present case reduces to Equation (5.47) of Chapter 5, from which the scan speed dependent diffusion current is found to be,

$$I_0 = \frac{\alpha q g_0}{\pi \mu L} \int_0^\infty \int_{-\infty}^\infty \exp(-\alpha z_0) \exp\left(\frac{\nu x}{L}\right) \frac{K_1\left[\sqrt{x^2 + z_0^2}/\mu L\right]}{\sqrt{x^2 + z_0^2}}\, dx z_0 dz_0, \qquad (6.37)$$

where K_1 is a first order Bessel function of the second kind. It is clear from Equation (6.37) that the lateral form of the exciting beam, in this low numerical aperture approximation, has no effect on the collected current, but, that the *magnitude* of the collected current depends on the *magnitude* of the scan velocity although not it's direction.

Figure (6.12) shows a plot of the diffusion current as a function of normalised scan velocity for a selection of diffusion lengths, from which it is clear that the photo-induced current is a strong function of the scan velocity especially at long diffusion lengths. This variation in the collected current may at first appear somewhat surprising, considering the infinite extent of the surface junction; but the junction current depends on the *gradient* of the induced minority carrier distribution at the surface and, from Figure (6.11), it is clear that this is indeed a function of the beam scan velocity.

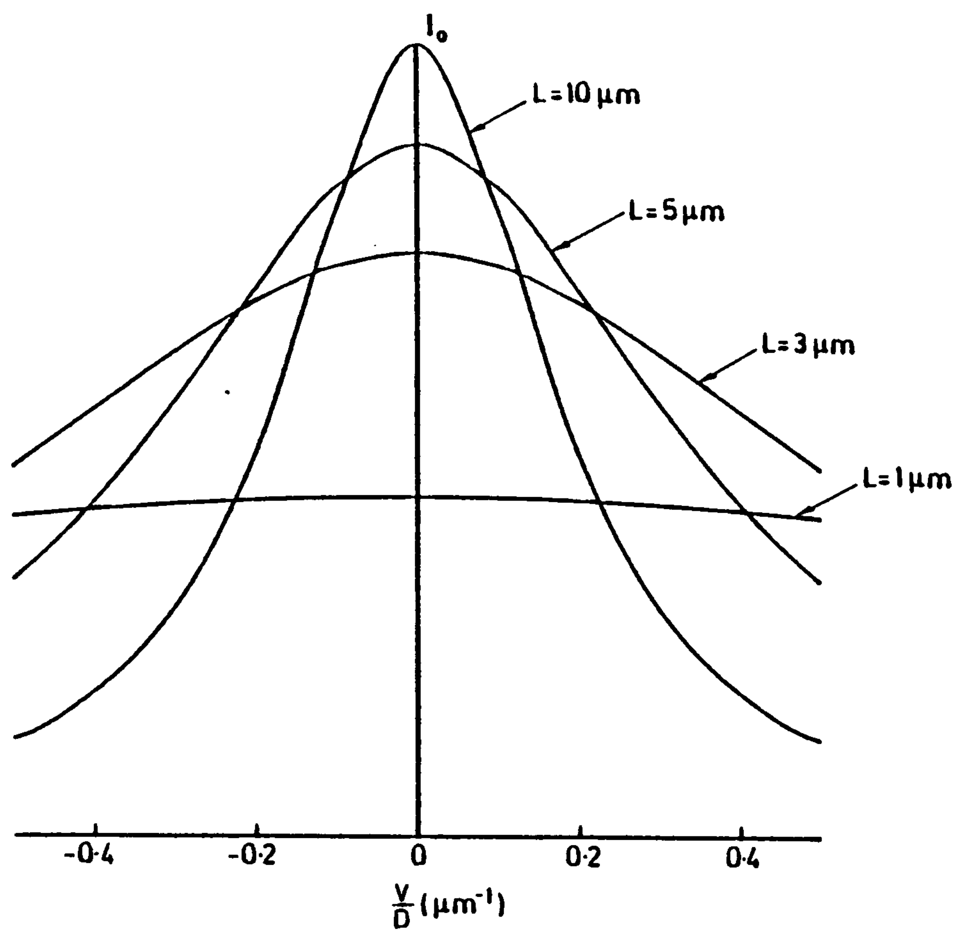

Figure 6.12. The photo-induced diffusion current collected by a semi-infinite Schottky barrier as a function of the beam scan speed for various diffusion lengths.

6.3 Effect of Scan Speed on Defect Imaging

After showing that the scan speed can effect the form of the collected photocurrent in both planar and perpendicular p-n junctions it is interesting to ask how the scan speed effects the form of the contrast obtained as an electrically active defect is imaged in the OBIC mode of the scanning optical microscope.

To investigate this effect we will consider a point defect in a semi-infinite Schottky barrier, since then we know that the modified minority carrier distribution, due to the presence of the defect, is given by the Neumann expansion to first order of the Fredholm integral equation given in Chapter 3, Equation (3.49). Since there is no radial symmetry here we can not apply the results of Chapter 3 directly, although the calculation for a point defect in the cartesian coordinate system is straightforward [19] and gives an expression for the scan speed dependent contrast, $C_v(\xi, a)$, as

$$C_v(\xi,a) = \Lambda(\nu,a)\cdot\exp\left(-\frac{\xi^2}{c^2}\right)\int_0^\infty\int_0^\infty \exp(-\alpha z_0)\exp\left(-\frac{r_0^2}{c^2}\right) I_0\left\{\left(\frac{2\xi}{c^2}+\frac{\nu}{L}\right)r_0\right\}$$
$$\left\{\frac{\exp\left[-\sqrt{r_0^2+(a-z_0)^2}/\mu L\right]}{\sqrt{r_0^2+(a-z_0)^2}} - \frac{\exp\left[-\sqrt{r_0^2+(a+z_0)^2}/\mu L\right]}{\sqrt{r_0^2+(a+z_0)^2}}\right\} r_0 dr_0 dz_0, \tag{6.38}$$

where, as before, a is the defect depth and I_0 is a modified Bessel function of the first kind and zero order. The scan position independent premultiplication factor, $\Lambda(\nu, a)$, is given by

$$\Lambda(\nu,a) = \frac{\gamma_0 a}{2\pi c^2}\cdot\frac{\int_{-\infty}^{\infty}\exp\left(-\frac{\nu x}{L}\right)\frac{K_1\left[\sqrt{x^2+a^2}/\mu L\right]}{\sqrt{x^2+a^2}}\,dx}{\int_0^\infty\int_{-\infty}^{\infty}\exp(-\alpha z_0)\exp\left(-\frac{\nu\rho}{L}\right)\frac{K_1\left[\sqrt{\rho^2+z_0^2}/\mu L\right]}{\sqrt{\rho^2+z_0^2}}\,d\rho z_0 dz_0}, \tag{6.39}$$

where ρ is an integration variable. It is clear from Equation (6.38) that for non zero scan speeds the contrast is no longer an even function of ξ, the laser-defect lateral separation, that is,

$$C_v(\xi,a) \neq C_v(-\xi,a). \tag{6.40}$$

We can also see from the argument of the Bessel function in Equation (6.38) that the direction of scanning is important. These observations suggest that, for non-zero scan speeds, the contrast curves will be asymmetric. Figure (6.13) shows the contrast curves, obtained from Equation (6.38), for a variety of scan speeds when the point defect is located $2\mu m$ below the semiconductor surface.

The asymmetry in the contrast curves is clear from Figure (6.13) as is the fact that the maximimum in the contrast does not occur directly over the defect ($\xi = 0$). This

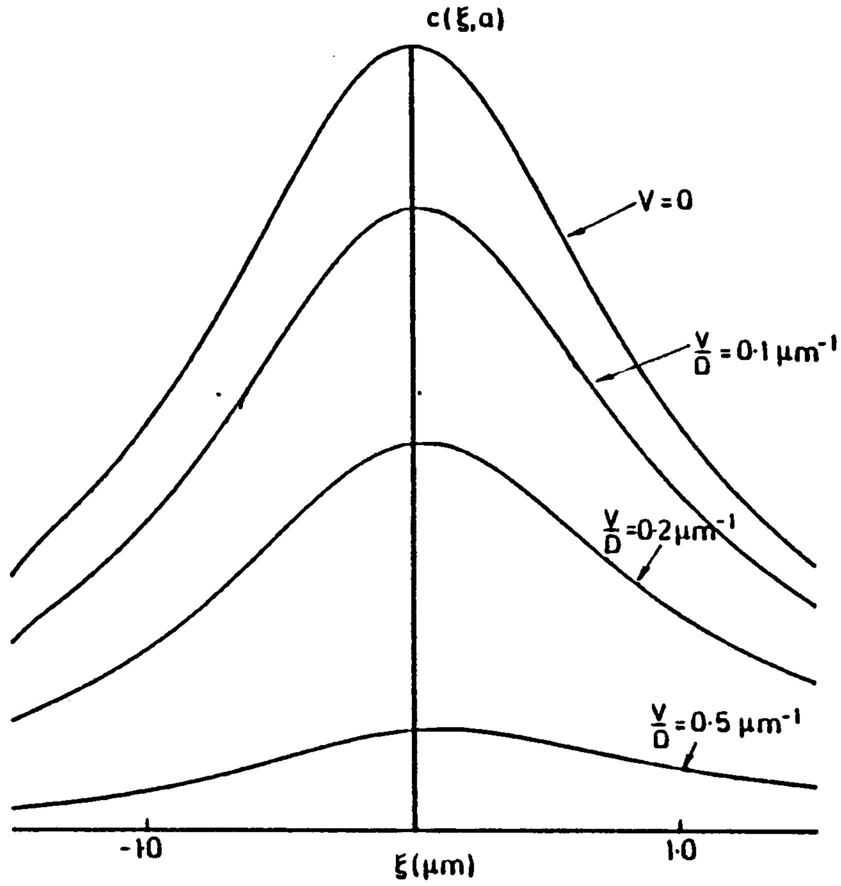

Figure 6.13. The contrast as a function of probe position, for various values of scan velocity. The case shown is for when $\alpha = 0.4\mu m^{-1}$, $L = 10.0\mu m$, $c = 0.5\mu m$ and a defect depth of $a = 2.0\mu m$.

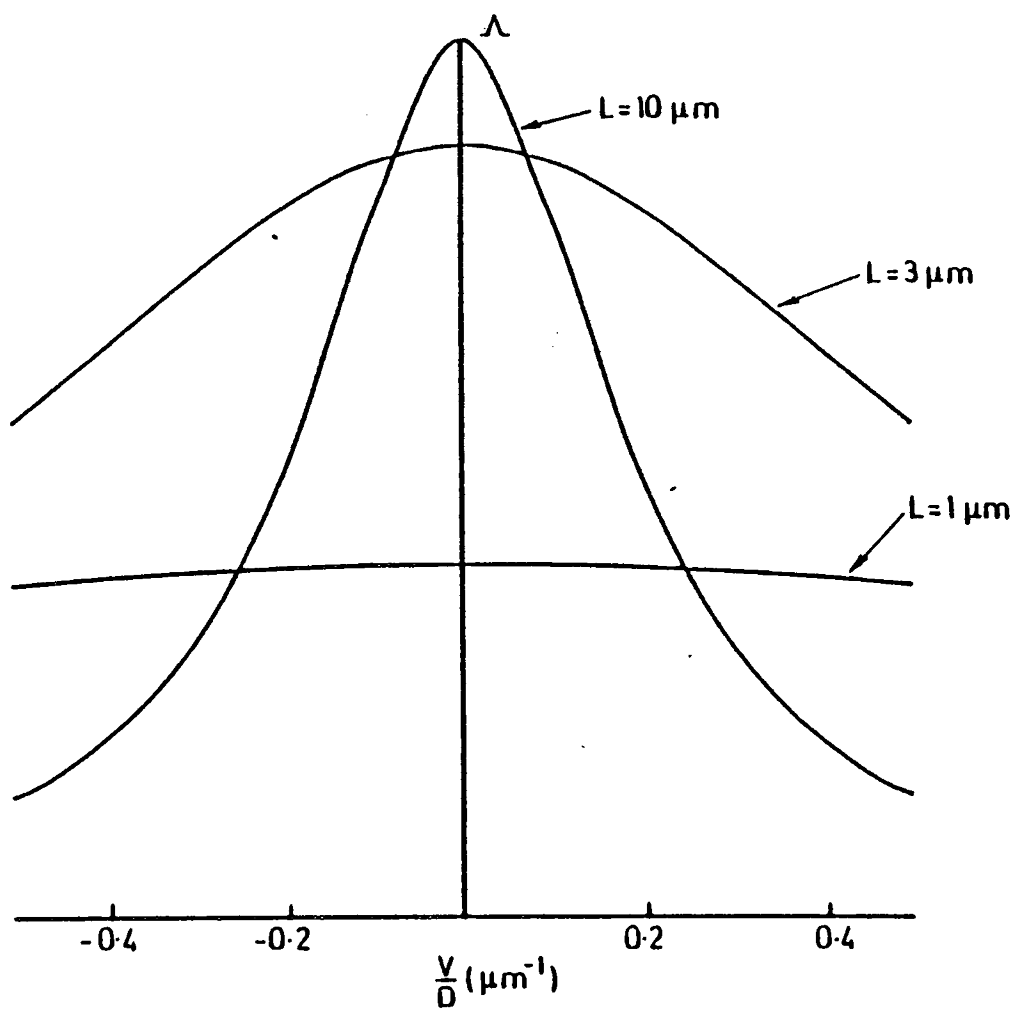

Figure 6.14. The variation of the premultiplying factor Λ as a function of the scan speed for various values of the diffusion length. The case shown is for when $\alpha = 0.4\mu m^{-1}$, $c = 0.5\mu m$ and s defect depth of $a = 2.0\mu m$.

offset in the contrast peak becomes greater at higher scan speeds. The magnitude of the contrast is also *reduced* with increasing scan velocity, which is primarily due to the variation of the premultiplying factor Λ with v, this can be seen from Figure (6.14) where Λ is plotted as a function of the scan velocity for a selection of diffusion lengths. The effect of the diffusion length on the contrast at a fixed scan velocity is shown in Figure (6.15a) where it can be seen that the general shape of the curves is independent of the value of L and so the resolution is not limited by the diffusion length, which agrees with the results of Chapter 3.

So far we have only considered defects at a depth of $2\mu m$, and so in Figure (6.15b) we show how the contrast curves vary as a function of defect depth, again for a fixed value of the scan velocity. It is clear from Figure (6.15b) that the maximum contrast occurs for defects located around $1\mu m$ beneath the surface, the reason for this is that the contrast is determined by the form of the carrier distribution, as shown in Chapter 3, and for the case of infinite surface recombination velocity that we are considering here the distribution peaks about $1\mu m$ beneath the surface, as can be seen from the surface plots in Chapter 3.

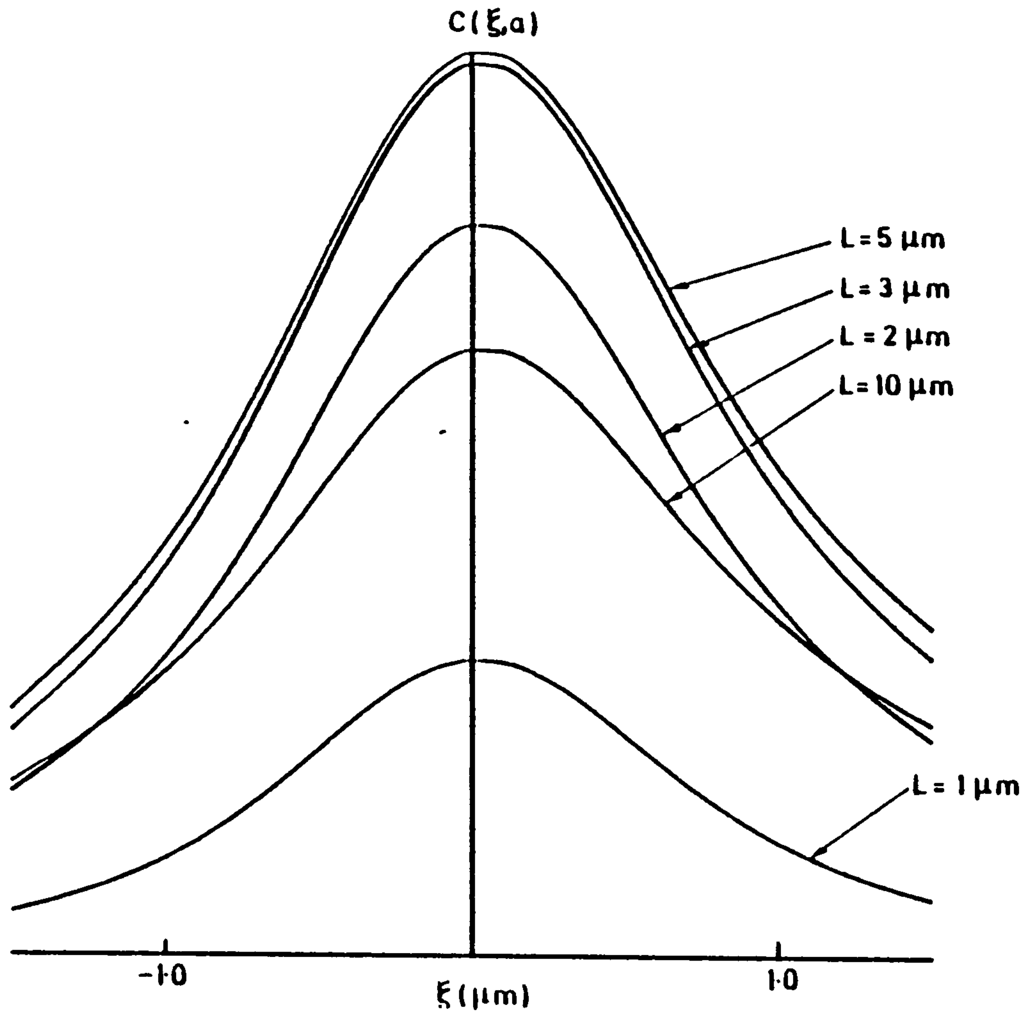

Figure 6.15a. The variation of the contrast with scan position for various values of the diffusion length. The curves are for the case when $\alpha = 0.4\mu m^{-1}$, $c = 0.5\mu m$, $a = 2.0\mu m$ and a scan speed of $v/D = 0.2\mu m^{-1}$.

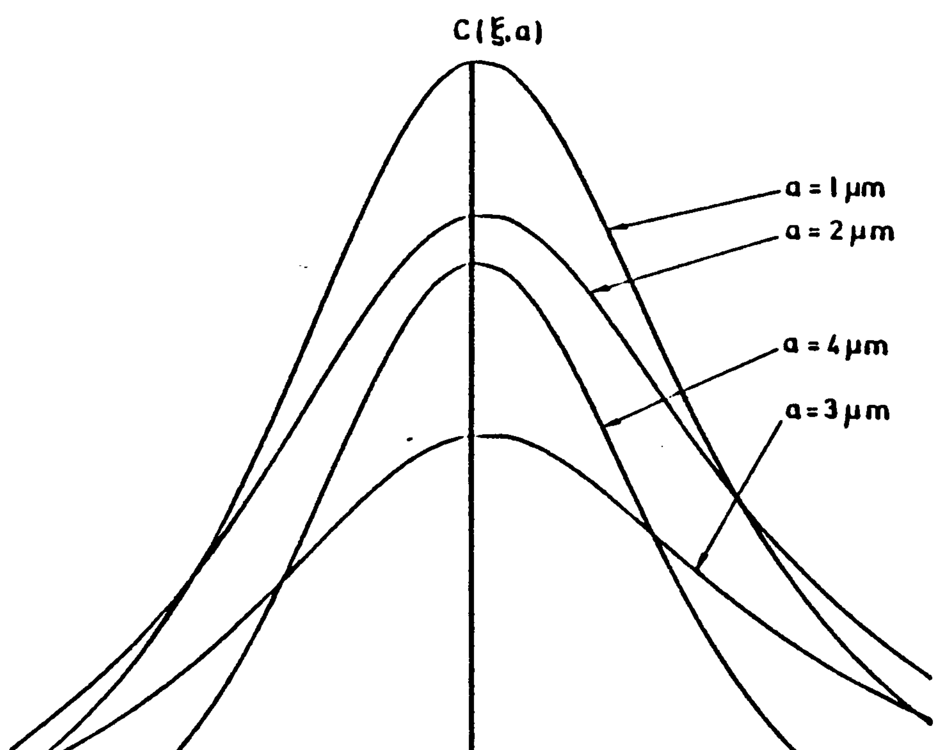

Figure 6.15b. The variation of the contrast with scan position for point defects at different depths, again for the case when $\alpha = 0.4\mu m^{-1}$, $c = 0.5\mu m$, $v/D = 0.2\mu m^{-1}$ and a diffusion length of $L = 10.0\mu m$.

6.4 Experimental Investigation of Scan Speed Effects

One common device in which we have observed scan speed effects is the Texas Instruments BU500 power transistor. For the purposes of OBIC investigations a cross section of the device may be represented by Figure (6.16) where the laser probe is shown scanning across the base-emitter junction, with the OBIC signal being monitored via the base and emitter contacts.

Figure (6.17) shows a combination of reflected light, at the top, and optical beam induced current (OBIC) images of the portion of the device shown schematically in Figure (6.16), where it is clear that the brightest parts of the OBIC image correspond to the location of the base-emitter p/n junctions. For quantitative analysis it is, in general, easier to consider line scans across a device, and Figure (6.18) shows the line scans corresponding to Figure (6.17), here the upper trace is the reflected light and the lower trace is the beam induced current.

It can be seen from the lower trace in Figure (6.18) that the OBIC line scan across the device is asymmetric, however as can be seen from the upper trace and Figure (6.16) the device itself *is* symmetrical about the base finger. This effect is shown clearly in Figure (6.19) where we show two OBIC line scans of the same part of the device, however, the top trace was obtained by scanning from right to left and the bottom by scanning left to right across the device.

We can investigate the effect of the scan speed on the OBIC image by considering just one side of the base finger and observing scans in opposite directions, differences in which can be seen by superimposing the two traces. Figure (6.20) shows a series of such images for decreasing scan speeds; at the highest speed, shown in Figure (6.20a), the difference in the OBIC traces is clearly visible, however, as the scan speed is decreased, which in our object scanning system means the magnification is *increased*, the traces become less different until at the lowest scan speed , shown in Figure (6.20e) the traces are identical (a full trace could not be obtained for this case as the magnification was too high).

It is interesting to note just how large an effect the scan velocity can have on the beam induced current images, even at the relatively low speeds used in obtaining these OBIC traces in a stage scanning microscope.

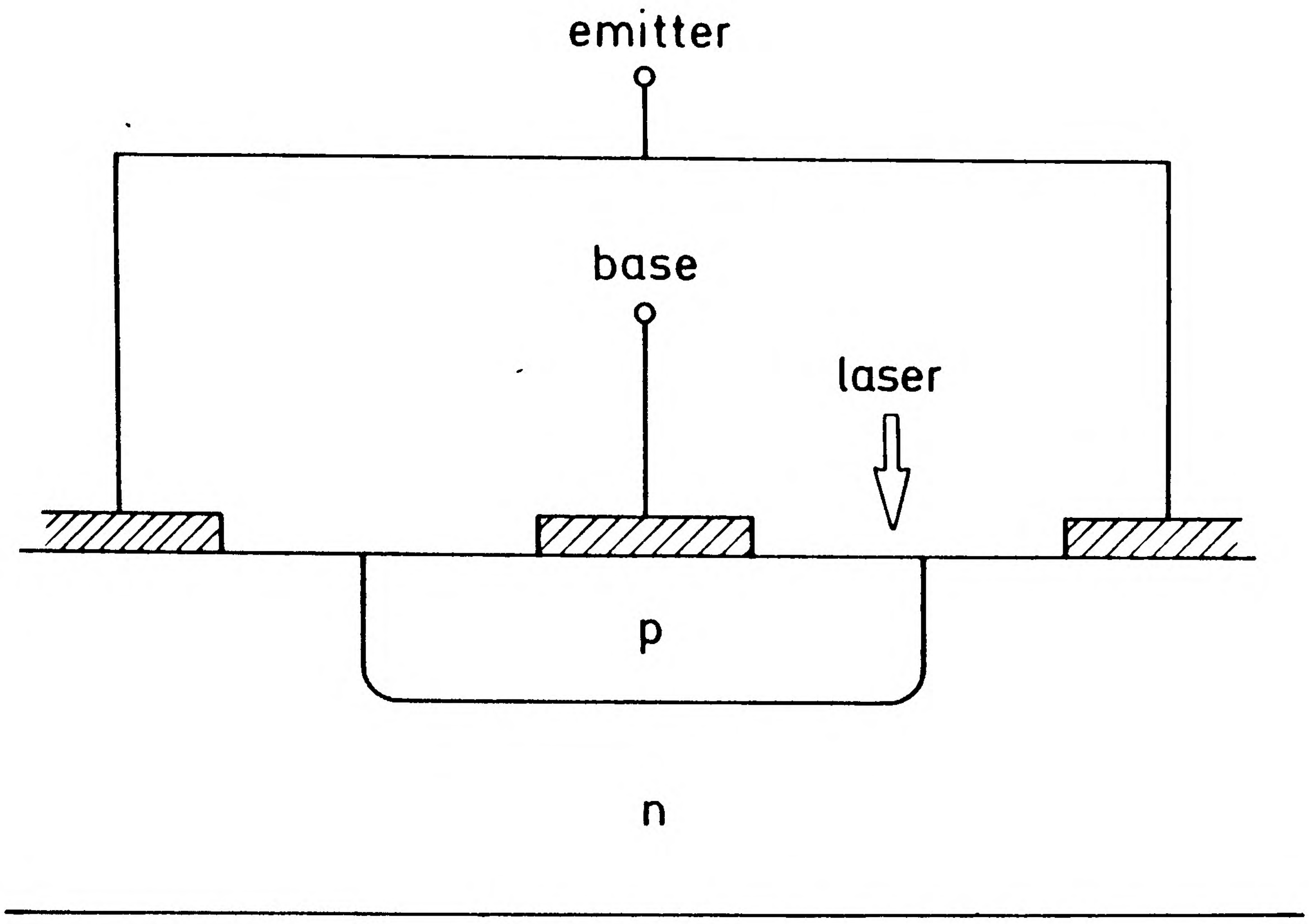

Figure 6.16. A schematic cross-section of Texas Instruments BU500 power transitor.

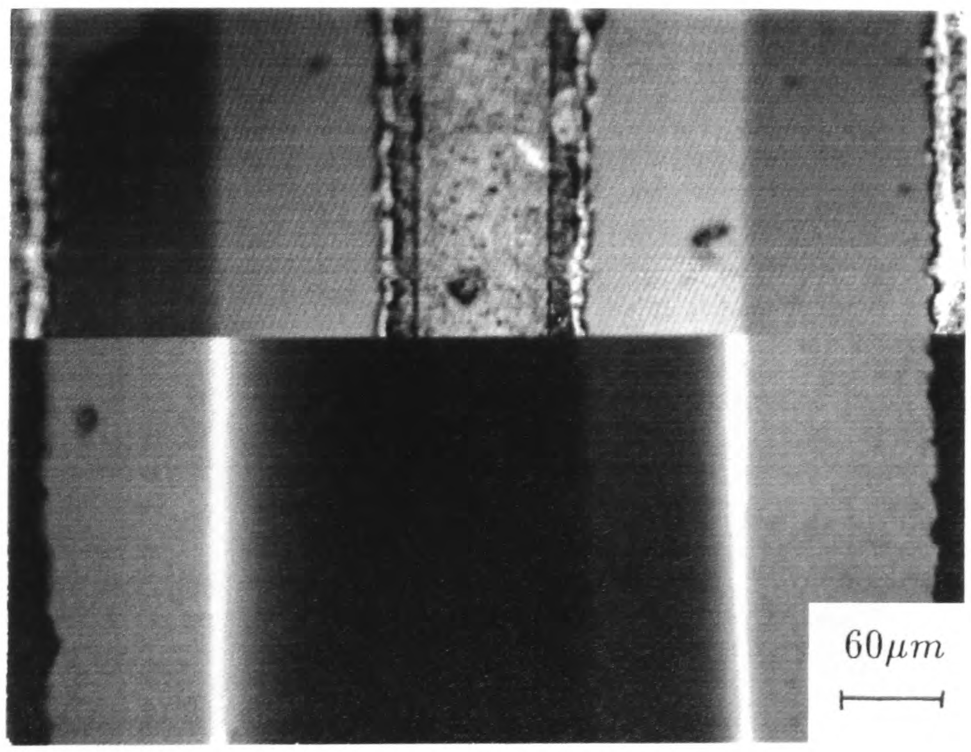

Figure 6.17. A combination of reflected light and beam induced current images of the base finger of a BU500 power transitor.

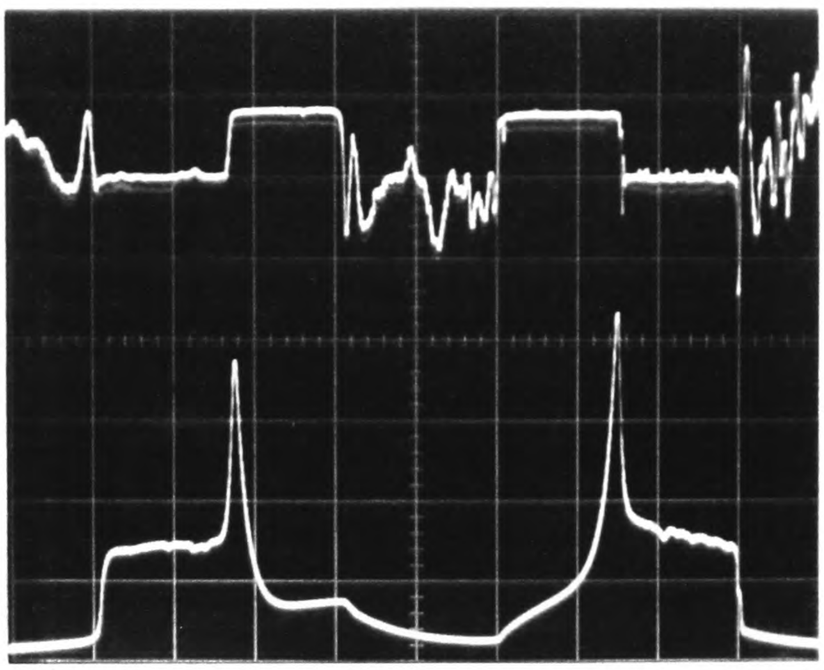

Figure 6.18. Line scans across the base finger, the upper trace represents the reflected light and the lower trace the optical beam induced current. The scale is such that one large division is equivalent to $40\mu m$.

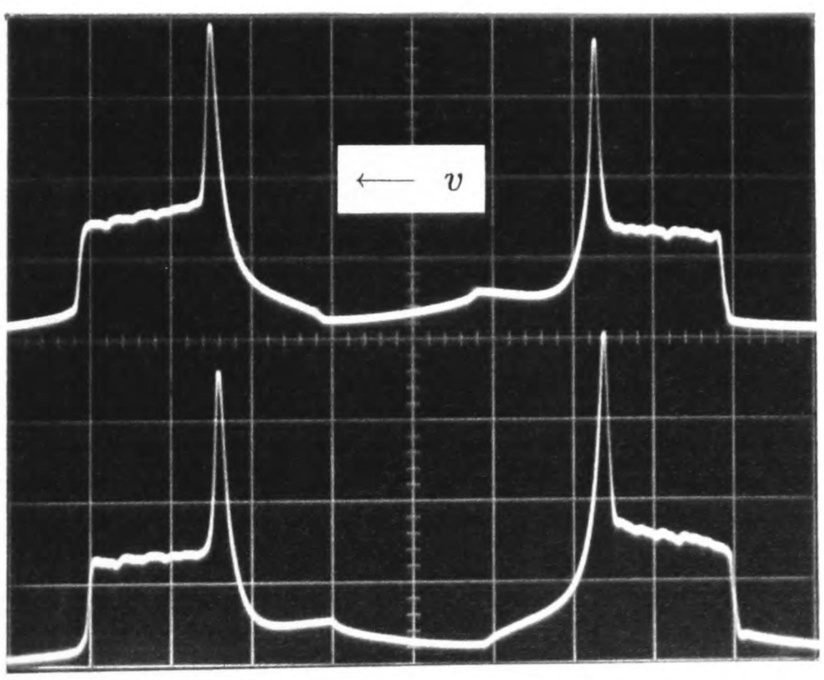

Figure 6.19. Two beam induced line scans across the base finger of the power transistor. The top trace was obtained by scanning from right to left and the lower by scanning from left to right, the scale is such that one large division represents $40\mu m$.

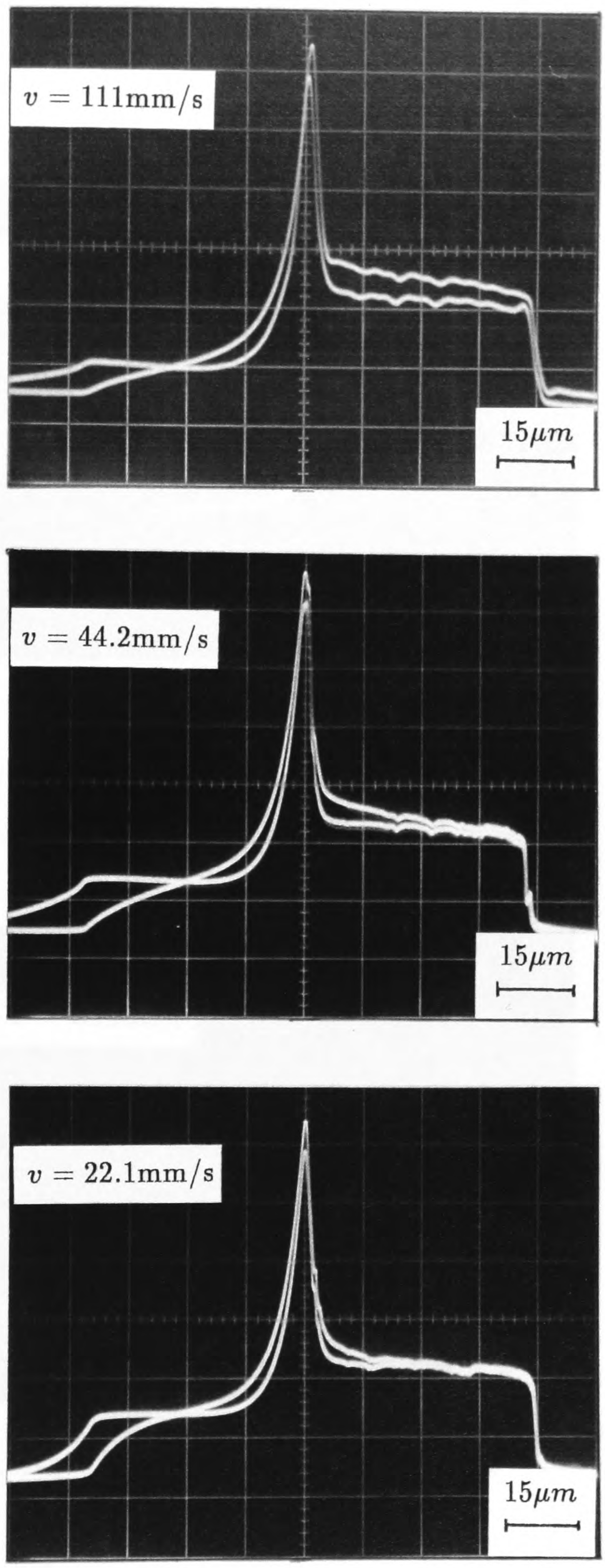

Figure 6.20. Two superimposed OBIC line scans obtained by scanning in opposite directions across one side of the base finger, the scan speed is (a) $v = 111$ mm/sec, (b) $v = 44.2$ mm/sec and (c) $v = 22.1$ mm/sec

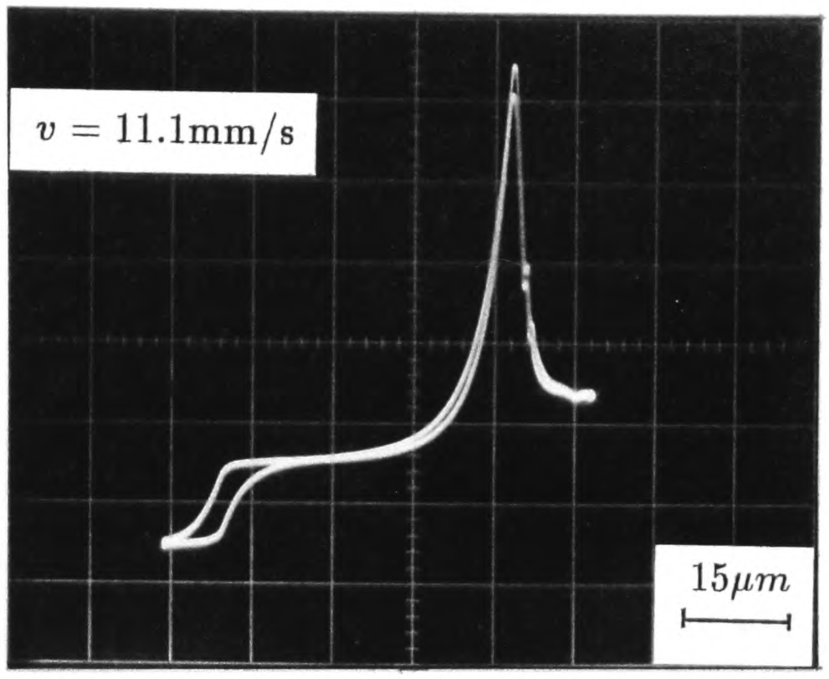

(d)

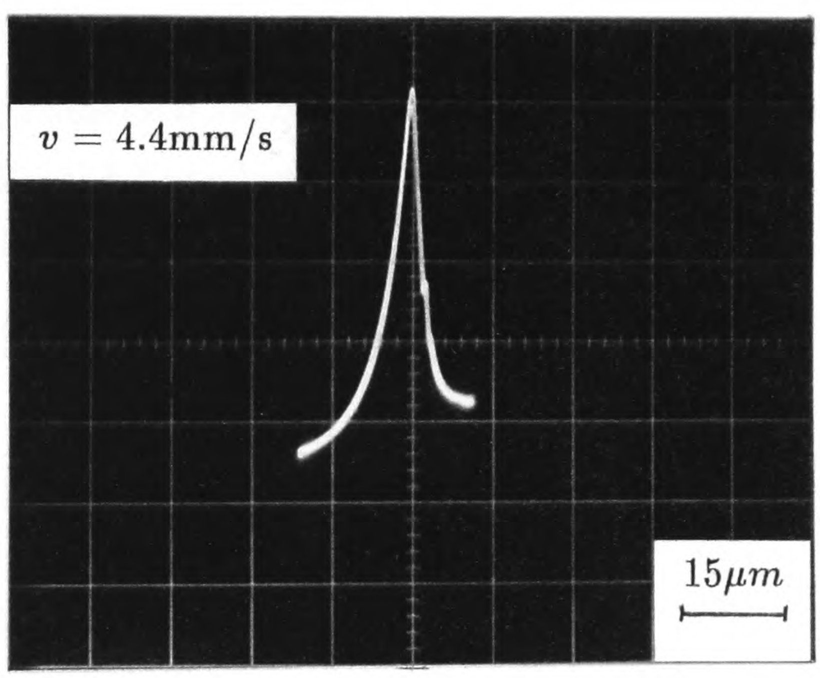

(e)

Figure 6.20. Two superimposed OBIC line scans obtained by scanning in opposite directions across one side of the base finger, the scan speed is (d) v = 11.1 mm/sec and (e) v = 4.4 mm/sec.

6.5 Conclusions

We have shown how the speed of scanning in a scanning optical microscope can effect the photoinduced currents collected by junctions both perpendicular and parallel to a semiconductor surface. The main reason for this is that the beam induced minority carrier distribution for a non-zero scan velocity becomes asymmetric, which leads to a scan speed dependent photocurrent. The magnitude of the effect is characterized by the ratio of the scan velocity to the diffusion velocity and, if this ratio is made very small, the scan speed effects will be unimportant and reliable results can be obtained by setting $v = 0$ in the theories. However, a typical value [20 p.191] of the diffusion velocity in silicon with doping in the region of $10^{17} cm^{-3}$ is about 4m/sec, which is comparable with scan speeds attainable as discussed in the introduction to this Chapter.

The scan speed was also shown to have an effect on the contrast obtained as a point defect in a Schottky barrier was scanned over. The main results being that the magnitude of the contrast is *decreased* with increasing scan speed and that the position of maximum contrast is shifted laterally from directly above the defect as the scan speed increases.

The general trends of the experimental results agreed with the predictions of the theory, although the theories of both section 6.2 and 6.3 are not directly applicable since neither of the geometries considered represents that of the BU500 power transistor. In order to model the actual device with any degree of certainty it would be necessary to construct a computer based numerical solution to the diffusion equation which could take into account the complicated boundary conditions of a real device.

Finally, it should be noted that although the analysis has been for the case of *optical* beam induced currents the general trends will also, of course, be present in the *electron* beam case.

CHAPTER 7:

TIME DEPENDENT PHOTOLUMINESCENCE

7.0 Introduction

One of the main attractions of using light or electron beams to excite current carriers in semiconductors is to try and measure material parameters nondestructively in whole unprocessed wafers. So far in this thesis we have discussed various techniques for the measurement of the minority carrier diffusion length or lifetime, such as the use of Steady State Beam Induced Currents in Chapter 4 and Time Dependent Beam Induced Currents in Chapter 5, however a major problem associated with both of these methods is the necessity for a rectifiying contact to be made to the specimen. The need for a rectifying contact arises since we have, in some way, to measure some property of the induced minority carrier distribution as a function of position in the wafer. The most convenient way to make the contact on an unprocessed wafer is, in general, to evaporate a suitable metal onto the surface to produce a Schottky barrier diode, or by use of a liquid electrolyte as mentioned in Chapter 4. However, for a measurement technique to be truely nondestructive we would, idealy, like to examine some property of the induced minority carrier distribution *without* making contact to the sample at all.

One such method for investgating the minority carrier distribution is via a capacative detection system, proposed by DiStefano [1], where a plate is positioned parallel to the semiconductor surface and the capacitance of the system measured as a function of the beam position. Another method relies on a radiative recombination being present in the sample since, if the cross-section for this recombination is high enough, the released light can give rise to a *photoluminescence* signal, the intensity of which can be measured by a suitable photodiode or photomultiplier [2,3,4]. In Chapter 2 high resolution scanning photoluminescence images of InP are shown, where it is clear that it is possible to resolve defects with dimensions of the order, or less than, one micron. This agrees with the predictions of the steady state theory for photoluminescence defect imaging, as described in Chapter 3. However, following the same arguments as presented in the introduction to Chapter 5, were time dependent beam induced currents where considered, it becomes clear that in order to use this photoluminescence technique to measure the minority carrier *lifetime* a time dependent theory for the generation of the signal is required.

Previous authors [5,6,7] have considered this problem, although in each case the analysis have been somewhat misleading since it is claimed the situation modelled is that where a *focussed* light beam is incident on the semiconductor surface. However, in the analyses either a point source [5] or the decaying point source approximation [6,7] is used to represent the spatial generation function and, as shown in Chapter 3, the minority carrier distribution predicted by such approximations is somewhat different from that given by a focussed light beam. For this reason the form of the photoluminescence signal predicted by the previous theories is expected to differ from that predicted by an analysis *including* focussing effects.

Therefore, in the following, we extend the previous work and calculate the photoluminescencent signal generated by a semi-infinite semiconductor slab when illuminated by an arbitrary, time varying, radially symmetric exciting beam. We then specialise to the practically important case of a focussed light beam. The analysis is for a three dimensional sample and makes use of the radial symmetry of the problem by introducing, as in previous Chapters, the Hankel transform of the induced minority carrier distribution. Finally, three important examples for the temporal form of the light beam are considered, these are; (i) Delta function excitation, (ii) Step and finite pulse exciation, and (iii) Harmonic excitation.

7.1 Time Dependent Photoluminescence Theory

The time dependent photoluminescence signal, $\mathcal{P}(t)$, can be found from the time dependent equivalent of Equation (3.63) of Chapter 3, which, in the absence of internal absorption of the luminescence, can be written,

$$\mathcal{P}(t) \propto \int_0^\infty \int_0^\infty \Delta p(r,z,t)\, r dr dz, \tag{7.1}$$

where $\Delta p(r,z,t)$ is the time dependent minority carrier distribution. It is straightforward to find $\Delta p(r,z,t)$ since it is simply the solution of the time dependent diffusion equation, given in Equation (5.2) of Chapter 5, subject to the relevant boundary conditions. If we choose to consider a semi-infinite semiconductor bounded by a surface which is charaterized by a surface recombination velocity, v_s, the boundary conditions are given in Equations (3.7a) and (3.7b).

Other authors have proceeded from this point, using the cartesian coordinate system, to either integrate the three dimensional diffusion equation over x and y [7] to give a one dimensional problem, or to find the three dimensional Green's function of the diffusion equation and fold this with a three dimensional source distribution. However, it is clear that the problem has a *natural* cylindrical symmetry, which we will exploit by use of the Hankel transform of the minority carrier distribution, $\Delta\bar{p}(\nu,z,t)$, as defined in Equation (4.2) of Chapter 4. The expression for the photoluminescence, given in Equation (7.1), can be then written,

$$\mathcal{P}(t) \propto \int_0^\infty \int_0^\infty \int_0^\infty \Delta\bar{p}(\nu,z,t) J_0(\nu r)\, \nu d\nu r dr dz, \tag{7.2}$$

which, evaluating the integrals in r and ν yields,

$$\mathcal{P}(t) \propto \int_0^\infty \Delta\bar{p}(0,z,t)\, dz. \tag{7.3}$$

The function $\Delta\bar{p}(0,z,t)$ is simply the solution of the transformed diffusion equation evaluated in the limit as the transform, $\nu \to 0$, that is,

$$D\frac{\partial^2}{\partial z^2}\Delta\bar{p}(0,z,t) - \frac{\Delta\bar{p}(0,z,t)}{\tau} + \bar{g}(0,z)\cdot f(t) = \frac{\partial}{\partial t}\Delta\bar{p}(0,z,t), \tag{7.4}$$

where, as in previous Chapters, $\bar{g}(\nu,z)$ is the Hankel transform of the spatial part of the generation function and $f(t)$ is the temporal part of the generation function. It is interesting to note here that to obtain the *three* dimensional photoluminescence signal we only need to solve the *one* dimensional diffusion equation, this is clearly a consequence of the symmetry of the problem. Equation (7.4) can be simplified by introducing the transformation

$$\Delta P(\nu,z,t) = \exp(t/\tau)\, \Delta\bar{p}(\nu,z,t), \tag{7.5}$$

since then Equation (7.4) becomes,

$$D\frac{\partial^2}{\partial z^2}\Delta P(0,z,t) + \bar{g}(0,z)\cdot f(t)\cdot \exp(t/\tau) = \frac{\partial}{\partial t}\Delta P(0,z,t), \tag{7.6}$$

from which the time dependence can be removed by use of the Laplace transformation, defined as,

$$\mathcal{L}\Big[\Delta P(\nu,z,t)\Big] = \Delta P^{\star}(\nu,z,p) = \int_0^{\infty} \exp(-pt)\Delta P(\nu,z,t)\,dt, \tag{7.7}$$

with $\mathcal{L}$ again denoting the Laplace transformation operator. This allows the diffusion equation to be finally written in the form,

$$\frac{\partial^2}{\partial z^2}\Delta P^{\star}(0,z,p) - q^2\Delta P^{\star}(0,z,p) = -\frac{1}{D}\bar{g}(0,z)\cdot F^{\star}\left(p-\frac{1}{\tau}\right), \tag{7.8}$$

where $F^{\star}(p)$ is the Laplace transformation of the temporal generation function, $f(t)$, and $q = \sqrt{p/D}$. Solving Equation (7.8) for $\Delta P^{\star}(0,z,p)$ subject to the transformed boundary conditions is straightforward, since it is simply Equation (3.12) of Chapter 3, and so we obtain,

$$\Delta P^{\star}(0,z,p) = \frac{1}{D}F^{\star}\left(p-\frac{1}{\tau}\right)\int_0^{\infty} G(p,z|z_0)\bar{g}(0,z_0)\,dz_0, \tag{7.9}$$

where the Green's function is given, from Chapter 3, Equation (3.14), as

$$G(p,z|z_0) = \frac{1}{q}\left\{\exp[-q|z-z_0|] + \left(\frac{q-s}{q+s}\right)\exp[-q(z+z_0)]\right\}, \tag{7.10}$$

here s is the normalised surface recombination velocity given by $s = v_s/D$. Integrating Equation (7.9) over z to obtain an expression for the photoluminescence, as indicated in Equation (7.3), yields

$$\mathcal{P}(t) \propto \frac{2}{D}\exp(-t/\tau)\,\mathcal{L}^{-1}\left[\frac{F^{\star}(p-1/\tau)}{p}\right.$$
$$\left.\int_0^{\infty}\left\{1-\left(\frac{s}{q+s}\right)\exp(-qz_0)\right\}\bar{g}(0,z_0)\,dz_0\right]. \tag{7.11}$$

Equation (7.11) is a general expression for the photoluminescence, due to arbitrary spatial and temporal generation functions, generated from a semi-infinite semiconducting slab.

We are now in a position to choose the form of the spatial and temporal generation functions, $g(r,z)$ and $f(t)$. If we choose to illuminate the sample with light from a high numerical aperture lens the form of $g(r,z)$ is given in Equation (3.1), and the form of $\bar{g}(0,z)$ from Equation (4.15), of Chapter 4, repeated here as,

$$\bar{g}(0,z) = \frac{g_0}{2\pi\ln(\mu)}\left\{\frac{\exp(-\alpha z)-\exp(-\alpha\mu z)}{z}\right\}, \tag{7.12}$$

where $\mu = (1 + 2\epsilon)$, $\epsilon = (\sin^2\theta)/4$ and $\sin\theta$ is the numerical aperture of the objective lens. It is clear from Equation (7.12) that $\bar{g}(0,z)$ *cannot* be represented by a simple exponential decay if the focussing effects are to be taken into account, as claimed by some authors [6,7]. However, in the limit of very low numerical apertures, that is $\sin\theta \to 0$, Equation (7.12) reduces to,

$$\bar{g}(0,z) \sim \frac{\alpha g_0}{2\pi} \exp(-\alpha z), \tag{7.13}$$

which is the form of $\bar{g}(0,z)$ that will be produced for *any* beam shape which can be represented in the form

$$g(r,z) = R(r) \cdot \exp(-\alpha z), \tag{7.14}$$

since then,

$$\bar{g}(0,z) = \left\{ \int_0^\infty R(r)\, r dr \right\} \exp(-\alpha z). \tag{7.15}$$

The form of the photoluminecence signal predicted from Equations (7.11) and (7.12) can now be demonstrated by considering various forms for the temporal generation function. In the following examples we consider the three important cases of; (i) Delta Function Excitation, (ii) Step and Finite Pulse Excitation, and finally (iii) Harmonic Excitation.

Example (i): Delta Function Excitation

For a light pulse which is very short compared with the minority carrier lifetime the temporal form of the generation function can be written as,

$$f(t) = \delta(t), \tag{7.16}$$

where $\delta(t)$ is the Dirac-delta function. From Equation (7.16) we see that $F^{\star}(p-1/\tau) = 1$ and so substitution into Equation (7.11), together with the form of $\bar{g}(0,z)$ from Equation (7.12), gives an expression for the photoluminescence as [8],

$$\mathcal{P}(t) \propto \exp\left(-\frac{t}{\tau}\right) \int_0^{\infty} \left\{ \operatorname{erf}\left(\frac{z_0}{2\sqrt{Dt}}\right) + \exp(s^2 Dt)\exp(sz_0)\operatorname{erfc}\left(\frac{z_0}{2\sqrt{Dt}} + s\sqrt{Dt}\right) \right\} \left(\frac{\exp(-\alpha z_0) - \exp(-\alpha\mu z_0)}{z}\right) dz_0, \tag{7.17}$$

where erf is an error function, erfc is an error function complement and we have used the inverse Laplace transformations tabulated in Carslaw and Jeager [9 p.494]. It should be noted that Equation (7.17) reduces to that given by other authors [6,7], by more complicated means, for the special case of $\sin\theta \to 0$.

If the expression in Equation (7.17) is normalised to it's value at $t = 0$, given by

$$\mathcal{P}(0) \propto \int_0^{\infty} \bar{g}(0, z_0)\, dz_0, \tag{7.18}$$

and we take the limit of the resulting expression for low surface recombination velocity, that is $s \to 0$, we find that, *independent* of the generation function, we obtain a simple exponential decay for the normalised photoluminescence, that is,

$$\left.\frac{\mathcal{P}(t)}{\mathcal{P}(0)}\right|_{s\to 0} = \exp\left(-\frac{t}{\tau}\right), \tag{7.19}$$

and so the minority carrier lifetime, τ may be measured simply from the decay of the normalised photoluminescence signal. On the other hand if the surface recombination is very high we obtain,

$$\left.\frac{\mathcal{P}(t)}{\mathcal{P}(0)}\right|_{s\to\infty} = \left\{ \frac{\int_0^{\infty} \operatorname{erf}\left(\frac{z_0}{2\sqrt{Dt}}\right) \bar{g}(0,z_0)\, dz_0}{\int_0^{\infty} \bar{g}(0,z_0)\, dz_0} \right\} \exp\left(-\frac{t}{\tau}\right), \tag{7.20}$$

and the decay is clearly nonexponential in time.

Figure (7.1) shows the form of the photoluminescent decay after a short light pulse, as given by Equation (7.17) for the case when $sL = 10.0$, $\alpha L = 1.0$ and for three different values of the numerical aperture. It is clear that, under these circumstances, the focussing action of the beam does not effect the *shape* of the decay curves, and indeed if we had normalised the signal and plotted $\mathcal{P}(t)/\mathcal{P}(0)$, the curves would have been

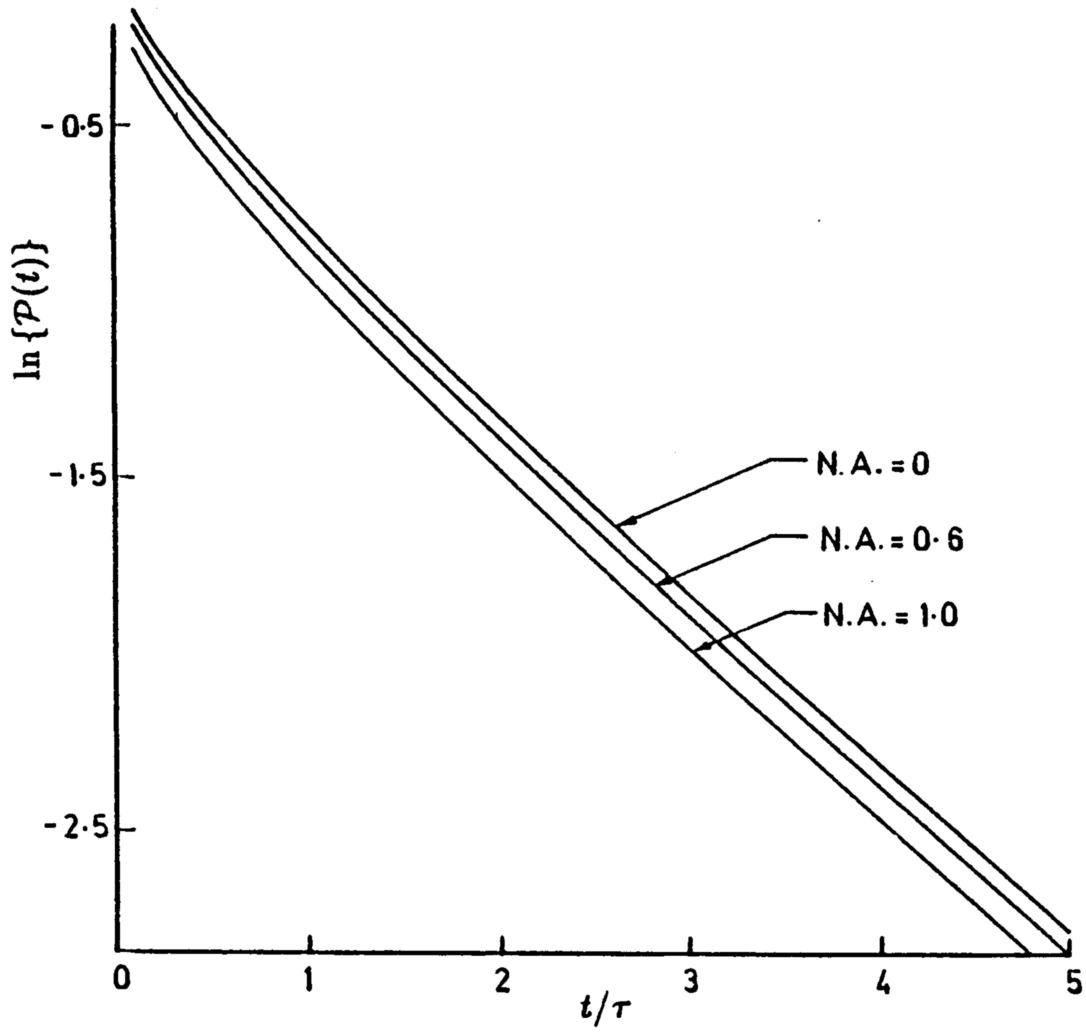

Figure 7.1. The logarithm of the photoluminescence signal as a function of time after a short light pulse. The case shown is for when $sL = 10.0$, $\alpha L = 1.0$ and numerical apertures of $\sin\theta \rightarrow 0$, $\sin\theta = 0.6$ and $\sin\theta = 1.0$.

indistinguishable. This is due to the value of the absorption coefficient, α, which means that, over the range of integration in Equation (7.11) where the integrand is significantly different from zero, Equation (7.12) can be approximated by the simple exponential decay, $\bar{g}(0, z_0) \sim \exp(-\alpha z)$. Evaluating Equation (7.11) in this low numerical aperture limit gives,

$$\left.\frac{\mathcal{P}(t)}{\mathcal{P}(0)}\right|_{\sin\theta\rightarrow 0} = \frac{\exp(-t/\tau)}{(s-\alpha)}\left\{ s\exp(\alpha^2 Dt)\mathrm{erfc}\left[\alpha\sqrt{Dt}\right] - \alpha\exp(s^2 Dt)\mathrm{erfc}\left[s\sqrt{Dt}\right]\right\}, \qquad (7.21)$$

this is just as obtained previously [6,7]. It is clear that the curves in Figure (7.1) appear to become straight at large values of t/τ and, as such, it is interesting to look for a large t expansion for the photoluminescence. Expanding the error function complements, using Equation (5.25) of Chapter 5, gives

$$\left.\frac{\mathcal{P}(t)}{\mathcal{P}(0)}\right|_{t/\tau\gg 1} \sim \frac{s+\alpha}{\alpha s\sqrt{\pi}} \cdot \frac{\exp(-t/\tau)}{\sqrt{t}}, \qquad (7.22)$$

and hence the response remains nonexponential even at large values of t, although clearly it is possible to measure the lifetime, τ by simply plotting $\ln\left[\sqrt{t}\cdot\mathcal{P}(t)/\mathcal{P}(0)\right]$ against t at large values of time.

Having shown that at high values of attenuation the photoluminescence decay can be well modelled by ignoring the focussing effects, it is interesting to ask how accurately the results are predicted if we take an even more idealized generation function. For example, if we assume that generation takes place at one point on the surface, the generation function can be written,

$$\bar{g}(0,z) = \delta(z), \tag{7.23}$$

which, upon substitution into Equation (7.11), yields

$$\frac{\mathcal{P}(t)}{\mathcal{P}(0)} = \exp\left(-\frac{t}{\tau}\right) \exp(s^2 Dt) \operatorname{erfc}(s\sqrt{Dt}). \tag{7.24}$$

Again expanding the error function complement for the large t/τ limit gives,

$$\left.\frac{\mathcal{P}(t)}{\mathcal{P}(0)}\right|_{t/\tau \gg 1} \sim \frac{1}{s\sqrt{\pi}} \frac{\exp(-t/\tau)}{\sqrt{t}}, \tag{7.25}$$

which clearly has the same temporal behaviour as in Equation (7.22).

Figure (7.2) shows the normalised photoluminescence decay after a short light pulse for two values of surface recombination velocity and various values of absorption, the special case of high absorption, where the generation function is given in Equation (7.23) is shown as the dotted curve.

It is clear that the *point source* idealization is more reliable at low values of surface recombination velocity and, as we have seen from Equation (7.19), the results are identical when $s = 0$.

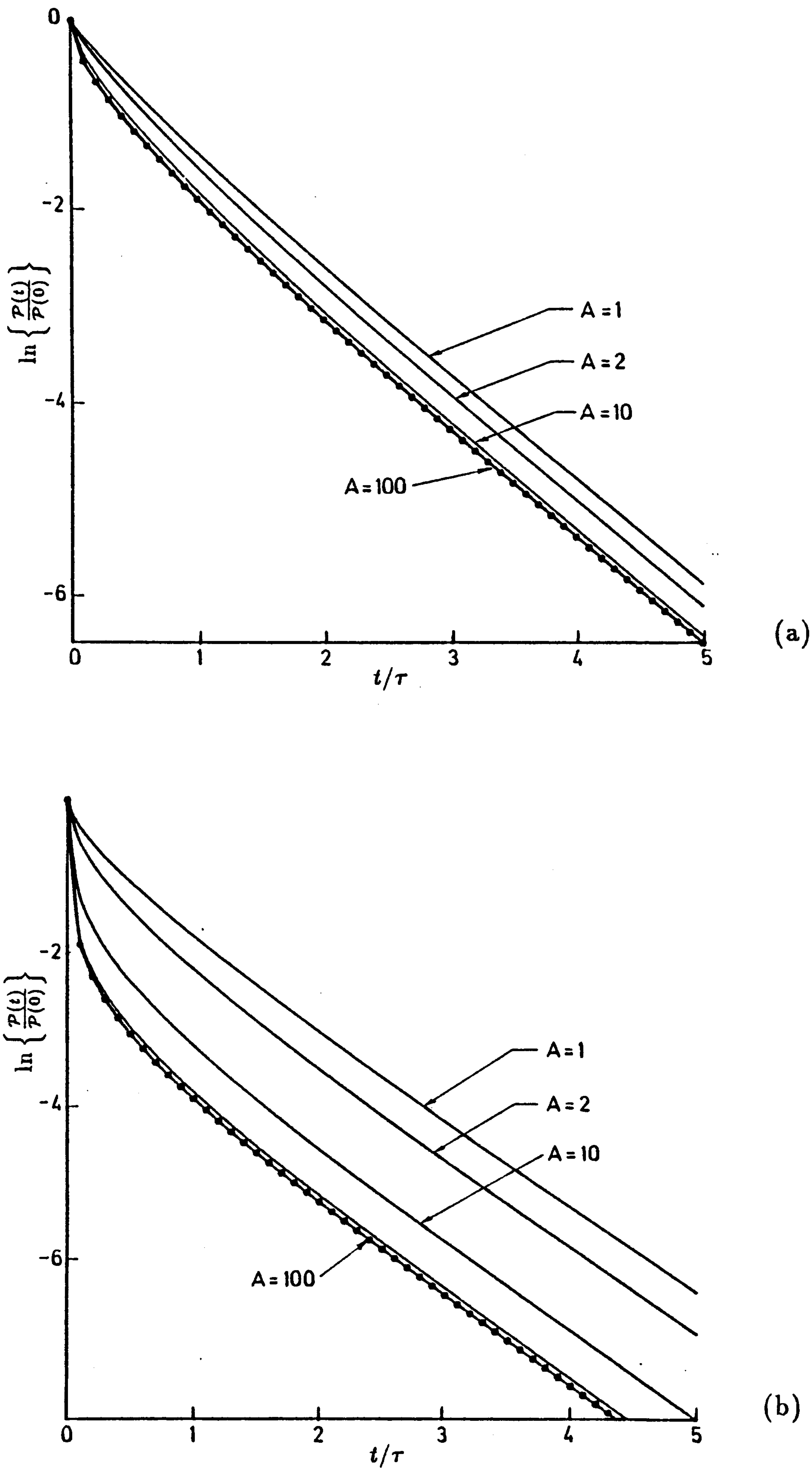

Figure 7.2. The decay of the normalised photoluminescence signal generated in a semi-infinite semiconductor after a short light pulse. The case shown is for various values of the normalised absorption coefficient, $A = \alpha L$, and when (a) $sL = 1.0$ and (b) $sL = 10.0$. The dotted curves represent the decay as predicted by the simple point source approximation of Equation (7.24).

Example (ii): Step and Finite Pulse Excitation

We now move on to consider the form of the photoluminescence signal due to a sudden increase in the light intensity such that $f(t)$ is given by Equation (5.28) of Chapter 5, and hence,

$$F^\star\left(1-\frac{1}{\tau}\right)=\frac{1}{p-\frac{1}{\tau}}. \tag{7.26}$$

Substitution into Equation (7.11) yields an expression [8] for the normalised photoluminescence signal which is plotted in Figure (7.3) for the low numerical aperture limit, since it is found again that the focussing of the beam does not effect the *shape* of the normalised response. The curves are shown for various values of surface recombination velocity and absorption coefficient.

It is interesting to note that, similarly to the delta function case of Example (i), if we take the limit of the response as $s \to 0$ we obtain,

$$\left.\frac{\mathcal{P}(t)}{\mathcal{P}(\infty)}\right|_{s\to 0}=1-\exp\left(-\frac{t}{\tau}\right), \tag{7.27}$$

which again is *independent* of the spatial generation function. It is tempting to ask again how good is the high absorption approximation where the generation function is given by Equation (7.23); under this assumption we find that the photoluminescence response has the simple form,

$$\mathcal{P}(t)\propto\frac{1}{(s^2L^2-1)}\left\{sL\,\mathrm{erf}\left[\sqrt{\frac{t}{\tau}}\right]+\exp(-t/\tau)\exp(s^2Dt)\mathrm{erfc}\left[s\sqrt{Dt}\right]-1\right\}, \tag{7.28}$$

which is plotted as the dotted line in Figure (7.3b) and is clearly a good approximation when $\alpha L \geq 10.0$.

Figure (7.4) shows the decay of the photoluminescence signal immediately after switching the beam off once the steady state has been reached, note that in the plots t now represents the time after switch-off.

Once again if we take the large t/τ limit of the response we arrive at

$$\mathcal{P}(t)\sim\frac{\exp(-t/\tau)}{\sqrt{t}}, \tag{7.29}$$

which is to be expected physically since the mechanism of carrier excitation should have no effect on the rate of recombination. Finally, for completeness we show in Figure (7.5) the form of the photoluminescence due to a light pulse of finite length, this is most easily modelled mathematically by summing to equal and opposite step responses separated appropriately in time, as in Example (ii) of Chapter 5.

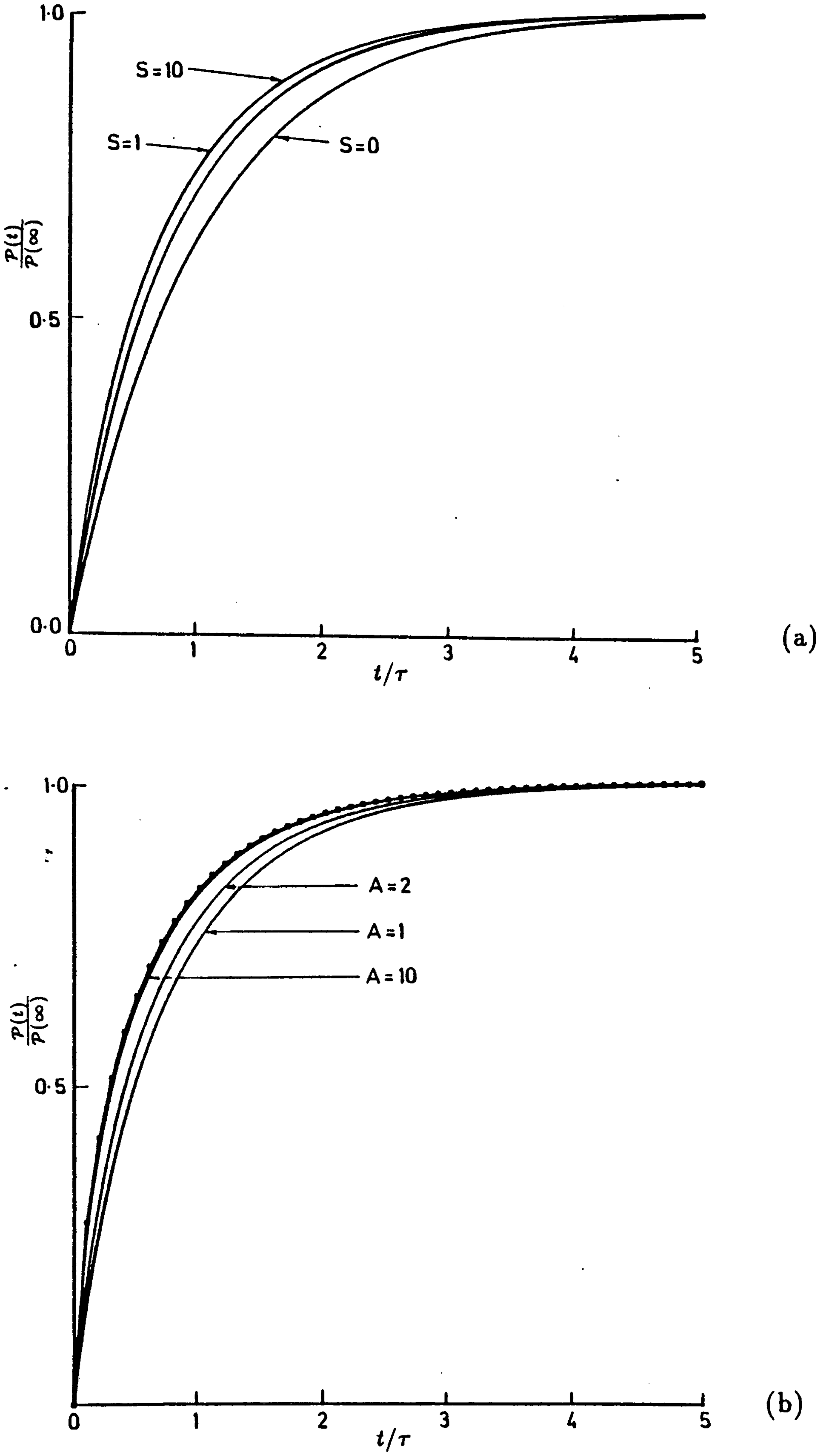

Figure 7.3. The rise of the photoluminescence signal, in the low numerical aperture limit, immediately after turning the exciting beam on. The cases shown are: (a) an absorption coefficient of $\alpha L = 1.0$ and for various values of surface recombination velocity and (b) a surface recombination velocity of $sL = 10.0$ and for various values of the normalised absorption coefficient $A = \alpha L$. Again the dotted curve represents the simple point source approximation of Equation (7.28)

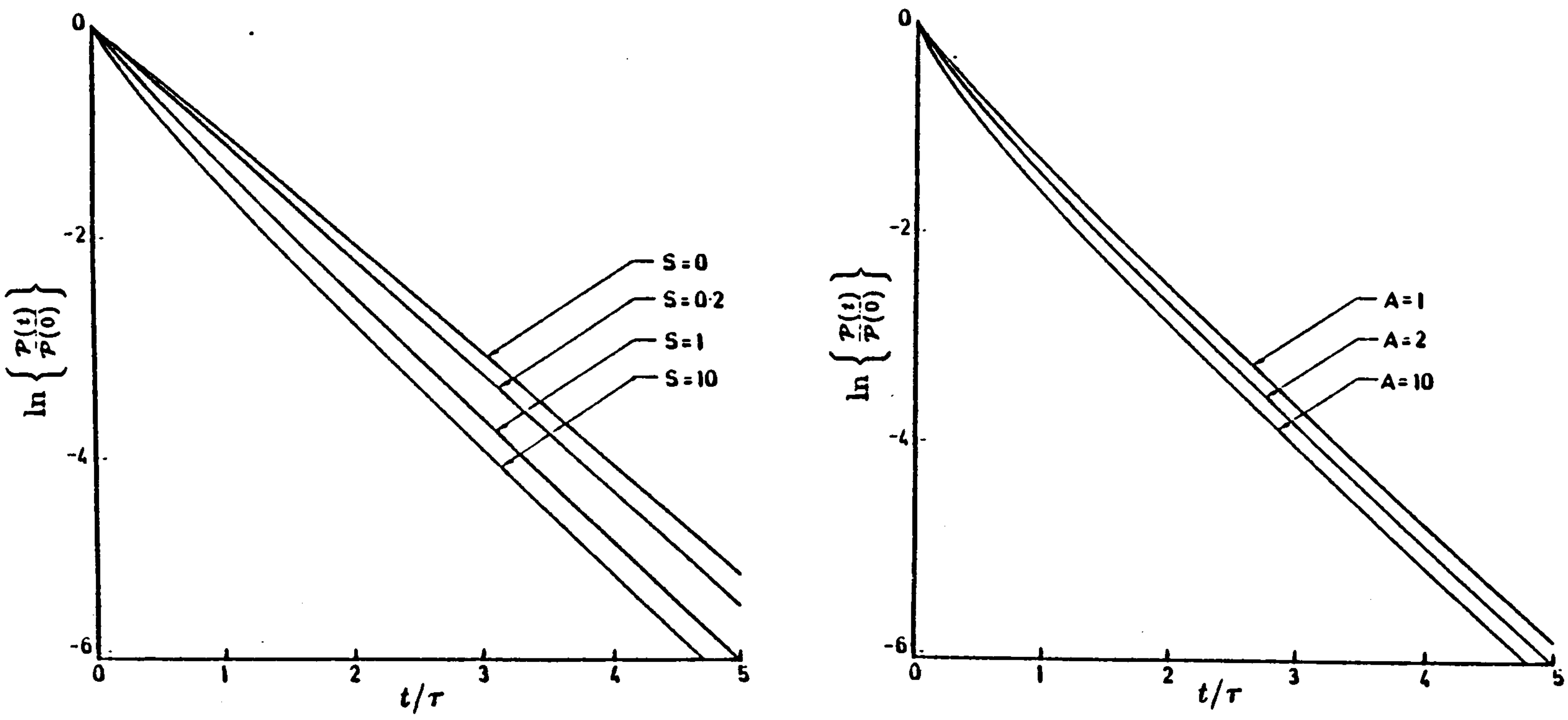

(a) (b)

Figure 7.4. The decay of photoluminescence signal from the steady state immediately after switching the beam off in the low numerical aperture limit. The cases shown are for when; (a) $\alpha L = 2.0$ and various values of the surface recombination velocity, and (b) $sL = 5.0$ and various values of the absorption coefficient.

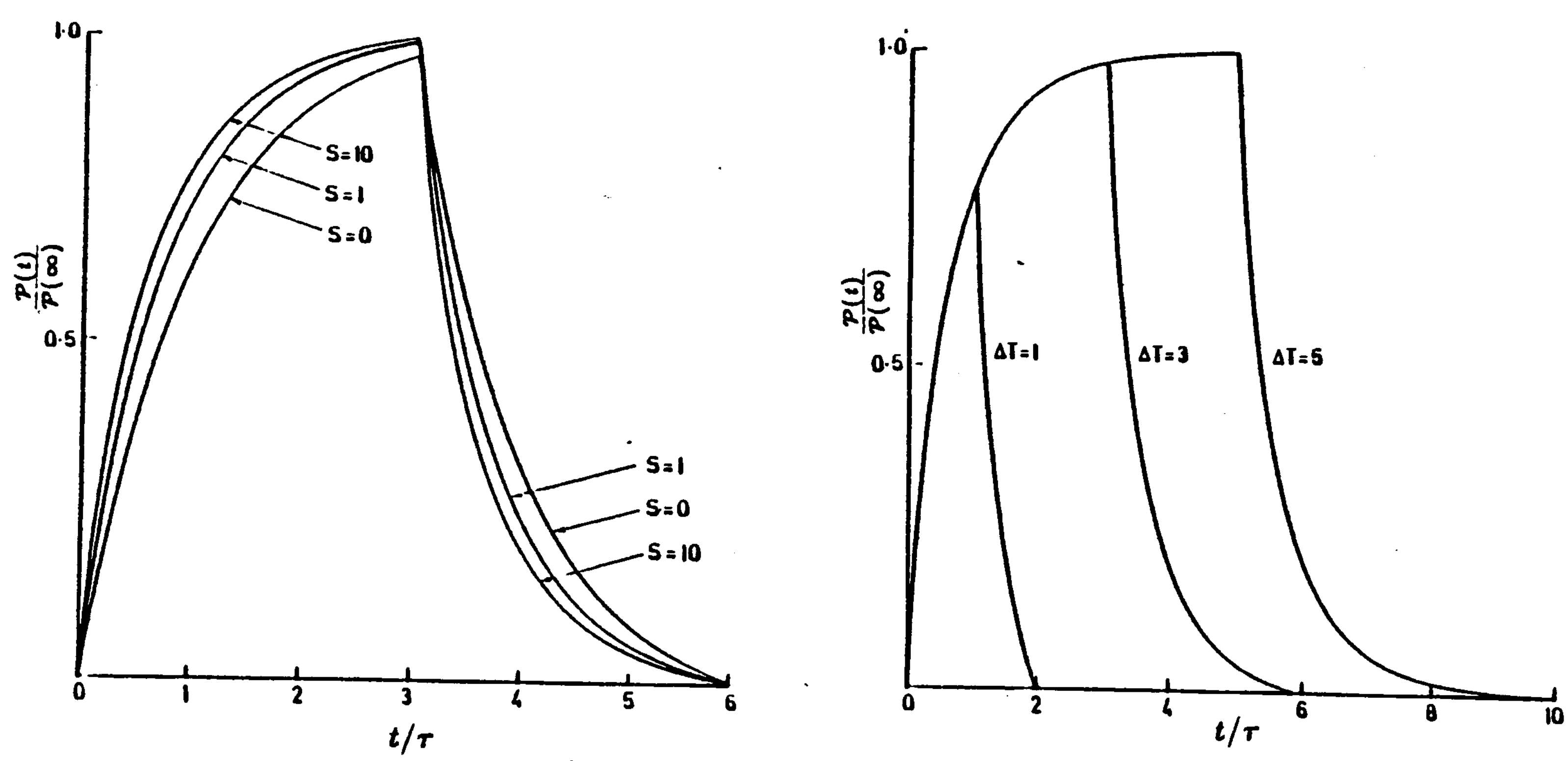

(a) (b)

Figure 7.5. The rise and fall of the photoluminescence signal due to an excitation pulse of finite length, again in the low numerical aperture limit. The cases shown are for when; (a) the absorption coefficient is $\alpha L = 2.0$ a pulse duration of 3τ and for various values of the surface recombination velocity, and (b) an absorption coefficient of $\alpha L = 2.0$, surface recombination velocity $sL = 10.0$ and pulse lengths of $\Delta T = \tau$, $\Delta T = 3\tau$ and $\Delta T = 5\tau$.

Example (iii): Harmonic Excitation

As an alternative method of measuring and displaying variations in the lifetime across a specimen Guidotti *et al.* [5] considered the phase shift between the photoluminescence signal and an harmonic generating beam. They assumed the temporal and spatial forms of the generation function could be represented as,

$$f(t) = (1 + m\cos(\omega t)) \tag{7.30a}$$

and,

$$\bar{g}(0,z) = \exp(-\alpha z), \tag{7.30b}$$

and that the surface recombination velocity, s, was zero. We now extend this analysis to include the effects of surface recombination velocity, attenuation and beam focusing. It is convenient to describe to temporal form of the generation function as

$$f(t) = \exp(i\omega t), \tag{7.31}$$

since we are interested in the phase shift of the photoluminescence and not it's magnitude. Under these circumstances we could find an expression for $F^{\star}(p - 1/\tau)$ and substitute into the general expression for the photoluminescence and then solve via the Laplace transform technique, similarly to the beam induced current case of Chapter 5. However, here we choose to demonstrate an alternative method in which we return to the time dependent diffusion equation, given in Equation (7.4), and look for solutions of the form,

$$\Delta\bar{p}(0,z,t) = \Delta\bar{p}(0,z)\exp(i\omega t). \tag{7.32}$$

Proceeding along these lines we find that $\Delta\bar{p}(0,z)$ is the solution of

$$D\frac{\partial^2}{\partial z^2}\Delta\bar{p}(0,z) - \frac{\bar{\omega}^2}{\tau}\Delta\bar{p}(0,z) = -\bar{g}(0,z) \tag{7.33}$$

where, $\bar{\omega} = \sqrt{1 + i\omega\tau}$. Equation (7.33) is easily solved by a Green's function approach and, upon intergation of $\Delta\bar{p}(0,z)$ over z, gives the photoluminescence at a frequency ω as,

$$\mathcal{P}(\omega) = \frac{K}{\bar{\omega}^2}\int_0^{\infty}\left\{1 - \left(\frac{sL}{\bar{\omega} + sL}\right)\exp(-\bar{\omega}z_0/L)\right\}\bar{g}(0,z_0)\,dz_0, \tag{7.34}$$

where K is a constant. If we now specialize to the case of low numerical apertures, such that the results can be applied to the imaging of whole wafers, $\bar{g}(0,z)$ is given by Equation (7.13) and upon substitution in Equation (7.34) we find that,

$$\mathcal{P}(\omega) \propto \frac{\bar{\omega} + (s + \alpha)L}{\bar{\omega}(\bar{\omega} + sL)(\bar{\omega} + \alpha L)}. \tag{7.35}$$

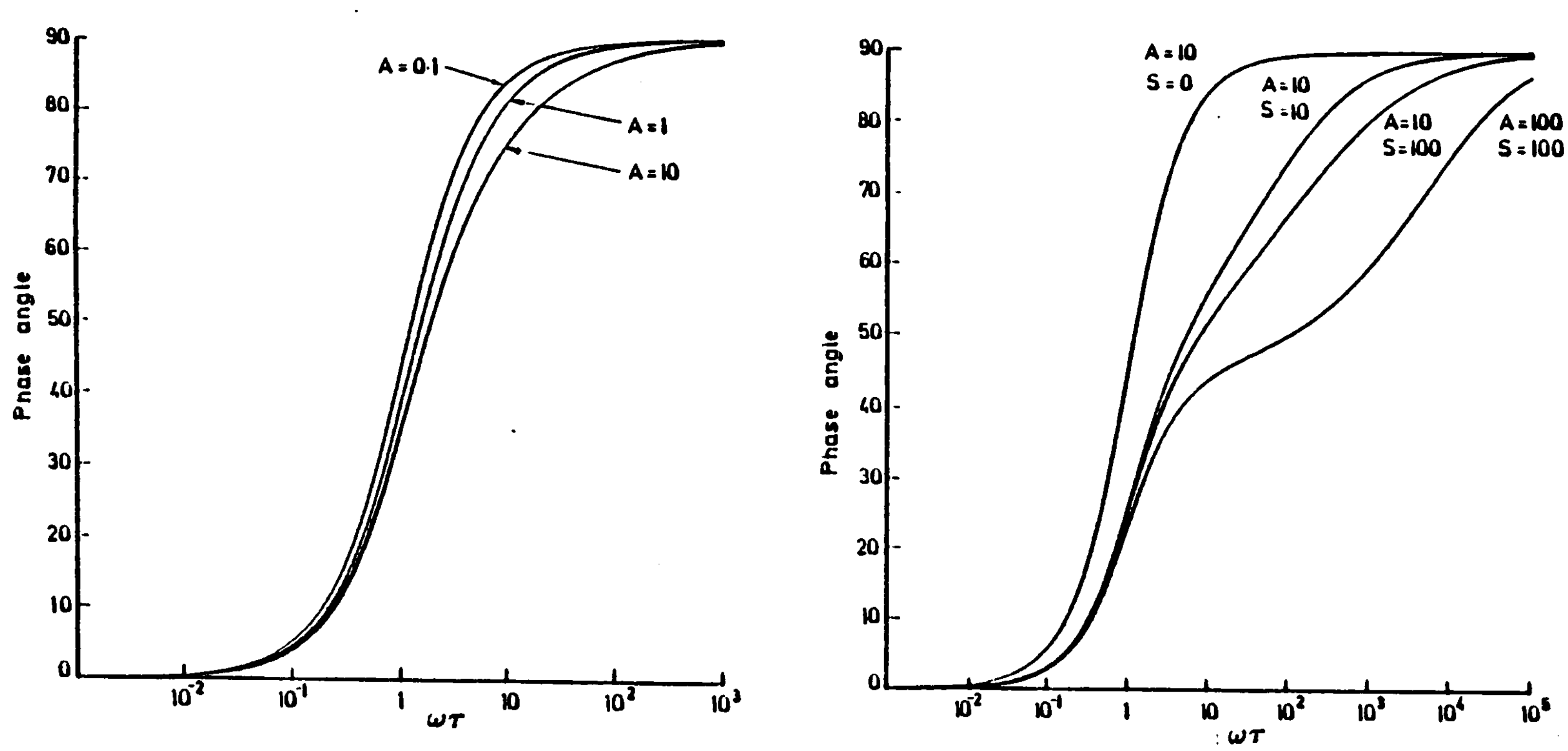

(a) (b)

Figure 7.6. The phase shift between the photoluminescence and the exciting beam for the low numerical approximation and the case when; (a) $sL = 1.0$ and various values of the normalised absorption coefficient, $A = \alpha L$, and (b) various higher values of the surface recombination velocity and absorption coefficient.

It is clear that the phase angle will be determined not only by the product $\omega\tau$, but also the surface recombination velocity and absorption coefficient. However, if we take the limit as $s \rightarrow 0$ we find the value of the absorption cofficient is unimportant and that,

$$\mathcal{P}(\omega) \propto \frac{1}{\bar{\omega}^2} \tag{7.36}$$

such that the phase angle, $\psi(\omega)$, between the photoluminescence and exciting beam is given simply as

$$\psi(\omega)\Big|_{s\rightarrow 0} = -\tan^{-1}(\omega\tau), \tag{7.37}$$

which is consistent with the results of Guidotti [5], although expressed slightly more simply here, and suggests an alternative method of measuring the minority carrier lifetime. Looking at the infinite s case we see that the phase shift now becomes,

$$\psi(\omega)\Big|_{s\rightarrow\infty} = -\tan^{-1}\left\{\frac{(\alpha L + 2)\omega\tau}{\alpha L + 1 - \omega^2\tau^2}\right\} \tag{7.38}$$

from which it is clear that there is no simple dependence of $\psi(\omega)$ on $\omega\tau$. Figure (7.6) shows the form of the phase angle as a function of $\omega\tau$ for various values of surface recombination velocity and absorption coefficient.

From Figure (7.6) we can see that the phase shift is critically dependent on the value of the surface recombination velocity, which suggests that great care is needed in extracting accurate lifetime measurements from data of this kind and that, to realistically use this method, values for both s and α must be known.

7.2 Conclusions

The photoluminescence generated in a semi-infinite semiconducting sample due to arbitrary spatial and temporal generation functions has been calculated. The results were specialised to the case where the excitation is via a high numerical aperture lens and for the cases where the temporal form of the generation function could be described by a delta function, a step or finite length pulse or a harmonic modulation of the beam intensity.

It was shown that the focussing of the beam did not greatly effect the *shape* of the resulting photoluminescence signal and that, in many cases, the correct trends could be predicted by assuming that generation only takes place at one discrete point on the surface.

Two methods were suggested for measurement of the minority carrier lifetime, the first involving the measurement of the decay of the photoluminescence after an exciting pulse of arbitrary length, and another where the phase shift between an harmonic exciting beam and the photoluminescence is measured as a function of modulation frequency. The first method has the advantage that, if data is taken at long times ($t/\tau \gg 1$) after the decay has begun, the measurement is independent of the surface recombination velocity, whereas, for the second method to be used reliably, values for the surface recombination velocity and absorption coefficient must be known. The main advantage of the second method over the first is that it is steady state and, as such, a better signal to noise ratio can be expected.

CHAPTER 8:
CONCLUSIONS AND FUTURE WORK

8.0 Conclusions

This thesis has been concerned with optical beam induced phenomena in semiconductors. The main drive behind the work has been to present a consistent model for the formation of the Optical Beam Induced Current (OBIC) and Photoluminescence (PL) signals obtained in the Scanning Optical Microscope (SOM).

We started in Chapter 2 by demonstrating the versitility of the SOM and showed some of the imaging modes that are available such as reflected light, confocal, OBIC and PL. It is from this Chapter that the motivation for the rest of the thesis stems since, from the experimental images given, it is clear that the OBIC and PL examination techniques can be extremely useful in semiconductor device examination and characterization *if* the techniques are well understood. Chapter 3 started by formulating a model which gave the distribution of minority carriers injected into a semi-infinite semiconductor by a highly convergent focussed light beam. The analysis in this Chapter differs from previous work in that the effects of beam *focussing* were included by considering an objective lens with finite numerical aperture. The resulting form of the induced minority carrier distribution was shown to be a strong function of the numerical aperture and to differ considerably from that predicted by simpler theories, where the beam shape is approximated by a simple Gaussian lateral profile. One of the most interesting points to arise here was the effect the numerical aperture has on the penetration depth of the minority carrier distribution. This point was considered in more detail by introducing a parameter termed the *information depth*, which was defined as the depth within which the majority (set at 90%) of the excess carriers existed.

Approximations to the full focussed beam theory were then considered, also in Chapter 3, by calculating the induced minority carrier distribution due to a exponentially decaying Gaussian beam, with the Gaussian half width being choosen as a function of the numerical aperture. It was found that, although the Gaussian beam was a good approximation to the full theory radially for all values of the numerical aperture, the axial fit was poor at high values of numerical aperture and over estimated the penetration depth considerably. The increase in effective absorption rate as the numerical aperture of the objective lense increases was then accounted for by introducing an effective absorption coefficient, which was shown to be a function of the numerical aperture, although this still underestimated the absorption rate at high numerical apertures.

To demonstrate the importance of the minority carrier distribution the imaging of electrically active defects in both the OBIC and PL techniques were considered as examples in Chapter 3. Here it was shown how the *contrast* obtained as a defect is imaged in both techniques depends on the illuminating lens numerical aperture and, in particular, the *resolution* of the techniques was calculated as a function of the numerical aperture. Two interesting points arose here; one being that when imaging defects which are not close to the semiconductor surface, that is at a depth of greater than about $1\mu m$, the optimum resolution is not obtained by using a high numerical aperture lens, as might initially be expected. This was shown to be true for both the OBIC and PL techniques. The other point was that the maximum resolution obtainable in the two techniques is comparable, which is interesting since, in the OBIC method it is essentially the *gradient* of the induced minority carrier distribution that is measured, whereas in the PL case it is the *intergral* of the distribution. This result is, however, in good agreement with the experimental images of Chapter 2.

We then moved on in Chapter 4 to consider the form of the steady state beam induced current in semiconductor devices where the collecting junction is parrallel to the semiconductor surface. The two main devices considered were the finite thickness Schottky barrier diode and the planar junction diode. In both cases the effect of beam focussing was again included via the numerical aperture of the objective lens. It was shown how, by measuring the OBIC signal as a function of reverse bias in the planar junction geometry, it is possible to measure the minority carrier diffusion length. However, it was clear from the results that in order to use the method reliably values for the surface recombination velocity and metalurgical junction depth have to be known, and that it is not until the collecting junction is very deep compared with the diffusion length that the results can be safely interpreted without a knowledge of the surface recombination velocity. This uncertainty in the surface recombination velocity and junction depth were removed by considering a Schottky barrier diode where the surface recombination velocity is known to be infinite owing to the presence of the surface junction. Again it was shown that it is possible to measure the minority carrier diffusion length, although here some simple curve fitting routines are neccesary since it is not possible to present the results in any simple straight line form.

Chapter 5 was an extension of the model given in Chaper 4 to include time dependence, with the device considered being a semi-infinite Schottky barrier diode. Initially it was shown how the induced minority carrier distribution becomes more diffuse and decays into the bulk of the semiconductor with time after a short light pulse. This effect was treated in more detail by the introduction of a *time dependent information depth*, which is the time dependent equivalent of the information depth as introduced in Chapter 3. It was then shown, by considering three examples for the temporal form of the generation function, how it is possible to measure the minority carrier lifetime by measuring the decay of the induced current after a light pulse of arbitrary length. One of the interesting points to note here is that the decay of the induced current is non-exponential in time even at large values of time after the decay has begun. Finally in Chapter 5 the imaging of electrically active defects as a function of time was considered and it was shown that, if images are recorded at short times after carrier injection and before the diffusion proccess has time to dominate, improved resolution OBIC images may be obtained.

Since most of the situations considered in this thesis are ones where the exciting beam is *scanned* at some velocity, v, relative to the specimen, Chapter 6 delt solely with the effect of scan velocity on the form of the beam induced current. The device geometries considered were ones where the collecting junction was either parrallel or perpendicular to the semiconductor surface. For the case when the junction was perpendicular to the surface it was shown that both the *magnitude* and *direction* of the scan speed can greatly effect the form of the collected current as a function of junction-beam separation. The effect is characterised by the ratio of the scan velocity to the diffusion velocity, and it was shown that it is not until this ratio is made very small that reliable results are obtained from the simpler scan speed independent theory. One interesting point that arose from this section was that it is possible to use the scan velocity as an extra free parameter in beam induced current problems. This is useful since usually there are two unkowns in the diffusion equation, the minority carrier lifetime, τ, and the minority carrier diffusion coefficient, D, and by being able to vary the scan speed, if only in direction, gives two simultaneous equations from which τ and D may both be found independently.

The effect of the scan velocity on the current induced in a semi-infinite Schottky barrier was then considered, also in Chapter 6, and it was shown that the collected photocurrent is a strong function of the *magnitude* of the scan speed although not it's direction. The imaging of electrically active defects using a finite beam scan speed was then considered and again it was shown that the scan speed can have a large effect. The specific case considered was that of a point defect in a semi-infinite Schottky barrier

and it was shown that, for a non zero scan speed, the *contrast* obtained as the defect is imaged in the OBIC method becomes asymmetric and decreases in magnitude with increasing scan speed. This is an important point to note since, in many scanning microscope systems, the speed of scanning used for ordinary visual inspection is much greater than that used for the recording of a permanent record, such as a photograph, and it is clear that in changing the scan speed the beam induced current image can change considerably. Finally in Chapter 6 an experimental investigation into the effects of the scan velocity on beam induced current measurements was presented. The device used for the experiments was one where the p-n junction was diffused into the sample and so neither the parrallel or perpendicular junction theories were directly applicable, however, it was shown that, in broad agreement with the theory, the beam induced current images were effected by both the magnitude and direction of the scan speed.
The photoluminescence signal generated in a semi-infinite semiconducting sample by a time varing focussed light beam was considered in Chapter 7. The analysis given was an extension of previous treatments by again including the effects of beam focussing via the objective lens numerical aperture. The form of the PL signal was then demonstrated by considering three examples for the temporal form of the generation function, these were; Delta Function excitation, Step and Finite Pulse excitation and finally Harmonic excitation. Two methods were suggested for the measurement of the minority carrier lifetime, one where the decay of the PL signal is measured as a function of time after an excitation pulse of arbitrary length and another where the phase shift between the harmonic exciting beam and the PL is measured. The first method has the advantage that, at sufficiently large times after the decay has begun, the decay rate is independent of the surface recombination velocity and absorption coefficient and, as such, it is straightforward to measure the lifetime. Whereas, in the phase shift method it was shown that the phase angle is critically dependent on both the value of the surface recombination velocity *and* absorption coefficient, and so for this method to be used with confidence values for these parameters must be known. The one advantage of the second method is that it is steady state and as such a better signal to noise ratio can be expected.

8.1 Future Work

The work presented in this thesis hopefully sets the scene for further research into the fields of both of theory and practice of semiconductor characterisation using optical beams. In this section we indicate some areas of research that follow directly from the work described so far and also present some suggestions for more future investigations.

(a) Minority Carrier Distribution

In Chapter 3 an analysis of the minority carrier distribution induced by a focussed light beam was given; it was pointed out that the analysis for the full focussed beam theory is rather involved and so various approximations where considered. The use of a Gaussian to approximate the lateral profile of the light distribution proved succesful in predicting the radial form of the induced minority carrier distribution, although the use of a simple exponetial decay for the axial form of the light distribution proved less adequate.

A more realistic approximation to the axial form of the generation function could be found by considering the rate at which the total *energy* in the exciting beam decays with distance into the semiconductor. Thus defining the function $E(z)$ as,

$$E(z) = 2\pi \int_0^{\infty} g(r,z)\, r dr, \tag{8.1}$$

we find that for *both* the Gaussian and decaying point source approximations of Chapter 3, $E(z)$ has the form

$$E_{\mathrm{a}}(z) = \alpha g_0 \exp(-\alpha z)\,. \tag{8.2}$$

However, from the expression given in Equation (3.1) for the focussed beam generation function we find that $E(z)$ has the form,

$$E_{\mathrm{f}}(z) = \frac{g_0}{\ln(\mu)} \left\{ \frac{\exp(-\alpha z) - \exp(-\alpha\mu z)}{z} \right\} \tag{8.3}$$

where, as previously, $\mu = 1 + (\sin^2\theta)/2$. This implies that a better approximation to the focussed beam theory could be obtained by using a Gaussian to represent the lateral profile of the light intensity and Equation (8.3) to represent the axial profile, such that the generation function could be written,

$$g(r,z) = \frac{g_0}{\pi c^2 \ln(\mu)} \exp\left(-\frac{r^2}{c^2}\right) \cdot \left\{ \frac{\exp(-\alpha z) - \exp(-\alpha\mu z)}{z} \right\}. \tag{8.4}$$

The disadvantage here is that when folding the Green's function with this generation function we will encounter integrals of the form $\int \exp(-ax)/x\, dx$, which means that the resulting minority carrier distribution will be expressed in terms of Exponential

Integrals instead of simple exponentials as was the case when $\exp(-\alpha z)$ was used. However, since the Exponential Integal is a well known function this should not present any real problems.

(b) Scan Speed Dependent Photoluminescence

Chapter 6 demonstrated how the speed of scanning in a scanning optical microscope can effect the form of the beam induced currents in both Schottky barrier diodes and devices where p-n junctions are perpendicular to the semiconductor surface. As an extension to this work it would be interesting to consider the effect of the scan speed on the PL signal obtained from a semiconducting sample.

The calculation would be fairly straightforward since the form of the *scan speed dependent* induced minority carrier distribution was found in Chapter 6 and, as was shown in Chaper 7, this leads directly to the PL signal. It would also be possible to investigate the effect of the scan speed on the contrast obtained as an electrically active defect is imaged in the PL technique since, as was shown in Chapter 3, the contrast function is directly proportional to the induced minority carrier distribution.

(c) Confocal Photoluminescence

An extension to the standard scanning photoluminescence technique could be made by using the confocal mode of the scanning optical microscope, as described briefly in Chapter 2. This would allow the sectioning properties of the confocal system to be used to give three dimensional information about the PL signal and would also probabaly increase the resolution. To be sure of the effect of the confocal system on the resolution of the PL technique a model would have to be developed to explain the imaging properties. This should be fairly straightforward using standard imaging theory, since the object to be imaged is essentially the minority carrier distribution, who's form is well known, as it is this distribution which leads to the PL signal.

(d) Modelling Real Devices

One of the main reasons for using optical beams to examine semiconductors is to try and characterize *real* devices, that is complicated structures consisting of many p-n junctions of various geometries. This thesis has modelled only the simplest of devices such as the Schottky barrier diode, a planar p-n junction diode and a device where a p-n junction of infinite depth is perpendicular to the semiconductor surface.

These ideal devices are extremely useful in obtaining a physical picture for the way in which the optical beam induced currents are formed since it is possible to calculate the beam induced currents analytically, or at worst, in terms of a single integral. The reasons for this being the simple form of the boundary conditions on the solution of the diffusion equation and the symmetry involved in problems. However, if we wish to model a *real* device the boundary conditions become much more complicated and the symmetry collapses leaving a problem which, in general, is intractible analytically. The way forward from here is then obviously via a computer based solution of the problem. Since the problem of calculating the beam induced current is essentially that of solving a partial differential equation there are a wide variety of standard methods available. One could imagine a completely general computer based solution where the user had simply to describe the set of boundary conditions, such as the position of the p-n junctions and surfaces, of the device to be modelled and the form of the beam induced current could be found. Although this may be extremely useful for a commercial semiconductor device manufacturer, very little would be contributed towards the basic understanding of the mechanism by which the beam induced current signals are formed. For this reason no purely computer base solutions have been developed during the work for this thesis.

APPENDIX A:

Calculation of the Hankel Transform of the Focussed Beam Generation Function

The surface integral in Equation (3.26) can be written in the form,

$$I_{\text{surf}} = \frac{\bar{g}(\nu, u)}{g_0 A \exp(-\alpha_u u) \exp(-u\beta\Delta^2)}$$
$$= \int_S \exp(-i2u\rho\Delta\cos\theta) \exp(-u\beta\rho^2)\, dS$$

that is,

$$I_{\text{surf}} = \int_S f(\rho, \theta)\, \rho d\rho d\theta, \tag{A.1}$$

where, as in Equation (3.26) S represents the region of overlap in Figure (3.4). The integration over the central circle $\rho = 1 - \Delta$ can be evaluated as [1 p.360]

$$I_{\text{circ}} = \int_0^{2\pi} \int_0^{1-\Delta} \exp(-i2u\rho\Delta\cos\theta) \exp(-u\beta\rho^2)\, \rho d\rho d\theta$$
$$= 2\pi \int_0^{1-\Delta} \exp(-u\beta\rho^2) J_0(2u\Delta\rho)\, \rho d\rho, \tag{A2}$$

where J_0 is a Bessel function of the first kind and zero order. We're now left to find to surface integral over the sectors such as the one shaded in Figure (3.4). Denoting the integral over this shaded region as $I_{\text{qd}}^{(1)}$ we have,

$$I_{\text{qd}}^{(1)} = \int_{1-\Delta}^{\sqrt{1-\Delta^2}} \int_{\theta_1}^{\pi/2} f(\rho, \theta)\, \rho d\rho d\theta, \tag{A3}$$

where θ_1 is the value of θ at which the vector ρ intersects the $\rho_1 = 1$ circle and can be found from the cosine rule as,

$$\cos(\theta_1) = \frac{1 - \rho^2 - \Delta^2}{2\rho\Delta} = \lambda \tag{A4}$$

and so $\theta_1 = \cos^{-1}\lambda$. Similarly the integration over the next sector can be written in the form

$$I_{\text{qd}}^{(2)} = -\int_{\sqrt{1-\Delta^2}}^{1-\Delta} \int_{\pi/2}^{\theta_2} f(\rho, \theta)\, \rho d\rho d\theta, \tag{A5}$$

here θ_2 is found from the intersection of ρ and the $\rho_2 = 1$ circle, giving

$$\cos(\theta_2) = \frac{\rho^2 + \Delta^2 - 1}{2\rho\Delta} = -\lambda \tag{A6}$$

such that $\theta_2 = \cos^{-1}(-\lambda)$. Following along these lines the third and fourth sector contibutions take the form

$$I_{\rm qd}^{(3)} = \int_{1-\Delta}^{\sqrt{1-\Delta^2}} \int_{\pi+\theta_1}^{3\pi/2} f(\rho,\theta)\,\rho d\rho d\theta, \tag{A7}$$

and,

$$I_{\rm qd}^{(4)} = -\int_{\sqrt{1-\Delta^2}}^{1-\Delta} \int_{3\pi/2}^{\pi+\theta_2} f(\rho,\theta)\,\rho d\rho d\theta. \tag{A8}$$

The surface integral, ignoring the contribution from the the $\rho = 1-\Delta$ circle, $I_{\rm circ}$ temporarily, can be expressed as the summation of Equations (A3), (A5), (A7) and (A8), that is,

$$I_{\rm qd} = I_{\rm qd}^{(1)} + I_{\rm qd}^{(2)} + I_{\rm qd}^{(3)} + I_{\rm qd}^{(4)},$$

such that,

$$I_{\rm qd} = \int_{1-\Delta}^{\sqrt{1-\Delta^2}} \left[\int_{\theta_1}^{\pi/2} - \int_{\theta_2}^{\pi/2} + \int_{\pi+\theta_1}^{3\pi/2} - \int_{\pi+\theta_2}^{3\pi/2}\right] f(\rho,\theta)\,d\theta\rho d\rho. \tag{A9}$$

The first and third terms and the second and fourth terms in Equation (A9) can be combined by making the substitution $\theta \to \theta - \pi$ in the second and fourth terms giving,

$$\begin{aligned} I_{\rm qd} = \int_{1-\Delta}^{\sqrt{1-\Delta^2}} & \left[2\int_{\theta_1}^{\pi/2} \exp(-u\beta\rho^2)\cos[2u\Delta\rho\cos\theta]\,d\theta \right. \\ & - \left. 2\int_{\theta_2}^{\pi/2} \exp(-u\beta\rho^2)\cos[2u\Delta\rho\cos\theta]\,d\theta\right] \rho d\rho, \end{aligned}$$

that is,

$$I_{\rm qd} = \int_{1-\Delta}^{\sqrt{1-\Delta^2}} \left[4\int_{\theta_1}^{\pi/2} \exp(-u\beta\rho^2)\cos[2u\Delta\rho\cos\theta]\,d\theta\right] \rho d\rho \tag{A10}$$

where, in the last line we've used the identity $\cos^{-1}(-\lambda) = \pi - \cos^{-1}(\lambda)$. One further simplification can be made to Equation (A10) by introducing the new variable $\theta \to \theta - \pi/2$, under this transformation the full expression, including the contribution from the $\rho = 1-\Delta$ circle given in Equation (A2), for the Hankel transform of the generation function $\bar{g}(\nu,u)$ becomes,

$$\begin{aligned} \bar{g}(\nu,u) = & g_0 A\exp(-\alpha_u u)\exp(-u\beta\Delta^2)\left\{2\pi\int_0^{1-\Delta} \exp(-u\beta\rho^2)\,J_0(2u\Delta\rho)\,\rho d\rho \right. \\ & + \left. 4\int_{1-\Delta}^{\sqrt{1-\Delta^2}} \int_0^{\sin^{-1}(\lambda)} \exp(-u\beta\rho^2)\cos(2u\Delta\rho\sin\theta)\,d\theta\rho d\rho\right\}. \end{aligned} \tag{A11}$$

APPENDIX B:

Calculation of the Hankel Transform of the Focussed Beam Carrier Distribution

To simplify the analysis it is useful to split the Greens function of Equation (3.14) into two terms, that is

$$G(\nu,u|u_0) = \left\{ G^{(1)}(\nu,u|u_0) + \left(\frac{\phi - s}{\phi + s}\right) G^{(2)}(\nu,u|u_0) \right\}, \qquad (B1)$$

where $G^{(1)}(\nu,u|u_0) = \exp(-\phi|u-u_0|)/\phi$ and $G^{(2)}(\nu,u|u_0) = \exp(-\phi(u+u_0))/\phi$. Folding the Greens function and source can now be split into two parts, considering the second part first we have,

$$\begin{aligned}
\Delta\bar{p}^{(2)}(\nu,u) &= -\frac{1}{Db^2}\int_0^\infty G^{(2)}(\nu,u|u_0)\bar{g}(\nu,u_0)\,du_0 \\
&= -\frac{g_0 A \exp(-\phi u)}{Db^2\phi}\left\{ 2\pi \int_0^\infty \int_0^{1-\Delta} \exp(-\phi u_0)\exp(-\Lambda u_0) J_0(2\Delta\rho u_0)\,\rho d\rho du_0 \right. \\
&\left. +4 \int_0^\infty \int_0^{1-\Delta} \int_0^{\sin^{-1}(\lambda)} \exp(-\phi u_0)\exp(-\Lambda u_0)\cos(2\Delta\rho u_0 \sin\theta)\, d\theta \rho d\rho du_0 \right\},
\end{aligned} \qquad (B2)$$

the expression for $\bar{g}(\nu,u)$ coming from either Equation (A11) or (3.27). The u_0 integrations can be performed using [1 p.707],

$$\int_0^\infty \exp\{-(\phi+\Lambda)u_0\} J_0(2\Delta\rho u_0)\,du_0 = \frac{1}{\sqrt{(\phi+\Lambda)^2 + 4\Delta^2\rho^2}}, \qquad (B3a)$$

and, [1 p.477]

$$\int_0^\infty \exp\{-(\phi+\Lambda)u_0\}\cos(2\Delta\rho\sin\theta u_0)\,du_0 = \frac{\Lambda+\phi}{(\Lambda+\phi)^2 + 4\Delta^2\rho^2\sin^2\theta}, \qquad (B3b)$$

the θ intergration can then be performed using [1 p.152],

$$\int_0^{\sin^{-1}(\lambda)} \frac{\Lambda+\rho}{[(\Lambda+\phi)^2 + 4\Delta\rho^2\sin^2\theta]}\,d\theta = \Gamma(\phi,\rho)\tan^{-1}\left\{\frac{\tan(\sin^{-1}(\lambda))}{(\Lambda+\phi)\Gamma(\phi,\rho)}\right\}, \qquad (B4)$$

where,

$$\Gamma(\phi,\rho) = \frac{1}{\sqrt{(\phi+\Lambda)^2 + 4\Delta^2\rho^2}}. \qquad (B6)$$

This gives an expression for $\Delta\bar{p}^{(2)}(\nu,u)$ as,

$$\Delta\bar{p}^{(2)}(\nu,u) = -\frac{g_0 A\exp(-\phi u)}{Db^2\phi}\left[2\pi\int_0^{1-\Delta}\Gamma(\phi,\rho)\,\rho d\rho + 4\int_{1-\Delta}^{\sqrt{1-\Delta^2}}\tan^{-1}\left\{\frac{\tan(\sin^{-1}(\lambda))}{(\Lambda+\phi)\Gamma(\phi,\rho)}\right\}\Gamma(\phi,\rho)\,\rho d\rho\right] \quad (B7)$$

Unfortunately, owing to the modulus sign in the exponent of $G^{(1)}(\nu,u|u_0)$ we are unable to simplify the form of $\Delta\bar{p}^{(1)}(\nu,u)$, this leaves the final expression for $\Delta\bar{p}(\nu,u)$ as the sum of $\Delta\bar{p}^{(1)}(\nu,u)$ and $\Delta\bar{p}^{(2)}(\nu,u)$ giving,

$$\begin{aligned}\Delta\bar{p}(\nu,u) = -\frac{g_0}{Db^2\phi}\Bigg\{\int_0^{\infty}\exp\left(-\phi|u-u_0|\right)\Bigg[2\pi\int_0^{1-\Delta}\exp\left(-\Lambda u_0\right)J_0(2\Delta\rho u_0)\rho\,d\rho \\ + 4\int_{1-\Delta}^{\sqrt{1-\Delta^2}}\int_0^{\sin^{-1}(\lambda)}\exp\left(-u\rho^2\beta\right)\cos(2u\Delta\rho\sin\theta)\,d\theta\rho d\rho\Bigg]\,du_0 \\ + \left(\frac{\phi-s}{\phi+s}\right)\exp(-\phi u)\Bigg[2\pi\int_0^{1-\Delta}\Gamma(\phi,\rho)\,\rho d\rho \\ + 4\int_{1-\Delta}^{\sqrt{1-\Delta^2}}\tan^{-1}\left\{\frac{\tan(\sin^{-1}(\lambda))}{(\Lambda+\phi)\Gamma(\phi,\rho)}\right\}\Gamma(\phi,\rho)\,\rho d\rho\Bigg]\Bigg\}.\end{aligned} \quad (B8)$$

APPENDIX C:

Derivation of The Finite Thickness Schottky Barrier Green's Function

The Greens function, $G(0,z|z_0)$ is, by definition, the solution of Equation (4.5) with the source term, $\bar{g}(0,z)/D$, replaced by a Dirac-delta function, such that

$$\frac{\partial^2}{\partial z^2}G(0,z|z_0) - \frac{G(0,z|z_0)}{L^2} = -\delta(z-z_0), \tag{C.1}$$

where the solution is subject to the boundary conditions of Equations (4.25) and (4.26). The solution has two distinct domains, that is $z < z_0$ and $z > z_0$. In each of these regions the right-hand side of Equation (C.1) is zero and so the Green's function can be written,

$$G(0,z|z_0) = Ae^{-z/L} + Be^{z/L}, \qquad \text{for} \qquad z < z_0, \tag{C.2a}$$

and,

$$G(0,z|z_0) = Ce^{-z/L} + De^{z/L}, \qquad \text{for} \qquad z > z_0, \tag{C.2b}$$

where A, B, C and D are constants. Equation (C.2a) has to satisfy the boundary condition at $z = w$, i.e. Equation (4.25), and Equation (C.2b) has to satisfy the boundary condition at $z = d$, given in Equation (4.26). Applying the these conditions to the Green's function shows that the constants have to satisfy;

$$Ae^{-w/L} + Be^{w/L} = 0, \tag{C.3a}$$

and,

$$D(1 - s_bL)e^{d/L} - C(1 + s_bL)e^{-d/L} = 0. \tag{C.3b}$$

We now have two equations and four unknowns. Extra constraints on the constants can be found by considering the solution at the special point $z = z_0$. For the Green's function to be continous at this point the solutions obtained in Equations (C.2a) and (C.2b) must be equal in the limit as $z \to z_0$, giving,

$$(C - A)e^{-z_0/L} + (D - B)e^{z_0/L} = 0. \tag{C.4}$$

The constraint on the gradients at $z = z_0$ can be found by integrating the diffusion equation, given in Equation (C.1), from some constant, say $z = z_1$ to z such that,

$$\int_{z_1}^{z} \frac{\partial^2}{\partial \bar{z}^2} G(0,\bar{z}|z_0)\, d\bar{z} - \frac{1}{L^2}\int_{z_1}^{z} G(0,\bar{z}|z_0)\, d\bar{z} = -\theta(z-z_0), \tag{C.5}$$

that is,

$$-\frac{\partial}{\partial \bar{z}} G(0,\bar{z}|z_0)\Big|_{\bar{z}=z} + \frac{\partial}{\partial \bar{z}} G(0,\bar{z}|z_0)\Big|_{\bar{z}=z_1} + \frac{1}{L^2}\int_{z_1}^{z} G(0,\bar{z}|z_0)\, d\bar{z} = \theta(z-z_0). \tag{C.6}$$

Here $\bar{z}$ is an integration variable and $\theta(z-z_0)$ is a step function defined to be unity for $z > z_0$ and zero for $z < z_0$. We can now consider the regions on either side of the Delta function by putting, $z = z_0 + \epsilon$ and $z = z_0 - \epsilon$ in turn, where ϵ is some real constant which can be as small as we please, since then from Equation (C.6) we have,

$$-\frac{\partial}{\partial \bar{z}} G(0,\bar{z}|z_0)\Big|_{\bar{z}=z_0+\epsilon} + \frac{\partial}{\partial \bar{z}} G(0,\bar{z}|z_0)\Big|_{\bar{z}=z_1} + \frac{1}{L^2}\int_{z_1}^{z_0+\epsilon} G(0,\bar{z}|z_0)\, d\bar{z} = 1, \tag{C.7a}$$

and,

$$-\frac{\partial}{\partial \bar{z}} G(0,\bar{z}|z_0)\Big|_{\bar{z}=z_0-\epsilon} + \frac{\partial}{\partial \bar{z}} G(0,\bar{z}|z_0)\Big|_{\bar{z}=z_1} + \frac{1}{L^2}\int_{z_1}^{z_0-\epsilon} G(0,\bar{z}|z_0)\, d\bar{z} = 0, \tag{C.7b}$$

subtracting Equation (C.7b) from (C.7a) yields,

$$-\frac{\partial}{\partial \bar{z}} G(0,\bar{z}|z_0)\Big|_{\bar{z}=z_0-\epsilon}^{\bar{z}=z_0+\epsilon} + \frac{1}{L^2}\int_{z_0-\epsilon}^{z_0+\epsilon} G(0,\bar{z}|z_0)\, d\bar{z} = 1, \tag{C.8}$$

and, letting $\epsilon \to 0$, we finally obtain the condition on the gradient of the Green's function on each side of the Delta function as,

$$\frac{\partial}{\partial \bar{z}} G(0,\bar{z}|z_0)\Big|_{\bar{z}=z_0-0}^{\bar{z}=z_0+0} = -1. \tag{C.9}$$

Equation (C.9) can be used to give the fourth equation relating the four constants A, B, C and D, such that now we have;

$$Ae^{-w/L} + Be^{w/L} = 0, \tag{C.10a}$$

$$D(1 - s_b L)e^{d/L} - C(1 + s_b L)e^{-d/L} = 0, \tag{C.10b}$$

$$(C - A)e^{-z_0/L} + (D - B)e^{z_0/L} = 0, \tag{C.10c}$$

$$(C - A)e^{-z_0/L} - (D - B)e^{z_0/L} = L. \tag{C.10d}$$

It is routine to solve between the above four equations to give expressions for the constants, this gives,

$$A = -e^{2w/L}B = \frac{-L}{2}e^{-(z_0-2w)/L} \cdot \left\{ \frac{e^{2z_0/L} + \left(\frac{1-s_bL}{1+s_bL}\right)e^{2d/L}}{e^{2w/L} + \left(\frac{1-s_bL}{1+s_bL}\right)e^{2d/L}} \right\}, \tag{C.11}$$

and,

$$C = \left(\frac{1 - s_b L}{1 + s_b L}\right) e^{2d/L} D = \frac{L}{2} e^{-(z_0 - 2d)/L} \left\{ \frac{e^{2z_0/L} - e^{2w/L}}{e^{2d/L} + \left(\frac{1+s_b L}{1-s_b L}\right) e^{2w/L}} \right\}. \quad (C.12)$$

Substituting the above values for A, B, C and D into the relevant expressions for the Green's function yields an expression for $G(0, z|z_0)$ as,

$$G(0, z|z_0)\Big|_{z<z_0} = L e^{-(z_0 - w)/L} \left\{ \frac{e^{2z_0/L} + \Gamma e^{2d/L}}{e^{2w/L} + \Gamma e^{2d/L}} \right\} \sinh\left(\frac{z - w}{L}\right), \quad (C.13a)$$

and,

$$G(0, z|z_0)\Big|_{z>z_0} = \frac{L}{2} e^{-(z_0 - d)L} \left(\frac{e^{2z_0/L} - e^{2w/L}}{e^{2w/L} + \Gamma e^{2d/L}} \right) \left(e^{(z-d)/L} + \Gamma e^{-(z-d)/L} \right), \quad (C.13b)$$

where the parameter Γ is defined in Equation (4.29). Equations (C.13a) and (C.13b) can be combined to give a single expression for the Green's function, applicable for all z, which is given in Equation (4.27).

APPENDIX D:

Publications Resulting From This Work

(1) T. Wilson and P. D. Pester, Optical Beam Induced Minority Carrier Distribution in Semiconductors, *Phys. Stat. Sol.(a)*, **97**, 323, (1986)

(2) T. Wilson and P. D. Pester, The Effect of Scan Velocity on the Measurement of Semiconductor Parameters by Optical Beam Excitation, *J. Appl. Phys.*, **61**, 2307, (1987)

(3) T. Wilson and P. D. Pester, Theory of Scan Speed Dependent Optical Beam Induced Current Images in Semiconductors, *Optik*, **76**, 18, (1987)

(4) T. Wilson and P. D. Pester, An Analysis of the Photoinduced Current From a Finely Focussed Light Beam in Planar p/n Junctions and Schottky Barrier Diodes, *I.E.E.E. Trans. Elect. Devices*, **ED-34**, 1564, (1987)

(5) T. Wilson and P. D. Pester, An Analysis of the Photoluminescence Generated in a Semi-infinite Semiconductor Slab by a Time Varying Focussed Convergent Laser Beam, *J. Appl. Phys.*, **63**, 871, (1988)

(6) E. M. McCabe, P. D. Pester and T. Wilson, Optical Beam Induced Current Imaging in Scanning Optical Microscopy, *Proc. SPIE. Vol* **809**, *Scanning Imaging Tech.* 31, (1987)

(7) T. Wilson and P. D. Pester, Information Depth in Optical Beam Induced Examination of Semiconductor Materials and Devices, *Phys. Stat. Sol.(a)*, **103**, 892, (1987)

(8) P. D. Pester and T. Wilson, An Analysis of the Photocurrent Induced in a Semi-infinite Schottky Barrier by a Time Varying Focussed Light Beam, *Phys. Stat. Sol.(a)*, **105**, 649, (1988)

(9) P. D. Pester and T. Wilson, Time Dependent Information Depth in Optical Probing of Semiconductor Materials and Devices, *Phys. Stat. Sol.(a)*, **106**, 577, (1988)

(10) P. D. Pester and T. Wilson, Time Dependent Theory of Optical Beam Induced Current Imaging of Defects in Semiconductors, *J. Appl. Phys.*, **64**, 1131, (1988)

(11) P. D. Pester and T. Wilson, Scan Speed Effects in Optical Beam Induced Current Imaging, *SPIE Santa Clara Symposium on Microlithography*, (1988)

(12) P. D. Pester and T. Wilson, Scanning Optical Microscopy of Semiconductor Devices, *To Be Published in Texas Instruments Tech. Journal* (1988)

(13) P. D. Pester and T. Wilson, Photoluminescence and Optical Beam Induced Current Imaging of Defects, *To Be Published in SPIE Proc. of The International Congress on Optical Science and Engineering, Hamburg*, (1988)

(14) P. D. Pester and T. Wilson, Photoluminescence and Optical Beam Induced Current Imaging of Defects, *To Be Published in Proc. of the 15th International Conference on Defects in Semiconductors, Budapest*, (1988)

In Preparation

(1) The Minority Carrier Distribution Induced in a Semi-infinite Semiconductor Due to a Highly Convergent Focussed Light Beam. *with T. Wilson*

(2) Comparison of Scanning Photoluminescence and Scanning Cathodoluminescence Images of Indium Phosphide. *with T. Wilson*

(3) Application of the Scanning Optical Microscope to the Examination of Semiconducting Power Devices. *with T. Wilson*

REFERENCES

Chapter 1

(1) J. Bardeen and W. H. Brattain, *Phys. Rev.*, **74**, 230, (1948)

(2) W. H. Brattain and J. Bardeen, *Phys. Rev.*, **74**, 231, (1948)

(3) J. Bardeen and W. H. Brattain, *Phys. Rev.*, **75**, 1208, (1949)

(4) W. Shockley, G. L. Pearson and J. R. Haynes, *Bell System Tech. Journal.*, **28**, 344, (1949)

(5) J. R. Haynes and W. Shockley, *Phys. Rev.*, **81**, 835, (1951)

(6) J. Bardeen, *Bell System Tech. Journal.*, **29**, 469, (1949)

(7) F. S. Goucher, *Phys. Rev.*, **78**, 816, (1950)

(8) F. S. Goucher, *Phys. Rev.*, **81**, 475, (1951)

(9) F. S. Goucher, G. L. Pearson, Sparks, Teal and W. Shockley *Phys. Rev.*, **81**, 637, (1951)

(10) L. B. Valdes, *Proc. Inst. Radio Engs.* **40**, 1420, (1952)

(11) D. B. Holt, *Quantitative Scanning Electron Microscopy*, (Academic Press, New York, 1974)

(12) B. Ralph, P. E. Echlin, H. J. G. Gunderson and D. C. Joy, *The Microscopy of Semiconducting Materials*, Proc. RMS Conf., Oxford, 1979, J. Microscopy, **118**, Parts 1 and 3, (1980)

(13) C. A. Warwick, *Scanning Microscopy*, **1**, 51, (1987)

(14) A. Cohn and G. Calendonia, *J. Appl. Phys.*, **41**, 3767, (1970)

(15) R. Shimizu, T. Ikuta, T. E. Everhart and W. J, DeVore, *J. Appl. Phys.*, **46**, 1581, (1975)

(16) R. Shimizu and T. E. Everhart, *Optik*, **36**, 59, (1972)

(17) C. Donolato, *Phys. Stat. Sol.(a)*, **65**, 649, (1981)

(18) T. Wilson and C. J. R. Sheppard, *Theory and Practice of Scanning Optical Microscopy*, (Academic Press, 1984)

(19) T. Wilson and J. N. Gannaway, *Electron Lett.*, **14**, 507, (1978)

(20) R. J. Nelson, *Inst. Phys. Conf. Ser.*, **45**, 256, (1978)

(21) J. Marek, A. G. Elliot, V. Wilke and R. Geiss, *Appl. Phys. Lett.*, **49**, 1732, (1986)

(22) T. Wilson, W. R. Osicki, J. N. Gannaway and G. R. Booker, *J. Mat. Sci.*, **14**, 961, (1979)

(23) T. Wilson and E. M. McCabe, *J. Appl. Phys.*, **59**, 2638, (1986)

Chapter 2

(1) T. Wilson and C. J. R. Sheppard, *Theory and Practice of Scanning Optical Microscopy*, (Academic Press, 1984)

(2) T. Wilson and J. N. Gannaway, *Electron Lett.*, **14**, 507, (1978)

(3) B. Drugge, E. Norlander and P. Edlund, *Physica Scripta*, **24**, 392, (1981)

(4) T. H. DiStefano in, *Nondestructive Evaluation of Semiconductor Materials and Devices*, (Plenum, New York, 1979)

(5) R. J. Nelson, *Inst. Phys. Conf. Ser.*, **45**, 256, (1978)

(6) J. Marek, A. G. Elliot, V. Wilke and R. Geiss, *Appl. Phys. Lett.*, **49**, 1732, (1986)

Chapter 3

(1) F. S. Goucher, *Phys. Rev.*, **81**, 475 (1951)

(2) F. S. Goucher, G. L. Pearson, Sparks, Teal and W. Shockley, *Phys. Rev.*, **81**, 637 (1951)

(3) W. Van Roosbroeck, *Phys. Rev.*, **91**(2), 282, (1953)

(4) W. Van Roosbroeck, *J. Appl. Phys.*, **26** (4), 380, (1955)

(5) G. H. Bryan, *Proc. Camb. Phil. Soc.*, **7**, (1891)

(6) C. Donolato, *Phys. Stat. Sol.(a)*, **65**, 649 (1981)

(7) F. Berz and H. Kuiken, *Sol. St. Elect.*, **19**, 437 (1976)

(8) O. Engström and B.Drugge, P. A. Tove, *Physica Scripta*, **18**, 357, (1978)

(9) S. M. Davison, R. M. Innes and S.M. Lindsay, *Sol. St. Elect.*, **25**(4), 261, (1982)

(10) C. Hu and C. Drowley, *Sol. St. Elect.*, **21**, 965, (1978)

(11) T. Wilson and P. D. Pester, *J. Appl. Phys.*, **61**, 2307, (1987)

(12) A. Sinha and S. K. Chattopadhyaya, *Sol. St. Elect.*, **19**, 3345, (1976)

(13) T. Wilson and P. D. Pester *Phys. Stat. Sol.(a)*, **97**, 323, (1986)

(14) T. Wilson and E. M. McCabe, *J. Appl. Phys.*, **58**, 2638, (1986)

(15) M. Born and E. Wolf. *Principles of Optics*, (Pergamon, Oxford, 1975)

(16) S. M. Sze, *Physics of Semiconductor Devices*, (Wiley, New York, 1981)

(17) P. M. Morse and H. Feshbach, *Methods of Theoretical Physics*, (McGraw-Hill, New York, 1953)

(18) H. S. Carslaw and J. C. Jeager, *Conduction of Heat in Solids*, (Oxford University Press, Oxford, 1959)

(19) R. M. Bracewell, *The Fourier Transform and its Applications*, (McGraw-Hill, New York, 1965)

(20) W. C. Dash and R. Newman *Phys. Rev.*, **99**, 1151, (1955)

(21) T. Wilson and P. D. Pester *Phys. Stat. Sol.(a)*, **103**, 631 (1987)

(22) P. D. Pester and T. Wilson *Phys. Stat. Sol.(a)*, **106**, 577 (1988)

(23) M. Abramowitz and I. Stegun, *Hanbook of Mathematical Functions* (Dover, New York 1970)

(24) C. Donolato, Optik, **52**, 19 (1979)

(25) T.Wilson and E. M. McCabe, *J. Appl. Phys.*, **61**, 191 (1986)

(26) T. Wilson and P. D. Pester, Optik **76**, 18 (1987)

(27) T. Wilson, E. M. McCabe and D. K. Hamilton, *J. Appl. Phys.*, **59**(3), 702, (1986)

(28) B. L. Moiseiwitsch, *Integral Equations*, (Longman, London, 1977) p.43

(29) P. Blood and J. W. Orton, *Rep. Prog. Phys.* **41**, 157 (1978)

(30) K. Lohnert and E. Kubalek, *Phys. Stat. Sol.(a)*, **83**, 307 (1984)

(31) T. Wilson and P. D. Pester, *J. Appl. Phys.*, **63**, 871 (1988)

(32) O. Von Roos, *J. Appl. Phys.*, **54**, 1390, (1983)

(33) A. Jakubowicz, *J. Appl. Phys.*, **58**, 4354, (1985)

(34) G. W. t'Hooft and C. Van Opdorp, *J. Appl. Phys.*, **41**, 1065, (1986)

(35) J. Stamnes, *Waves in Focal Regions*, (Adam Hilger, Bristol, 1986)

(36) G. N. Watson, *Treatise on the Theory of Bessel Functions*, (Cambridge University Press, Cambridge, 1966)

(37) I. S. Gradshteyn and I. M. Ryzhik, *Tables of Integrals, Series, and Products* (Academic Press, Orlando, 1980)

Chapter 4

(1) E. N. Clarke (*Chairman*), *Proc. Inst. Radio Eng.* **49**, 1292, (1961)

(2) D. K. Schoder and H. C. Nathanson, *Sol. St. Elect.*, **13**, 577, (1970)

(3) S. M. Davidson, R. M. Innes and S. M. Lindsay, *Sol. St. Elect.*, **25**, 261, (1982)

(4) C. Hu and C. Drowley, *Sol. St. Elect.*, **21**, 965, (1978)

(5) B. Drugge, E. Nordlander and P. Edlund, *Physica Scripta*, **24**, 392, (1981)

(6) W. Shockley, G. L. Pearson and J. R. Haynes, *Bell System Tech. Journal.*, **28**, 344, (1949)

(7) F. S. Goucher, *Phys. Rev.*, **81**, 475, (1951)

(8) J. R. Haynes and W. Shockley, *Phys. Rev.*, **81**, 835, (1951)

(9) F. S. Goucher, G. L. Pearson, Sparks, Teal and W. Shockley, *Phys. Rev.*, **81**, 637, (1951)

(10) P. M. Morse and H. Feshbach, *Methods of Theoretical Physics*, (McGraw-Hill, New York, 1953)

(11) T. Wilson and P. D. Pester, IEEE Trans on Electron Devices, **ED-34**, 1564, (1987)

(12) F. S. Goucher *Phys. Rev.*, **78**, 816, (1950)

(13) O. Engström, B. Drugge and P. A. Tove, *Phys. Scripta*, **18**, 357, (1968)

(14) C. H. Seager *J. Appl. Phys.*, **53**, 5968, (1982)

(15) C. A. Dimitriadis, *I.E.E.E. Trans. Electron Devices*, **32**, 1761, (1985)

(16) T. Wilson and P. D. Pester, *Phys. Stat. Sol.(a)*, **97**, 323, (1986)

(17) J. Marek, *J. Appl. Phys.*, **55**, 318, (1984)

(18) R. M. Bracewell, *The Fourier Transfrom and its Applications*, (McGraw-Hill, New York, 1965)

(19) M. Abramotwitz and I. Stegun, *Handbook of Mathematical Functions*, (Dover, New York, 1970)

(20) S. M. Sze, *Physics of Semiconductor Devices*, (2ed. Wiley, New York, 1981)

(21) W. C. Dash and R. Newmann, *Phys. Rev.*, **99**, 1151, (1955)

Chapter 5

(1) W. Van Roosbroeck, *Phys. Rev.*, **91**, 282, (1953)

(2) T. Wilson and P. D. Pester, *Phys. Stat. Sol.(a)*, **97**, 323, (1986)

(3) P. M. Morse and H. Feshbach, *Methods of Theoretical Physics*, (Mc Graw-Hill, New York, 1953)

(4) P. D. Pester and T. Wilson, *Phys. Stat. Sol.(a)*, **105**, 649, (1988)

(5) H. S. Carslaw and J. C. Jeager, *Conduction of Heat in Solids*, (Oxford University Press, 1959)

(6) M. Abramowitz and I. Stegun, *Handbook of Mathematical Functions*, (Dover, New York, 1970)

(7) P. D. Pester and T. Wilson, *Phys. Stat. Sol.(a)*, **106**, 577, (1988)

(8) T. Wilson and P. D. Pester, *IEEE Trans. Electron Devices*, **ED-34**, 1564, (1987)

(9) P. D. Pester and T. Wilson, *J. Appl. Phys., In Press*

(10) T. Wilson and P. D. Pester *Optik*, **76**, 18, (1987)

(11) T. Wilson and E. M. McCabe, *J. Appl. Phys.*, **61**, 191, (1986)

Chapter 6

(1) L. Reimer, *Scanning Electron Microscopy*, (Springer, Berlin, 1985)

(2) D. E. Newbury, D. C. Joy, P. Echlin, C. E. Fiori and J. I. Goldstein, *Advanced Scanning Electron Microscopy and X-Ray Analysis*, (Plenum, New York, 1986)

(3) T. Wilson and C. J. R. Sheppard, *Theory and Practice of Scanning Optical Microscopy*, (Academic Press, London, 1984)

(4) F. S. Goucher, G. L. Pearce, Sparks, Teal and W. Schockley, *Phys. Rev.*, **81**, 637, (1951)

(5) F. Berz and H. K. Kuiken, *Sol. St. Elect.*, **19**, 437, (1976)

(6) C. Hu and C. Drowley, *Sol. St. Elect.*, **21**, 965, (1978)

(7) W. H. Hackett, *J. Appl. Phys.*, **43**, 1649, (1972)

(8) W. Van Roosbroeck, *J. Appl. Phys.*, **26**, 380, (1955)

(9) G. H. Bryan, *Proc. Camb. Phil. Soc.*, **7**, 246, (1891)

(10) G. H. Bryan, *Proc. Lond. Math. Soc.*, **22**, 424, (1891)

(11) H. S. Carslaw, *Phil. Mag.*, **4**, 162, (1902)

(12) E. W. Hobson, *Proc. Lond. Math. Soc.*, **19**, 279, (1887)

(13) H. S. Carslaw and J. C. Jeager, *Conduction of Heat in Solids*, (Oxford Univ. Press, Oxford, 1959)

(14) G. Adam, *Physica*, **20**, 1037, (1954)

(15) T. H. DiStefano, in *Nondestructive Evaluation of Semiconductor Materials and Devices.*, (Plenum, New York, 1979)

(16) T. Wilson and P. D. Pester, *J. Appl. Phys.*, **61**, 2307, (1987)

(17) I. S. Gradsteyn and I. M. Ryzhik, *Tables of Integrals, Series and Products*, (Academic Press, New York, 1980)

(18) G. N. Watson, *A Treatise on the Theory of Bessel Functions*, (Cambridge University Press, Cambridge, 1966)

(19) T. Wilson and P. D. Pester, *Optik*, **76**, 18, (1987)

(20) R. A. Colclaser, *Microelectronics: Processing and Device Design*, (Wiley, New York, 1980)

Chapter 7

(1) T. H. DiStefano, in *Non Destructive Evaluation of Semiconductor Materials and Devices*, (Plenum, New York, 1970)

(2) R. J. Nelson, *Inst. Phys. Conf. Ser.*, **45**, 256, (1978)

(3) J. Marek, A. G. Elliot, V. Wilke and R. Geiss, *Appl. Phys. Lett*, **49**, 1732, (1986)

(4) P. L. Gourley, M. Longerbone, S. L. Zhang and H. Morkoç, *Appl. Phy. Lett*, **51**, 599, (1987)

(5) D. Guidotti, J. S. Batchelder, J. A. Van Vechten and A. Finkel, *Appl. Phy. Lett*, **48**, 68, (1986)

(6) D. E. Ioannou and R. J. Redhill, *J. Appl. Phys.*, **56**, 1797, (1984)

(7) G. W. t'Hooft and C. Van Opdorp, *J. Appl. Phys.*, **60**, 1065, (1986)

(8) T. Wilson and P. D. Pester, *J. Appl. Phys.*, **63**, 873, (1988)

(9) H. S. Carslaw and J. C. Jeager, *Conduction of Heat in Solids*, (Oxford University Press, 1959)

Appendix A

(1) M. Abromowitz and I. Stegun, *Hanbook of Mathematical Functions*, (Dover, New York, 1970)

Appendix B

(1) I. S. Gradshteyn and I. M. Ryzhik, *Tables of Integrals, Series, and Products*, (Academic Press, Orlando, 1980)

ERRATUM

P D PESTER
D.PHIL. THESIS 1988

PAGE:

3-6	Last line: ..... exponents in Equation (3.24) to be ..... Should read: ..... exponents in Equation (3.23) to be .....
3-8	First line: ..... $\nu = \Delta/2$ ..... Should read: ..... $\nu = 2\Delta$ .....
3-28	7th line from bottom: ..... wavelength incident of ..... Should read: ..... wavelength of .....
4-14	Figure 4.7(b): x-scale should read w/d
5.3	Equation 5.8: $\partial^2/\partial Z$ Should read: $\partial^2/\partial Z^2$
5.10	Figure 5.4 figure caption: ..... Equation (5.27) ..... Should read: .....Equation (5.24) and; ..... Equation (5.26) ..... Should read: ..... Equation (5.23)
5.20	Equation 5.54: dr_r Should read: dr_o
6-10	Line 7: ..... In[Io(ξ)] ..... Should read: ..... In[I(ξ)] .....

SPELLING ERRORS

Page	Line	Word
iv	3	encouragement
1-5	2	necessary
3.11	18	semiconductor
3.36	Figure 3.22 Caption	coefficient
4.3	23	differentiation
6.1	2	geometries
6-5	5	integral
6-17	12	Schottky
7-10	21	arrive